Stability Theory and Hamiltonian Dynamics in the Euler Ideal Fluid Equations

Joachim Worthington

A thesis submitted in fulfilment of
the requirements for the degree of
Doctor of Philosophy

School of Mathematics and Statistics
Faculty of Science
University of Sydney

May 2017

Statement of Authorship

This is to certify that to the best of my knowledge, the content of this thesis is my own work. This thesis has not been submitted for any degree or other purposes.

This thesis contains material from

- Holger R. Dullin, Robert Marangell, and Joachim Worthington. "Instability of Equilibria for the Two-Dimensional Euler Equations on the Torus." *SIAM Journal on Applied Mathematics* 76.4 (2016): 1446-1470.
- Holger R. Dullin and Joachim Worthington. "Stability Results for Idealised Shear Flows on a Rectangular Periodic Domain." *In Submission*, arXiv preprint arXiv:1608.06109 (2016).

Chapters 2 and 3 are largely based on material included in these two papers, which has been substantially extended and rewritten for inclusion here. I was the lead author and corresponding author for both these papers.

I certify that the intellectual content of this thesis is the product of my own work and that all the assistance received in preparing this thesis and sources have been acknowledged.

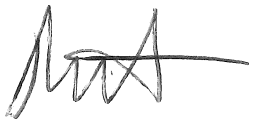

Joachim Worthington
30/03/2017

As supervisor for the candidature upon which this thesis is based, I can confirm that the authorship attribution statements above are correct.

Holger Dullin
30/03/2017

Acknowledgements

I would like to extend my deepest gratitude to my supervisor Holger Dullin and my associate supervisor Robert Marangell. Holger's broad and systematic knowledge has made me a better mathematician, but his kindness and patience has made me a better person, and I will always be grateful for this. I could not have asked for a better mentor and role model. Robby's creativity and enthusiasm has led to dozens of ideas that would've never occurred to me, and his generosity and positivity was a welcome reassurance during inevitable difficulties. They have made my time as a PhD candidate such a positive experience, and I can't thank them enough for all the time and work they've put in.

I would also like to thank the many people who have made suggestions and helped with the content of this thesis. In particular, James Meiss and Yuri Latushkin made suggestions which led to significant developments in this thesis. Georg Gottwald, Sheehan Olver, and Geoff Vasil also made very useful suggestions and helped with questions I had throughout this thesis.

I would like to thank all the staff in the School of Mathematics and Statistics at the University of Sydney, which has become my second home. The postgraduate coordinators, Samuel Müeller and Marek Rutkowski, have been invaluable in their advice and encouragement. The general staff have made the School of Mathematics a warm and welcoming place to work, and I am very grateful for their assistance. I am also grateful to the many staff who have dedicated time to helping me in my teaching duties, which has been a welcome complement to my research.

Finally I would like to thank my friends and family, particularly Ting-Ying Chang. Their support has reassured and encouraged me throughout my studies. My gratitude for their sympathetic ears and sense of perspective cannot be overstated.

Abstract

The study of shear flow steady states has led to a wealth of research in the field of fluid dynamics. By studying shear flows, we can understand how a fluid behaves and how coherent structures arise. In this thesis, we primarily study the stability of shear flows in the Euler equations. The Euler equations describe the dynamics of an ideal fluid which is incompressible, inviscid, and experiences no external forces. These equations can be formulated as a Poisson system, which we exploit to study stability.

We study the family of shear flows of the Euler equations with vorticity of the form $\Omega(x, y) = \cos(\kappa_x p_x x + \kappa_y p_y y)$ on a two-dimensional periodic domain of size $\left[0, {}^{2\pi}/_{\kappa_x}\right) \times \left[0, {}^{2\pi}/_{\kappa_y}\right)$. We prove that if $p_y = 0$ and $\kappa_x |p_x| < \kappa_y$, this shear flow is linearly stable. If $\sqrt{\kappa_x^2 p_x^2 + \kappa_y^2 p_y^2} > {}^{(3+2\sqrt{3})}/_2$, we prove the corresponding shear flow is nonlinearly unstable. In addition, we discuss the spectrum of the linearisation of shear flows more generally and explore a related Jacobi problem. There is a known Poisson structure preserving truncation of the Euler equations. We prove analogous stability results in this system and discuss the qualitative differences. We extend a previously known Poisson integrator for this truncation of the Euler equations to a general two-dimensional periodic domain.

The Euler equations on a three-dimensional periodic domain are less well-understood. In this domain we formulate the dynamics in terms of the vorticity Fourier modes. This is then used to study shear flows and prove similar stability results as for the two-dimensional case. We show that the linearised equations split into subsystems which have equivalent dynamics to the subsystems of the two-dimensional linearised equations. This is used to prove the existence of a family of linearly stable shear flows, and another of linearly unstable shear flows. For a dense set of parameter values, the linearised system has a nontrivial nilpotent part leading to linear instability. This is linked to the nonnormality of the system, which indicates a transition to turbulence. We also show that the Euler equations on a three-dimensional periodic domain can be formulated as a Poisson system. We finally present some numerical results demonstrating and exploring the results of this thesis.

Contents

Chapter 1

Introduction and Literature

1.1. Introduction

In 1790, Leonard Euler described a set of equations to model the dynamics of an ideal fluid. These equations are now known as the *Euler ideal fluid equations*, or simply Euler equations. Over the subsequent two centuries, the study of these equations has led to an abundance of new mathematical ideas and results. However, many questions still remain unresolved. Our understanding of the dynamics of fluids and gases is constantly improving as we glean further insight into the solutions to the Euler equations.[1]

The Euler equations admit a class of steady states known as *shear flows*. Shear flows are a family of flows with fluid moving parallel to a fixed direction. These flows have been well-studied since the late nineteenth century, inspiring results in the fluid dynamics community and the broader field of dynamical systems. Understanding when shear flows are stable, when they are unstable, and how they lose stability has contributed much towards our understanding of how fluid moves and behaves.

In this thesis, we present a study of the linearised spectrum of shear flows of the Euler equations on a periodic domain with arbitrary side lengths in two and three dimensions. This builds upon and extends previous work and is a step towards a complete description of the spectrum. The techniques and results in this thesis take advantage of a Poisson system formulation of the Euler equations. This structure is not only mathematically convenient and elegant, but very natural to the Euler equations. Approaching the system with this framework allows us to exploit the structure associated with a Poisson system to answer questions about stability.

The key new results of this thesis are as follows. We prove the existence of a family of linearly stable sinusoidal parallel shear flows for the Euler equations on a two-dimensional periodic domain. We further prove that almost all other sinusoidal shear flows are nonlinearly unstable. We then discuss a Poisson structure preserving finite-mode truncation of this system, which leads to the development of an accurate and efficient Poisson integrator. On a three-dimensional periodic

[1] In the electronic version of this document, all references to chapters, sections, figures, and citations can be clicked to take you to the relevant page.

domain we show that the linearised system splits into subsystems equivalent to those that occur in the two-dimensional problem. This allows us to develop related results and show the existence of a set of linearly stable shear flows and another set of linearly unstable shear flows in the three-dimensional problem. However, there are additional technical details related to the nonnormality of the linearised system and the existence of nilpotent subsystems. These are fundamental differences to the two-dimensional shear flows. We finally present a new Poisson structure for the Euler equations on a three-dimensional periodic domain. Numerical experiments are included to analyse and extend these analytic results.

1.2. Background and History

We now summarise the key background for this thesis. The Euler equations are introduced, as well as their broader context in the study of fluid dynamics. Hamiltonian dynamics and stability theory are discussed in the context of hydrodynamical systems. We then discuss structure-preserving Poisson truncations of the Euler equations, and existing work on the use of these truncations. Finally, some related stability results for shear flows in a variety of contexts are presented.

1.2.1. Fluid Dynamics and the Euler Equations. The study of the motion of fluids is known as *hydrodynamics*. The field of hydrodynamics has provided mathematicians and physicists with an abundance of questions, many with deep mathematical implications. An intuitive understanding of fluid behaviour guided the design of ships and aqueducts built by the Romans in the fourth century BCE. The earliest known attempt to formalise these ideas came from Leonardo da Vinci (1452-1519), who computed the equation for the conservation of mass in a steady flow [**Whi99**]. Over the following centuries, the work of experimentalists and mathematicians developed both our understanding of fluid flows and attempts to harness their power for our own means. The results of experimental studies of gas and liquid fluid flows have led to improved designs for aeroplanes, boats, turbines, parachutes, and countless other useful inventions.

In 1757, Leonhard Euler derived the first version of the equations that would come to bear his name, the *Euler equations* of fluid dynamics. The Euler equations describe the dynamics of an ideal fluid. In this context, an ideal fluid is *incompressible* (it has a constant density), *inviscid* (it has zero viscosity and therefore no friction), and does not experience any external force. Euler's fluid dynamics equations are often cited as one of the first examples of a partial differential equation [**Chr07**]. The mathematical analysis of these equations has and led to the development of new fields which continue growing today.

From a mathematical perspective, the Euler equations are a source of many interesting and important research areas and have had a profound impact on the

broader mathematical community [**Con07**]. Study in partial differential equations, dynamical systems, harmonic analysis, integrable systems, and other fields has been inspired and enriched by problems stemming from the Euler equations. Many of these problems remain unsolved [**Yud03, Con07**]. For instance, questions of well-posedness [**Wu97, Wu99**] and the existence of finite-time blowup [**CCF**$^+$] (where singularities arise in finite time from smooth initial conditions) in general remain unresolved in the Euler equations. Mathematically, these are deep question which probe both the limits of our understanding of the differential equations involved and the broader question of the relationship between the model and the physical system it describes. A review of some of the mathematical problems in fluid dynamics can be found in [**FS02, FS03, FS04**].

Among the active areas of research is the study of the Euler equations on a three-dimensional domain, and how this relates to the same equations on a two-dimensional domain. Although the governing equations are superficially the same, the dynamics can exhibit very different behaviours [**GGK00, Con07**]. Many results which are understood for the two-dimensional domain are unknown in the three-dimensional domain [**Gib08**]. Coherent structures such as vortices that are common in the two-dimensional domain are not observed in the three-dimensional domain. This reflects the increased mathematical complexity of the problem in a three-dimensional domain, which can be noted by comparing the number and type of constants of motions for the domains [**YM16**]. A common approach is to discuss flows which are in some sense "between" two-dimensional and three-dimensional flows, such as two-and-a-half dimensional flows [**Gib08**] and epi-two-dimensional flows [**YM16**].

In addition to an analytic approach, a numerical description of the dynamics of a fluid is of great importance to the scientific and industrial communities. In the twentieth and twenty-first centuries, advancements in technology and the parallel development of computational fluid dynamics has meant that flows can be computed relatively quickly to a high degree of accuracy. Computational fluid dynamics is used in many areas, such as aircraft design, weather prediction models, and analysis of pipe flow for transportation of liquids.

As most useful models for effects such as drag rely on the viscosity of the fluid, the Euler equations seemed of little use to experimentalists and engineers. The Euler equations were generalised in the 19th century to the more general *Navier-Stokes equations*, which model the dynamics of a viscous flow (that is, a flow with nonzero viscosity). Although this is a more physically realistic scenario, the equations are usually too difficult to analyse in detail. A compromise was struck in the early twentieth century when it was shown that some flows can be described using *boundary-layer* methods [**AAR01, Whi99, Tay71**]. There a fluid is divided into a small layer with nonzero viscosity near a boundary (either an object or an interface between fluids) and a larger layer with zero viscosity.

The Euler equations can then be used to describe the flow of the inviscid layer, and the Navier-Stokes equation to describe the viscous layer. Thus both the Euler equations and the Navier-Stokes equations are used in modelling the system.

An important question from a mathematical perspective is whether the Euler equations can be considered the zero-viscosity limit of the Navier-Stokes equations, and the relationship between solutions of the two sets of equations [**Con95**]. This is closely related to the question of finite-time blowup; if we have sufficiently smooth initial conditions and no boundary on the domain, then the Euler equations are the limit of the Navier-Stokes equations. Otherwise, the answer is generically unknown except in special cases; for example see [**IP06**].

1.2.2. Steady States, Stability and Turbulence. A key theme in the field of dynamical systems is the study of steady states and equilibria. An *equilibrium* is a state of a system where the dynamics are constant. Reference is often made to a *steady state* of a system; this is a state where some property of the system is unchanging with respect to time. For instance, in ideal fluid flow we consider a steady state where the vorticity is constant with respect to time. However, this constant vorticity induces a nonzero fluid velocity and a nonconstant flow of the system. Thus a steady state is an equilibrium with respect to some frame of reference. A description of the dynamics of a system near a steady state is a powerful step towards understanding the full dynamics of the system, particularly in systems that are too complex to describe in toto.

In particular, the full dynamics of a system can often be inferred from analysing the *stability* of steady states. Intuitively, a steady state is said to be stable if a *perturbation* or small change away from the steady state will not change the dynamics dramatically. Otherwise it is unstable, and after a perturbation the system will move further from the steady state. There are many formal definitions and ideas of stability and instability, all seeking to capture this idea in different ways. The study of stability is of key importance in experimental research; a stable steady state can often be observed, whereas an unstable steady state will almost never occur naturally, or only occur for a short length of time.

In the theory of hydrodynamics, the study of steady states and their stability is of high interest. An early experiment to study this concept was conducted by Osborne Reynolds in 1883 [**Rey83**]. Reynolds described experimental results regarding *laminar flow* in a tube, and the conditions under which laminar flow is lost. Laminar flow is a smooth flow where fluid travels along straight lines. Reynolds observed that by changing the conditions of the experiment, the fluid would transition from laminar flow to a chaotic state we now refer to as a *turbulent flow*. From a dynamical systems perspective, the laminar flow is a stable steady state, and if it becomes unstable as parameters change the flow will transition to a chaotic turbulent flow. This work popularised the concept of the *Reynolds number*, which was originally conceived by Sir George Stokes in 1851 [**Sto51**].

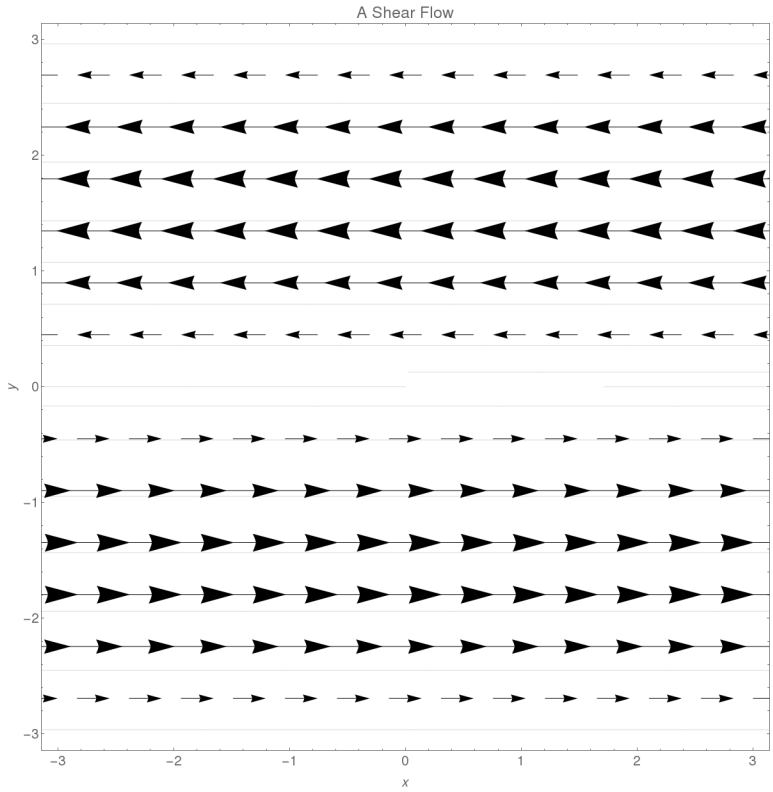

Figure 1.1 – In a shear flow, fluid travels along parallel flow lines, illustrated above. The velocity of fluid on different flow lines varies. Here the fluid flows in two different directions, with sinusoidal velocity profile. As the flow is parallel to the sides of the domain, this is a parallel shear flow.

The Reynolds number of a flow can be calculated by the formula

$$\mathrm{Re} = \frac{\rho v L}{\mu} \tag{1.2.1}$$

where ρ is the density of the fluid, v is the velocity of the flow, L is the characteristic length, and μ is the viscosity. For a low value of the Reynolds number, viscous forces are dominant, and laminar flow is expected. For a high value of the Reynolds number, turbulent flow is expected. Although this is simple enough to experimentally measure and physically justify, it is more difficult to analytically describe how and why the flows lose stability. Of particular note is that the Reynolds number is singular in the "inviscid limit" when $\mu \to 0$. However, this is not to imply that fluids with zero viscosity are necessarily turbulent. The Reynolds number suggests whether the flow will be turbulent or not, but does not provide a mathematical mechanism causing stability or instability to occur.

A *shear flow* is a flow where the flowlines along which the fluid travels are all parallel, but the velocity of flow along such lines can vary. An example of

such a flow is illustrated in Figure 1.1. The laminar flow described by Stokes and Reynolds is an example of such a flow in a tube. Shear flows with zero viscosity were studied by Lord Rayleigh [**Ray79**]. That paper introduced Rayleigh's equation, which is an eigenvalue problem for the evolution of perturbations from a shear flow. From these eigenvalues, one can infer whether such a shear flow is stable or not. This gives a mathematical insight into why and how these flows lose stability, and the transition from stability to instability. This transition is known as the *transition to turbulence*, which is still widely studied today. The equivalent of Rayleigh's equation for a viscous flow is the Orr-Sommerfeld equation, named after William Orr and Arnold Sommerfeld [**Orr07, Som08**].

The causes of a transition to turbulence are not always clear, but many mathematical explanations have been developed. Notably, turbulence often will not appear in a system linearised around a shear flow but will appear in the full nonlinear system. These nonlinear effects are often difficult to analyse. It has been shown [**TTRD93, GG94, BDT95**] that the destabilising effect of the nonlinear dynamics can be predicted by looking at the *normality* of the system. If the eigenvectors of the linearised system are near parallel, perturbations perpendicular to these eigenvectors can become stable on a sufficiently long timescale that nonlinear effects will dominate. This means that although the linearised system will be stable, the nonlinear system can be unstable and turbulence will occur. An explanation and overview of this concept is given by Grossmann in [**Gro00**].

Knowing the stability of steady states in hydrodynamical systems is key to understanding a number of physical phenomena. For instance, *Kelvin-Helmholtz instability* describes an instability that occurs when two layers of a fluid are flowing at different velocities [**Hel68, Tho71**]. This accounts for the structure of the atmosphere in gaseous planets, such as the vortex at the giant red spot on Jupiter. It also explains the dynamics of wind near the surface of a large body of water. Another example is *Rayleigh-Taylor instability* which can occur between two layers of fluid with different densities [**Str83, Tay50**]. Such instabilities occur in interstellar gas and can generate ocean currents. Understanding the mechanisms by which flows lose stability allows more accurate models to be developed and deeper insights to be made.

1.2.3. Poisson Systems and Fluid Mechanics. A useful theoretical framework in the study of hydrodynamic stability is the theory of *noncanonical Hamiltonian systems* or *Poisson systems*. Hamiltonian systems were developed as a reformulation of the principles of Lagrangian mechanics. The theory of Lagrangian mechanics was developed by Lagrange in 1788 to describe Newtonian mechanics in a natural way for a generalised coordinate system. Hamiltonian mechanics reformulates this in terms of the energy of the system, which is physically intuitive. The guiding principal of both Hamiltonian and Lagrangian mechanics is

employing calculus of variations to ensure the principal of least action is satisfied [**Arn78, Mei07**].

Canonical Hamiltonian systems typically describe the dynamics of systems which can be modelled by a particle or set of particles, each with a position and an associated momentum. The position and momentum are conjugate variables with dynamics given by Hamilton's equations. However, the principals of Hamiltonian mechanics can be applied to a broader class of systems which are not necessarily described using such coordinates. *Poisson systems* (also known as noncanonical Hamiltonian systems) generalise Hamiltonian systems to a set of systems whose dynamics can be derived from the principal of least action [**Arn78, MQR98**]. Throughout this thesis, we will frequently formulate the systems we study as Poisson systems, and discuss and exploit the advantages of such a formulation.

One advantage to formulating a problem as a Poisson system is that it allows one to use the ideas and methods of Hamiltonian stability theory. In particular, the conserved quantities of a Poisson system such as the energy and the Casimirs can be fixed and the stability under perturbations that conserve these quantities can be analysed. In fluid dynamics, there have been many successes describing common flow models as Poisson systems. A summary of such systems was compiled by Kolev [**Kol07**].

Arnold [**Arn66b, AK98**] showed that the dynamics of an ideal fluid can be described geometrically by studying the geodesics (or shortest paths) on a Riemannian manifold. Specifically, they are given by the geodesics on the group of volume preserving diffeomorphisms [**Zha08**]. This Hamiltonian system is discussed in depth in Morrison [**Mor98**]. Arnold shows that this structure can be exploited to show that the shear flow with velocity profile $\cos(y)$ is *energy-Casimir stable* in a two-dimensional periodic domain with side length X and 2π if and only if $X < 2\pi$ [**Arn66a, AK98**]. This method relies on restricting perturbations to the subspace defined by fixing the energy and Casimir constants, and is described in [**HMRW85, Mor98**] and in a more general setting in [**PRW04, OPBR05**]. It is a very useful method for showing stability in a strong nonlinear sense, equivalent to Lyapunov stability.

1.2.4. Structure-Preserving Truncations. As discussed in the previous section, there are a number of advantages to describing fluid dynamics with Poisson systems. However, when calculating and analysing flows numerically it is typically not possible to use the full infinite-dimensional systems required to fully capture the Euler equations. Often a Galerkin-style truncation down to some set of important modes is made, and the resulting dynamics analysed [**Ors77**]. However, such a truncation will usually not conserve the Poisson structure.

Fortunately, in the case of the Euler equations in a two-dimensional periodic domain there is a known finite-dimensional truncation that conserves the Poisson

structure. Fairlie and Zachos [**FZ89, FFZ89**] showed that the group of symplectic diffeomorphisms of the torus $\mathbb{T}^2$ is equivalent to the infinite special unitary group $\mathrm{SU}(\infty)$. Thus the finite-dimensional group $\mathrm{SU}(N)$ can be used to approximate the group of symplectic diffeomorphisms on the torus. This was discussed further in [**Hop89, BHSS91, PR90**].

It was then noted by Zeitlin [**Zei91, Zei05**] that this group of symplectic diffeomorphisms could also be used to describe the dynamics of the Euler equations as described by Arnold. This gives an explicit finite-dimensional Poisson system called the *sine-bracket truncation* that approximates the dynamics of the Euler equations. A numerical evaluation of this truncation was completed by Dowker and Wolski [**DW92**]. There is a similar construction on the spherical domain [**Zei04**]; this may have interesting applications for studying the flow of a fluid around a planet or planet-like structure.

An advantage of using this structure preserving truncation over a Galerkin-style truncation is the appearance of Casimir conserved quantities. The sine-bracket truncation described by Zeitlin has a set of Casimirs, with additional Casimirs appearing as the truncation size is increased. These Casimirs can be exploited to study energy-Casimir stability, as discussed above in the untruncated system. They can also be studied from a statistical perspective as in Abramov [**Abr02**] or used to develop a Poisson integrator that conserves the values of the Casimirs as in McLachlan [**McL93**]. This Poisson integrator is discussed and extended in Section 3.3 of this thesis. For comparison, a Galerkin-style truncation is often used in both numerical and analytic studies of the Euler equations [**KB08**]; the two truncations have their uses in different contexts. Peradzynski, Makaruk and Owczarek [**PMO01**] discuss the merits of each truncation in numerical calculations. Shear flows have been studied in the sine-bracket truncated system [**DWM16**], including an energy-Casimir stability result that only exists in the sine-bracket truncated system [**DW16**]. These results are included in this thesis in Chapter 3. There are also interesting results in other systems with equivalent truncations. For instance, the Poisson structure-preserving truncated flow on a sphere [**Zei04**] is integrable for small truncation values [**Dul13**].

1.2.5. Stability Results for the Euler Equations. As the bulk of this thesis is concerned with the stability of shear flows with sinusoidal velocity profiles, we now collect some related results for similar flows. We take care to note the domain size and type, inclusion or exclusion of viscosity, and the type of stability considered, as different studies consider different scenarios.

Consider the shear flow steady state of the ideal fluid Euler equations with velocity of the form

$$\mathbf{v} = \begin{pmatrix} -\Gamma \kappa_y p_y \sin(\kappa_x p_x x + \kappa_y p_y y) \\ \Gamma \kappa_x p_x \sin(\kappa_x p_x x + \kappa_y p_y y) \end{pmatrix} \tag{1.2.2}$$

for some constants $\Gamma \in \mathbb{R}$, $p_x, p_y \in \mathbb{Z}$ on a periodic domain of size

$$\mathcal{D} = \left[-\frac{\pi}{\kappa_x}, \frac{\pi}{\kappa_x}\right) \times \left[-\frac{\pi}{\kappa_y}, \frac{\pi}{\kappa_y}\right) \tag{1.2.3}$$

for constants $\kappa_x, \kappa_y \in \mathbb{R}^+$. The Euler equations themselves and the associated domain are discussed in detail in Section 2.2.

Such sinusoidal shear flows and their stability have been studied in many forms and with many approaches. Rayleigh's equation [**Ray79**] is used to study parallel shear flows. Parallel shear flows are equivalent to (1.2.2) with $p_x = 0$ or $p_y = 0$; for a sinusoidal shear, these flows have the form

$$\mathbf{v} = \begin{pmatrix} \sin(\kappa_y p_y y) \\ 0 \end{pmatrix}. \tag{1.2.4}$$

Rayleigh studied parallel shear flows in a pipe flow. For a pipe flow, the domain can be modelled as having no boundary in the y direction and walls at the boundary in the x direction. For such a domain, Rayleigh's criterion can be used to determine eigenvalues and conclude the stability or instability of a flow. Such systems are widely studied today, particularly in relation to the transition to turbulence [**MMSE09, AWH10, AMdL$^+$11**].

Arnold described the Euler equations with the periodic domain (1.2.3) in a new geometric way; as geodesics on the manifold of volume-preserving diffeomorphisms. With this approach, he proved that the flow with velocity profile $\mathbf{v} = (\sin(\kappa_y y), 0)$ is stable if and only if the domain size satisfies $\kappa_y/\kappa_x \leq 1$ (see [**AK98**] example 4.6; also [**Arn66b, Arn66a**]). To be precise, it was shown that such steady states are *energy-Casimir stable*. This means the steady state is nonlinearly Lyapunov stable under the class of perturbations that preserve the Casimirs. Energy-Casimir stability is discussed in a more general sense in [**WG96, WG98**]. A discussion of how this is used to show the stability of sinusoidal and other parallel shear flows is included in [**DH66**]. A similar approach that also exploits the structure of the system is developed in Hirota, Morrison and Hattori [**HMH14**]. There a condition is developed for linear instability of parallel shear flows by taking a variational approach.

A common area of research is parallel shear flows on a domain periodic in both directions. One can then ask how the size of the domain affects stability. For example, Belenkaya, Friedlander and Yudovich [**BFY99**] studied such inviscid parallel flows on a two-dimensional domain $2\pi/\kappa_x$ periodic in x and $2\pi/\kappa_y$ periodic in y. They calculated curves of spectrum for $p_y < \kappa_x$, and therefore demonstrated instability. In this thesis it is shown that in two and three dimensions these parallel shear flows are linearly stable for sufficiently narrow domains in Theorems 2.6.1 and 4.3.6. Belenkaya et al. also consider highly oscillatory shear flows, as $p_y \to \infty$. Compare this to Section 6.2 of this thesis where we consider the spectrum in the limit $\kappa_x \to 0$. This can in some sense be considered the dual

problem. Similar analysis was completed by Lin [**Lin03, Lin04**] and Butta [**BN10**].

Understanding the mechanisms by which a flow loses stability is of physical importance, as natural processes will introduce perturbations that may differ in character. A discussion of how parallel steady states can lose stability is presented in [**PW82**]. Two distinct ways a parallel shear flow can lose stability are shown. Most notably, they discuss how a parallel shear flow can lose stability through perturbations which are solely parallel to the flow. This corresponds to a disturbance which travels in the same direction as the fluid, and leads to different long-term behaviour than a disturbance travelling perpendicular to the flow.

The related problem of parallel viscous shear flow stability is also well-studied. Meshalkin and Sinai [**MS61**] studied the flow with velocity $\mathbf{v} = (\sin(p_y y), 0)$ (as per Arnold [**AK98**]) in a domain periodic in y only. Notably, that work makes use of continued fraction convergence arguments. Compare this to the arguments in the inviscid problem in [**Li00**] and the Jacobi operator introduced in Section 2.9.4 of this thesis. Beck and Wayne [**BW13**] showed that the corresponding parallel shear flows are "metastable" in the Navier-Stokes equations with a two-dimensional periodic domain. They showed that such shear flows lose stability on a slower timescale than the natural decay of the steady state, and so maintain their structure as they decay.

There are fewer results for general sinusoidal shear flows with vorticity of the form $\mathbf{v} = (-p_y \sin(p_x x + p_y y), p_x \sin(p_x x + p_y y))$ on a square periodic domain. Li [**Li00**] described the splitting of the linearised system into subsystems. He then showed that only finitely many of these subsystems can contribute instability. This suggests a natural description of the type and number of nonimaginary eigenvalues. This thesis continues this idea to describe some of these eigenvalues analytically. Li used a continued fraction type argument to calculate eigenvalues of the linearised inviscid system. Latushkin, Li and Stanislavova [**LLS04**] showed that the continuous spectrum of the linearised system is the full imaginary axis (extending previous work by Shvidkoy and Latushkin [**SL03**]), and provided an upper bound on the number of nonimaginary eigenvalues. Conjecture 6.1.8 presents a result which if proven would sharpen this bound and generalise it to an anisotropic domain. Latushkin et al. also showed that the spectral mapping theorem holds for the linearised Euler equations. Together with the work of Friedlander, Strauss, and Vishik [**FSV97**] this shows that eigenvalues with positive real part in the linearised problem imply nonlinear instability in the Euler equations. This allows us to conclude nonlinear instability from linear instability results. A similar result was previously proven for the Navier-Stokes equations by Yudovich [**Yud65**]. In this thesis, we prove that almost all sinusoidal shear flows are nonlinearly unstable in the two-dimensional domain in Theorem 2.7.53. For

a three-dimensional domain, we prove almost all shear flows are linearly unstable in Theorem 4.4.1.

1.3. Thesis Outline

1.3.1. Motivating Examples. We now present some examples to motivate and illustrate the results of this thesis. A fluid has a velocity $\mathbf{v}$ and a vorticity Ω. The Euler equations for the flow of an ideal fluid are the partial differential equation

$$\frac{\partial \Omega}{\partial t} + \mathbf{v} \cdot (\nabla \Omega) = 0 \tag{1.3.1}$$

and the incompressibility condition

$$\nabla \cdot \mathbf{v} = 0. \tag{1.3.2}$$

We also have the relation

$$\Omega = \nabla \times \mathbf{v} \tag{1.3.3}$$

between the velocity and vorticity. In this thesis we are concerned with the dynamics of these equations on periodic domains in two and three dimensions. In two dimensions the domain is (1.2.3) for constants $\kappa_x, \kappa_y > 0$. On this domain $\mathbf{v} \in \mathbb{R}^2$ and $\Omega \in \mathbb{R}$.

On the two-dimensional periodic domain the Euler equations admit a family of steady states with velocity given by (1.2.2) and vorticity

$$\Omega^* = \Gamma(p_x^2\kappa_x^2 + p_y^2\kappa_y^2)\cos(p_x\kappa_x x + p_y\kappa_y y) \tag{1.3.4}$$

for some constants $p_x, p_y \in \mathbb{Z}$ not all zero and nonzero $\Gamma \in \mathbb{R}$. A key goal of this thesis is to classify the stability and describe the spectrum of these steady states in terms of the p_i, κ_i parameters.

If $p_y = 0$, this is an example of a parallel shear flow. For the case $p_x = 1$, $p_y = 0$ this is the flow described by Arnold in [**Arn66a, AK98**]. Arnold proved that this flow is energy-Casimir stable if and only if $\kappa_y/\kappa_x > 1$. We wish to describe the general class of parallel shear flows for $p_x \in \mathbb{Z}$. For example, consider $p_x = 2$, $p_y = 0$. The shear flow is then given by the velocity

$$\mathbf{v}^* = \begin{pmatrix} 0 \\ \sin(2\kappa_x) \end{pmatrix}. \tag{1.3.5}$$

This flow is illustrated in Figure 1.2.

If we linearise the Euler equations around this shear flow, we discover that number and size of the nonimaginary eigenvalues depends dramatically on the aspect ratio of the domain κ_y/κ_x. This is illustrated in Figure 1.3, which shows the absolute value of the real part of the eigenvalues as a function of the domain size. If $\kappa_y/\kappa_x < 2$, we observe nonimaginary eigenvalues that will occur with Hamiltonian symmetry (that is, if λ is an eigenvalue, so are $-\lambda$ and $\pm\bar{\lambda}$). Thus, there are eigenvalues with positive real part and the shear flow is linearly unstable.

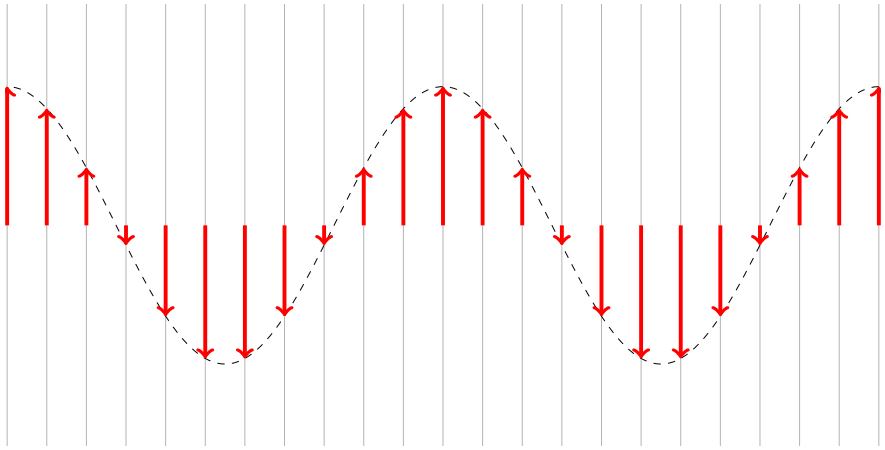

Figure 1.2 – An illustration of the velocity of the parallel shear flow (1.3.5). The red arrows show the direction of the fluid flow, with their length representing magnitude of the velocity. The domain is periodic in both dimensions. This flow is linearly stable for certain domain sizes.

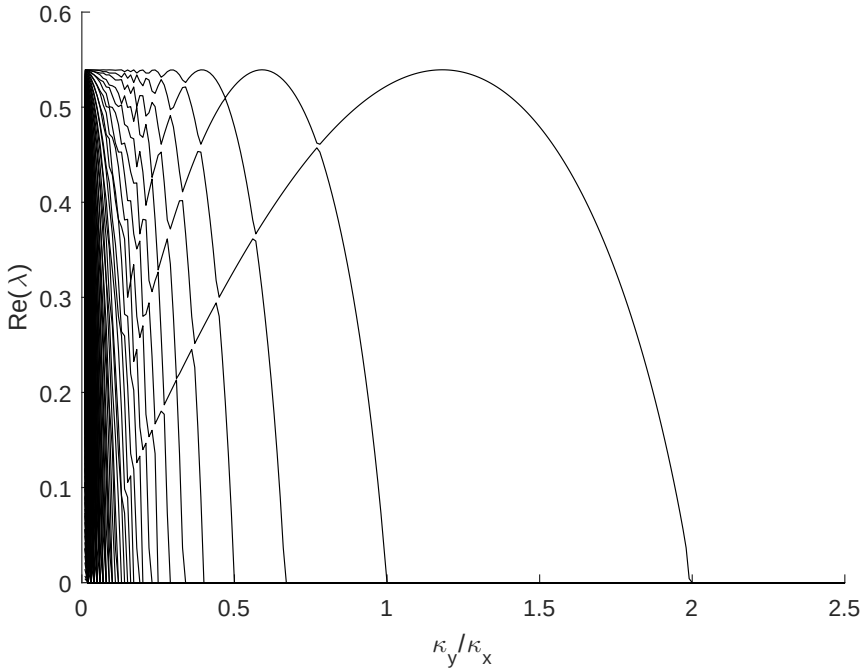

Figure 1.3 – For the shear flow (1.3.5), the positive real part of the eigenvalues of the linearised system as a function of the domain size κ_y/κ_x. Note that for $\kappa_y/\kappa_x > 2$, there are no nonimaginary eigenvalues. Thus the shear flow is linearly stable if and only if $\kappa_y/\kappa_x > 2$.

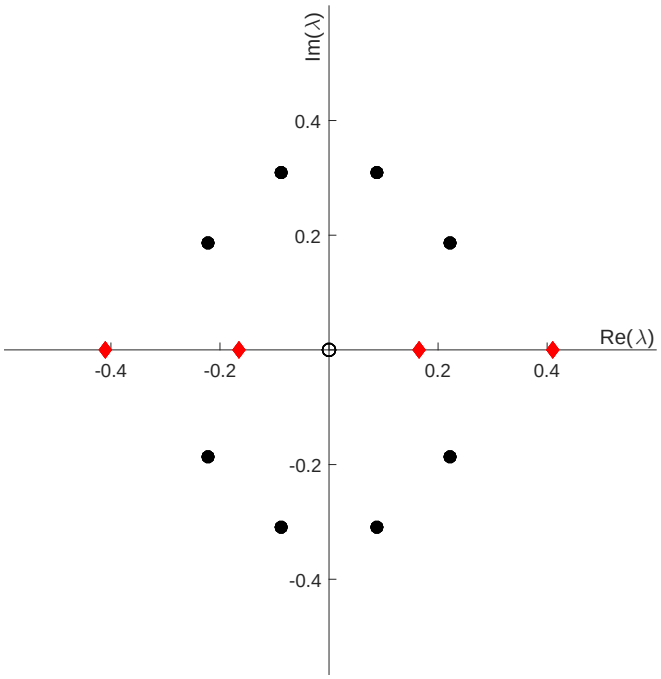

Figure 1.4 – The nonimaginary eigenvalues of the linearisation around the shear flow (1.3.6). As there are eigenvalues with positive real part, the shear flow is linearly unstable. Real eigenvalues are plotted as red diamonds, and complex eigenvalues are plotted as black circles.

By known results [**FSV97, SL03**] this linear instability can be used to confirm the system is nonlinearly unstable.

A more surprising result occurs in the case $\kappa_y/\kappa_x > 2$. For this domain the linearised system is antisymmetric and there are only imaginary eigenvalues. Thus the shear flow is linearly stable. We generalise this result to all parallel flows for appropriate domain sizes in Theorem 2.6.1, which proves the existence of a family of linearly stable parallel shear flows.

A further observation from Figure 1.3 is that as $\kappa_y/\kappa_x \to 0$, there are infinitely many nonimaginary eigenvalues. We will study this numerically in Section 6.2 and show that in this limit, the discrete eigenvalues fill out a set of continuous curves.

For all other shear flows with $p_x, p_y \neq 0$ or $p_y = 0$ and $\kappa_y/\kappa_x < p_x$ we numerically observe that the shear flow is unstable. Consider the shear flow with velocity

$$\mathbf{v}^* = \begin{pmatrix} -\sin(2x+y) \\ 2\sin(2x+y) \end{pmatrix} \tag{1.3.6}$$

on the square domain $\kappa_x = \kappa_y = 1$. We linearise the Euler equations around this flow and calculate the nonimaginary eigenvalues. These eigenvalues are shown

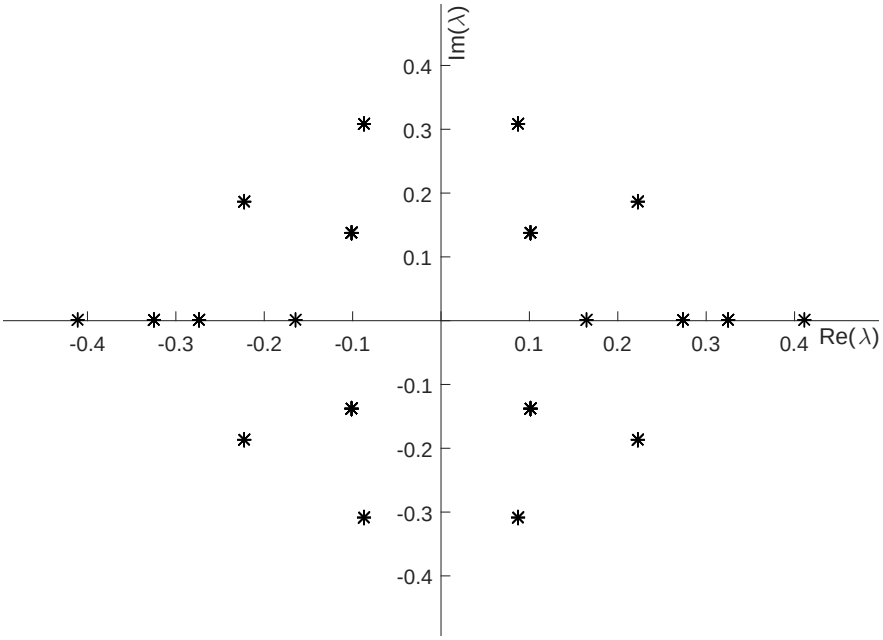

Figure 1.5 – The nonimaginary eigenvalues of the linearisation around the shear flow (1.3.8) in a three-dimensional domain. The domain is the isotropic domain $\kappa_x = \kappa_y = \kappa_z = 1$.

in Figure 1.4. In particular, we observe eigenvalues with positive real part and conclude that the shear flow is linearly unstable. Again, we appeal to the results of [**FSV97, SL03**] to show this shear flow is therefore nonlinearly unstable. In Theorem 2.7.53 we prove an analytical result confirming this instability. We show that for almost all p_x, p_y there exists a lower bound on a positive real eigenvalue. This is a step towards the goal of describing the full linearised spectrum of shear flows of the form (1.2.2). Conjecture 6.1.8 describes this full spectrum, including the number and type of nonimaginary eigenvalues.

In three dimensions the periodic domain has lengths

$$\mathcal{D}_3 = \left[-\frac{\pi}{\kappa_x}, \frac{\pi}{\kappa_x}\right) \times \left[-\frac{\pi}{\kappa_y}, \frac{\pi}{\kappa_y}\right) \times \left[-\frac{\pi}{\kappa_z}, \frac{\pi}{\kappa_z}\right) \tag{1.3.7}$$

and the relevant quantities have different dimensions: $\mathbf{v} \in \mathbb{R}^3$, $\Omega \in \mathbb{R}^3$.

We consider shear flows in this domain. For example, consider the shear flow with velocity

$$\mathbf{v}^* = \begin{pmatrix} -\sin(2x+y) \\ 2\sin(2x+y) \\ 0 \end{pmatrix}. \tag{1.3.8}$$

In the two-dimensional cross section (ignoring dynamics in the third dimension), this is the same flow as (1.3.6). For an isotropic domain with $\kappa_x = \kappa_y = \kappa_z = 1$,

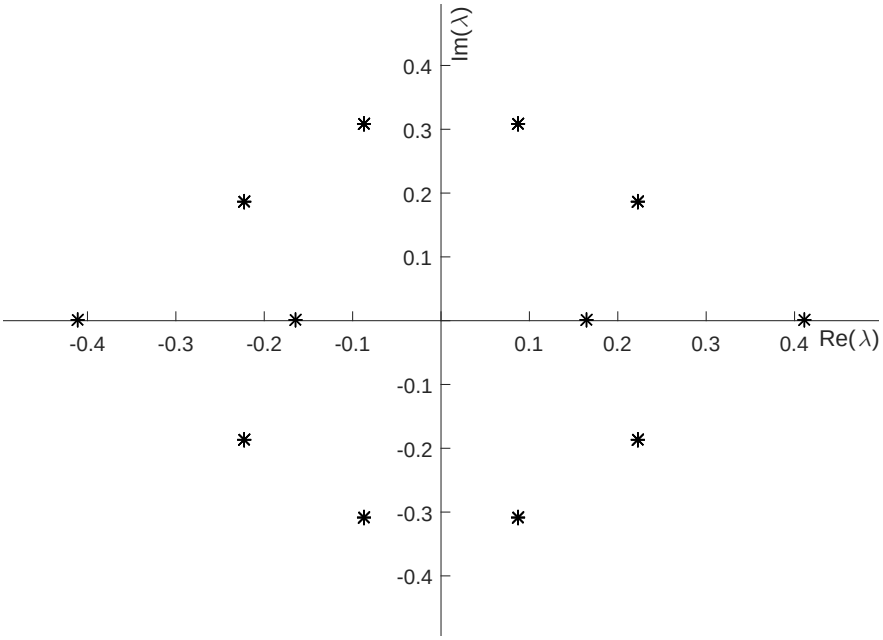

Figure 1.6 – The nonimaginary eigenvalues of the linearisation around the shear flow (1.3.8). The domain $\kappa_x = \kappa_y = 1$, $\kappa_z = 10$ is chosen sufficiently wide in the z dimension so that the spectrum is the same as the spectrum of the linearisation of (1.3.6). This can be noted by comparing the eigenvalue locations with Figure 1.4.

the linearised spectrum is shown in Figure 1.5. As per the two-dimensional domain, there are nonimaginary eigenvalues with positive real parts, and thus instability.

If we take a domain sufficiently wide in the κ_z direction, something interesting happens. The dynamics in the z direction become irrelevant for the nonimaginary spectrum, and the spectrum is shown in Figure 1.6. The nonimaginary eigenvalues have the same values as the nonimaginary eigenvalues of the corresponding two-dimensional flow (1.3.6) shown in Figure 1.4.

In fact, in Chapter 4 we prove that with under appropriate transformations, the spectrum of any linearised shear flow in three dimensions can be described in terms of the spectrum of linearised shear flows in two dimensions. Thus, we can extend the conclusions made for the shear flows in two dimensions, and identify linearly stable and linearly unstable shear flows in three dimensions. For instance, (1.3.8) is linearly unstable, as the spectrum in Figure 1.6 has eigenvalues with positive real part. This shear flow will be linearly unstable for any choice of domain size $\kappa_x, \kappa_y, \kappa_z$. In Theorem 4.4.1 this is proven to be true for all shear flows with vorticity of the form $\Omega^* = 2\mathbf{\Gamma}\cos(\kappa_x p_x x + \kappa_y p_y y + \kappa_z p_z z)$ given that $\kappa_x^2 p_x^2 + \kappa_y^2 p_y^2 + \kappa_z^2 p_z^2 > \left(\sqrt{3} + {}^3\!/_2\right)^2$.

There also exist linearly stable shear flows in the three-dimensional periodic domain. Corresponding to the linearly stable shear flows in two dimensions, consider a flow such as

$$\mathbf{v}^* = \begin{pmatrix} 0 \\ 0 \\ \sin(2x) \end{pmatrix} \tag{1.3.9}$$

equivalent to (1.3.5). If $\kappa_x = 1$ and $\kappa_y, \kappa_z > 2$, the spectrum of the linearisation of this flow is imaginary, and thus the flow is spectrally stable. Unlike the linearisation of (1.3.5), the linearisation is not diagonalisable. This will contribute constant unstable dynamics in the linearised system, so the shear flow (1.3.9) is spectrally but not linearly stable. Compare this to the shear flow

$$\mathbf{v}^* = \begin{pmatrix} 0 \\ \varphi \sin(2x) \\ -\sin(2x) \end{pmatrix} \tag{1.3.10}$$

where $\varphi = \frac{\sqrt{5}+1}{2}$ (chosen because it is the most irrational number in the sense that its continued fraction representation converges very slowly). On a domain with size $\kappa_x = 1,\ \kappa_y = 3,\ \kappa_z = 3$, the shear flow (1.3.10) has no nonimaginary eigenvalues in the linearisation and is therefore spectrally stable. Furthermore, the linearisation is diagonalisable so the flow is also linearly stable. This is due to the choice of $\varphi \notin \mathbb{Q}$, by Proposition 4.2.70. We prove a general result for stable parallel shear flows in Theorem 4.3.6. There is a subtle interdependency between the velocity of the shear flow, the size of the domain, and the resulting stability or instability. In Section 4.2.9, we find a condition for the linearisation to be diagonalisable. In Section 4.3.3 we interpret nondiagonalisable flows in terms of nonlinear instability and transition to turbulence. This is related to the nonnormality of the associated operator.

1.3.2. Chapter by Chapter Outline. In Chapter 2, we study the Euler equations on a two-dimensional periodic domain within a noncanonical Hamiltonian framework. We begin by introducing Poisson dynamics and the related notation and concepts, and prove a theorem showing that the linearisation of a Poisson system around an equilibrium is itself a Poisson system. Next, the Euler equations on a two-dimensional periodic domain are discussed and it is shown that they can be written as a Poisson system. The sinusoidal shear flow steady states with vorticity $\Omega^* = \cos(\kappa_x p_x x + \kappa_y p_y y)$ are introduced, and the linearisation around these states is calculated and shown to block diagonalise into subsystems which we call classes. A simple proof shows that only finitely many of these classes can contribute linear instability. For parallel shear flows $\Omega^* = \cos(\kappa_x p_x x)$ and sufficiently narrow domains, no classes contribute linear instability and we can conclude that the steady state is linearly stable.

We then show that for almost all sinusoidal shear flows not of the stable form we can prove the existence of a positive real eigenvalue. We show that such an eigenvalue must be greater than an explicitly calculated positive lower bound. Combining this with existing results, this implies these shear flows are nonlinearly unstable. We then discuss the full nonimaginary spectrum for the linearisation of the shear flows. A connection is shown between the linearised classes and Jacobi operators; this is used to prove stability results in some exceptional cases. The relationship between the linearised Euler equations, Jacobi operators, and the associated moment problem is an intriguing connection which may shed light on the full spectrum of the linearised system.

In Chapter 3, a finite-mode truncation of the Euler equations that preserves the Poisson structure is discussed. First described by Zeitlin [**Zei91**], this is known as the sine-bracket truncation. We discuss the advantages and disadvantages of the sine-bracket truncation in terms of analytic tractability and numerical usefulness. Many of the stability results for the full system in Chapter 2 are also proven for the sine-bracket truncated system in Section 3.2. In certain cases, the stability results can be strengthened for the sine-bracket truncated system. For certain truncation values there exist energy-Casimir stable parallel shear flows, which are only linearly stable in the untruncated system. We discuss the Poisson integrator developed by McLachlan [**McL93**] for this system and generalise it to an anisotropic domain. This allows for efficient and accurate calculation of flows for the Euler equations.

In Chapter 4, we extend our analysis to shear flows for the Euler equations on a three-dimensional periodic domain. The introduction of a third spatial dimension increases the complexity of the analysis significantly. We formulate the Euler equations as an infinite-dimensional system of differential equations on the Fourier modes of the vorticity. We then describe shear flows in this system analogous to those for the Euler equations on a two-dimensional domain and linearise around such flows. This linearised system decomposes into subsystems naturally. By a series of simplifications and transformations, we show that typically the dynamics of these subsystems reduces to the dynamics of a corresponding linearised subsystem for the two-dimensional domain. Thus we can make conclusions about the linear stability or instability of shear flows in three dimensions by relating them to corresponding shear flows in two dimensions. These stability results are highly sensitive to the original parameters, so the shear flows cannot be strongly stable. This is related the existence and significance of highly nonnormal subsystems, and how they can induce nonlinear instability and a transition to turbulence.

In Chapter 5 we show that there exists a Poisson structure for the Euler equations on a three-dimensional periodic domain. This can be reduced to the divergence-free subspace, which simplifies the space of admissible dynamics. This

result is very promising as it allows us to analyse the structure of the Euler equations in three dimensions using a Hamiltonian framework.

In Chapter 6, numerical results relating to the previous chapters are presented. The spectrum of the linearised Euler equations is explored in detail for two- and three-dimensional domains. This accords with the instability results of Chapters 2 and 4. The numerical results suggest a full description of the nonimaginary spectrum, which is presented as a conjecture. A method for calculating a bound on some nonimaginary eigenvalues is demonstrated, and the continuous spectrum of the sine-bracket truncated system is approximated. We also calculate some sample flows for the sine-bracket truncated system using the Poisson integrator developed in Chapter 3. These flows illustrate the stability results proven in Chapters 2 and 3.

Finally, in Chapter 7 we provide a conclusion and discuss the successes and limitations of this thesis, as well as possible new avenues for future research.

Chapter 2

Stability Theory in the Two-Dimensional Euler Equations

The Euler ideal fluid equations have a class of steady states known as shear flows. In this chapter, we demonstrate the existence of a family of shear flows that are linearly stable on a two-dimensional periodic domain. We also prove that another set of shear flows are nonlinearly unstable. To do so, we first discuss the theory of Poisson systems. We then introduce the Euler equations and formulate them as a Poisson system, which is then linearised around sinusoidal shear flows.

By a generalisation of a known class decomposition to an anisotropic domain, we demonstrate that parallel sinusoidal shear flows are linearly stable for sufficiently narrow domain sizes. For another set of sinusoidal shear flows we calculate an explicit lower bound for a positive real eigenvalue of the linearisation. This allows us to conclude that such shear flows are nonlinearly unstable, and is a first step to a complete description of the spectrum. The full spectrum of linearised shear flows is discussed. Finally, we demonstrate a connection between the subsystems of the linearised Euler equations and an associated Jacobi problem.

2.1. Poisson Dynamics

Many dynamical systems of physical importance have a geometric structure to them in the sense that there exist fundamental structure which remain invariant under their dynamics. This kind of behaviour can be described by a class of dynamical systems called *Hamiltonian systems*. In a classical Hamiltonian system, the evolution of the position and conjugate momentum variables are given by Hamilton's equations. These dynamics then preserve the *symplectic structure* of these variables. Hamiltonian dynamics are commonly used to describe scenarios involving an object or a set of objects with a kinetic energy under the influence of a potential energy. The structure of the equations leads to some simple but powerful ideas; for instance, autonomous systems with Newtonian forces conserve energy so the dynamics lie on surfaces of constant energy. Many problems of astrophysical significance [**DW14**] and equations arising in the field of integrable systems [**DP16**] can be discussed from such a viewpoint, which allows the results and ideas of Hamiltonian mechanics to be employed.

This idea can be generalised to a larger class of systems that do not necessarily have a "position/momentum" dichotomy. Many systems can be written as *Poisson systems* (or *noncanonical Hamiltonian systems*), a generalisation of

Hamiltonian systems. Here, the coordinates used are not constrained to occur in conjugate pairs. However, they must have a *Poisson structure*. If a dynamical system can be written in Poisson form, we have access to a range of techniques applicable to Poisson systems. For instance, we can analyse the Casimirs (constants of motion inherent to a Poisson structure), discuss energy-Casimir stability [**HMRW85, AK98**], and develop integrators that respect the Poisson structure [**Rut83, CH11**].

We begin this chapter by introducing the notation and ideas of Poisson dynamics. We then present a linearisation method for Poisson systems. This demonstrates that under mild assumptions the linearised dynamics of a Poisson system about an equilibrium can also be expressed as a Poisson system which can be calculated simply.

2.1.1. Definitions. We begin by making some basic definitions and introduce the notation associated with Poisson systems.

Definition 2.1.1 (Poisson manifold, Poisson bracket)**.** *A* **Poisson manifold** $(M, \{.,.\})$ *is a smooth manifold endowed with a Poisson Bracket operation.*

A **Poisson bracket** *is a bilinear binary operator*

$$\{.,.\} : C^2(M,\mathbb{R}) \times C^2(M,\mathbb{R}) \to C^2(M,\mathbb{R}) \tag{2.1.2}$$

(where $C^2(M,\mathbb{R})$ is the space of twice-differentiable real-valued functions defined on the manifold M) satisfying the following properties. For all $f, g, h \in C^2(M,\mathbb{R})$, $a \in \mathbb{R}$:

- $\{f,g\} = -\{g,f\}$ *(antisymmetry);*
- $\{f+g,h\} = \{f,h\} + \{g,h\}$, $\{af,g\} = a\{f,g\}$ *(bilinearity));*
- $\{fg,h\} = f\{g,h\} + g\{f,h\}$ *(derivation);*
- $\{f,\{g,h\}\} + \{g,\{h,f\}\} + \{h,\{f,g\}\} = 0$ *(Jacobi property).*

For all such brackets there exists a **Poisson structure matrix** *J (in general dependent on the phase space variables) such that the Poisson Bracket can be written as*

$$\{f,g\} = \nabla f^{\mathsf{T}} J \nabla g. \tag{2.1.3}$$

A discussion of the structure matrix is included in Meiss [**Mei07**].

In terms of the structure matrix $J = (J_{i,j})$, the antisymmetry of the bracket in f and g is equivalent to the antisymmetry of J

$$J^{\mathsf{T}} = -J \tag{2.1.4}$$

and the Jacobi identity is equivalent to the identity

$$\sum_l \left[J_{i,l}\frac{\partial J_{j,k}}{\partial z_l} + J_{j,l}\frac{\partial J_{k,i}}{\partial z_l} + J_{k,l}\frac{\partial J_{i,j}}{\partial z_l} \right] = 0 \tag{2.1.5}$$

for all j, k, i where the phase space coordinates are $z_1, z_2, ..., z_n$ [**Olv00**].

Definition 2.1.6 (Casimir)**.** *A* **Casimir** *of a Poisson system* $(M, \{.,.\})$ *is a function* $C : M \to \mathbb{R}$ *such that* $\{f, C\} = 0$ *for all* f*. Equivalently,* $J\nabla C = 0$*.*

Definition 2.1.7 (Poisson System)**.** *A* **Poisson System** *is a triple* $(M, \{.,.\}, H)$ *where* M *is a Poisson manifold with Poisson bracket* $\{.,.\}$*, and* $H : M \to \mathbb{R}$ *is a real-valued function on the manifold. Then the Poisson dynamics of this system are*

$$\frac{\mathrm{d}}{\mathrm{d}t}z = X_H(z) = \{z, H\} \tag{2.1.8}$$

where $z \in M$*.*

The Casimir functions are constant under the Poisson dynamics as

$$\frac{\mathrm{d}}{\mathrm{d}t}(C) = \{C, H\} = -\{H, C\} = 0 \tag{2.1.9}$$

by definition of a Casimir function. Similarly, the Hamiltonian H is constant as

$$\frac{\mathrm{d}}{\mathrm{d}t}(H) = \{H, H\} = 0 \tag{2.1.10}$$

by the antisymmetry of the bracket (so $\{f, f\} = -\{f, f\} = 0$ for any function f).

2.1.2. Linearising a Poisson System. When linearising around an equilibrium of a Poisson system, the resulting linear system also has a Poisson structure. We can calculate this structure by forming a linear combination of the Hamiltonian and the Casimirs which has vanishing derivative at the equilibrium. Note that in a canonical Hamiltonian system, there are no Casimirs and the gradient of the Hamiltonian always vanishes at an equilibrium.

This process is based on existing ideas; for instance it is part of the stability method outlined in [**HMRW85**] and used in [**DW16**]. We present it in a more explicit form here for clarity and completeness.

Theorem 2.1.11 (Linearising a Poisson System)**.** *Let* $(M, \{.,.\}, H)$ *be a Poisson system with phase space coordinates* x *and structure matrix* $J(x)$*. Let the Casimirs of* $(M, \{.,.\})$ *be* $C_1, ..., C_n$ *for some (possibly zero or infinite)* $n \in \mathbb{N}$*. Let* $x_{\mathrm{eq}} \in M$ *be an equilibrium point of the dynamics of the Poisson system such that* $X_H(x_{\mathrm{eq}}) = 0$ *and assume* $\nabla C_i(x_{\mathrm{eq}})$ *span the kernel of* $J(x_{\mathrm{eq}})$*. Then the linearisation of the flow* X_H *around* x_{eq} *is*

$$\dot{z} = J(x_{\mathrm{eq}})D^2\tilde{H}(x_{\mathrm{eq}})z \tag{2.1.12}$$

where z *are the linearised coordinates around* x_{eq}*, the linearised Hamiltonian is*

$$\tilde{H} = H - \sum_i \alpha_i C_i \tag{2.1.13}$$

and the constants α_i *are chosen so that* $\nabla\tilde{H} = 0$*. This is a Poisson system with structure matrix* $J(x_{\mathrm{eq}})$ *and Hamiltonian* $z^{\mathsf{T}}D^2\tilde{H}z$*.*

Proof. As x_{eq} is an equilibrium of the Poisson dynamics, $J(x_{\text{eq}})\nabla H(x_{\text{eq}}) = 0$ and so $\nabla H(x_{\text{eq}}) \in \ker(J(x_{\text{eq}}))$. By assumption, at x_{eq} the gradients $\nabla C_i(x_{\text{eq}})$ span the kernel of $J(x_{\text{eq}})$, so there exist constants α_i such that

$$\nabla H(x_{\text{eq}}) = \sum_i \alpha_i \nabla C_i(x_{\text{eq}}). \tag{2.1.14}$$

Let $x = x_{\text{eq}} + z$ and linearise at x_{eq}. Then the linearised dynamics are

$$\dot{z} = (J'(x_{\text{eq}})\nabla H(x_{\text{eq}}) + J(x_{\text{eq}})D^2H(x_{\text{eq}}))z. \tag{2.1.15}$$

But linearising the condition $J\nabla C = 0$ for Casimirs gives

$$J'(x_{\text{eq}})\nabla C_i(x_{\text{eq}}) + J(x_{\text{eq}})D^2C_i(x_{\text{eq}}) = 0. \tag{2.1.16}$$

Thus

$$\begin{aligned}
\dot{z} &= (J'(x_{\text{eq}})\nabla H(x_{\text{eq}}) + J(x_{\text{eq}})D^2H(x_{\text{eq}}))z \\
&= \sum_i (\alpha_i J'(x_{\text{eq}})\nabla C_i(x_{\text{eq}}) + J(x_{\text{eq}})D^2H(x_{\text{eq}}))z \\
&= \sum_i (-\alpha_i J(x_{\text{eq}})D^2C_i(x_{\text{eq}}) + J(x_{\text{eq}})D^2H(x_{\text{eq}}))z \\
&= \sum_i (J(x_{\text{eq}})D^2(\sum_i H - \alpha_i C_i)(x_{\text{eq}}))z \\
&= J(x_{\text{eq}})D^2\tilde{H}z.
\end{aligned} \tag{2.1.17}$$

This is the vector field of the Poisson system with constant structure matrix $J(x_{\text{eq}})$ and quadratic Hamiltonian $z^{\mathsf{T}}D^2\tilde{H}z$. Note that if H and C_i are quadratic, this Hamiltonian is exactly $\tilde{H}$. □

This procedure will be used in Section 2.4.2.

2.2. The Euler Equations

Our attention now turns to the Euler fluid equations. We begin by introducing some general fluid mechanics notation and ideas, followed by the *Euler equations* for *ideal flow*; that is, flow that is incompressible and inviscid. We restrict our attention to such a flow on a two-dimensional periodic domain. An *anisotropic* domain, i.e. one in which the two periodic boundaries are not equally spaced, is considered; although this may seem a relatively minor point, it can have a dramatic effect on the resulting dynamics of the system. This system has been studied in some detail, for example in [**FSV97, BFY99, Arn66a**], though the isotropic domain is more commonly studied.

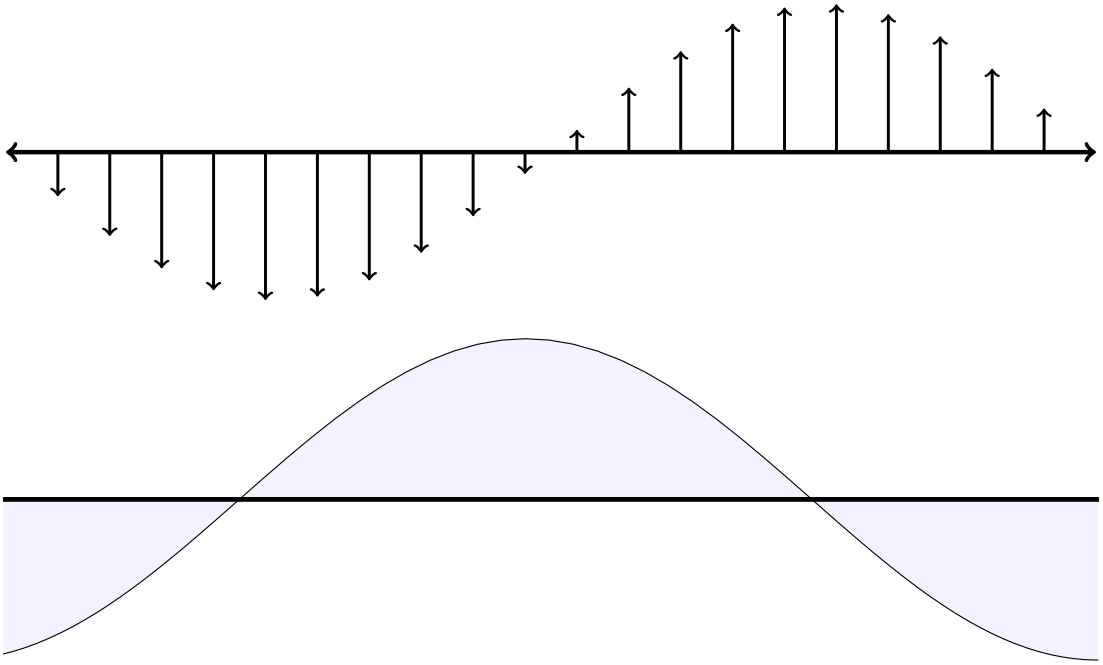

Figure 2.1 – The relationship between the velocity and vorticity of a flow. Top: the velocity of a fluid flowing across a line. Bottom: The corresponding vorticity along this line. When the fluid is shearing around a fixed point, the vorticity is high (in this configuration, positive for anticlockwise, negative for clockwise).

2.2.1. Definitions and Notation. When discussing fluid mechanics, there are two common descriptions of the motion of a fluid (see [**Mey82**] for a discussion) :

- a *Lagrangian description* identifies individual "particles" of fluid, and describes their movement via the position function $\mathbf{x_a}(t)$ for the position of particle $\mathbf{a}$ at time t;
- an *Eulerian description* concerns itself with the fluid flow past a fixed point; the dynamics are described by the *velocity field* $\mathbf{v}(\mathbf{x}, t)$, for the velocity of the fluid passing through the position $\mathbf{x}$ at time t.

We will use the Eulerian convention, as it gives a more useful "global view" of the dynamics of the fluid. If needed, one can recover the Lagrangian description through the time derivative of the velocity field (also known as the *material derivative*; see [**Whi99**]). Call the domain of the fluid flow (sometimes called a *fluid domain*) $\mathcal{D}$.

The *fluid velocity* $\mathbf{v}(\mathbf{x}, t)$ is a vector field measuring the velocity of a fluid particle at position $\mathbf{x} \in \mathcal{D}$ at time $t \in \mathbb{R}$, $t \geq 0$. The *vorticity* $\Omega(\mathbf{x}, t)$ is the curl

of the velocity,

$$\Omega = \nabla \times \mathbf{v}. \tag{2.2.1}$$

Vorticity generalises the idea of angular momentum to a fluid. For a flow in two spatial dimensions, Ω is real valued; for three or more spatial dimensions, it is vector valued. The relationship between the velocity and the vorticity is illustrated in Figure 2.1. One can think of vorticity as the rotational force experienced by a pinwheel at a point in the fluid.

An *ideal fluid flow* describes the dynamics of an ideal fluid; that is, a fluid which is

- inviscid (there is no viscosity and therefore no effect of friction),
- incompressible (the density of the fluid is constant),
- and experiences no external forces.

The condition for a flow to be incompressible is that the divergence of the velocity must vanish,

$$\nabla \cdot \mathbf{v} = 0. \tag{2.2.2}$$

For incompressible fluid flow in two dimensions, there exists a *stream function* $\Psi(\mathbf{x}, t)$ which generates the velocity vector field. It satisfies the relation

$$\mathbf{v} = \nabla \times \mathbf{\Psi} \tag{2.2.3}$$

where $\mathbf{\Psi} = (0, 0, \Psi)$ and $\mathbf{v} = (u, v, 0)$ for velocity components u, v. The fluid flows along lines of constant stream function.

Consider the two-dimensional case with spatial coordinates $\mathbf{x} = (x, y)$ and velocity function $\mathbf{v} = (u, v)$ (that is, the fluid velocity is u in the x direction, and v in the y direction). The stream function and vorticity are both real-valued. Equivalently, they can be thought of as vectors in $\mathbb{R}^3$ pointing perpendicular to the (x, y) plane. This becomes a useful analogy when considering three-dimensional flows, as in Chapter 4.

The vorticity is related to the velocity by

$$\Omega = \frac{\partial v}{\partial x} - \frac{\partial u}{\partial y} \tag{2.2.4}$$

and the stream function is related to the velocities by

$$u = \frac{\partial \psi}{\partial y}, \quad v = -\frac{\partial \Psi}{\partial x}. \tag{2.2.5}$$

Thus the stream function is related to the vorticity by

$$\begin{aligned} \Omega &= \frac{\partial}{\partial x}\left(-\frac{\partial \Psi}{\partial x}\right) - \frac{\partial}{\partial y}\left(\frac{\partial \psi}{\partial y}\right) \\ &= -\nabla^2 \Psi. \end{aligned} \tag{2.2.6}$$

2.2.2. The Euler Ideal Fluid Equations. We now define the *incompressible Euler ideal fluid equations*, or Euler equations. These describe the dynamics of an ideal fluid. Written in terms of the vorticity, the Euler equations are the partial differential equation

$$\frac{\partial \Omega}{\partial t} + \mathbf{v} \cdot (\nabla \Omega) = 0 \tag{2.2.7}$$

and the incompressibility condition

$$\nabla \cdot \mathbf{v} = 0. \tag{2.2.8}$$

The Euler equations capture the essence of ideal fluid behaviour. They were first formulated by Euler in the mid-eighteenth century [**Eul55**], and have since held a dramatic influence over the development of many fields of mathematics [**Con07**].

A common use for the Euler equations is in the study of the *free boundary problem* [**CCF**$^+$]. In the free boundary problem, the dynamics of the interface between two fluids or a fluid and a vacuum are studied. An inviscid approximation works well in the case of large Reynolds number (about $\mathrm{Re} > 10^4$). It also is a good approximation in channels with a short duct, such as a wind tunnel with a narrow nozzle [**Whi99**]. One can use ideal fluids to describe the dynamics in appropriate regions, and "patch" these together with solutions for nonzero viscosity to get a full description of the dynamics of a fluid in a more complicated situation.

The Euler equations are also of physical significance as the inviscid limit of the Navier-Stokes equations [**Con95**]. For a two-dimensional domain, the Euler equations exist as the inviscid limit of the Navier-Stokes equations for a smooth initial condition. There is also significant research into the finite-time blowup of the Euler equations [**CCF**$^+$], and the transition to turbulence in the Euler equations [**BM92**].

2.2.3. Euler Equations on a Two-Dimensional Periodic Domain. We now formulate the Euler equations on a periodic domain. There are a number of reasons one may wish to study this problem. From a mathematical point of view, periodicity is very convenient as it allows us to expand the vorticity as a Fourier series. There have also been results showing that behaviours observed in numerical experiments on a periodic domain can also be observed in a real-world experiment with a walled domain [**PW82, Pum96**].

We thus define the periodic domain

$$\mathcal{D}_{\boldsymbol{\kappa}} = \left[-\frac{\pi}{\kappa_x}, \frac{\pi}{\kappa_x}\right) \times \left[-\frac{\pi}{\kappa_y}, \frac{\pi}{\kappa_y}\right) \tag{2.2.9}$$

where $\boldsymbol{\kappa} = (\kappa_x, \kappa_y)$ and κ_x, κ_y are positive. Then the velocity, vorticity and stream function are continuous on this domain. By redefining the units of length,

we assume without loss of generality that

$$|\boldsymbol{\kappa}| = \sqrt{\kappa_x^2 + \kappa_y^2} = 1. \tag{2.2.10}$$

Due to this normalisation, for the two-dimensional case we usually consider the effect of the ratio κ_y/κ_x rather than either individual length.

We introduce some notation to describe this domain: define the *anisotropy matrix*

$$K := \begin{pmatrix} \kappa_x & 0 \\ 0 & \kappa_y \end{pmatrix}. \tag{2.2.11}$$

Define the weighted inner product

$$\langle \mathbf{j}, \mathbf{k} \rangle := (K\mathbf{j})^{\mathsf{T}}(K\mathbf{k}) \tag{2.2.12}$$

and the induced norm

$$|\mathbf{j}|_{\boldsymbol{\kappa}} := \sqrt{\langle \mathbf{j}, \mathbf{j} \rangle}. \tag{2.2.13}$$

Note that in the isotropic case $\kappa_y/\kappa_x = 1$, $K = \mathbb{I}$ and the inner product and norm are the Euclidean dot product and magnitude respectively.

The partial differential equation (2.2.7) can be written as

$$\begin{aligned} \frac{\partial \Omega}{\partial t} &= \frac{\partial \Psi}{\partial x}\frac{\partial \Omega}{\partial y} - \frac{\partial \Psi}{\partial y}\frac{\partial \Omega}{\partial x} \\ \Omega &= -\nabla^2 \Psi \end{aligned} \tag{2.2.14}$$

using (2.2.5). These coupled partial differential equations govern the dynamics of Ω and Ψ.

As Ω is now periodic, we can expand it as a Fourier series in both spatial directions. Define the Fourier coefficients

$$\omega_{\mathbf{j}}(t) := \frac{\kappa_x \kappa_y}{(2\pi)^2} \iint_{\mathcal{D}} \Omega(\mathbf{x}, t) e^{-i\langle \mathbf{j}, K^{-1}\mathbf{x} \rangle} \mathrm{d}x\mathrm{d}y \tag{2.2.15}$$

for each $\mathbf{j} = (j_x, j_y) \in \mathbb{Z}^2$. Note that $\langle \mathbf{j}, K^{-1}\mathbf{x} \rangle = \kappa_x j_x x + \kappa_y j_y y$. We can think of the Fourier coefficients $\omega_{\mathbf{j}}$ as belonging on a $\mathbb{Z}^2$ integer lattice of values of the corresponding mode numbers $\mathbf{j}$. This will be become a very useful way to think about these coefficients. See Figure 2.4 for an example of such a lattice.

Now the vorticity is given by

$$\Omega(\mathbf{x}, t) = \sum_{\mathbf{j} \in \mathbb{Z}^2} \omega_{\mathbf{j}}(t) e^{i\langle \mathbf{j}, K^{-1}\mathbf{x} \rangle}. \tag{2.2.16}$$

As the vorticity is real-valued, we must also impose the condition

$$\omega_{\mathbf{j}} = \overline{\omega_{-\mathbf{j}}}. \tag{2.2.17}$$

Equivalently we can expand the stream function by defining the modes

$$\psi_{\mathbf{j}}(t) := \frac{\kappa_x \kappa_y}{(2\pi)^2} \iint_{\mathcal{D}} \Psi(\mathbf{x}, t) e^{-i\langle \mathbf{j}, K^{-1}\mathbf{x} \rangle} \mathrm{d}x\mathrm{d}y \tag{2.2.18}$$

so

$$\Psi(\mathbf{x},t) = \sum_{\mathbf{j}\in\mathbb{Z}^2} \psi_{\mathbf{j}}(t) e^{i\langle \mathbf{j}, K^{-1}\mathbf{x}\rangle} \tag{2.2.19}$$

and

$$\psi_{\mathbf{j}} = \overline{\psi_{-\mathbf{j}}}. \tag{2.2.20}$$

(Recall that the existence of the stream function is equivalent to (2.2.8) being satisfied.)

We now rewrite (2.2.6) in terms of these coefficients:

$$\begin{aligned}\sum_{\mathbf{j}\in\mathbb{Z}^2} \omega_{\mathbf{j}}(t) e^{i\langle \mathbf{j}, K^{-1}\mathbf{x}\rangle} &= -\nabla^2 \left(\sum_{\mathbf{j}\in\mathbb{Z}^2} \psi_{\mathbf{j}}(t) e^{i\langle \mathbf{j}, K^{-1}\mathbf{x}\rangle} \right) \\ &= \sum_{\mathbf{j}\in\mathbb{Z}^2} (j_x^2\kappa_x^2 + j_y^2\kappa_y^2)\psi_{\mathbf{j}}(t) e^{i\langle \mathbf{j}, K^{-1}\mathbf{x}\rangle}\end{aligned} \tag{2.2.21}$$

so

$$\omega_{\mathbf{j}} = |\mathbf{j}|_{\boldsymbol{\kappa}}^2 \psi_{\mathbf{j}}. \tag{2.2.22}$$

Substituting (2.2.16) and (2.2.19) into (2.2.14),

$$\sum_{\mathbf{j}\in\mathbb{Z}^2} \dot{\omega}_{\mathbf{j}}(t) e^{i\langle \mathbf{j}, K^{-1}\mathbf{x}\rangle} = \kappa_x\kappa_y \sum_{\mathbf{k},\mathbf{l}\in\mathbb{Z}^2} (k_x l_y - k_y l_x)\omega_{\mathbf{k}}\psi_{\mathbf{l}} e^{i\langle \mathbf{k}+\mathbf{l}, K^{-1}\mathbf{x}\rangle} \tag{2.2.23}$$

(where $\dot{z} = \frac{\mathrm{d}z}{\mathrm{d}t}$ is the usual time derivative) so

$$\dot{\omega}_{\mathbf{j}}(t) = \kappa_x\kappa_y \sum_{\mathbf{k}+\mathbf{l}=\mathbf{j}} \mathbf{l}\times\mathbf{k}\, \omega_{\mathbf{l}}\psi_{\mathbf{k}}. \tag{2.2.24}$$

We have here used the notation $\mathbf{j}\times\mathbf{k} = j_x k_y - j_y k_x$ for all $\mathbf{j},\mathbf{k}\in\mathbb{R}^3$. This is a projection of the usual cross product down from $\mathbb{R}^3\times\mathbb{R}^3\to\mathbb{R}^3$ to $\mathbb{R}^2\times\mathbb{R}^2\to\mathbb{R}$.

Note that

$$\begin{aligned}\dot{\omega}_{\mathbf{0}}(t) &= \kappa_x\kappa_y \sum_{\mathbf{k}} (-\mathbf{k}\times\mathbf{k})\omega_{\mathbf{k}}\psi_{\mathbf{l}} \\ &= 0.\end{aligned} \tag{2.2.25}$$

Thus $\omega_{\mathbf{0}}$ is constant. This corresponds to the fact that on a periodic domain, there is zero net circulation, so the average vorticity over the whole domain is zero. Thus $\omega_{\mathbf{0}} = 0$ as discussed in [**BW13**] for example.

Now the dynamics of Fourier coefficients are governed by the differential equations

$$\dot{\omega}_{\mathbf{j}}(t) = \kappa_x\kappa_y \sum_{\mathbf{k}\neq\mathbf{0}} (\mathbf{k}\times\mathbf{j})\omega_{\mathbf{j}+\mathbf{k}} \frac{\omega_{-\mathbf{k}}}{|\mathbf{k}|_{\boldsymbol{\kappa}}^2}. \tag{2.2.26}$$

Here we have used the identity (2.2.22) and reordered the summation. We can omit the $\omega_{\mathbf{0}}$ term as we know from above that it is constant and zero.

2.3. Hamiltonian Euler Equations

Having introduced the Euler equations, we now write them as a Poisson system, granting us access to the methods discussed in Section 2.1. That such a structure exists in the Euler equations is well known [**MG80**]; see [**Mor06**] for a thorough discussion. The formulation here is simplified by the choice of domain, as we work directly on the Fourier coefficients. We also discuss the Casimirs of the system.

2.3.1. Ideal Fluid Bracket.

Definition 2.3.1 (Ideal Fluid Poisson Bracket)**.** *The ideal fluid Poisson Bracket is given in Fourier Space by*

$$\{f,g\} = \kappa_x\kappa_y \sum_{\mathbf{j},\mathbf{k}} \frac{\partial f}{\partial \omega_{\mathbf{j}}}\frac{\partial g}{\partial \omega_{\mathbf{k}}}(\mathbf{k}\times\mathbf{j})\omega_{\mathbf{j}+\mathbf{k}}. \tag{2.3.2}$$

The corresponding (infinite dimensional) Poisson structure matrix J has entries

$$J_{\mathbf{j},\mathbf{k}} = \kappa_x\kappa_y(\mathbf{k}\times\mathbf{j})\omega_{\mathbf{j}+\mathbf{k}} \tag{2.3.3}$$

so $\{f,g\} = \sum_{\mathbf{j},\mathbf{k}} J_{\mathbf{j},\mathbf{k}}\frac{\partial f}{\partial\omega_{\mathbf{j}}}\frac{\partial g}{\partial\omega_{\mathbf{k}}}$. Note that J is a matrix indexed by two two-vectors. This is a generalisation of the usual ideal fluid bracket for the square case $K=\mathbb{I}$ (see e.g. [**Li00, Zei91**]). There is some freedom here in whether the factor $\kappa_x\kappa_y$ is included in the Poisson structure or the Hamiltonian; this is true of any constant. We choose to include the factor in the bracket.

We can verify that this Poisson bracket is antisymmetric

$$\begin{aligned} J_{\mathbf{j},\mathbf{k}} &= \kappa_x\kappa_y(\mathbf{k}\times\mathbf{j})\omega_{\mathbf{j}+\mathbf{k}} \\ &= -\kappa_x\kappa_y(\mathbf{j}\times\mathbf{k})\omega_{\mathbf{k}+\mathbf{j}} \\ &= -J_{\mathbf{k},\mathbf{j}} \end{aligned} \tag{2.3.4}$$

and satisfies the Jacobi identity via (2.1.5)

$$\begin{aligned} &\sum_{\mathbf{l}}\left[J_{\mathbf{i},\mathbf{l}}\frac{\partial J_{\mathbf{j},\mathbf{k}}}{\partial\omega_{\mathbf{l}}} + J_{\mathbf{j},\mathbf{l}}\frac{\partial J_{\mathbf{k},\mathbf{i}}}{\partial\omega_{\mathbf{l}}} + J_{\mathbf{k},\mathbf{l}}\frac{\partial J_{\mathbf{i},\mathbf{j}}}{\partial\omega_{\mathbf{l}}}\right] \\ &\quad= \kappa_x\kappa_y\big[J_{\mathbf{i},\mathbf{j}+\mathbf{k}}(\mathbf{k}\times\mathbf{j}) + J_{\mathbf{j},\mathbf{k}+\mathbf{i}}(\mathbf{i}\times\mathbf{k}) + J_{\mathbf{k},\mathbf{i}+\mathbf{j}}(\mathbf{j}\times\mathbf{i})\big] \\ &\quad= \kappa_x\kappa_y\big[(\mathbf{j}\times\mathbf{i})(\mathbf{k}\times\mathbf{j}) + (\mathbf{k}\times\mathbf{i})(\mathbf{k}\times\mathbf{j}) + (\mathbf{k}\times\mathbf{j})(\mathbf{i}\times\mathbf{k}) \\ &\qquad + (\mathbf{i}\times\mathbf{j})(\mathbf{i}\times\mathbf{k}) + (\mathbf{i}\times\mathbf{k})(\mathbf{j}\times\mathbf{i}) + (\mathbf{j}\times\mathbf{k})(\mathbf{j}\times\mathbf{i})\big]\omega_{\mathbf{i}+\mathbf{j}+\mathbf{k}} \\ &\quad= 0 \end{aligned} \tag{2.3.5}$$

by the antisymmetry of the cross product.

The Hamiltonian can be derived from the kinetic energy per unit area

$$\begin{aligned}\mathcal{H} &= \frac{\kappa_x\kappa_y}{(2\pi)^2}\iint_{\mathcal{D}} ||\mathbf{v}||^2 \mathrm{d}x\mathrm{d}y \\ &= \iint_{\mathcal{D}} \Omega\Psi \mathrm{d}x\mathrm{d}y\end{aligned} \tag{2.3.6}$$

(see [**AK98**]).

In terms of the Fourier modes, the Hamiltonian is

$$\mathcal{H} = \sum_{\mathbf{j}\neq\mathbf{0}} \frac{\omega_{-\mathbf{j}}^{\mathsf{T}}\omega_{+\mathbf{j}}}{|\mathbf{j}|_{\boldsymbol{\kappa}}^2}. \tag{2.3.7}$$

Then the differential equations (2.2.26) are the Poisson equations $\dot{\omega}_{\mathbf{j}} = \{\omega_{\mathbf{j}}, \mathcal{H}\}$.

2.3.2. Casimirs of the Ideal Fluid bracket. The bracket (2.3.2) has Casimirs corresponding to the *generalised enstrophy invariants* [**AK98, Zei91, YM16**]. For the full system (2.2.7) there exist infinitely many conserved quantities of the form

$$\mathcal{C}_f = \iint_{\mathcal{D}} f(\Omega)\mathrm{d}\mathbf{x} \tag{2.3.8}$$

for an arbitrary smooth function f. We can define an independent set

$$\mathcal{C}_n = \frac{\kappa_x\kappa_y}{(2\pi)^2}\iint_{\mathcal{D}} \Omega^n \mathrm{d}\mathbf{x} \tag{2.3.9}$$

for $n \in \mathbb{N}$ (we have divided through by the area of $\mathcal{D}$ for convenience). In Fourier space, this becomes

$$\mathcal{C}_n = \sum_{\mathbf{j}_i} \omega_{\mathbf{j}_1}\omega_{\mathbf{j}_2}...\omega_{\mathbf{j}_n}, \quad \sum_{i=1}^{n}\mathbf{j}_i = \mathbf{0}. \tag{2.3.10}$$

For $n = 1$, $\mathcal{C}_1 = \omega_{\mathbf{0}}$ which we have already verified is conserved (and identically zero). For $n = 2$,

$$\mathcal{C}_2 = \sum_{\mathbf{j}} \omega_{-\mathbf{j}}\omega_{\mathbf{j}} \tag{2.3.11}$$

the usual enstrophy [**Con07**]. This enstrophy has units of (length/time)^2.

The enstrophy is a useful quantity in the study of turbulent flows in the Navier-Stokes equations [**FMRT01**]. We will also see that a key difference between two- and three-dimensional flow is the number and type of constants; in the three-dimensional domain, there are no enstrophy invariants, instead replaced by the *helicity* (see Section 4.1.2).

2.4. Shear Flows and Linearisation

The Euler equations have a family of steady states called *shear flows*. Shear flows are flows in which there is a cross-sectional velocity/vorticity profile across the domain (see Figure 2.2). These flows are well-studied. For instance, the Rayleigh Criterion [**AK98**] gives a necessary but not sufficient condition for instability of such flows. As we have periodic boundaries, such a profile can be oriented in essentially any direction.

We focus specifically on sinusoidal shear flows, which become simple in the Fourier coefficient space. The Poisson formulation of the Euler equations is linearised using Theorem 2.1.11, and as a result we obtain the linearised equations as a Poisson system. We then observe the known results that this linear system decouples into infinitely many subsystems or "classes" of interdependent modes, all governed by linear Poisson systems.

2.4.1. Steady States. The partial differential equation (2.2.7) with periodic boundary conditions (2.2.9) admits a general family of steady state solutions of the form

$$\begin{aligned} \Psi^* &= f(\langle \mathbf{p}, K^{-1}\mathbf{x}\rangle) \\ \Omega^* &= -|\mathbf{p}|_{\boldsymbol{\kappa}}^2 f''(\langle \mathbf{p}, K^{-1}\mathbf{x}\rangle) \end{aligned} \tag{2.4.1}$$

for any fixed $\mathbf{p} \in \mathbb{Z}^2$ and smooth 2π periodic function $f : \mathbb{R} \to \mathbb{R}$. We can verify that this is a steady state:

$$\begin{aligned} \frac{\partial \Omega}{\partial t} &= \frac{\partial \Psi}{\partial x}\frac{\partial \Omega}{\partial y} - \frac{\partial \Psi}{\partial y}\frac{\partial \Omega}{\partial x} \\ &= (\kappa_x p_x f')(-\kappa_y p_y |\mathbf{p}|_{\boldsymbol{\kappa}}^2 f''') - (\kappa_y p_y f')(-\kappa_x p_x |\mathbf{p}|_{\boldsymbol{\kappa}}^2 f''') \\ &= 0. \end{aligned} \tag{2.4.2}$$

A specific example is the family of *sinusoidal shear flows* with vorticity given by $\Omega^* = \alpha\cos(\langle \mathbf{p}, K^{-1}\mathbf{x}\rangle) + \beta\sin(\langle \mathbf{p}, K^{-1}\mathbf{x}\rangle)$ for constants $\alpha, \beta \in \mathbb{R}$. We will focus our attention on this case. Note that we can write $\Omega^* = 2\Gamma\cos(\langle \mathbf{p}, K^{-1}\mathbf{x}\rangle + \theta)$, where $\theta = \pm\tan^{-1}\left(\frac{-\beta}{\alpha}\right)$ and $\Gamma = \pm\frac{\sqrt{\alpha^2+\beta^2}}{2}$. The signs of θ and Γ will depend on the signs of α and β. If $\alpha = 0$, then take $\theta = \frac{\pi}{2}$. Define $\mathbf{c} = \frac{\theta}{|\mathbf{p}|^2}K\mathbf{p}$, so $\Omega^* = 2\Gamma\cos(\langle \mathbf{p}, K^{-1}(\mathbf{x}+\mathbf{c})\rangle)$. Thus by taking the translation by $\mathbf{c}$ we need only consider the steady states with vorticity of the form

$$\Omega^* = 2\Gamma\cos(\langle \mathbf{p}, K^{-1}\mathbf{x}\rangle). \tag{2.4.3}$$

An example is illustrated in Figure 2.2. As (2.2.7) is symmetric in both spatial directions, we need only consider values of $\mathbf{p} = (p_x, p_y)$ with $p_x, p_y \geq 0$. The corresponding stream function is

$$\Psi^* = \frac{2\Gamma}{|\mathbf{p}|_{\boldsymbol{\kappa}}^2}\cos(\langle \mathbf{p}, K^{-1}\mathbf{x}\rangle) \tag{2.4.4}$$

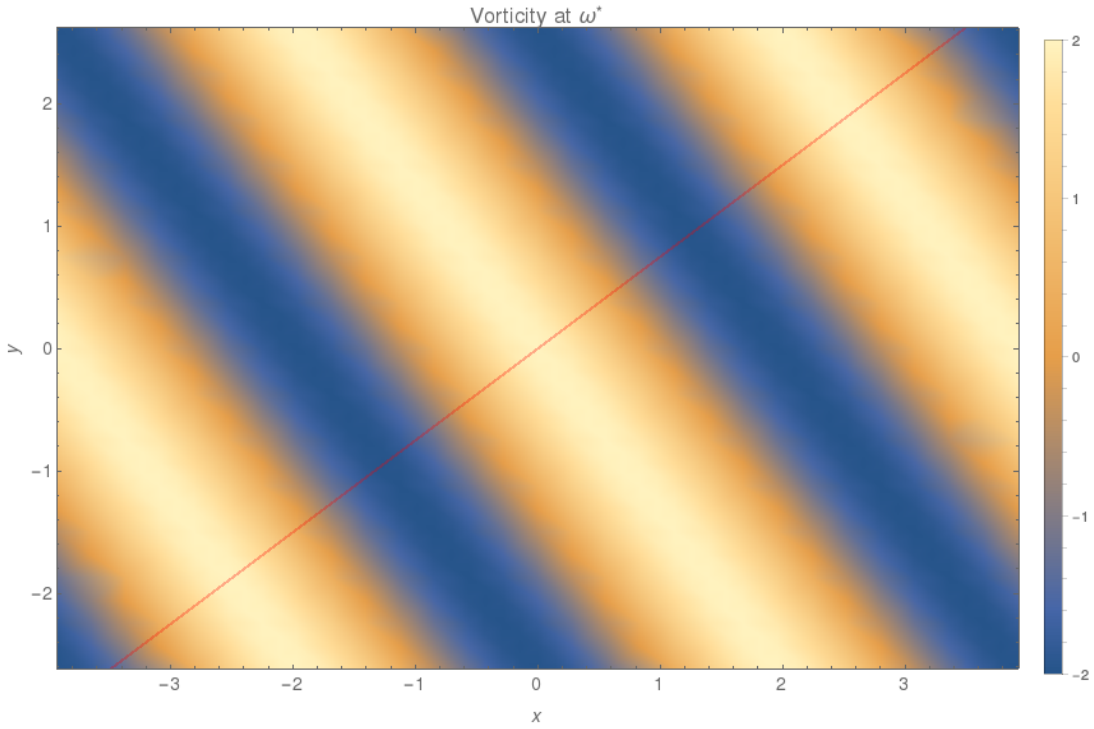

Figure 2.2 – The vorticity associated with the steady state (2.4.3). The parameters are $\mathbf{p} = (2, 1)$, $\kappa_y/\kappa_x = 1.5$, and $\Gamma = 1$. The colours indicate the vorticity at a point, orange for high vorticity and blue for low vorticity. A red line shows the vector $K\mathbf{p}$; this is perpendicular to the contours of constant vorticity. The boundaries are periodic. Compare with Figure 2.3, which shows the corresponding velocity.

and the velocity is

$$\mathbf{v}^* = \frac{2\Gamma}{|\mathbf{p}|^2_{\boldsymbol{\kappa}}} \sin(\langle \mathbf{p}, K^{-1}\mathbf{x} \rangle) \begin{pmatrix} -\kappa_y p_y \\ \kappa_x p_x \end{pmatrix}. \tag{2.4.5}$$

The velocity vector field is illustrated in Figure 2.3.

This steady state is an example of a shear flow, which has been well studied. Many works [**Arn66a, FSV97, BFY99**] study *parallel shear flows*, where $\mathbf{p} = (p_x, 0)$ or $\mathbf{p} = (0, p_y)$. They are a subset of the full set of steady states for an ideal fluid described in [**Li00**]. Equivalent flows in the Navier-Stokes equation with an exponentially decaying factor are studied in [**BW13**] and referred to as "bar states" [**YMC03**].

Written in Fourier space, the steady state (2.4.3) is and equilibrium given by

$$\omega^*_{\mathbf{j}} = \begin{cases} \Gamma & \text{if } \mathbf{j} = \pm\mathbf{p} \\ 0 & \text{otherwise.} \end{cases} \tag{2.4.6}$$

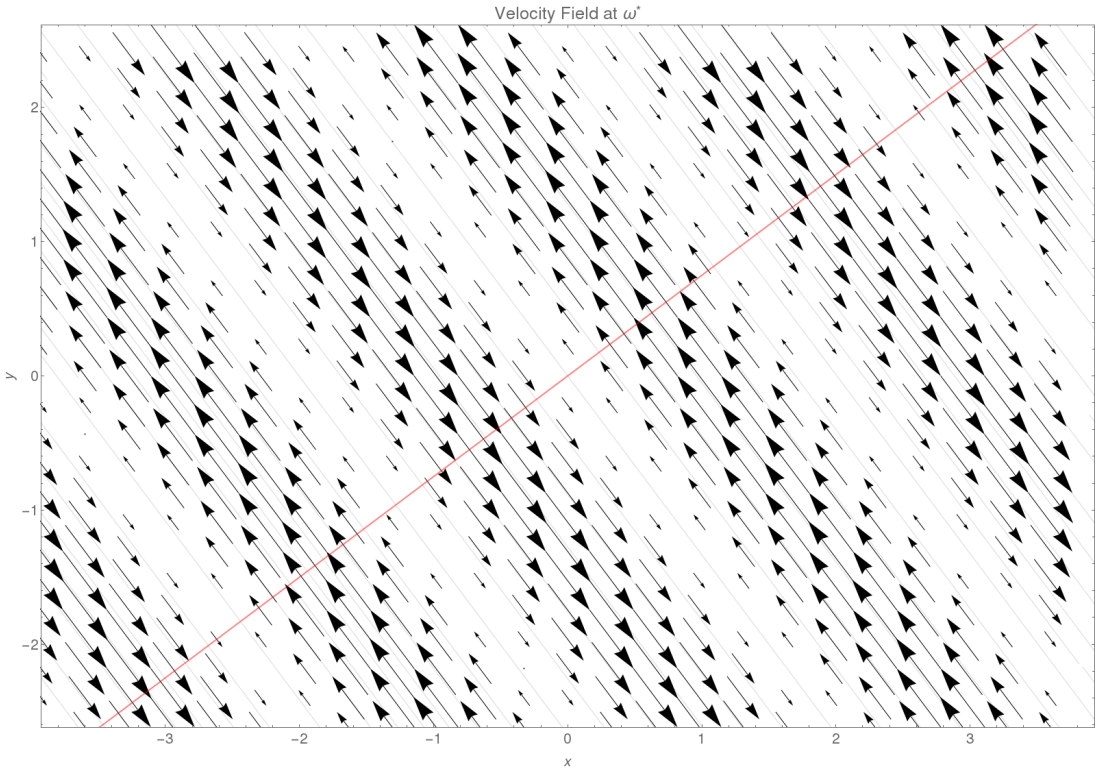

Figure 2.3 – The vector field of the velocity corresponding to the steady state (2.4.3). The same parameter values as in Figure 2.2 are used. The red line indicates the vector $K\mathbf{p}$; flow is always perpendicular to this vector. One can observe the shearing effect as the velocity changes magnitude and direction along this line. Compare with Figure 2.1, which shows the corresponding vorticity.

Note that the general shear flow steady state (2.4.1) can be characterised as an equilibrium in Fourier space where only modes of the form $\omega_{k\mathbf{p}}$ are nonzero.

2.4.2. Linearisation and Class Decomposition. We now linearise the Poisson system given by the bracket (2.3.2) and Hamiltonian (2.3.7) around the equilibrium (2.4.6). We will follow the procedure described in Section 2.1.2.

As the bracket(2.3.2) is noncanonical, $\nabla\mathcal{H}|_{\Omega^*}$ is not necessarily zero. In fact,

$$\nabla\mathcal{H}|_{\Omega^*} = \frac{\Gamma}{|\mathbf{p}|^2_{\boldsymbol{\kappa}}}(\omega_{-\mathbf{p}}\mathbf{e}_{\mathbf{p}} + \omega_{\mathbf{p}}\mathbf{e}_{-\mathbf{p}}) \tag{2.4.7}$$

where $\mathbf{e_j}$ is the unit vector pointing in the direction of $\omega_{\mathbf{j}}$. Similarly, the derivative of the Casimir (2.3.11) at the equilibrium is

$$\nabla\mathcal{C}_2|_{\Omega^*} = \Gamma(\omega_{-\mathbf{p}}\mathbf{e}_{\mathbf{p}} + \omega_{\mathbf{p}}\mathbf{e}_{-\mathbf{p}}). \tag{2.4.8}$$

We must find a linear combination of the Hamiltonian and the Casimirs such that the gradient vanishes at the equilibrium in order to apply Theorem 2.1.11. This is straightforward; define

$$\tilde{\mathcal{H}} = \mathcal{H} - \frac{1}{2|\mathbf{p}|^2_{\boldsymbol{\kappa}}}\mathcal{C}_2 = -\frac{1}{2}\sum_{\mathbf{j}\neq\mathbf{0}} \rho_{\mathbf{j}}\omega_{-\mathbf{j}}\omega_{\mathbf{j}}, \tag{2.4.9}$$

$$\rho_{\mathbf{j}} = \frac{1}{|\mathbf{p}|^2_{\boldsymbol{\kappa}}} - \frac{1}{|\mathbf{j}|^2_{\boldsymbol{\kappa}}}. \tag{2.4.10}$$

Now $\tilde{\mathcal{H}}|_{\Omega^*} = 0$ and $\nabla\tilde{\mathcal{H}}|_{\Omega^*} = \mathbf{0}$.

Next we must linearise the Poisson structure by evaluating the bracket (2.3.2) at the equilibrium. Then

$$J_{\mathbf{j},\mathbf{k}}|_{\Omega^*} = \begin{cases} \kappa_x\kappa_y(\mathbf{p}\times\mathbf{j})\Gamma \text{ if } \mathbf{j}+\mathbf{k}=\mathbf{p}, \\ -\kappa_x\kappa_y(\mathbf{p}\times\mathbf{j})\Gamma \text{ if } \mathbf{j}+\mathbf{k}=-\mathbf{p}, \\ 0 \text{ otherwise.} \end{cases} \tag{2.4.11}$$

Then the new Poisson bracket is

$$\{f,g\}|_{\Omega^*} = \kappa_x\kappa_y\Gamma(\mathbf{p}\times\mathbf{j})\sum_{\mathbf{j}}\left(\frac{\partial f}{\partial\omega_{\mathbf{j}}}\frac{\partial g}{\partial\omega_{\mathbf{p}-\mathbf{j}}} - \frac{\partial f}{\partial\omega_{\mathbf{j}}}\frac{\partial g}{\partial\omega_{-\mathbf{p}-\mathbf{j}}}\right), \tag{2.4.12}$$

which is the nonlinear bracket evaluated at the equilibrium Ω^*. Note this bracket is now constant with respect to the modes, and the Hamiltonian $\tilde{\mathcal{H}}$ is quadratic. Thus this is a linear Poisson system, and (2.4.9) and (2.4.12) together comprise the linearisation of our Poisson system around the steady state. Compare this procedure to the first few steps of the stability "algorithm" described in [**HMRW85**]. We will return to this idea in Sections 2.6.2 and 3.2.4.

Calculating the differential equations for $\omega_{\mathbf{j}}$ explicitly (writing $\omega_{\mathbf{j}}$ for the linearisation about Ω^* from now on)

$$\begin{aligned} \dot{\omega}_{\mathbf{j}} = \{\omega_{\mathbf{j}}, F\} &= \sum_{\mathbf{k}} \kappa_x\kappa_y\Gamma(\mathbf{k}\times\mathbf{j})\omega_{-\mathbf{k}}\rho_{\mathbf{k}}(\delta_{\mathbf{k}+\mathbf{j},\mathbf{p}} + \delta_{\mathbf{k}+\mathbf{j},-\mathbf{p}}) \\ &= \kappa_x\kappa_y\Gamma(\mathbf{p}\times\mathbf{j})\left(\rho_{\mathbf{j}+\mathbf{p}}\omega_{\mathbf{j}+\mathbf{p}} - \rho_{\mathbf{j}-\mathbf{p}}\omega_{\mathbf{j}-\mathbf{p}}\right) \end{aligned} \tag{2.4.13}$$

This shows that the linearised equations decouple into subsystems; the dynamics of the mode $\omega_{\mathbf{a}}$ depend only on the modes $\omega_{\mathbf{a}\pm\mathbf{p}}$, and hence the linearised differential equations split into subsystems consisting of modes $\omega_{\mathbf{a}+k\mathbf{p}}$ for $k\in\mathbb{Z}$. Following the convention of [**Li00**], we refer to each of these subsytems as a *class* of Fourier modes. This idea is illustrated in illustrated in Figure 2.4. In terms of the structure matrix, this means J can be block diagonalised into blocks that govern the dynamics of a class of modes $\omega_{\mathbf{a}+k\mathbf{p}}$.

To make the splitting into subsystems explicit write

$$\tilde{\mathcal{H}} = -\sum_{\mathbf{a}\in\mathcal{A}} H_{\mathbf{a}}, \quad H_{\mathbf{a}} = \frac{1}{2}\sum_{k\in\mathbb{Z}}\rho_k\omega_k^2 \tag{2.4.14}$$

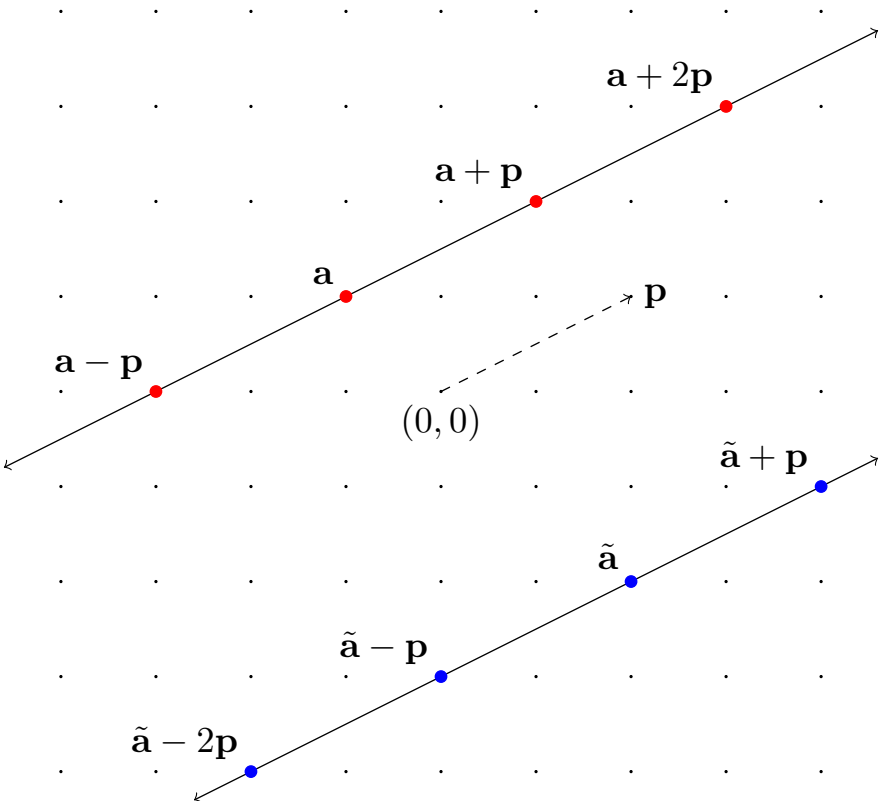

Figure 2.4 – Class decomposition of the linearised system. The dynamics of a mode $\omega_{\mathbf{a}}$ depend only on $\omega_{\mathbf{a}\pm\mathbf{p}}$; extending this, the modes $\omega_{\mathbf{a}+n\mathbf{p}}$ form a subsystem. These modes all lie on the line through $\mathbf{a}$ parallel to $\mathbf{p}$. For this figure, $\mathbf{p}=(2,1)$. There are two classes shown, the class led by $\mathbf{a}=(-1,1)$ (red dots) and the class led by $\tilde{\mathbf{a}}=(2,-2)$ (blue dots).

where $\mathcal{A}$ is the principal domain of mode numbers given by

$$\mathcal{A}=\{\mathbf{a}\in\mathbb{Z}^2 \mid -\frac{1}{2}|\mathbf{p}|_{\boldsymbol{\kappa}}^2<\langle\mathbf{a},\mathbf{p}\rangle\leq\frac{1}{2}|\mathbf{p}|_{\boldsymbol{\kappa}}^2\} \tag{2.4.15}$$

and for a fixed $\mathbf{a}$ we define

$$\omega_k:=\omega_{\mathbf{a}+k\mathbf{p}},\quad \rho_k:=\rho_{\mathbf{a}+k\mathbf{p}}=\frac{1}{|\mathbf{p}|_{\boldsymbol{\kappa}}^2}-\frac{1}{|\mathbf{a}+k\mathbf{p}|_{\boldsymbol{\kappa}}^2} \tag{2.4.16}$$

where $k\in\mathbb{Z}$ is now an integer, rather than a vector. The modes with mode numbers $\mathbf{a}+k\mathbf{p}$ form the *class led by* $\mathbf{a}$. Note the difference between ω_k, ρ_k for $k\in\mathbb{Z}$, and $\omega_{\mathbf{j}}$, $\rho_{\mathbf{j}}$ for $\mathbf{j}\in\mathbb{Z}^2$. In the former case, we are studying the dynamics of a single class only; in the latter case we are considering the dynamics of the full system.

The principal domain of Fourier mode indices $\mathcal{A}$ is illustrated in Figure 2.5. $\mathcal{A}$ is chosen so that for all $\mathbf{j}\in\mathbb{Z}^2$, $\mathbf{j}=\mathbf{a}+k\mathbf{p}$ for some unique $\mathbf{a}\in\mathbb{Z}^2$ and $k\in\mathbb{Z}$.

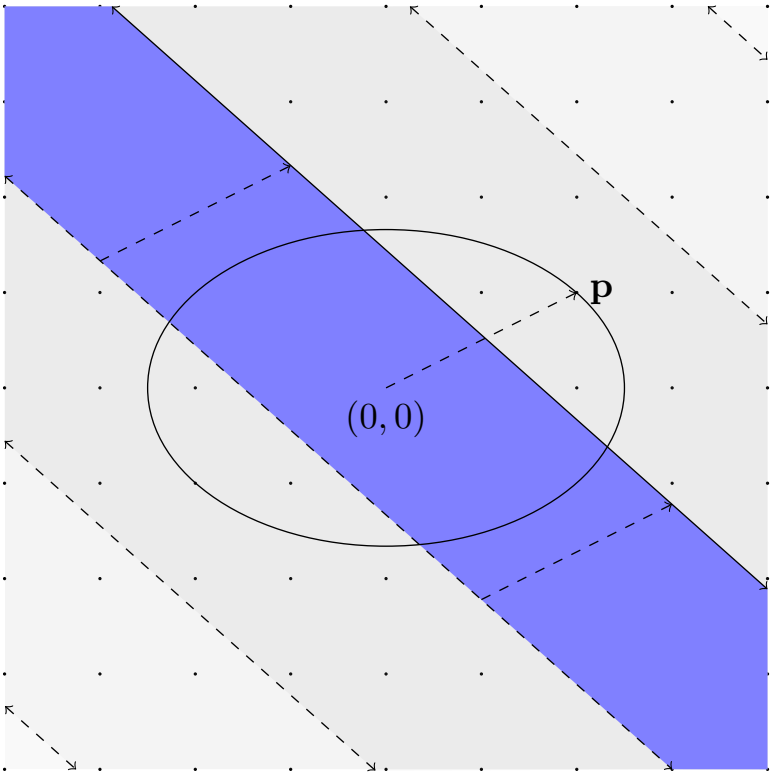

Figure 2.5 – The principal domain of Fourier modes, $\mathcal{A}$ (shown here in blue). Translations of $\mathcal{A}$ by $\mathbf{p}$ cover the whole domain of modes. This domain is chosen such that if $\mathbf{a} \in \mathcal{A}$ is not in the unstable ellipse (2.5.2) shown, $\mathbf{a} + k\mathbf{p}$ is not in the ellipse for any $k \in \mathbb{Z}$.

Denote the set of indices in a class by

$$\Sigma_{\mathbf{a}} = \{\mathbf{a} + k\mathbf{p} \mid k \in \mathbb{Z}\}. \tag{2.4.17}$$

Then for each $\mathbf{a} \in \mathcal{A}$ there is an associated linearised subsystem on the modes $\omega_{\mathbf{j}}$ for $\mathbf{j} \in \sigma_{\mathbf{a}}$ which is a Poisson system with respect to the Poisson bracket

$$\{f, g\}_{\mathbf{a}} = \alpha \sum_{k \in \mathbb{Z}} \left[\frac{\partial f}{\partial \omega_k} \frac{\partial g}{\partial \omega_{k+1}} - \frac{\partial f}{\partial \omega_{k+1}} \frac{\partial g}{\partial \omega_k} \right] \tag{2.4.18}$$

with Hamiltonian $H_{\mathbf{a}}$, where

$$\alpha = \alpha(\mathbf{a}, \mathbf{p}) = \Gamma \kappa_x \kappa_y \mathbf{a} \times \mathbf{p}. \tag{2.4.19}$$

It is important to note that if $\mathbf{a}$ and $\mathbf{p}$ are parallel, $\alpha(\mathbf{a}, \mathbf{p}) = 0$. Such "trivial" classes cannot contribute instability as the associated differential equations are $\dot{\omega}_k = 0$ for all k. This corresponds to the fact that perturbations within the class of modes $\omega_{n\mathbf{p}}$ move from our selected equilibrium Ω^* to another shear flow of the

form (2.4.1) perpendicular to $\mathbf{p}$. These shear flows can be written as

$$\omega_{\mathbf{j}} = \begin{cases} \Gamma_k \text{ if } \mathbf{j} = \pm k\mathbf{p} \\ 0 \text{ otherwise.} \end{cases} \tag{2.4.20}$$

Our shear flow is a special case of this with $\Gamma_1 = \Gamma$, $\Gamma_k = 0$ for all $k \neq 1$. Thus perturbations in the direction of a mode $\omega_{n\mathbf{p}}$ simply perturbs to another steady state, so there is not instability under such perturbations. This is related to the work of Pierrehumbert and Widnall [**PW82**] who discussed perturbations parallel to a shear flow.

The differential equations for the bi-infinite vector of Fourier coefficients

$$\omega = (..., \omega_{-1}, \omega_0, \omega_1, \omega_2, ...) \tag{2.4.21}$$

in the subsystem $H_{\mathbf{a}}$ are

$$\dot{\omega} = \alpha M \omega \tag{2.4.22}$$

where

$$M = \begin{pmatrix} \ddots & \vdots & \vdots & \vdots & \vdots & \vdots & \ddots \\ \cdots & 0 & \rho_{-1} & 0 & 0 & 0 & \cdots \\ \cdots & -\rho_{-2} & 0 & +\rho_0 & 0 & 0 & \cdots \\ \cdots & 0 & -\rho_{-1} & 0 & +\rho_1 & 0 & \cdots \\ \cdots & 0 & 0 & -\rho_0 & 0 & \rho_2 & \cdots \\ \cdots & 0 & 0 & 0 & -\rho_1 & 0 & \cdots \\ \ddots & \vdots & \vdots & \vdots & \vdots & \vdots & \ddots \end{pmatrix} \tag{2.4.23}$$

and ρ_k is given by (2.4.10). It is worth mentioning that we represent the linear operator M as an infinite matrix. This is for notational convenience; compare this to [**LLS04**] where operator notation is used for the same object.

Note that M can be written as $M = JS$ where

$$J = \begin{pmatrix} \ddots & \vdots & \vdots & \vdots & \vdots & \vdots & \ddots \\ \cdots & 0 & +1 & 0 & 0 & 0 & \cdots \\ \cdots & -1 & 0 & +1 & 0 & 0 & \cdots \\ \cdots & 0 & -1 & 0 & +1 & 0 & \cdots \\ \cdots & 0 & 0 & -1 & 0 & +1 & \cdots \\ \cdots & 0 & 0 & 0 & -1 & 0 & \cdots \\ \ddots & \vdots & \vdots & \vdots & \vdots & \vdots & \ddots \end{pmatrix}, \tag{2.4.24}$$

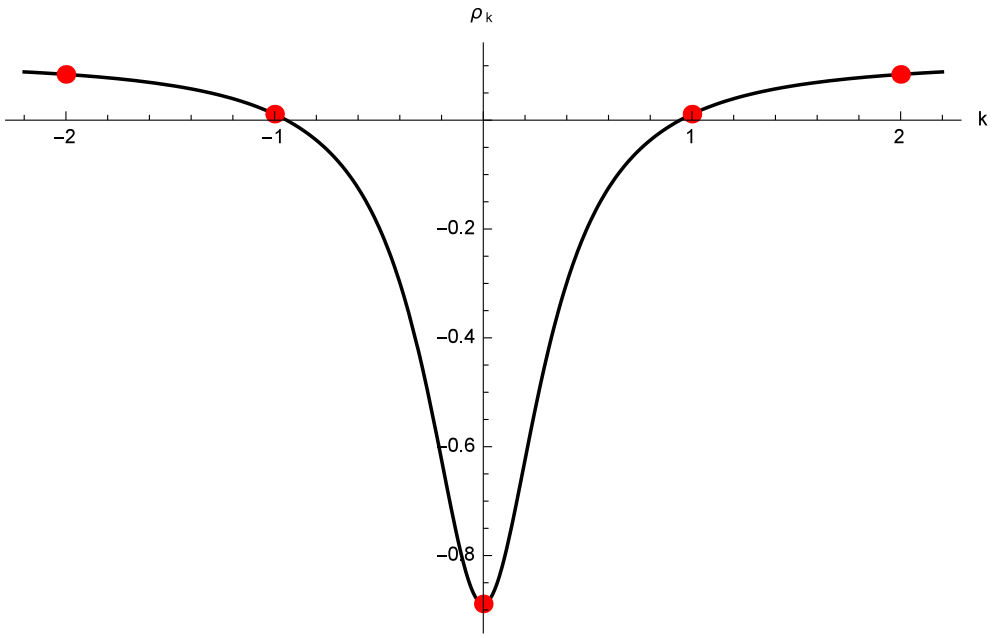

Figure 2.6 – An illustrative graph of the function ρ_k. Here k is shown for continuous values of k for illustrative purposes; in an actual class k takes only integer values. For this figure, $\mathbf{p} = (2, 0)$, $\mathbf{a} = (0, 1)$, $\kappa_y/\kappa_x = 1$. Note that as $|k| \to \infty$, $\rho_k \to 1/|\mathbf{p}|^2$, the minimum value is $\rho_0 = 1/|\mathbf{p}|^2_{\boldsymbol{\kappa}} = 1/|\mathbf{a}|^2_{\boldsymbol{\kappa}}$, and ρ_k is monotonically increasing for $k > 0$ and monotonically decreasing for $k < 0$.

$$S = \begin{pmatrix} \ddots & \vdots & \vdots & \vdots & \vdots & \vdots & \ddots \\ \cdots & \rho_{-2} & 0 & 0 & 0 & 0 & \cdots \\ \cdots & 0 & \rho_{-1} & 0 & 0 & 0 & \cdots \\ \cdots & 0 & 0 & \rho_0 & 0 & 0 & \cdots \\ \cdots & 0 & 0 & 0 & \rho_1 & 0 & \cdots \\ \cdots & 0 & 0 & 0 & 0 & \rho_2 & \cdots \\ \ddots & \vdots & \vdots & \vdots & \vdots & \vdots & \ddots \end{pmatrix}. \tag{2.4.25}$$

This is the matrix form of the Hamiltonian system with Hamiltonian $H_{\mathbf{a}}$, so αJ is the structure matrix for the linearised bracket and $H_{\mathbf{a}} = \frac{1}{2}\omega^{\mathsf{T}} S\omega$. Note that the constant α can be included in either the definition of $H_{\mathbf{a}}$ or J without any effect on the dynamics.

We make some observations about ρ_k:

- $\rho_\infty := \lim_{|k|\to\infty} \rho_k = \frac{1}{|\mathbf{p}|^2_{\boldsymbol{\kappa}}}$;
- $\rho_0 = \frac{1}{|\mathbf{p}|^2_{\boldsymbol{\kappa}}} - \frac{1}{|\mathbf{a}|^2_{\boldsymbol{\kappa}}}$;
- $\rho_0 \leq \rho_k < \rho_\infty$ for all $k \in \mathbb{Z}$ and $\mathbf{a} \in \mathcal{A}$;
- ρ_k is monotonically increasing if $k \geq 0$ and monotonically decreasing if $k < 0$.

These facts are illustrated in Figure 2.6.

2.5. Class Decomposition and Stability

We now discuss the stability of the linearised system derived in the previous section. These shear flows are of physical interest; numerical results for fluids in a periodic domain have been shown to agree with experimental results in a walled domain [**Pum96, PW82**]. Identifying the stability of shear flows thus may be able to explain the behaviour of physical systems. Of particular interest are cases when such flows are stable; this means that such flows may be observable.

In this section, we first introduce the unstable ellipse, a generalisation of an object used to identify in which modes instability can occur. A simple proof is presented to show that modes in classes outside the unstable ellipse cannot contribute linear instability. In the anisotropic case, we can adjust the size of the domain for a new result: for certain parameter values, the shear flows (2.4.3) are linearly stable. This is a generalisation of the result in [**AK98**]; there $\mathbf{p} = (1, 0)$ and for $\kappa_y > \kappa_x$ there is Energy-Casimir stability. In this case, there is only linear stability. A discussion is presented explaining why this cannot be extended to energy-Casimir stability in the sense of [**HMRW85**]. We also calculate the stable continuous spectrum of the classes.

2.5.1. The Unstable Ellipse. Having split the system into subsystems, we now wish to explore which of these subsystems contribute linear instability. We consider classes led by some $\mathbf{a} \in \mathcal{A}$, the principal domain of Fourier modes illustrated in Figure 2.5. Numerically, it becomes clear that only some finite set of modes contribute nonimaginary eigenvalues. This corresponds to the examples in Section 1.3.1 where each linearised system had some small number of nonimaginary eigenvalues.

This observation leads to the definition of the *unstable ellipse*. The unstable ellipse is a generalisation of the unstable disc presented in [**Li00**] to the case $\kappa_y/\kappa_x \neq 1$. Essentially, the ellipse classifies classes into those that can contribute instability and those that cannot. If a class does not intersect the ellipse, it cannot contribute instability, and thus can be disregarded when searching for instabilities.

Definition 2.5.1 (The Unstable Ellipse)**.** *The unstable ellipse $D_{\mathbf{p}}$ is the region in the space of Fourier modes given by*

$$D_{\mathbf{p}} := \{\mathbf{x} \in \mathbb{R}^2 \mid |\mathbf{x}|_{\boldsymbol{\kappa}} < |\mathbf{p}|_{\boldsymbol{\kappa}}\}. \tag{2.5.2}$$

This ellipse is shown for various parameter values in Figure 2.7. Note that the shape of $D_{\mathbf{p}}$ does not depend on κ_x, κ_y but only on the ratio κ_y/κ_x. The eccentricity of the ellipse is $e = \sqrt{1 - \frac{\kappa_x^2}{\kappa_y^2}}$.

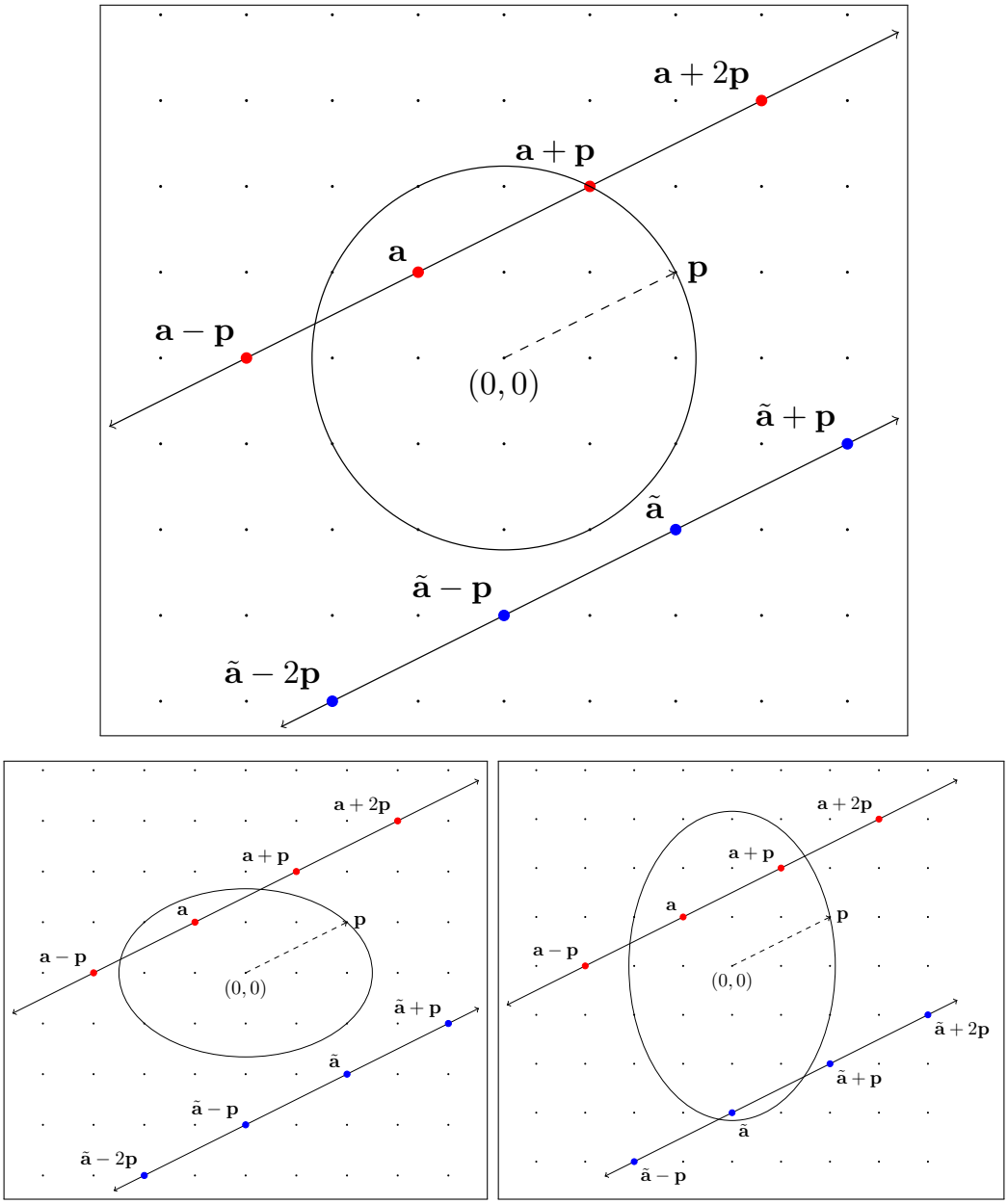

Figure 2.7 – The unstable ellipse defined by Equation (2.5.2). For all three figures, $\mathbf{p} = (2, 1)$ and the classes led by $\mathbf{a} = (-1, 1)$ and $\tilde{\mathbf{a}} = (2, -2)$ are shown. Top: $\kappa_y/\kappa_x = 1$. In this case the ellipse is a disc, as per [**Li00**]. Bottom left: $\kappa_y/\kappa_x = \frac{3}{2}$. The ellipse still passes through $\mathbf{p}$ and has centre the origin, but the lengths of the axes have changed. Bottom right: $\kappa_y/\kappa_x = \frac{2}{3}$. Now the ellipse is large enough that the class through $\tilde{\mathbf{a}}$ intersects the ellipse. This will change the spectrum of the linearised problem. Note that the shape of the ellipse depends only on the ratio κ_y/κ_x, so we normalise $\boldsymbol{\kappa} = (\kappa_x, \kappa_y)$ so that $|\boldsymbol{\kappa}| = 1$.

The semi-major and semi-minor axes of the unstable ellipse have lengths $|\mathbf{p}|_{\boldsymbol{\kappa}}/\kappa_x$ and $|\mathbf{p}|_{\boldsymbol{\kappa}}/\kappa_y$. The ellipse passes through the point $\mathbf{p}$ for all values of κ_x, κ_y. In the special case of a parallel shear flow $\mathbf{p} = (p_x, 0)$ (or equivalently $\mathbf{p} = (0, p_y)$), varying κ_x, κ_y does not change the x-intercepts $\pm p_x$. However, this still changes the values of the y-intercepts. This will be important in Section 2.6.

It is important to note that for $\mathbf{a} \in \mathcal{A}$, the principal domain of modes, $\mathbf{a} \notin D_{\mathbf{p}}$ implies that $\mathbf{a} + k\mathbf{p} \notin D_{\mathbf{p}}$ for all $k \in \mathbb{Z}$. This is illustrated in Figure 2.5. This will be important for our notation, and motivates the choice of domain $\mathcal{A}$.

We make a simple but important observation.

Lemma 2.5.3. *A lattice point $\mathbf{a} + k\mathbf{p}$ is inside the unstable ellipse if and only if the corresponding ρ_k is negative, and on the boundary if and only if $\rho_k = 0$:*

$$\begin{aligned} \mathbf{a} + k\mathbf{p} \in D_{\mathbf{p}} &\iff \rho_k < 0; \\ \mathbf{a} + k\mathbf{p} \in \partial D_{\mathbf{p}} &\iff \rho_k = 0; \\ \mathbf{a} + k\mathbf{p} \notin \overline{D_{\mathbf{p}}} &\iff \rho_k > 0. \end{aligned} \tag{2.5.4}$$

The notation $\overline{A} = A \cup \partial A$ represents the closure of $\mathcal{A}$.

Proof. Noting that $\mathbf{a} + k\mathbf{p} \in D_{\mathbf{p}}$ if and only if $|\mathbf{a} + k\mathbf{p}|_{\boldsymbol{\kappa}} < |\mathbf{p}|_{\boldsymbol{\kappa}}$ by definition of $D_{\mathbf{p}}$, this is clear from the definition of $\rho_{\mathbf{j}}$ (2.4.10). □

This is illustrated in Figure 2.7. In the top figure, $\mathbf{a} \in D_{\mathbf{p}}$ and $\mathbf{a} + \mathbf{p} \in \partial D_{\mathbf{p}}$, so in that class, $\rho_0 < 0$, $\rho_1 = 0$ and $\rho_k > 0$ for all $k \neq 0, 1$. In the class led by $\tilde{\mathbf{a}}$, $\tilde{\mathbf{a}} + k\mathbf{p} \notin D_{\mathbf{p}} \cup \partial D_{\mathbf{p}}$ for all k, so $\rho_k > 0$ for all k.

Note that it is possible that the line through $\mathbf{a}$ parallel to $\mathbf{p}$ can intersect $D_{\mathbf{p}}$ without any lattice point on the line lying inside $D_{\mathbf{p}}$. Then the line which contains all modes in the class intersects the unstable ellipse, but no modes in the class lie in the ellipse. This implies $\rho_k \geq 0$ for all k and the class will not contribute instability.

2.5.2. Stable Classes and Stable Spectra. We claim that a class that does not intersect the ellipse at any lattice point is a linearly stable subsystem and thus cannot contribute linear instability to the full system. We now present a proof of this result. This result is known and proven by Li [**Li00**] for the case $K = \mathbb{I}$, and here generalised for the anisotropic case $K \neq \mathbb{I}$ with a new proof. We also discuss the stable spectrum which is also the continuous spectrum in this problem [**SL03**].

Theorem 2.5.5 (Stable Classes)**.** *For all choices of $\mathbf{a}$ such that $\Sigma_{\mathbf{a}} \cap \overline{D_{\mathbf{p}}} = \emptyset$, the corresponding subsystem is linearly stable.*

Proof. Define the transform T:

$$T := \begin{pmatrix} \ddots & \vdots & \vdots & \vdots & \vdots & \vdots & \ddots \\ \cdots & \rho_{-2}^{-1/2} & 0 & 0 & 0 & 0 & \cdots \\ \cdots & 0 & \rho_{-1}^{-1/2} & 0 & 0 & 0 & \cdots \\ \cdots & 0 & 0 & \rho_{0}^{-1/2} & 0 & 0 & \cdots \\ \cdots & 0 & 0 & 0 & \rho_{1}^{-1/2} & 0 & \cdots \\ \cdots & 0 & 0 & 0 & 0 & \rho_{2}^{-1/2} & \cdots \\ \ddots & \vdots & \vdots & \vdots & \vdots & \vdots & \ddots \end{pmatrix}. \tag{2.5.6}$$

If $\Sigma_{\mathbf{a}} \cap \overline{D_{\mathbf{p}}} = \emptyset$, then $\rho_k > 0$ for all k by Lemma 2.5.3, and thus T is a real diagonal matrix. Then define

$$\begin{aligned} \tilde{M} &:= T^{-1} M T \\ &= \begin{pmatrix} \ddots & \vdots & \vdots & \vdots & \vdots & \vdots & \ddots \\ \cdots & 0 & (\rho_{-2}\rho_{-1})^{1/2} & 0 & 0 & 0 & \cdots \\ \cdots & -(\rho_{-2}\rho_{-1})^{1/2} & 0 & (\rho_{-1}\rho_{0})^{1/2} & 0 & 0 & \cdots \\ \cdots & 0 & -(\rho_{-1}\rho_{0})^{1/2} & 0 & (\rho_{0}\rho_{1})^{1/2} & 0 & \cdots \\ \cdots & 0 & 0 & -(\rho_{0}\rho_{1})^{1/2} & 0 & (\rho_{1}\rho_{2})^{1/2} & \cdots \\ \cdots & 0 & 0 & 0 & -(\rho_{1}\rho_{2})^{1/2} & 0 & \cdots \\ \ddots & \vdots & \vdots & \vdots & \vdots & \vdots & \ddots \end{pmatrix}. \end{aligned} \tag{2.5.7}$$

This is equivalent to writing the system in terms of coordinates $v_k = \sqrt{\rho_k}\omega_k$.

Now $\tilde{M}$ is real and skew-symmetric, so $i\tilde{M}$ is Hermitian and therefore is diagonalisable and has only real spectrum. Thus by similarity, M is diagonalisable and has only imaginary spectrum, and thus the subsystem is linearly stable. Thus it cannot contribute instability to the full system.

Alternatively, one can observe that if $\rho_k > 0$ for all k, the Hamiltonian $H_{\mathbf{a}}$ is positive definite. As the Hamiltonian is constant, it acts as a Lyapunov function for the growth, and thus the dynamics are Lyapunov stable. □

This result generalises similar results for the $\kappa_y/\kappa_x = 1$ case in [**Li00**]. This shows that we need only look at a finite number of classes to address instability; specifically, the classes that have a nonempty intersection with the unstable ellipse. Note that the above proof does not address classes with $\rho_k = 0$ for some k. These classes must be treated carefully; we will discuss them in Section 2.9.2.

We can also describe the continuous spectrum of M for all classes. This shows that the result of [**LLS04**] is valid for the anisotropic case $\kappa_y/\kappa_x \neq 1$.

Proposition 2.5.8 (Continuous spectrum of a class)**.** *The operator M has continuous spectrum*

$$\sigma_{\text{ess}}(M) = \frac{1}{|\mathbf{p}|_{\boldsymbol{\kappa}}^2}[-2, 2]i. \tag{2.5.9}$$

Proof. Define

$$\begin{aligned} M_\infty &:= \begin{pmatrix} \ddots & \vdots & \vdots & \vdots & \vdots & \vdots & \ddots \\ \cdots & 0 & \rho_\infty & 0 & 0 & 0 & \cdots \\ \cdots & -\rho_\infty & 0 & +\rho_\infty & 0 & 0 & \cdots \\ \cdots & 0 & -\rho_\infty & 0 & +\rho_\infty & 0 & \cdots \\ \cdots & 0 & 0 & -\rho_\infty & 0 & \rho_\infty & \cdots \\ \cdots & 0 & 0 & 0 & -\rho_\infty & 0 & \cdots \\ \ddots & \vdots & \vdots & \vdots & \vdots & \vdots & \ddots \end{pmatrix} \\ &= \rho_\infty J \end{aligned} \tag{2.5.10}$$

where $\rho_\infty = \lim_{|k|\to\infty} \rho_k = \frac{1}{|\mathbf{p}|_{\boldsymbol{\kappa}}^2}$ and J is as per (2.4.24). Now $P = M - M_\infty$ decays like $\frac{1}{k^2}$ as $k \to \pm\infty$, and so P is a compact operator [**LLS04**].

As iJ is Hermitian, J only has imaginary eigenvalues. Now consider the operator $J - i\lambda\mathbb{I}$ for some $\lambda \in \mathbb{R}$. Consider this acting on a sequence $\mathbf{v} = (..., v_{-1}, v_0, v_1, v_2, ...)$, so $(J - i\lambda\mathbb{I})\mathbf{v} = (..., v_{k+1} - i\lambda v_k - v_{k-1}, ...)$. Then form the Fourier transform of this new sequence

$$\begin{aligned} \mathcal{F}[(J - i\lambda\mathbb{I})\mathbf{v}](x) &= \sum_{k=-\infty}^{\infty} (v_{k+1} - i\lambda v_k - v_{k-1}) e^{ikx} \\ &= \sum_{k=-\infty}^{\infty} (v_k e^{-ix} - i\lambda v_k - v_k e^{ix}) e^{ikx} \\ &= -i(2\sin x + \lambda) \sum_{k=-\infty}^{\infty} v_k e^{ikx} \\ &= -i(2\sin x + \lambda)\mathcal{F}[\mathbf{v}](x). \end{aligned} \tag{2.5.11}$$

If and only if $2\sin x + \lambda \neq 0$ for all real x, then we can construct the inverse of the operator $(J - i\lambda\mathbb{I})$ as

$$(J - i\lambda\mathbb{I})^{-1} = \mathcal{F}^{-1} \frac{1}{-i(2\sin x + \lambda)} \mathcal{F}. \tag{2.5.12}$$

Therefore $i\lambda$ is in the spectrum of J if and only if $2\sin x - \lambda = 0$ for some x, i.e. $\lambda \in [-2, 2]$. Thus the spectrum of $\frac{1}{|\mathbf{p}|_{\boldsymbol{\kappa}}^2} J$ is $\frac{2i}{|\mathbf{p}|_{\boldsymbol{\kappa}}^2}[-1, 1]$. By Weyl's theorem on the spectrum of compact perturbations of operators, see e.g. [**RS78**], the essential spectrum of $\frac{1}{|\mathbf{p}|_{\boldsymbol{\kappa}}^2} J + P$ is equal to the essential spectrum of $\frac{1}{|\mathbf{p}|_{\boldsymbol{\kappa}}^2} J$. Thus the essential spectrum of M is $\frac{2i}{|\mathbf{p}|_{\boldsymbol{\kappa}}^2}[-1, 1]$. □

This argument is based on the proof originally appearing in Latushkin, Li and Stanislavova [**LLS04**]. To find the full continuous spectrum of the problem, consider the factor α that occurs in every class subsystem. The full continuous

spectrum is

$$\begin{aligned}\sigma_{\text{ess}} &= \bigcup_{\mathbf{a}\in\mathcal{A}} |\alpha(\mathbf{a},\mathbf{p})|[-2,2]i \\ &= \frac{\kappa_x\kappa_y\Gamma}{|\mathbf{p}|_{\boldsymbol{\kappa}}^2} \bigcup_{\mathbf{a}\in\mathcal{A}} |\mathbf{a}\times\mathbf{p}|[-2,2]i.\end{aligned} \tag{2.5.13}$$

As $\mathbf{a}$ takes all values in $\mathcal{A}$, $\mathbf{a}\times\mathbf{p}$ grows without bound, and so the continuous spectrum is the entire imaginary axis $\sigma_{\text{ess}} = i\mathbb{R}$.

2.6. Stable Shear Flows

In the previous section, we saw that all but finitely many classes do not introduce instability to the full problem. This leads to an interesting new result: a subset of the flows of the form (2.4.3) are linearly stable. Previously, this was only known in the case $\mathbf{p} = (1,0)$ and $\kappa_y/\kappa_x > 1$. The new extension is for all $\mathbf{p}$ of the form $\mathbf{p} = (p_x, 0)$. Such equilibria correspond to *parallel shear flows* of the form $\cos(\kappa_x p_x x)$. This result in some sense extends Arnold's result for $\mathbf{p} = (1,0)$ [**Arn66a**], though we will see that the stability result here is more general but weaker (linear stability rather than Energy-Casimir stability).

The existence of stable steady states is of some general interest. Although the stability in this case is for periodic inviscid flows and is only linear stability, the result is suggestive of the existence of related flows in other systems. For instance, "metastability" results exist for parallel shear flows with nonzero viscosity per Beck and Wayne [**BW13**], and the analogous scenario for channel flows (for instance, periodic in one dimension only) is a common area of research [**McH94**].

2.6.1. Linearly Stable Parallel Shear Flows.

Theorem 2.6.1 (Linearly Stable Parallel Shear Flows)**.** *If $\mathbf{p} = (p_x, 0)$ and $\kappa_x|p_x| < \kappa_y$, the parallel shear flow*

$$\Omega^* = 2\Gamma\cos(\kappa_x p_x x) \tag{2.6.2}$$

is linearly stable. Equivalently, if $\mathbf{p} = (0, p_y)$ and $\kappa_y|p_y| < \kappa_x$, the stationary solution $\Omega^* = 2\Gamma\cos(\kappa_y p_y y)$ is linearly stable.

Proof. If $\mathbf{p} = (p_x, 0)$, the condition $\rho_k \le 0$ is equivalent to

$$(a_x + kp_x)^2 + \left(\frac{\kappa_y}{\kappa_x}a_y\right)^2 \le p_x^2 < \left(\frac{\kappa_y}{\kappa_x}\right)^2 \tag{2.6.3}$$

where $\mathbf{a} = (a_x, a_y)$. As a_x, a_y, p_x are integers, this implies $a_y = 0$. Thus $\mathbf{a} = (a_x, 0)$.

But then $\alpha(\mathbf{a},\mathbf{p}) = \kappa_x\kappa_y\Gamma(a_x,0)\times(p_x,0) = 0$. Thus all classes either do not intersect the unstable ellipse (so $\rho_k > 0$ for all k), or they satisfy $\alpha(\mathbf{a},\mathbf{p}) = 0$.

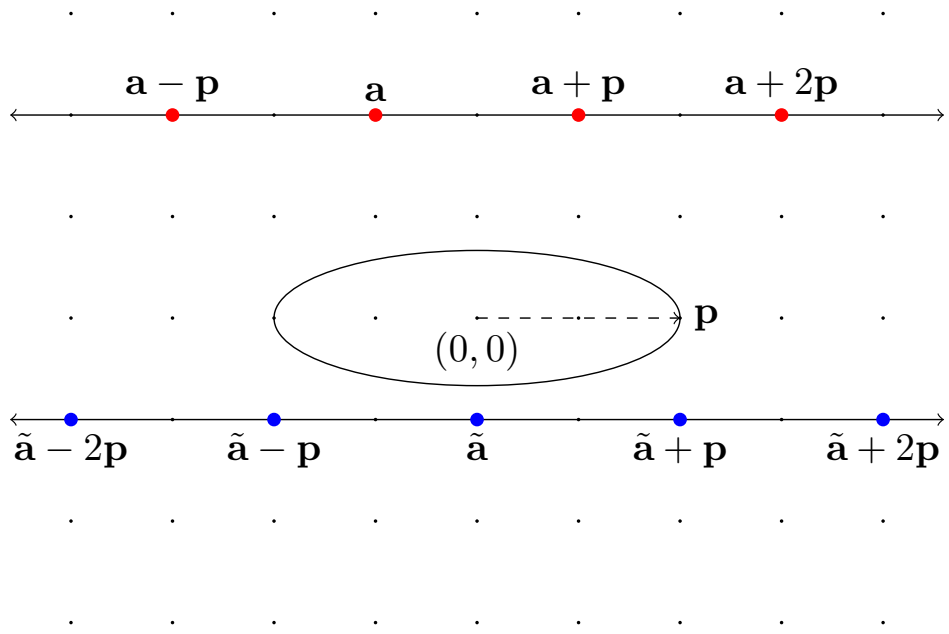

Figure 2.8 – The unstable ellipse for a linearly stable shear flow. For certain choices of $\mathbf{p}$, κ_x and κ_y, no classes will intersect the unstable ellipse except parallel to $\mathbf{p}$. This will lead to linear stability. For this figure, $\mathbf{p} = (2, 0)$, and $\kappa_y/\kappa_x = 3 > 2$. Thus the condition $|p_x| < |\kappa_y/\kappa_x|$ is satisfied.

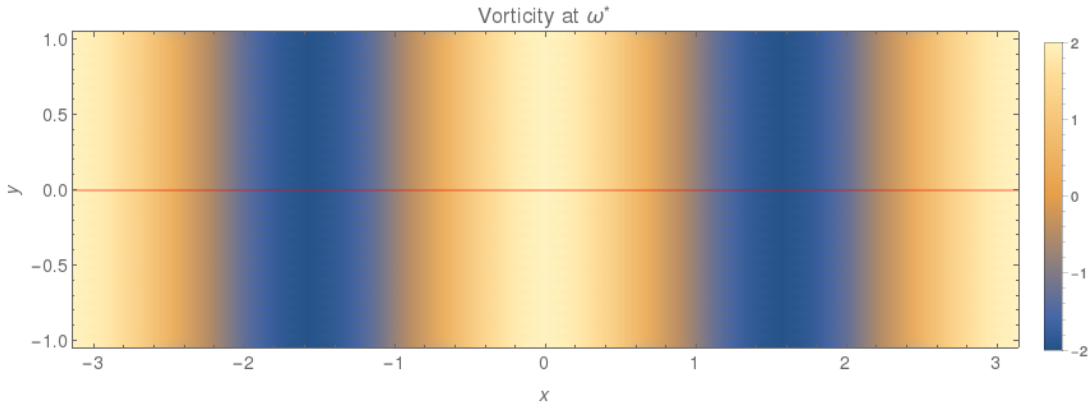

Figure 2.9 – The vorticity for a linearly stable steady state. Here, $\mathbf{p} = (2, 0)$, $\kappa_y/\kappa_x = 3$, and $\Gamma = 1$. Compare with Figure 2.2, which shows the vorticity of a nonparallel shear flow.

If they do not intersect the unstable ellipse, they cannot contribute instability by Theorem 2.5.5. If $\alpha = 0$, the modes in the class are constant and so they cannot contribute instability. Thus there are no classes that contribute instability, and we conclude the flow is linearly stable. Thus the shear flow with vorticity $\Omega^* = 2\Gamma \cos(\kappa_x p_x x)$ is linearly stable.

The analogous result holds when $\mathbf{p} = (0, p_y)$ and $\kappa_y |p_y| < \kappa_x$. Then the steady state $\Omega^* = 2\Gamma \cos(\kappa_y p_y y)$ is linearly stable. □

See Figure 2.8 for an illustration of the condition for a stable flow. The unstable ellipse is "squashed" so that sufficiently few lattice points lie inside the ellipse. This is not possible if p_x, p_y are both nonzero; as the ellipse always passes through $\mathbf{p}$ and is axisymmetric, it will always have both semi-major and semi-minor axes of length greater than $\max(|p_x|, |p_y|)$ and thus will contain a lattice point that is not on the line through $\mathbf{0}$ and $\mathbf{p}$. Figure 2.9 shows an example of the vorticity of a stable steady state.

We can interpret this result as follows. On a torus sufficiently long in one direction, a shear flow that varies sinusoidally in that direction only is linearly stable. This interpretation may lead to some interesting extensions and implications. For instance, it may be possible that other parallel shear flows of the form (2.4.1) with $p_y = 0$ satisfy a similar result, not just sinusoidal flows. It may also be possible to make analogies with flows on a cylinder, which one can think of as a torus with one infinitely long dimension.

2.6.2. Energy-Casimir Stability Analysis. In Theorem 2.6.1, we showed that a subset of the family of steady states (2.4.3) are linearly stable. However, we cannot extend this to nonlinear energy-Casimir stability in the sense of Arnold [**AK98**]. The idea of Energy-Casimir stability is to restrict our system to ensure perturbations preserve the Casimirs. We consider only dynamics on the submanifold defined by fixing all Casimirs constant. Then if the energy/Hamiltonian is positive definite near the steady state over the dynamics of the system, we infer that the steady state is stable. The general procedure for showing nonlinear stability in the energy-Casimir sense is discussed in [**HMRW85, Mor98**].

In this case we restrict the quadratic form $\tilde{\mathcal{H}}$ (2.4.9) to the complement of the gradients of the Casimirs (2.3.10). We must take $\tilde{\mathcal{H}}$ rather than $\mathcal{H}$ (2.3.7) as the derivative must vanish at the equilibrium. This allows us to consider stability while locally fixing the values of the Casimirs.

The derivative of the Casimirs $\mathcal{C}_n$ (2.3.10) is given by

$$(\nabla \mathcal{C}_n)_{\mathbf{j}} = \sum \omega_{\mathbf{k}_1} \omega_{\mathbf{k}_2} ... \omega_{\mathbf{k}_{n-1}} \tag{2.6.4}$$

where the sum is over all indices such that

$$\sum_{i=1}^{n-1} \mathbf{k}_i = -\mathbf{j}. \tag{2.6.5}$$

Evaluating this at the steady state,

$$(\nabla \mathcal{C}_n(\Omega^*))_{(n-2m-1)\mathbf{p}} = \binom{n-1}{m} \Gamma^{n-1} \tag{2.6.6}$$

for all $m \in \mathbb{N}$, and

$$(\nabla \mathcal{C}_n(\Omega^*))_{\mathbf{j}} = 0 \tag{2.6.7}$$

for all $\mathbf{j}$ not of the form $(n - 2m - 1)\mathbf{p}$.

Thus the linear approximation of the Casimirs $\mathcal{C}_n$ at the equilibrium Ω^* is given by a linear combination of the modes $\omega_{k\mathbf{p}}$ where $k = -n, -n+2, \ldots, n-2, n$. Then the span of the linear approximations of all Casimirs $\mathcal{C}_1, \mathcal{C}_2, \ldots$ is *all* linear combinations of the modes $\omega_{k\mathbf{p}}$ for $k \in \mathbb{Z}$.

In the case $\kappa_y/\kappa_x = 1$, $\mathbf{p} = (1, 0)$ the Hessian $D^2\tilde{\mathcal{H}}$ has eigenvalues zero originating from $\rho_{\pm\mathbf{p}} = 0$. Any dynamics in these neutral directions are made constant by fixing the Casimirs, and energy-Casimir stability follows. This is the Fourier space version of Arnold's theorem (for the original, see section 4 of [**AK98**]).

For our new linearly stable cases with $\kappa_y > \kappa_x |p_x| > 1$, the quadratic form $\tilde{\mathcal{H}}$ is indefinite, specifically at lattice points $\omega_{\mathbf{j}}$ where $\mathbf{j} \in D_{\mathbf{p}}$. This implies they are of the form $\mathbf{j} = (j_x, 0)$, $|j_x| < |p_x|$ so $\rho_{\mathbf{k}} < 0$. One cannot achieve definiteness of $\tilde{\mathcal{H}}$ by restricting to fixed values of the Casimirs for these modes, as they are not at integer multiples of $\mathbf{p}$. That is, the second variation cannot be made definite by fixing the Casimirs, so we cannot find the convexity estimates required by [**HMRW85**]. Our argument is equivalent to considering the most general linear combination of Casimirs to construct $\tilde{\mathcal{H}}$ as suggested in [**HMRW85**], and then to observe that restricting to the constant Casimir submanifold $\tilde{\mathcal{H}}$ is not definite for the case at hand.

We thus cannot conclude nonlinear energy-Casimir stability for these linearly stable steady states. This is a qualitative difference between the parallel shear flow with $\mathbf{p} = (1, 0)$ and the general case $\mathbf{p} = (p_x, 0)$.

2.7. Unstable Shear Flows and Nonlinear Instability

In the previous section, we showed that in special cases, flows of the form (2.4.3) are stable. However, as one may expect, this result is only for very particular values of $\mathbf{p}$ and $\boldsymbol{\kappa}$. More generically (in the sense that it occurs for a greater proportion of parameter values) we can expect the steady state is nonlinearly unstable. We will show analytically that this is almost always the case.

In this section, we show that for fixed κ_x and κ_y all but finitely many values of $\mathbf{p}$ give a nonlinearly unstable steady state. As we know that classes that do not intersect the unstable ellipse cannot contribute linear instability, we only consider classes that do intersect the unstable ellipse. Based on numerical evidence as shown in Section 1.3.1, we make conjectures about the spectrum of (2.4.23) based on the number and type of intersections the class has with the unstable ellipse.

We then analytically show nonlinear instability in all but finitely many cases of $\mathbf{p}$. To do so, we begin by taking a finite-mode truncation of our linearised Poisson system. An upper bound on the size of eigenvalues is found. We then

show that for the finite-mode truncation, there is linear instability for all classes that intersect the unstable ellipse at one mode only. To do so, we consider the associated characteristic polynomial.

Under some assumptions on the values ρ_k, we then show there is a lower bound for a positive real eigenvalue independent of the truncation size. It is then shown that a class satisfying the conditions on ρ_k exists for all but finitely many values of $\mathbf{p}$ for a given domain size κ_x, κ_y. Combined with the spectral gap result for the Euler equations [**FSV97**], this proves nonlinear instability for these steady states.

2.7.1. Intersections with the Unstable Ellipse. Having established in Theorem 2.5.5 that only classes that intersect the unstable ellipse can contribute instability, we now turn our attention to the different ways that this can occur. There are six possibilities:

a) $\Sigma_{\mathbf{a}}$ intersects $\partial D_{\mathbf{p}}$ once;
b) $\Sigma_{\mathbf{a}}$ intersects $D_{\mathbf{p}}$ once;
c) $\Sigma_{\mathbf{a}}$ intersects $D_{\mathbf{p}}$ once and $\partial D_{\mathbf{p}}$ once;
d) $\Sigma_{\mathbf{a}}$ intersects $D_{\mathbf{p}}$ twice;
e) $\Sigma_{\mathbf{a}}$ intersects $\partial D_{\mathbf{p}}$ twice;
f) $\Sigma_{\mathbf{a}}$ intersects $D_{\mathbf{p}}$ once and $\partial D_{\mathbf{p}}$ twice.

The locations of the values of $\mathbf{a}$ that lead to these cases are illustrated in Figure 2.10. There are no other possibilities, as classes can only intersect $\overline{D_{\mathbf{p}}}$ at most three times. This is because the ellipse lies wholly between the lines $\langle \mathbf{a}, \mathbf{p} \rangle = |\mathbf{p}|_{\boldsymbol{\kappa}}^2$ and $\langle \mathbf{a}, \mathbf{p} \rangle = -|\mathbf{p}|_{\boldsymbol{\kappa}}^2$. These lines are orthogonal to $\mathbf{p}$ in the $\boldsymbol{\kappa}$-norm, and the corresponding distance between these lines is $|2\mathbf{p}|$. Thus a class cannot intersect more than three times, and can only intersect three times if two of the lattice points are on the boundary, as in (f).

Note that when we talk about intersections, we can only consider the discrete integer points on $\Sigma_{\mathbf{a}}$; the line that the modes in the class lie on may intersect $D_{\mathbf{p}}$ in other regions, or without having any points in $\Sigma_{\mathbf{a}}$ lie in $D_{\mathbf{p}}$.

Based on numerical evidence as discussed in Section 1.3.1, we can hypothesise about the eigenvalues of (2.4.23) in each of these cases:

- in cases (a), (e) and (f), there are only imaginary eigenvalues;
- in cases (b) and (c), there is a pair of real eigenvalues;
- in case (d), there are four nonimaginary eigenvalues - either two real pairs or a complex quadruplet.

The real eigenvalues occur in pairs $\pm\lambda$ and the complex eigenvalues occur in quadruplets $\pm u \pm iv$, due to the Hamiltonian symmetry of the spectrum. Numerical results supporting this can be found in Section 6.1.2, and this is presented as Conjecture 6.1.8.

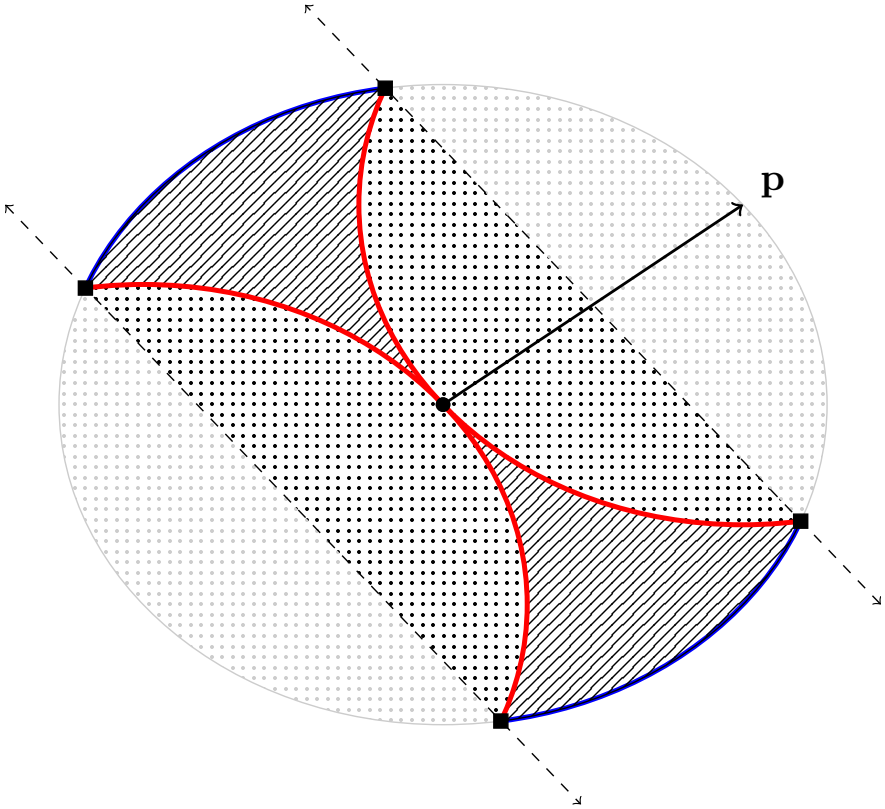

Figure 2.10 – For different values of $\mathbf{a} \in \mathcal{A}$, we can expect different nonimaginary eigenvalues in the associated class. The dashed lines show the edges of the principal domain $\mathcal{A}$, and the ellipse shown is the unstable ellipse $D_{\mathbf{p}}$. For $\mathbf{a}$ outside the unstable ellipse, there are no nonimaginary eigenvalues. Otherwise, there are six cases that can occur. The blue outer curve shows $\mathbf{a}$ such that $\mathbf{a} \in \partial D_{\mathbf{p}}$; this is case (a). The area with diagonal lines shows the values of $\mathbf{a}$ such that $\mathbf{a} \in D_{\mathbf{p}}$ but $\mathbf{a} \pm \mathbf{p} \notin D_{\mathbf{p}}$; this is case (b). The red inner curves show $\mathbf{a}$ such that $\mathbf{a} \in D_{\mathbf{p}}$ and $\mathbf{a} + \mathbf{p} \in \partial D_{\mathbf{p}}$ or $\mathbf{a} - \mathbf{p} \in \partial D_{\mathbf{p}}$; this is case (c). The dotted area shows the values of $\mathbf{a}$ such that $\mathbf{a} \in D_{\mathbf{p}}$ and $\mathbf{a} + \mathbf{p} \in D_{\mathbf{p}}$ or $\mathbf{a} - \mathbf{p} \in D_{\mathbf{p}}$; this is case (d). The four black squares are values of $\mathbf{a}$ for which $\mathbf{a} \in \partial D_{\mathbf{p}}$ and $\mathbf{a} - \mathbf{p} \in \partial D_{\mathbf{p}}$; this is case (e). The black dot at the origin is the value of $\mathbf{a}$ for which $\mathbf{a} \in D_{\mathbf{p}}$, $\mathbf{a} + \mathbf{p} \in \partial D_{\mathbf{p}}$ and $\mathbf{a} - \mathbf{p} \in \partial D_{\mathbf{p}}$; this is case (f). Knowing which of these regions $\mathbf{a}$ occurs in indicates the number and type of nonimaginary eigenvalues.

The cases (e) and (f) are exceptional. Case (f) only occurs when $\mathbf{a} = \mathbf{0}$; as noted previously, this implies that $\alpha = 0$ and so this class cannot contribute instability and can be ignored. Case (e) is very exceptional; this occurs when

$$\mathbf{a} = \begin{pmatrix} \frac{1}{2} & \pm\frac{\sqrt{3}}{2}\frac{\kappa_y}{\kappa_x} \\ \mp\frac{\sqrt{3}}{2}\frac{\kappa_x}{\kappa_y} & \frac{1}{2} \end{pmatrix} \mathbf{p}. \tag{2.7.1}$$

As $\mathbf{a}, \mathbf{p} \in \mathbb{Z}^2$, this means $\frac{\kappa_y}{\kappa_x} = \eta\sqrt{3}$ for some integer η. But then we also require that p_x is a multiple of η, and $\frac{p_x}{\eta} \equiv p_y \bmod 2$. Combining these conditions, all valid values can be expressed by

$$\begin{aligned} K &= \frac{1}{\sqrt{1+3\mu_1^2}} \begin{pmatrix} 1 & 0 \\ 0 & \mu_1\sqrt{3} \end{pmatrix}, \quad \mathbf{p} = \begin{pmatrix} \mu_1\mu_2 \\ \mu_2 + 2\mu_3 \end{pmatrix}, \\ \mathbf{a} &= \begin{pmatrix} 2\mu_1\mu_2 + 3\mu_1\mu_3 \\ \mu_3 \end{pmatrix} \text{ or } \begin{pmatrix} -\mu_1\mu_2 - 3\mu_1\mu_3 \\ \mu_2 + \mu_3 \end{pmatrix} \end{aligned} \tag{2.7.2}$$

for any choices of $\kappa_x \in \mathbb{R}^+$, $\mu_1, \mu_2, \mu_3 \in \mathbb{Z}$, $\mu_1 > 0$. Only for these values of K and $\mathbf{p}$ will there be choices of $\mathbf{a}$ such that $\Sigma_{\mathbf{a}}$ intersects $\partial D_{\mathbf{p}}$ twice. These cases, along with (a) and (c), are discussed in Section 2.9.2.

Of the generic cases, the easiest to address is (b). In terms of our coefficients ρ_k, this scenario means $\rho_0 < 0$ and $\rho_k > 0$ for all $k \neq 0$. Under some mild additional assumptions, we can prove that this leads to the main matrix (2.4.23) having a pair of real eigenvalues, and additionally calculate an explicit lower bound.

2.7.2. A Finite-Mode Truncation. To study the unstable spectrum that makes up the discrete spectrum of the full partial differential equation, we truncate to a finite-mode approximation. Here we take a simple Galerkin-style projection of our problem down to a finite set of Fourier modes. In Chapter 3 a more sophisticated Poisson structure-preserving truncation is discussed and employed.

There are two approaches to this; we can truncate to a finite set of modes before linearising, or linearise and then truncate. The former approach is more sensible for considering the full problem; we must consider all possible classes. Such an approach would mean there are only finitely many differential equations (2.2.26), and the problem would then be numerically tractable. However, the structure of the bracket (2.3.2) is lost and we no longer have a Poisson system.

However, as we are now only interested in the existence of discrete spectra, it is fine to truncate after linearisation. In particular, we can truncate within a particular class $\Sigma_{\mathbf{a}}$.

Assume we have fixed some $\mathbf{a} \in \mathcal{A}$ and are considering the associated class. Choose some truncation values $m < n \in \mathbb{Z}$. Now project the differential equations (2.4.22) to the set of modes ω_k with $m \leq k \leq n$ setting all other modes and their derivatives to zero. Then the new differential equations are $\dot{\omega} = \alpha M_m^n \omega$ where

$\omega = (\omega_m, \omega_{m+1}, ..., \omega_{n-1}, \omega_n)$, $\alpha = \alpha(\mathbf{a}, \mathbf{p})$ is still (2.4.19), and

$$M_m^n = \begin{pmatrix} 0 & \rho_{m+1} & 0 & \cdots & 0 & 0 & 0 \\ -\rho_m & 0 & \rho_{m+2} & \cdots & 0 & 0 & 0 \\ 0 & -\rho_{m+1} & 0 & \cdots & 0 & 0 & 0 \\ \vdots & \vdots & \vdots & \ddots & \vdots & \vdots & \vdots \\ 0 & 0 & 0 & \cdots & 0 & \rho_{n-1} & 0 \\ 0 & 0 & 0 & \cdots & -\rho_{n-2} & 0 & \rho_n \\ 0 & 0 & 0 & \cdots & 0 & -\rho_{n-1} & 0 \end{pmatrix}. \tag{2.7.3}$$

The stability result of Theorem 2.5.5 still holds; if $\rho_k > 0$ for all $m \leq k \leq n$, M_m^n has only imaginary eigenvalues. By truncating the transformation (2.5.6), the result follows.

We should also note that the truncated, linearised system is Poisson; by truncating (2.4.24) and (2.4.25) one recovers the structure matrix and Hamiltonian. Therefore, there is a Hamiltonian symmetry to the eigenvalues; if λ is an eigenvalue of M_N, so are $-\lambda$, $\bar{\lambda}$, and $-\bar{\lambda}$.

2.7.3. An Upper Bound for Eigenvalues. We first prove a simple upper bound for all eigenvalues of (2.7.3).

Proposition 2.7.4. *If $\lambda \in \mathbb{C}$ is an eigenvalue of M_m^n,*

$$|\lambda| \leq 2 \max_{m \leq k \leq n} \{|\rho_k|\} \leq 2 \max\{\rho_\infty, -\rho_0\}. \tag{2.7.5}$$

Proof. Consider some $\lambda \in \mathbb{C}$, not necessarily an eigenvalue. Assume $|\lambda| > 2|\rho_k|$ for all $m \leq k \leq n$. Now consider

$$A = \lambda \mathbb{I} - M_m^n = \begin{pmatrix} \lambda & -\rho_{m+1} & \cdots & 0 & 0 \\ \rho_m & \lambda & \cdots & 0 & 0 \\ \vdots & \vdots & \ddots & \vdots & \vdots \\ 0 & 0 & \cdots & \lambda & -\rho_n \\ 0 & 0 & \cdots & \rho_{n-1} & \lambda \end{pmatrix}. \tag{2.7.6}$$

We will now show that A is diagonally dominated. Note that the row sums are $\sum_{j \neq i} |A_{i,j}| = |\rho_{i+m+1}| + |\rho_{i+m-1}|$ for all $1 < i < n - m + 1$, $\sum_{j \neq 1} |A_{1,j}| = |\rho_{m+1}|$, and $\sum_{j \neq 1} |A_{n-m+1,j}| = |\rho_{n-1}|$. All of these are strictly less than $|A_{i,i}| = |\lambda|$. Thus A is strictly diagonally dominated and therefore nonsingular [**HJ12**]. Thus λ cannot be an eigenvalue of M_m^n, and by contradiction, all eigenvalues of M_m^n must satisfy $|\lambda| \leq 2 \max |\rho_k|$ for all k.

Furthermore, we know that $\rho_0 \leq \rho_k < \rho_\infty$ for all $k \in \mathbb{Z}$. Thus $\lambda \leq 2 \max\{\rho_\infty, -\rho_0\}$. Explicitly, if $|\mathbf{a}|_{\boldsymbol{\kappa}} < \sqrt{2}|\mathbf{p}|_{\boldsymbol{\kappa}}$, $|\lambda| \leq -2\rho_0$, otherwise $|\lambda| \leq 2\rho_\infty$. Note that in the second case, this bound coincides with the size of the continuous spectrum (2.5.9). □

2.7.4. The Characteristic Polynomial. Introduce the characteristic polynomial of (2.7.3)

$$\mathcal{M}_m^n(x) = \det(xI - M_m^n). \tag{2.7.7}$$

As M_m^n is tridiagonal, $\mathcal{M}_m^n$ can be recursively defined by expansion from top left to bottom right

$$\begin{aligned} &\mathcal{M}_m^m(x) = x, \qquad \mathcal{M}_m^{m+1}(x) = x^2 + \rho_{m+1}\rho_m, \\ &\mathcal{M}_m^n(x) = x\mathcal{M}_m^{n-1}(x) + \rho_n\rho_{n-1}\mathcal{M}_m^{n-2}(x). \end{aligned} \tag{2.7.8}$$

or by expansion from bottom right to top left

$$\begin{aligned} &\mathcal{M}_n^n(x) = x, \qquad \mathcal{M}_{n-1}^n(x) = x^2 + \rho_{n-1}\rho_n, \\ &\mathcal{M}_m^n(x) = x\mathcal{M}_{m+1}^n(x) + \rho_m\rho_{m+1}\mathcal{M}_{m+2}^n(x). \end{aligned} \tag{2.7.9}$$

We prove a simple lemma.

Lemma 2.7.10. *If $\rho_k > 0$ for all $m \le k \le n$, $\mathcal{M}_m^n(x) > 0$ for all $x > 0$.*

Proof. If $n = m$, $\mathcal{M}_m^m(x) = x > 0$. If $n = m + 1$, $\mathcal{M}_m^{m+1} = x^2 + \rho_{m+1}\rho_m > 0$. Assume $\mathcal{M}_m^\eta(x) > 0$ for all $m \le \eta < n$ and $x > 0$. Then

$$\begin{aligned} \mathcal{M}_m^n(x) &= x\mathcal{M}_m^{n-1}(x) + \rho_n\rho_{n-1}\mathcal{M}_m^{n-2}(x) \\ &> 0 \end{aligned} \tag{2.7.11}$$

as $x, \rho_n, \rho_{n-1} > 0$ and using the assumption. Thus by induction, the result follows. □

Note that the recursive definitions (2.7.8) and (2.7.9) satisfy the condition for Favard's theorem [**Fav36**]. Thus the polynomials $\mathcal{M}_m^n(x)$ are orthogonal for $j = 1, 2, 3, ...$ with respect to an inner product with some weight function. This is due to the connections between this system and an associated Jacobi operator; we will explore this connection in Section 2.9 For details see [**Sze39**]; note that in this case the weight function will not always be positive.

The following identities will be useful:

$$\mathcal{M}_m^n(0) = \begin{cases} \prod_{k=m}^n \rho_k & \text{if } n-m \text{ is odd,} \\ 0 & \text{if } n-m \text{ is even.} \end{cases} \tag{2.7.12}$$

$$\frac{\mathrm{d}}{\mathrm{d}x}\mathcal{M}_m^n(x)\bigg|_{x=0} = \begin{cases} 0 & \text{if } n-m \text{ is odd,} \\ \sum_{k=0}^{\frac{n-m}{2}} \left(\prod_{j=m, j\neq m+2k}^n \rho_j\right) & \text{if } n-m \text{ is even.} \end{cases} \tag{2.7.13}$$

These can be proved by simple induction arguments. We can simplify the last of these: if $\rho_k \neq 0$ for all k and $n - m$ is even,

$$\frac{\mathrm{d}}{\mathrm{d}x}\mathcal{M}_m^n(x)\bigg|_{x=0} = \left(\prod_{j=m}^n \rho_j\right)\left(\sum_{k=0}^{\frac{n-m}{2}} \frac{1}{\rho_{m+2k}}\right). \tag{2.7.14}$$

2.7.5. Finite-Truncation Instability. We first show that if $\rho_0 < 0$, $\rho_k \geq 0$ there is some nonzero real eigenvalue. Because of the Hamiltonian symmetry of the spectrum this means there is a positive and negative pair of real eigenvalues and so there is linear instability. This is then extended to show that under certain conditions there is pair of real eigenvalues with an explicit lower bound independent of the truncation used.

Proposition 2.7.15 (Existence of a real eigenvalue)**.** *If $\rho_0 < 0$, and $\rho_k \geq 0$ for all $k \neq 0$, then for sufficiently large $N \in \mathbb{Z}$, M^N_{-N} has a nonzero real eigenvalue.*

Proof. If $\rho_0 < 0$ and $\rho_k \geq 0$ for all $k \neq 0$, then either $\rho_1 = 0$, or $\rho_{-1} = 0$, or $\rho_k > 0$ for all $k \neq 0$ (see Section 2.7.1).

If $\rho_1 = 0$ and N is odd, then

$$\begin{aligned} \frac{\mathrm{d}}{\mathrm{d}x}\mathcal{M}^N_{-N}(x)\bigg|_{x=0} &= \prod_{k=-N,k\neq 1}^{N} \rho_k \\ &< 0 \end{aligned} \tag{2.7.16}$$

as $\rho_0 < 0$, $\rho_k > 0$ for all $k \neq 0, 1$. Similarly if $\rho_{-1} = 0$ and N is odd, $\frac{\mathrm{d}}{\mathrm{d}x}\mathcal{M}^N_{-N}(x)\big|_{x=0} < 0$.

If $\rho_k > 0$ for all $k \neq 0$, by (2.7.14)

$$\frac{\mathrm{d}}{\mathrm{d}x}\mathcal{M}^N_{-N}(x)\bigg|_{x=0} = \left(\prod_{j=-N}^{N} \rho_j\right)\left(\sum_{k=0}^{N} \frac{1}{\rho_{-N+2k}}\right). \tag{2.7.17}$$

Now

$$\prod_{j=-N}^{N} \rho_j < 0 \tag{2.7.18}$$

as $\rho_0 < 0$, $\rho_k > 0$ for all $k \neq 0$.

If N is odd, then $\frac{1}{\rho_{-N+2k}} > 0$ for all k, and thus $\frac{\mathrm{d}}{\mathrm{d}x}\mathcal{M}^N_{-N}(x)\big|_{x=0} < 0$. If N is even, $\sum_{k=0}^{N} \frac{1}{\rho_{-N+2k}} > 0$ for a sufficiently large value of N. This is because $\frac{1}{\rho_0}$ is finite and negative, and $\frac{1}{\rho_k} \to |\mathbf{p}|^2_{\boldsymbol{\kappa}} > 0$ as $|k| \to \infty$. Thus for large enough truncation values, $\frac{\mathrm{d}}{\mathrm{d}x}\mathcal{M}^N_{-N}(x)\big|_{x=0} < 0$.

In all cases, $\mathcal{M}^N_{-N}(0) = 0$ as $N - (-N) = 2N$ is even. As the constant term is zero, and the linear term is negative, then the lowest order nonzero coefficient of the polynomial is negative.

We now argue by contradiction. Assume all roots of the polynomial are imaginary (say $i\zeta_k$) or complex ($\gamma_j + i\delta_j$) or zero. Then because eigenvalues occur in positive and negative pairs due to the Hamiltonian symmetry as well as

conjugate pairs the polynomial has the form

$$\begin{aligned}\mathcal{M}^N_{-N}(x) &= x^{n_1} \times \prod_{k=1}^{n_2}(x - i\zeta_k)(x + i\zeta_k) \\ &\quad \times \prod_{j=1}^{n_3}[(x - \gamma_j - i\delta_j)(x - \gamma_j + i\delta_j)(x + \gamma_j - i\delta_j)(x + \gamma_j + i\delta_j)] \\ &= x^{n_1}\prod_{k=1}^{n_2}(x^2 + \zeta_k^2)\prod_{j=1}^{n_3}\left(x^4 - 2x^2(\gamma_j^2 - \delta_j^2) + (\gamma_j^2 + \delta_j^2)^2\right).\end{aligned}$$

The lowest order nonzero coefficient (the coefficient of x^{n_1}) is

$$\prod_{k=1}^{n_2}(\zeta_k^2)\prod_{j=1}^{n_3}\left((\gamma_j^2 + \delta_j^2)^2\right) > 0. \tag{2.7.19}$$

But we know that the lowest order nonzero coefficient of $\mathcal{M}^N_{-N}$ is negative. Thus by contradiction there must be some real eigenvalue, which will occur in a positive and negative pair. Thus there is a positive real eigenvalue. □

2.7.6. A Lower Bound for a Real Eigenvalue. In the previous section, we showed there is a real eigenvalue of M^N_{-N} for appropriate values of ρ_k and N. However, this does not preclude the possibility that the eigenvalue shrinks to zero as the truncation size increases. Therefore, we must now find a lower bound for such eigenvalues that does not depend on the truncation size. For a fixed domain size $\boldsymbol{\kappa}$ such a lower bound exists for almost all values of $\mathbf{p}$.

Lemma 2.7.20. *If $N > 2$, $\rho_0 < 0$, $\rho_k > 0$ for all $k \neq 0$, and $\rho_0 + \rho_2 < 0$, then*

$$\mathcal{M}^N_{-N}(\lambda^*) < 0 \tag{2.7.21}$$

where $\lambda^* = \sqrt{-\rho_1(\rho_0 + \rho_2)}$.

Proof. Begin by noting that

$$\mathcal{M}^\gamma_{-N}(\sqrt{-\rho_1(\rho_0 + \rho_2)}) \geq 0 \tag{2.7.22}$$

for all $\gamma < 0$ by Lemma 2.7.10, as $\sqrt{-\rho_1(\rho_0 + \rho_2)} > 0$. By applying (2.7.9) twice,

$$\mathcal{M}^1_{-N}(x) = (x^2 + \rho_1\rho_0)\mathcal{M}^{-1}_{-N}(x) + \rho_0\rho_{-1}x\mathcal{M}^{-2}_{-N}(x) \tag{2.7.23}$$

so

$$\mathcal{M}^1_{-N}(\lambda^*) = -\rho_1\rho_2\mathcal{M}^{-1}_{-N}(\lambda^*) + \rho_0\rho_{-1}\lambda^*\mathcal{M}^{-2}_{-N}(\lambda^*). \tag{2.7.24}$$

As $\rho_0 < 0$, $\rho_k > 0$ for all $k \neq 0$, and $\mathcal{M}^{-1}_{-N}, \mathcal{M}^{-2}_{-N}$ take positive values for positive arguments, $\mathcal{M}^1_{-N}(\lambda^*) < 0$.

Now, by applying (2.7.9) repeatedly:

$$\begin{aligned}\mathcal{M}^2_{-N}(\lambda^*) &= (\lambda^{*2} + \rho_1(\rho_0+\rho_2))\lambda^*\mathcal{M}^{-1}_{-N}(\lambda^*) \\ &\quad + (\lambda^{*2} + \rho_2\rho_1)\rho_0\rho_{-1}\mathcal{M}^{-2}_{-N}(\lambda^*) \\ &= -\rho_1\rho_0^2\rho_{-1}\mathcal{M}^{-2}_{-N}(\lambda^*).\end{aligned} \tag{2.7.25}$$

As $\rho_1, \rho_{-1} > 0$, $\rho_0 < 0$ and $\mathcal{M}^{-2}_{-N}$ is positive by Lemma 2.7.10, it follows that

$$\mathcal{M}^2_{-N}(\sqrt{-\rho_1(\rho_0+\rho_2)}) < 0.$$

Now for $\gamma > 2$, we make a recursive argument:

$$\mathcal{M}^{\gamma}_{-N}(\lambda^*) = \lambda^*\mathcal{M}^{\gamma-1}_{-N}(\lambda^*) + \rho_\gamma\rho_{\gamma-1}\mathcal{M}^{\gamma-2}_{-N}(\lambda^*). \tag{2.7.26}$$

Now $\lambda^* > 0$ and $\rho_\gamma\rho_{\gamma-1} > 0$ (as $\gamma > 2$). By induction, as $\mathcal{M}^1_{-N}(\lambda^*) < 0$, $\mathcal{M}^2_{-N}(\lambda^*) < 0$, then $\mathcal{M}^{\gamma}_{-N}(\lambda^*) < 0$ for all $\gamma \geq 1$. Therefore we conclude that $\mathcal{M}^N_{-N}(\sqrt{-\rho_1(\rho_0+\rho_2)}) < 0$. □

One can make the equivalent argument if $\rho_0 + \rho_{-2} < 0$, with the lower bound $\lambda^* = \sqrt{-\rho_{-1}(\rho_0+\rho_{-2})}$ instead. If $\rho_0+\rho_{-2} < 0$ and $\rho_0+\rho_2 < 0$, we can define the lower bound $\lambda^* = \max(\sqrt{-\rho_{-1}(\rho_0+\rho_{-2})}, \sqrt{-\rho_1(\rho_0+\rho_2)})$.

Lemma 2.7.27 (Lower Bound for Real Eigenvalues)**.** *If* $\mathbf{a} \in D_{\mathbf{p}}$ *and* $\mathbf{a}+k\mathbf{p} \notin D_{\mathbf{p}}$ *for all* $k \neq 0$*, and*

$$\lambda^* = \sqrt{-\rho_1(\rho_0+\rho_2)} \tag{2.7.28}$$

is real and nonzero, there exists a real $\lambda > \lambda^*$ *such that* λ *is an eigenvalue of* M^N_{-N} *for all sufficiently large* N*. Similarly if*

$$\lambda^\dagger = \sqrt{-\rho_{-1}(\rho_0+\rho_{-2})} \tag{2.7.29}$$

is real and nonzero, there exists $\lambda > \lambda^\dagger$ *such that* λ *is an eigenvalue of* M^N_{-N} *for all sufficiently large* N*.*

Proof. The leading order term of $\mathcal{M}^N_{-N}(x)$ is x^{2N+1}, and does not depend on ρ_k. Thus, $\lim_{x\to\infty}\mathcal{M}^N_{-N}(x) > 0$. Additionally we know from Lemma 2.7.20 that $\mathcal{M}^N_{-N}(\lambda^*) < 0$ under the conditions given. Also, $\mathcal{M}^N_{-N}(x)$ is a real-valued function for real values of x. Thus by the intermediate value theorem, there exists some $\lambda > \lambda^*$ such that $\mathcal{M}^N_{-N}(\lambda) = 0$. By definition, λ is an eigenvalue of M^N_{-N}. By the same argument, $\lambda^\dagger$ is also a lower bound. If λ^* and $\lambda^\dagger$ are both real, there is some real eigenvalue $\lambda > \max(\lambda^*, \lambda^\dagger)$. □

Thus there is an eigenvalue, and there is a lower bound on the eigenvalue that does not depend on the truncation size. Thus it will persist to the full infinite matrix. This lower bound is illustrated in Figure 2.18 in a reduced coordinate frame.

2.7.7. Conditions for Existence of a Lower Bound. In the previous section we showed that under appropriate conditions on the coefficients ρ_k, the class has a positive real eigenvalue greater than an explicit lower bound. We now show that under certain conditions on $\mathbf{p}$, there exist corresponding values of $\mathbf{a}$ such that the required conditions on the ρ_k coefficients are satisfied.

Lemma 2.7.30 (Appropriate Choices for $\mathbf{a}$)**.** *For all* $\mathbf{p}$ *such that*

$$|\mathbf{p}|_{\boldsymbol{\kappa}} > \frac{3+2\sqrt{3}}{2}, \tag{2.7.31}$$

there exists at least one choice of $\mathbf{a} \in \mathcal{A}$ *such that the reality conditions of Lemma 2.7.27 are satisfied for sufficiently large* N*.*

In the isotropic case $\kappa_y/\kappa_x = 1$*, there is an appropriate choice of* $\mathbf{a}$ *for all* $\mathbf{p}$ *except* $(1,0)^\mathsf{T}, (1,1)^\mathsf{T}, (1,2)^\mathsf{T}$ *(and permutations and sign changes thereof).*

Proof. For the lower bound for a real eigenvalue $\lambda^* = \sqrt{-\rho_1(\rho_0+\rho_2)}$ (or equivalently $\lambda^\dagger = \sqrt{-\rho_{-1}(\rho_0+\rho_{-2})}$) given in Lemma 2.7.27 to be real and positive, and hence a valid bound, we require $\rho_0 < 0$, $\rho_{\pm 1} > 0$, and $\rho_0 + \rho_2 < 0$ (or $\rho_0 + \rho_{-2} < 0$). As ρ_k is monotonic away from $k = 0$, this implies $\rho_k > 0$ for all $k \neq 0$.

If $\rho_0 < 0$ and $\rho_k > 0$ for all $k \neq 0$, then $|\mathbf{a}| < |\mathbf{p}|$ and $|\mathbf{a} \pm \mathbf{p}| > |\mathbf{p}|$. This is true if and only if $\mathbf{a}$ is in the shaded region in Figure 2.11 (top).

If $|\mathbf{a}|_{\boldsymbol{\kappa}} < (\sqrt{3}-1)|\mathbf{p}|_{\boldsymbol{\kappa}}$, then $|\mathbf{a} \pm 2\mathbf{p}|_{\boldsymbol{\kappa}} \leq |\mathbf{a}|_{\boldsymbol{\kappa}} + 2|\mathbf{p}|_{\boldsymbol{\kappa}} < (\sqrt{3}+1)|\mathbf{p}|_{\boldsymbol{\kappa}}$ by the triangle inequality. Thus

$$\begin{aligned}
\rho_0 + \rho_2 &= \frac{2}{|\mathbf{p}|_{\boldsymbol{\kappa}}^2} - \frac{1}{|\mathbf{a}|_{\boldsymbol{\kappa}}^2} - \frac{1}{|\mathbf{a}+2\mathbf{p}|_{\boldsymbol{\kappa}}^2} \\
&< \frac{2}{|\mathbf{p}|^2} - \frac{1}{|(\sqrt{3}-1)\mathbf{p}|^2} - \frac{1}{|(\sqrt{3}+1)\mathbf{p}|^2} \\
&= \frac{1}{|\mathbf{p}|^2}\left(2 - \frac{1}{(\sqrt{3}-1)^2} - \frac{1}{(\sqrt{3}+1)^2}\right) \\
&= 0.
\end{aligned} \tag{2.7.32}$$

Similarly, if $|\mathbf{a}|_{\boldsymbol{\kappa}} < (\sqrt{3}-1)|\mathbf{p}|_{\boldsymbol{\kappa}}$ then $\rho_0 + \rho_{-2} < 0$. This condition is illustrated in Figure 2.11 (bottom).

We thus need to show there exists $\mathbf{a} \in \mathbb{Z}^2$ such that $|\mathbf{a}|_{\boldsymbol{\kappa}} < (\sqrt{3}-1)|\mathbf{p}|_{\boldsymbol{\kappa}}$ and $|\mathbf{a} \pm \mathbf{p}|_{\boldsymbol{\kappa}} > |\mathbf{p}|_{\boldsymbol{\kappa}}$. The condition for this to be possible is shown geometrically in Figure 2.12. The idea is to circumscribe an ellipse in this region, tangent to the curves $|\mathbf{x}|_{\boldsymbol{\kappa}} = (\sqrt{3}-1)|\mathbf{p}|_{\boldsymbol{\kappa}}$, $|\mathbf{x}+\mathbf{p}|_{\boldsymbol{\kappa}} = |\mathbf{p}|_{\boldsymbol{\kappa}}$ and $|\mathbf{x}-\mathbf{p}|_{\boldsymbol{\kappa}} = |\mathbf{p}|_{\boldsymbol{\kappa}}$. The interior of

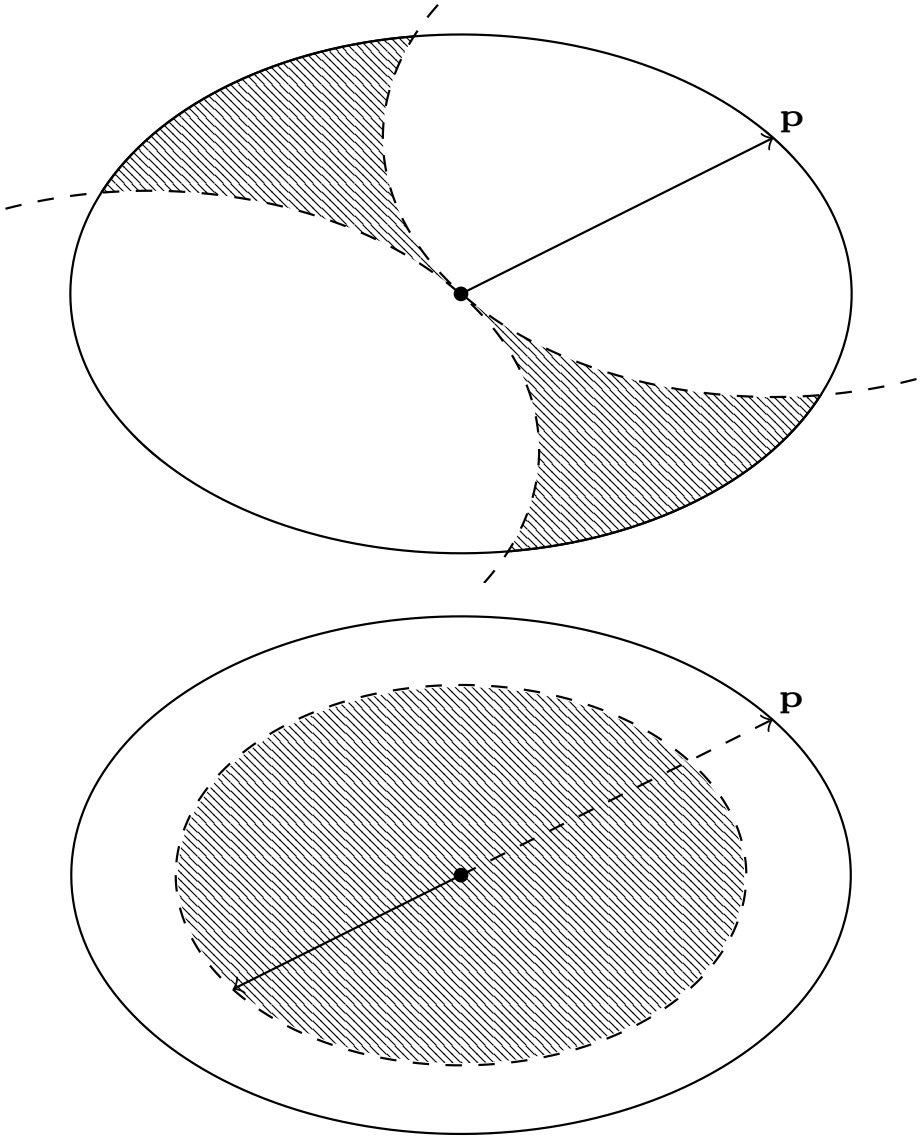

Figure 2.11 – The conditions for Lemma 2.7.30, shown in Fourier coefficient space. Top: the outer solid ellipse is $D_{\mathbf{p}}$. The two dashed arcs are translations of the boundary of the unstable ellipse, $|\mathbf{x}-\mathbf{p}|_{\boldsymbol{\kappa}} = |\mathbf{p}|_{\boldsymbol{\kappa}}$ and $|\mathbf{x}+\mathbf{p}|_{\boldsymbol{\kappa}} = |\mathbf{p}|_{\boldsymbol{\kappa}}$. The shaded region is bounded by these three curves. If and only if $\mathbf{a}$ is in the interior of the shaded region, then $\rho_0 < 0$ and $\rho_1, \rho_{-1} > 0$. Note that the shaded region lies wholly within the principal domain of modes $\mathcal{A}$ shown in Figure 2.5. Bottom: the outer solid ellipse is $D_{\mathbf{p}}$. The shaded area is the region $|\mathbf{x}|_{\boldsymbol{\kappa}} < (\sqrt{3}-1)|\mathbf{p}|_{\boldsymbol{\kappa}}$. If $\mathbf{a}$ is in the shaded area, then $\rho_0 + \rho_2 < 0$ and $\rho_0 + \rho_{-2} < 0$.

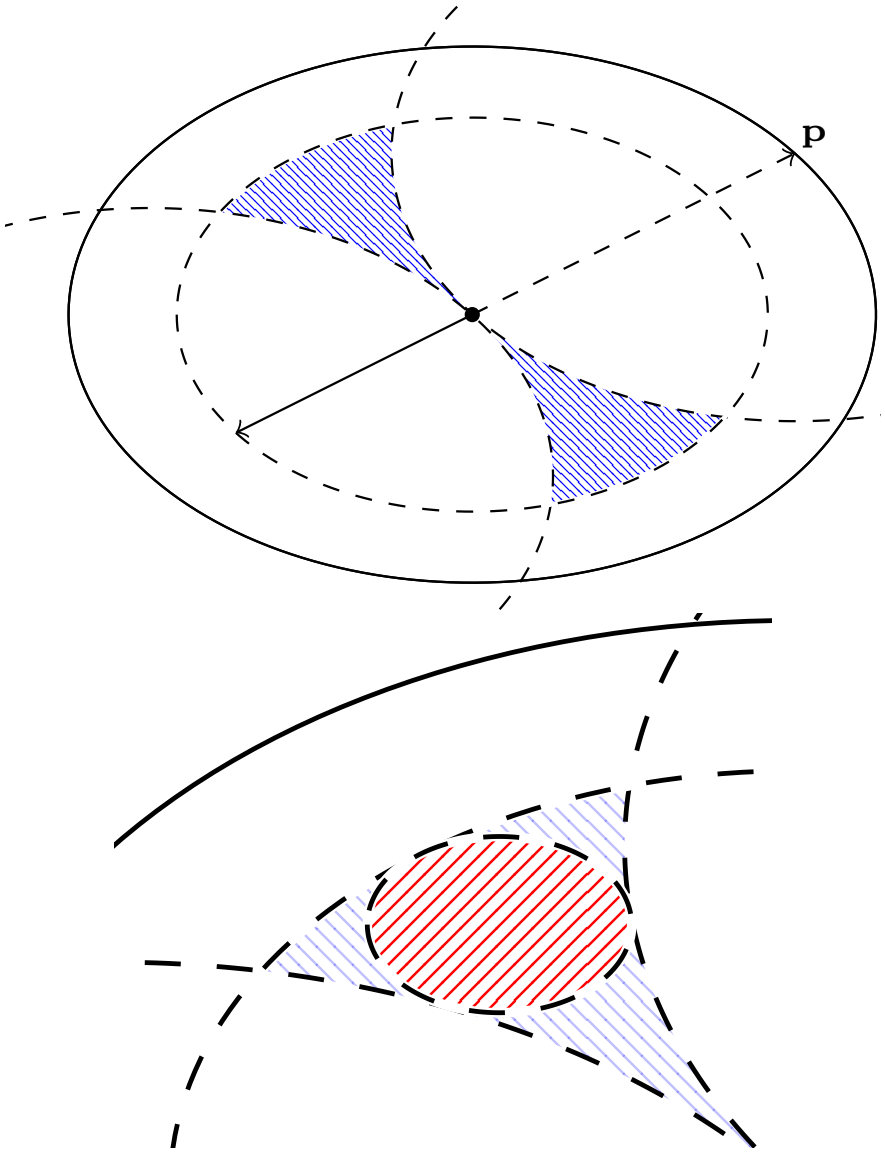

Figure 2.12 – The conditions for Lemma 2.7.30, shown in Fourier coefficient space. Top: the intersection of the two conditions in Figure 2.11. If **a** lies in the shaded blue region indicated, the conditions of Lemma 2.7.30 are satisfied. Lower: magnified detail from the upper figure, with inscribed ellipse. The red shaded region shows the largest axisymmetric ellipse circumscribed by the blue region. The ellipse is tangent to the three dashed curves. As we can explicitly describe this ellipse, we can verify that an integer lattice point occurs in this region under the condition (2.7.31).

this ellipse is the region

$$\kappa_x^2\left(x+\frac{\kappa_y p_y}{\sqrt{3}\kappa_x}\right)^2+\kappa_y^2\left(y-\frac{\kappa_x p_x}{\sqrt{3}\kappa_y}\right)^2<\left(\frac{2\sqrt{3}-3}{3}|\mathbf{p}|_{\boldsymbol{\kappa}}\right)^2. \tag{2.7.33}$$

Call this region E. This is shown in Figure 2.12 (bottom). This ellipse is tangent to $|\mathbf{x}-\mathbf{p}|_{\boldsymbol{\kappa}}=|\mathbf{p}|_{\boldsymbol{\kappa}}$ at

$$\left((1-\frac{\sqrt{3}}{2})p_x-\frac{1}{2}\left(\frac{\kappa_y}{\kappa_x}\right)p_y,\ \ \frac{1}{2}\left(\frac{\kappa_x}{\kappa_y}\right)p_x+(1-\frac{\sqrt{3}}{2})p_y\right), \tag{2.7.34}$$

to $|\mathbf{x}-\mathbf{p}|_{\boldsymbol{\kappa}}=|\mathbf{p}|_{\boldsymbol{\kappa}}$ at

$$\left(-(1-\frac{\sqrt{3}}{2})p_x-\frac{1}{2}\left(\frac{\kappa_y}{\kappa_x}\right)p_y,\ \ \frac{1}{2}\left(\frac{\kappa_x}{\kappa_y}\right)p_x-(1-\frac{\sqrt{3}}{2})p_y\right), \tag{2.7.35}$$

and $|\mathbf{x}|_{\boldsymbol{\kappa}}=(\sqrt{3}-1)|\mathbf{p}|_{\boldsymbol{\kappa}}$ at

$$\left(-(\sqrt{3}-1)\left(\frac{\kappa_y}{\kappa_x}\right)p_2,\ \ (\sqrt{3}-1)\left(\frac{\kappa_x}{\kappa_y}\right)p_1\right). \tag{2.7.36}$$

All that remains is to show that there exists an integer lattice point $\mathbf{a}\in E\cap\mathcal{A}$. For an ellipse of the form

$$\frac{(x-x_0)^2}{a^2}+\frac{(y-y_0)^2}{b^2}=1, \tag{2.7.37}$$

the largest possible square inscribed inside the ellipse has sides of length $\frac{2ab}{\sqrt{a^2+b^2}}$. In the case of (2.7.33), this length is

$$l=\frac{2(2\sqrt{3}-3)}{3\sqrt{\kappa_x^2+\kappa_y^2}}|\mathbf{p}|_{\boldsymbol{\kappa}}. \tag{2.7.38}$$

If this length $l>1$, then the interior of the square must contain an integer lattice point. Rearranging gives the condition

$$|\mathbf{p}|_{\boldsymbol{\kappa}}>\frac{3+2\sqrt{3}}{2}\sqrt{\kappa_x^2+\kappa_y^2}. \tag{2.7.39}$$

As $\boldsymbol{\kappa}$ is normalised, $\sqrt{\kappa_x^2+\kappa_y^2}=1$ and the result follows. □

Note that this is a sufficient but not necessary condition on $\mathbf{p}$ for a value of $\mathbf{a}$ to exist that satisfies the conditions of Lemma 2.7.27. The inequality (2.7.32) is not sharp. Thus there may be values of $\mathbf{a}$ that satisfy Lemma 2.7.27 for values of $\mathbf{p}$ that do not satisfy (2.7.31).

As a particular example, in the isotropic case $\kappa_y/\kappa_x=1$ the condition (2.7.31) becomes

$$|\mathbf{p}|>\frac{3\sqrt{2}+2\sqrt{6}}{2}\approx 4.57. \tag{2.7.40}$$

Checking the small number of $\mathbf{p}$ values with $|\mathbf{p}| < 4.57$, there are appropriate lattice points $\mathbf{a}$ for most such $\mathbf{p}$. The following table shows an appropriate value for $\mathbf{a}$ for corresponding parameter values $\mathbf{p}$.

$\mathbf{p}$	$(4,2)^\mathsf{T}$	$(4,1)$	$(4,0)$	$(3,3)^\mathsf{T}$	$(3,2)^\mathsf{T}$
$\mathbf{a}$	$(-1,2)^\mathsf{T}$	$(1,-2)^\mathsf{T}$	$(0,-2)^\mathsf{T}$	$(1,-1)^\mathsf{T}$	$(1,-2)^\mathsf{T}$

$\mathbf{p}$	$(3,1)^\mathsf{T}$	$(3,0)^\mathsf{T}$	$(2,2)^\mathsf{T}$	$(2,0)^\mathsf{T}$
$\mathbf{a}$	$(1,-2)^\mathsf{T}$	$(0,2)^\mathsf{T}$	$(-1,2)^\mathsf{T}$	$(0,-1)^\mathsf{T}$

(2.7.41)

These points are shown in Figure 2.13 (top) as blue dots. For reflections and rotations of these, the corresponding reflection or rotation of $\mathbf{a}$ satisfies the condition (note that it is only in the case $\kappa_y/\kappa_x = 1$ that $(p_x, p_y) \to (p_y, p_x)$ is a symmetry). Thus in the isotropic case the only values of $\mathbf{p}$ that do not have a corresponding $\mathbf{a}$ satisfying the conditions of Lemma 2.7.30 are the reflections and rotations of $\mathbf{p} = (2,1)^\mathsf{T}, (1,2)^\mathsf{T}, (1,1)^\mathsf{T}, (1,0)^\mathsf{T}, (0,1)^\mathsf{T}$.

In the special case $\mathbf{p} = (p_x, 0)$, this bound can be improved. Consider the lattice point $\mathbf{a} = (0,1)$. Then $\mathbf{a} \pm \mathbf{p} = (p_x, \pm 1) \notin D_\mathbf{p}$. Furthermore, if $p_x < \frac{1}{\sqrt{3}-1}\frac{\kappa_y}{\kappa_x}$, then $|\mathbf{a}|_{\boldsymbol{\kappa}} < (\sqrt{3}-1)|\mathbf{p}|_{\boldsymbol{\kappa}}$. Thus this satisfies the requirements of Lemma 2.7.27. Similarly if $\mathbf{p} = (0, p_y)$ and $p_y > \frac{3+2\sqrt{3}}{2}\sqrt{1 + (\frac{\kappa_x}{\kappa_y})^2}$, $\mathbf{a} = (1,0)$ satisfies the requirements of Lemma 2.7.27.

In fact, for all choices of κ_x and κ_y all but a finite number of values of $\mathbf{p}$ will admit an $\mathbf{a}$ that satisfies the condition of Lemma 2.7.27. Figures 2.13 and 2.14 show how the existence of an appropriate value of $\mathbf{a}$ given $\mathbf{p}$ changes depending on κ_x, κ_y. Figure 2.15 shows how the number of values of $\mathbf{p}$ for which valid $\mathbf{a}$ exist changes as a function of κ_y/κ_x.

2.7.8. Unstable Shear Flows. In Section 2.7.6 it was shown that under certain conditions on the coefficients ρ_k there is a positive real eigenvalue of the linearised class. In Section 2.7.7 we showed that under certain conditions on $\mathbf{p}$, there exists at least one value of $\mathbf{a}$ so that the ρ_k coefficients in the corresponding class satisfy the conditions in Section 2.7.6. We now prove that this eigenvalue has an eigenvector in ℓ^2, and hence by the spectral gap theorem show the shear flows are nonlinearly unstable. This is a key result of this thesis.

Lemma 2.7.42. *If*

$$\lambda^* = \sqrt{-\rho_1(\rho_0 + \rho_2)} \tag{2.7.43}$$

is real, the infinite dimensional linearised system given by (2.4.22) *has a positive real eigenvalue λ whose eigenvector is in ℓ^2.*

Proof. According to Lemma 2.7.20, given the required conditions on $\mathbf{p}$ there exists at least one positive real eigenvalue with some lower bound (independent

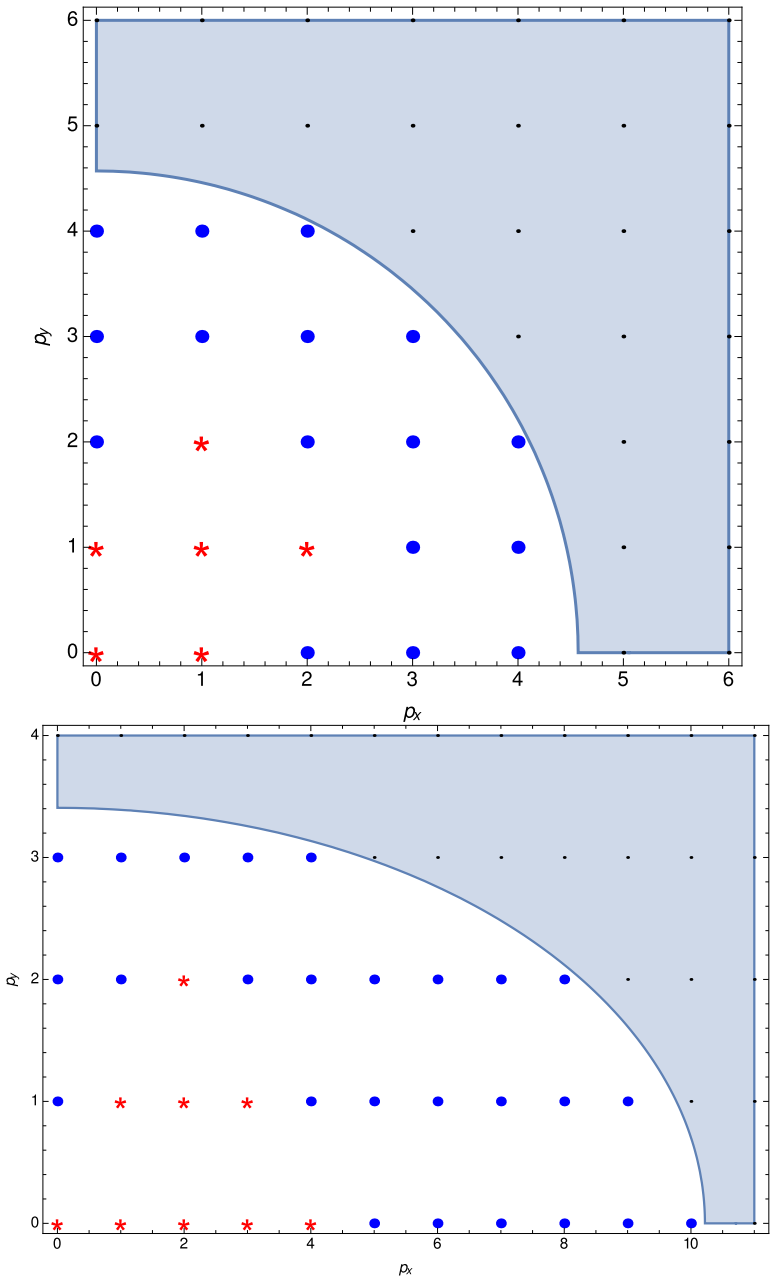

Figure 2.13 – Valid values of $\mathbf{p}$ for condition (2.7.31). For fixed values of κ_x, κ_y, a finite number of values of $\mathbf{p}$ will not satisfy condition (2.7.31). Any value of $\mathbf{p}$ in the shaded region satisfies condition (2.7.31). As (2.7.31) is nonstrict, for any κ_x, κ_y there exist $\mathbf{p}$ not satisfying (2.7.31) such that there still exist $\mathbf{a} \in \mathcal{A}$ that satisfy the conditions of Lemma 2.7.20. These values of $\mathbf{p}$ are shown as filled blue dots. All other values of $\mathbf{p}$ are shown as red asterisks; there are only finitely many such values for any given κ_x, κ_y. Top: square case $\kappa_y/\kappa_x = 1$. Bottom: $\kappa_y/\kappa_x = 3$.

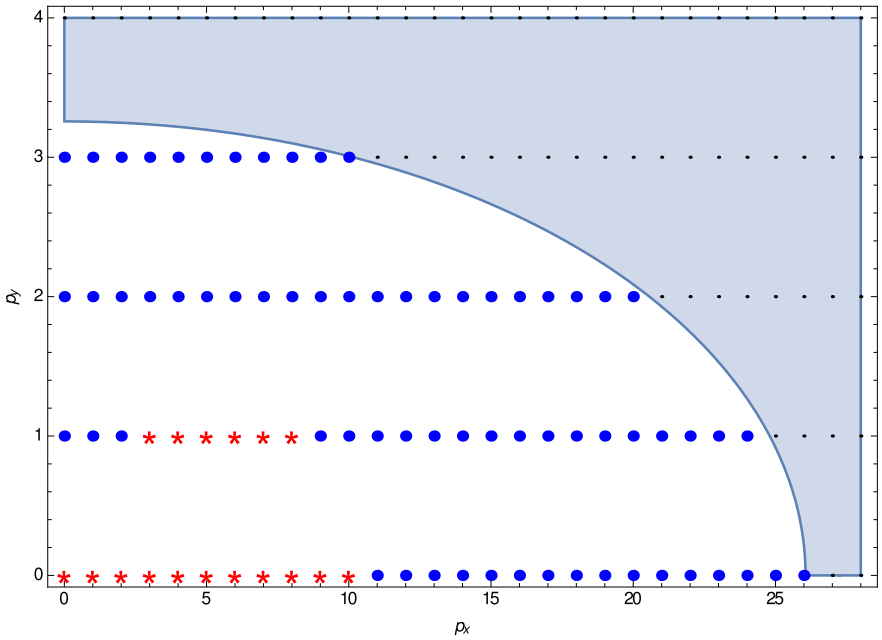

Figure 2.14 – Continued from Figure 2.13. Here $\kappa_y/\kappa_x = 8$ which is further from 1 and so more values of $\mathbf{p}$ occur outside the shaded area. As $\kappa_y/\kappa_x \to 0$ or ∞, the number of $\mathbf{p}$ outside the shaded area diverges (see Figure 2.15).

of N) of (2.7.3) for any sufficiently large truncation value N. By taking the limit $N \to \infty$ we can conclude there exists some positive real eigenvalue λ of (2.4.23).

Now consider an eigenvector associated with this eigenvalue

$$\mathbf{v} = (..., v_{-1}, v_0, v_1, v_2, ...)^{\mathsf{T}}. \tag{2.7.44}$$

For this to correspond to a real L^2 eigenfunction of the full problem (that is, for the Fourier series to converge), we need these Fourier coefficients to decay sufficiently fast: they need to be a sequence in ℓ^2.

The entries of the (infinite dimensional) eigenvector v_k of (2.4.23) corresponding to the eigenvalue λ satisfy the recursion relation

$$\lambda v_k = \alpha(\rho_{k+1} v_{k+1} - \rho_{k-1} v_{k-1}). \tag{2.7.45}$$

Since all $\rho_k \neq 0$ by assumption this can be rewritten as

$$v_{k+1} = \frac{\lambda}{\rho_{k+1}} v_k + \frac{\rho_{k-1}}{\rho_{k+1}} v_{k-1} \tag{2.7.46}$$

(scaling out the nonzero constant factor of α).

Consider the limiting behaviour as $k \to +\infty$. Then $\rho_k \to \frac{1}{|\mathbf{p}|^2_{\boldsymbol{\kappa}}}$. In this limit solutions to (2.7.46) behave like solutions to

$$v_{k+1} = \lambda |\mathbf{p}|^2_{\boldsymbol{\kappa}} v_k + v_{k-1}, \tag{2.7.47}$$

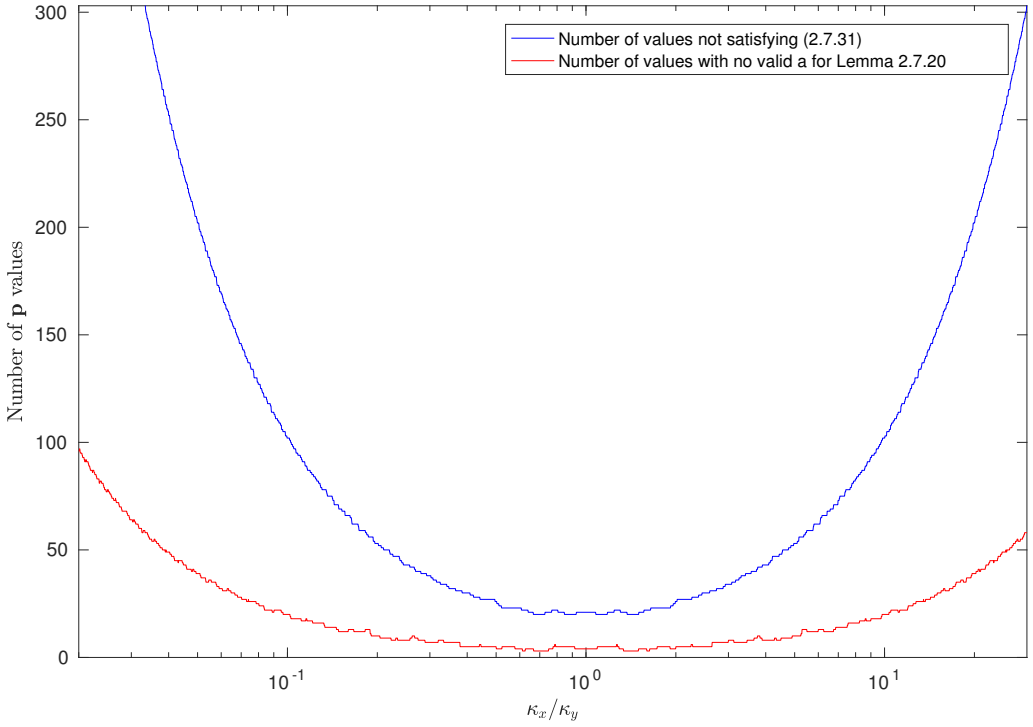

Figure 2.15 – The number of $\mathbf{p}$ values that do not satisfy the conditions of Theorem 2.7.53 as a function of the ratio κ_y/κ_x. For this plot, we consider only $\mathbf{p} = (p_x, p_y)$ with $p_x, p_y \geq 0$ and not both zero. The upper blue line shows the number of $\mathbf{p}$ values that do not satisfy (2.7.31). The lower red line shows that number of $\mathbf{p}$ values for which no $\mathbf{a}$ exists that satisfies the conditions of Lemma 2.7.20. A log scale is used on the κ_y/κ_x axis. As $\kappa_y/\kappa_x \to 0$ or $\kappa_y/\kappa_x \to \infty$, both curves diverge. The values are at their lowest around $\kappa_y/\kappa_x = 1$. For all other $\mathbf{p} \in \mathbb{Z}^2$, there exists a valid $\mathbf{a}$ and Theorem 2.7.53 proves instability.

see for example [**Hen81**].

This linear recurrence has the general solution

$$v_k = C_1\mu_1^k + C_2\mu_2^k \tag{2.7.48}$$

where $C_1, C_2 \in \mathbb{R}$ are constants and μ_1, μ_2 are solutions to $\mu^2 - \lambda|\mathbf{p}|_{\boldsymbol{\kappa}}^2\mu - 1 = 0$. Thus $\mu_1\mu_2 = -1$ and without loss of generality $|\mu_1| < 1$, $|\mu_2| > 1$ (note that we cannot have $|\mu_1| = |\mu_2| = 1$ as $\lambda|\mathbf{p}|_{\boldsymbol{\kappa}}^2 \neq 0$ for nonzero eigenvalues).

Now as $\mathbf{v}$ is an eigenvector associated with a real eigenvalue, the span of the eigenvector is an invariant subspace of the Hamiltonian system with Hamiltonian $H(\omega) = \frac{1}{2}\sum_k \rho_k\omega_k^2$ by (2.4.14). In fact, let $\omega(0) = \mathbf{v}$, then $\omega(t) = e^{\lambda t}\mathbf{v}$. As the Hamiltonian is an integral of the motion, $H(\mathbf{v}) = H(e^{\lambda t}\mathbf{v})$. By taking the limit $t \to -\infty$, $H(\mathbf{v}) = H(0) = 0$.

Therefore,

$$H(\mathbf{v}) = \sum_k \rho_k v_k^2 = 0; \tag{2.7.49}$$

$$\sum_{k\neq 0} \rho_k v_k^2 = -\rho_0 v_0^2. \tag{2.7.50}$$

Now, if $C_2 \neq 0$,

$$\sum_{k\neq 0} \rho_k v_k^2 \sim \sum_{k\neq 0} \rho_k (C_2 \mu_2^k)^2 \to \infty, \tag{2.7.51}$$

as $\rho_k \to \frac{1}{|\mathbf{p}|_{\boldsymbol{\kappa}}^2}$ and $\rho_k > 0$ for all $k \neq 0$. But ρ_0 and v_k are finite, so there is a contradiction. Thus $C_2 = 0$ and $v_k = C_1 \mu_1^k$ in the asymptotic limit, where $|\mu_1| < 1$. This is exponential decay, which is sufficient for the Fourier series to converge.

Similarly for $k \to -\infty$, the limiting behaviour is governed by

$$v_{k-1} = -\lambda |\mathbf{p}|_{\boldsymbol{\kappa}}^2 v_k + v_{k-1}. \tag{2.7.52}$$

Again, this means v_k is asymptotic to $C_1\mu_1^k + C_2\mu_2^k$ for $|\mu_1| < 1$, $|\mu_2| > 1$. By the same argument as above, we conclude that $C_1 = 0$ and so $v_k = C_2\mu_2^k$ as $k \to \infty$. Thus the Fourier coefficients decay exponentially on both sides with $|k|$, and hence $\mathbf{v}$ is in ℓ^2. □

Now we can combine the results regarding real eigenvalues and the associated eigenvectors from the preceding sections and the conditions on $\mathbf{p}$ to conclude nonlinear instability.

Theorem 2.7.53. *The steady state*

$$\Omega^* = \alpha \cos(\kappa_x p_x x + p_y \kappa_y y) + \beta \sin(\kappa_x p_x x + \kappa_y p_y y) \tag{2.7.54}$$

is nonlinearly unstable for all $\mathbf{p} = (p_x, p_y)^\mathsf{T}$ *satisfying*

$$|\mathbf{p}|_{\boldsymbol{\kappa}} > \frac{3 + 2\sqrt{3}}{2}. \tag{2.7.55}$$

For a fixed κ_x, κ_y*, this condition is satisfied for all but finitely many values of* $\mathbf{p}$*.*

Proof. By Lemma 2.7.30, for all $\mathbf{p}$ satisfying (2.7.55) there exists some $\mathbf{a}$ such that $\rho_0 < 0$, $\rho_k > 0$ for all $k \neq 0$ and $\rho_0 + \rho_2 < 0$ and $\rho_0 + \rho_{-2} < 0$. Thus by Lemma 2.7.42 there exists a real positive eigenvalue λ of (2.7.3) for a sufficiently large value of N. Moreover, the eigenvalue is greater than

$$\max(\sqrt{-\rho_1(\rho_0 + \rho_2)}, \sqrt{-\rho_{n-1}(\rho_0 + \rho_{n-2})}) \tag{2.7.56}$$

which is positive and independent of the choice of truncation size N. The truncation size N can be increased without bound. Hence there is a hyperbolic eigenvalue of (2.4.22) in the limit $N \to \infty$ and the spectrum of the linearised PDE leads to instability. Now recall that any steady state of the form

$\Omega^* = \alpha\cos(\kappa_x p_x x + p_y\kappa_y y) + \beta\sin(\kappa_x p_x x + p_y\kappa_y y)$ can be rewritten in the form $\Omega^* = 2\Gamma\cos(\kappa_x p_x x + p_y\kappa_y y)$ by a coordinate transformation and so the instability result follows.

By Lemma 2.7.42, the eigenvector associated with the eigenvalue λ is in ℓ^2. The classes led by $\mathbf{a}$ and $-\mathbf{a}$ have the same spectrum, and thus the corresponding eigenvectors can be combined to construct coefficients $\omega_{\mathbf{k}}$ of a real eigenfunction V_λ corresponding to λ. Since the eigenvectors $\mathbf{v}$ are in ℓ^2 the periodic function V_λ is in L^2. Together with the result in Latushkin, Li and Stanislavova [**LLS04**] which shows that the spectral mapping theorem holds, this establishes linear instability. To conclude nonlinear instability we refer to the work of Friedlander, Strauss and Vishik [**FSV97**] and Shvidkoy and Latushkin [**SL03**]. In [**FSV97**] it is shown that sufficient conditions for nonlinear instability are linear instability together with a 'spectral gap' condition. In [**SL03**] it is shown that the continuous spectrum of the linearised Euler operator in the cases we are considering is $i\mathbb{R}$. Because of the presence of a point of discrete spectrum bounded away from the imaginary axis, we have a spectral gap, and hence nonlinear instability. □

We stress that this result is not sharp, in the sense that the condition (2.7.55) is sufficient but not necessary. As shown in Figure 2.13, for a fixed value of $\boldsymbol{\kappa}$ there are many values of $\mathbf{p}$ that do not satisfy (2.7.55) but still have an associated class $\mathbf{a}$ such that Lemma 2.7.20 holds and there is therefore a positive real eigenvalue and hence instability. In fact, the observations of Section 2.7.1 are supported by numerical evidence shown in Section 6.1, and lead to the observation that for any values of $\mathbf{p}$ not of the form described in Section 2.6, the associated shear flow is nonlinearly unstable. This is formulated as Conjecture 6.1.8.

2.8. Spectrum Classification

In the previous section, for many classes we proved the existence of a positive real eigenvalue. In this section, we numerically build a fuller picture of the nonimaginary spectrum associated with a class. We begin by showing that all classes can be reduced by a series of transformations to a class with parameters $\mathbf{p} = (1,0)^\mathsf{T}$, ${}^{\kappa_y}/_{\kappa_x} = 1$. We then describe how the size and type of the eigenvalues vary depending on the choice of $\mathbf{a}$ in these reduced coordinates.

2.8.1. Rotated Coordinates. Consider the linearised system (2.4.22). Define the new parameters

$$\tilde{\mathbf{p}} := K\mathbf{p}, \quad \tilde{\mathbf{a}} = K\mathbf{a} \tag{2.8.1}$$

where K is the aspect matrix (2.2.11). Then

$$\rho_k = \frac{1}{|\tilde{\mathbf{p}}|^2} - \frac{1}{|\tilde{\mathbf{a}} + k\tilde{\mathbf{p}}|^2} \tag{2.8.2}$$

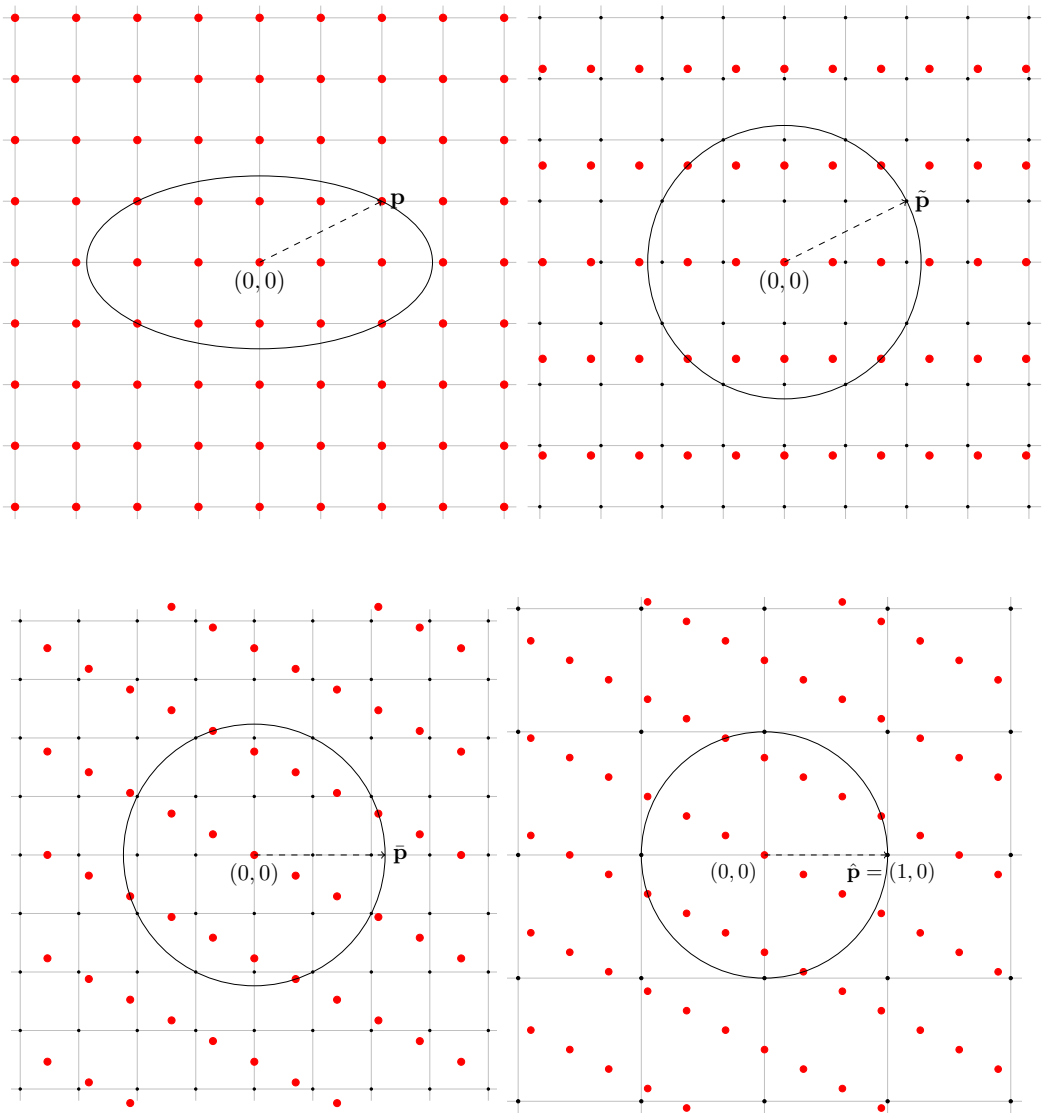

Figure 2.16 – How the lattice of valid values of $\hat{\mathbf{a}}$ is deformed by the transformation defined by (2.8.5). In each figure, the lattice $\mathbb{Z}^2$ is shown with black dots connected by grid lines, and the transformed unstable ellipse and $\mathbf{p}$ are shown. The red dots show the transformed lattice of relevant values of $\mathbf{a}$. Top left: the untransformed lattice $\mathbb{Z}^2$. Top right: the scaling $\tilde{\mathbf{a}} = K\mathbf{a}$ is applied to transform $K \to \mathbb{I}$. The admissible values of $\tilde{\mathbf{a}}$ are shown as red dots. The unstable ellipse is now a circle, the unstable disc per [**Li00**]. Bottom left: the rotation $\bar{\mathbf{a}} = R_{\tilde{\mathbf{p}}}\tilde{\mathbf{a}}$ is applied to rotate $\tilde{\mathbf{p}}$ parallel to the x-axis. The lattice of admissible values of $\bar{\mathbf{a}}$, shown in red, is accordingly rotated. Bottom right: the scaling by a factor of $1/|\mathbf{p}|_\kappa$ transforms $\bar{\mathbf{p}}$ to the unit vector in the x-direction. Admissible values of $\hat{\mathbf{a}}$ are shown as red dots.

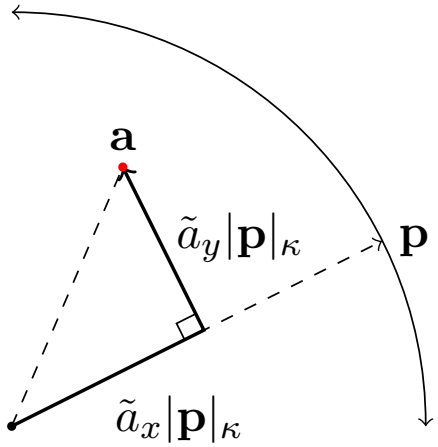

Figure 2.17 – The relationship between $\mathbf{a}$ and $\mathbf{p}$ and the new parameters $\tilde{a}_x$, $\tilde{a}_y$. The parameter $\tilde{a}_x$ measures the length of the projection of $\mathbf{a}$ onto $\mathbf{p}$, and $\tilde{a}_y$ measures the length of the component of $\mathbf{a}$ orthogonal to $\mathbf{p}$. Both parameters are normalised by $|\mathbf{p}|_{\boldsymbol{\kappa}}$. For $\kappa_y/\kappa_x = 1$, this is the usual vector projection and rejection as shown; for $\kappa_y/\kappa_x \neq 1$ it is the orthogonal decomposition in the $\boldsymbol{\kappa}$ inner product (2.2.12).

where $|\mathbf{x}|$ is the standard Euclidean norm, and the scaling factor $\alpha = \Gamma\tilde{\mathbf{a}} \times \tilde{\mathbf{p}}$. The factor of α will occur in the full differential equations $\dot{\omega} = \alpha M\omega$, and so multiplies any eigenvalues. Thus the linearised subsystem is equivalent to that of a class with an isotropic domain $K = \mathbb{I}$.

Next, define

$$R_{\tilde{\mathbf{p}}} := \frac{1}{\sqrt{\tilde{p}_x^2 + \tilde{p}_y^2}} \begin{pmatrix} \tilde{p}_x & \tilde{p}_y \\ -\tilde{p}_y & \tilde{p}_x \end{pmatrix}. \tag{2.8.3}$$

The matrix $R_{\tilde{\mathbf{p}}} \in SO(2)$ so $R_{\tilde{\mathbf{p}}}^{\mathsf{T}} R_{\tilde{\mathbf{p}}} = R_{\tilde{\mathbf{p}}} R_{\tilde{\mathbf{p}}}^{\mathsf{T}} = \mathbb{I}$ and $\det(R_{\tilde{\mathbf{p}}}) = 1$. Let $\bar{\mathbf{p}} = R_{\tilde{\mathbf{p}}}\tilde{\mathbf{p}} = (|\tilde{\mathbf{p}}|, 0)^{\mathsf{T}} = (\bar{p}_x, 0)$ and $\bar{\mathbf{a}} = R_{\tilde{\mathbf{p}}}\tilde{\mathbf{a}} = (\bar{a}_x, \bar{a}_y)$. Then $\alpha = -\bar{a}_y\bar{p}_x$, and ρ_k remains unchanged as norms are invariant under rotation. Finally if we introduce the transformation $\hat{\mathbf{a}} = \frac{\bar{\mathbf{a}}}{\bar{p}_x}$, then $\alpha = -\hat{a}_y$ and

$$\rho_k = \left(1 - \frac{1}{(\hat{a}_x + k)^2 + \hat{a}_y^2}\right). \tag{2.8.4}$$

This system is now the same as the linearised system with $\Gamma \to {}^1\!/_{\bar{p}_1^2}\Gamma = {}^1\!/_{|\mathbf{p}|_{\boldsymbol{\kappa}}^2}\Gamma$, $\mathbf{p} = (1, 0)^{\mathsf{T}}$ and $\mathbf{a} = \hat{\mathbf{a}}$. Ignoring the scaling factors of Γ and $\frac{1}{|\mathbf{p}|_{\boldsymbol{\kappa}}}$, which will be the same for all classes, we can define the scaling per class as $\alpha = |a_y|$ (the sign of α can be ignored by the Hamiltonian symmetry of the problem; for all eigenvalues λ, $-\lambda$ is also an eigenvalue). Thus up to a time rescaling to change

the constant factor and the transformation

$$\hat{\mathbf{a}} = \frac{1}{|\mathbf{p}|_{\boldsymbol{\kappa}}} R_{\mathbf{p}} K \mathbf{a} \tag{2.8.5}$$

for $\mathbf{a} \in \mathbb{Z}^2$, we can perform all numerics on this simplified system

$$\mathbf{p} = \begin{pmatrix} 1 \\ 0 \end{pmatrix}, \quad \mathbf{a} = \begin{pmatrix} \tilde{a}_x \\ \tilde{a}_y \end{pmatrix}, \quad K = \mathbb{I}, \quad \alpha = |a_y|. \tag{2.8.6}$$

We use the notation $\tilde{a}_x, \tilde{a}_y$ to indicate we are using the reduced parameters, rather than the original parameter $\mathbf{a} \in \mathbb{Z}^2$.

It is very important to note this does not imply that the linearised problem (2.4.13) does not depend on the K or $\mathbf{p}$. Our class parameters $\tilde{a}_x, \tilde{a}_y$ in this adjusted system will no longer have values is $\mathbb{Z}$. Instead, $(\tilde{a}_x, \tilde{a}_y)$ must take values on a stretched, rotated and scaled version of such a lattice. We could not reconstruct the full problem from these classes without summing over the transformed lattice, which would require a transformation back to the original coordinates. Thus is it is natural that we cannot make the same transformations to simplify the original partial differential equation. See Figure 2.16 for an illustration of the relationship between the new lattice of relevant values of $(\tilde{a}_x, \tilde{a}_y)$ and $\mathbb{Z}^2$, and Figure 2.17 for the relationship between the original $\mathbf{a}$ and the reduced parameters $\tilde{a}_x$ and $\tilde{a}_y$.

To study the eigenvalues numerically, we consider only the spectrum of $\alpha M = |\tilde{a}_y| M$ where M is defined as in (2.4.23) with $\mathbf{p} = (1, 0)$. Now the principal domain of parameters $(\tilde{a}_x, \tilde{a}_y)$ is

$$\mathcal{A} = \{(\tilde{a}_x, \tilde{a}_y) \in \mathbb{R}^2 \mid -\frac{1}{2} < \tilde{a}_x \leq \frac{1}{2}\}. \tag{2.8.7}$$

We consider all real values of $\mathbf{a} \in \mathcal{A}$, ignoring for the moment that for an actual linearisation only a discrete set of values will actually occur.

These reduced parameters gives us a convenient setting to study the lower bound $\lambda^* = \max(\sqrt{-\rho_1(\rho_0 + \rho_2)}, \sqrt{-\rho_{-1}(\rho_0 + \rho_{-2})})$ described in Lemma 2.7.20. This is shown in Figure 2.18.

We can use these parameters to describe the type and number of nonimaginary eigenvalues as a function of $\tilde{a}_x$ and $\tilde{a}_y$. Figure 2.19 shows that there are four generic possibilities for nonimaginary eigenvalues; no nonimaginary eigenvalues, one pair of real eigenvalues, two pairs of real eigenvalues, and a complex quadruplet of eigenvalues. The figure shows how these four possibilities depend on the parameters. The boundary curve between two pairs of real eigenvalues and a complex quadruplet is not known analytically; it is calculated numerically. This corresponds to the observations of Section 2.7.1, as illustrated in Figure 2.10. This regions there are related to the regions in Figure 2.19 by the affine transformation (2.8.5).

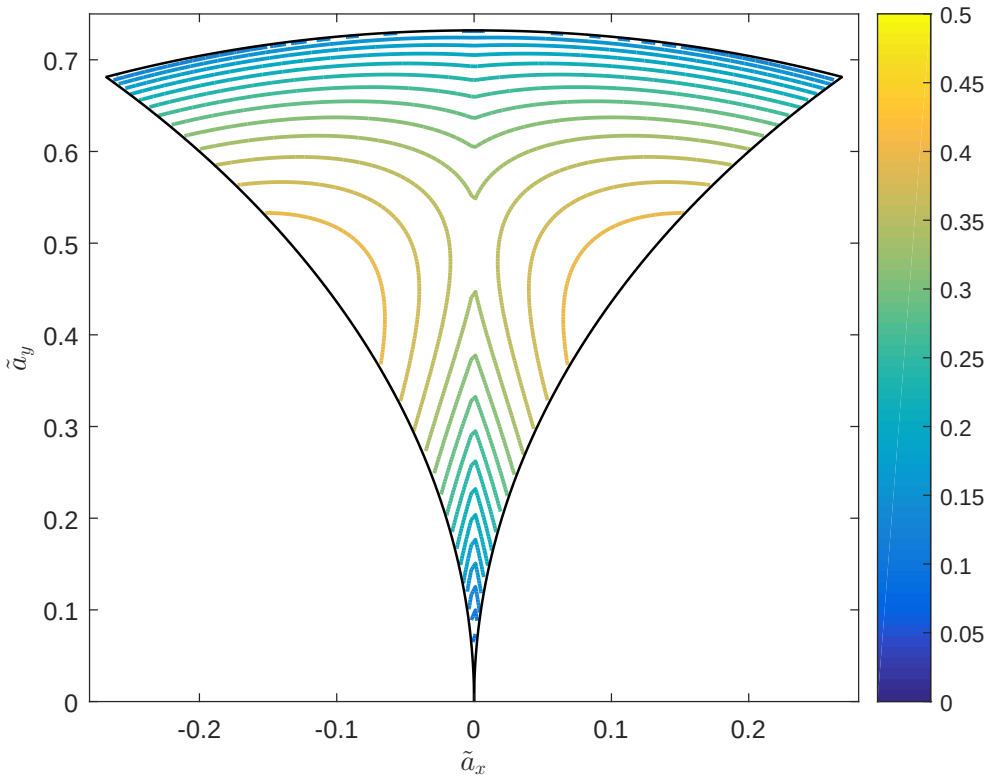

Figure 2.18 – Contour plot of the lower bound $\alpha\lambda^*$ from (2.7.28) for the real eigenvalue of αM as a function of $(\tilde{a}_x, \tilde{a}_y)$. Only the area where the lower bound is real and positive is shown. Note that we can take the larger of $\sqrt{-\rho_{-1}(\rho_0+\rho_{-2})}$ and $\sqrt{-\rho_1(\rho_0+\rho_2)}$, hence the symmetry across $\tilde{a}_x = 0$. Also note that $\alpha = \tilde{a}_y$ in the reduced coordinates. The figure can also be reflected across $\tilde{a}_y = 0$. The curves $(\tilde{a}_x \pm 1)^2 + \tilde{a}_y^2 = 1$ and $\tilde{a}_x^2 + \tilde{a}_y^2 = \sqrt{3} - 1$ are shown; compare the shape with the region shown in Figure 2.12.

Figure 2.20 illustrates how the bifurcations between types of eigenvalues occur. Figures 2.21 and 2.22 show the values of the eigenvalues at some of the bifurcation boundaries; note that these figures include the factor of α.

2.9. The Half-Class Operator and Associated Jacobi Problem

In the previous section, we asserted that bifurcations occur when $\tilde{a}_x^2 + \tilde{a}_y^2 = 1$ and $(\tilde{a}_x \pm 1)^2 + \tilde{a}_y^2 = 1$. To study these boundary cases in further depth, we now draw a connection between the matrix (2.4.23) and Jacobi operators.

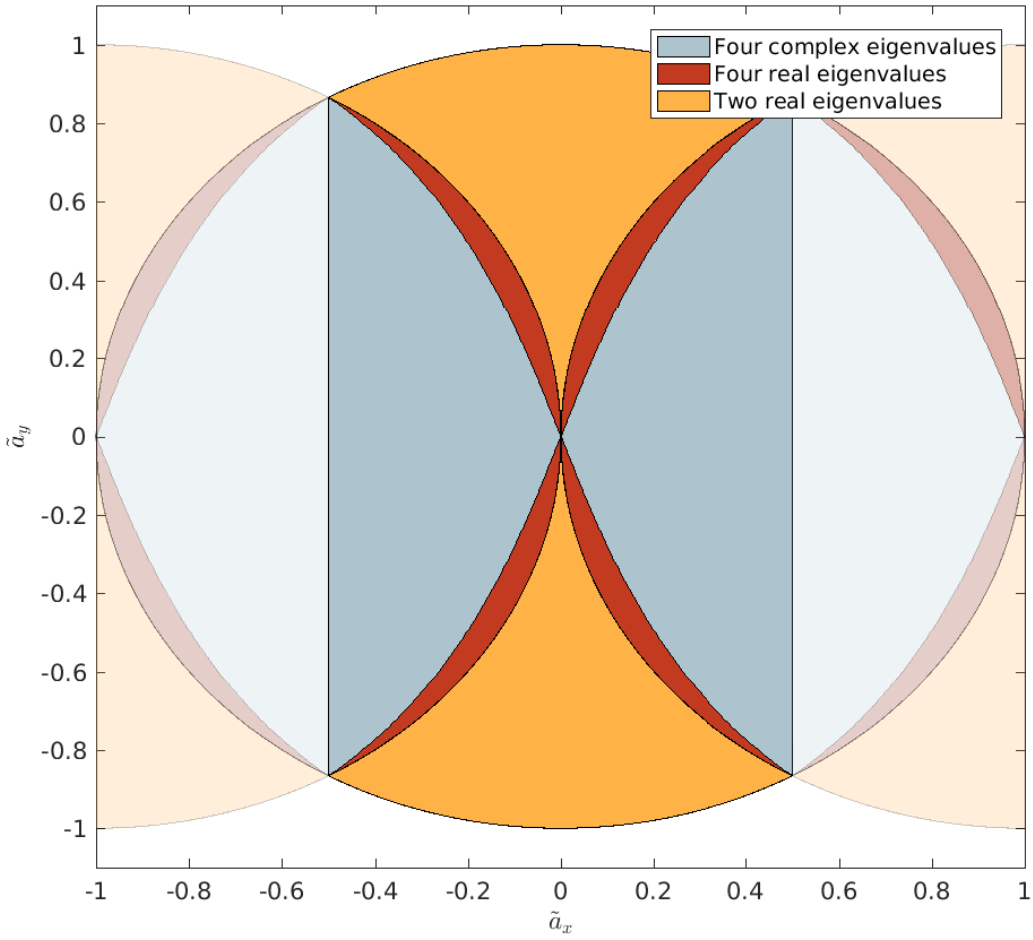

Figure 2.19 – The type and number of nonimaginary eigenvalues of M as a function of $(\tilde{a}_x, \tilde{a}_y) \in \mathcal{A}$. For this figure, we use the reduced coordinates with $\mathbf{p} = (1,0)^\mathsf{T}$, $K = \mathbb{I}$. The result is the same for all values of K, $\mathbf{p}$ up to rotation and scaling as shown in Figure 2.16. For values of $(\tilde{a}_x, \tilde{a}_y)$ in the yellow region, there are two nonimaginary eigenvalues, which occur as a real pair $\pm\lambda$. This region is bounded by the curves $\tilde{a}_x^2+\tilde{a}_y^2 = 1$, $(\tilde{a}_x-1)^2+\tilde{a}_y^2 = 1$, and $(\tilde{a}_x+1)^2+\tilde{a}_y^2 = 1$. In the blue and red regions, there are four nonimaginary eigenvalues; in the blue region, they are a complex quadruplet $\pm\alpha \pm \beta i$, and in the red region they are two real pairs $\pm\alpha$, $\pm\beta$. If $\tilde{a}_x, \tilde{a}_y$ are not in any of these regions, there are no nonimaginary eigenvalues. The faded regions are outside the principal domain $-1/2 < \tilde{a}_x \leq 1/2$ and are translations of the regions inside the principal domain by $(1,0)$. This shows the full unstable disc $\tilde{a}_x^2 + \tilde{a}_y^2 = 1$.

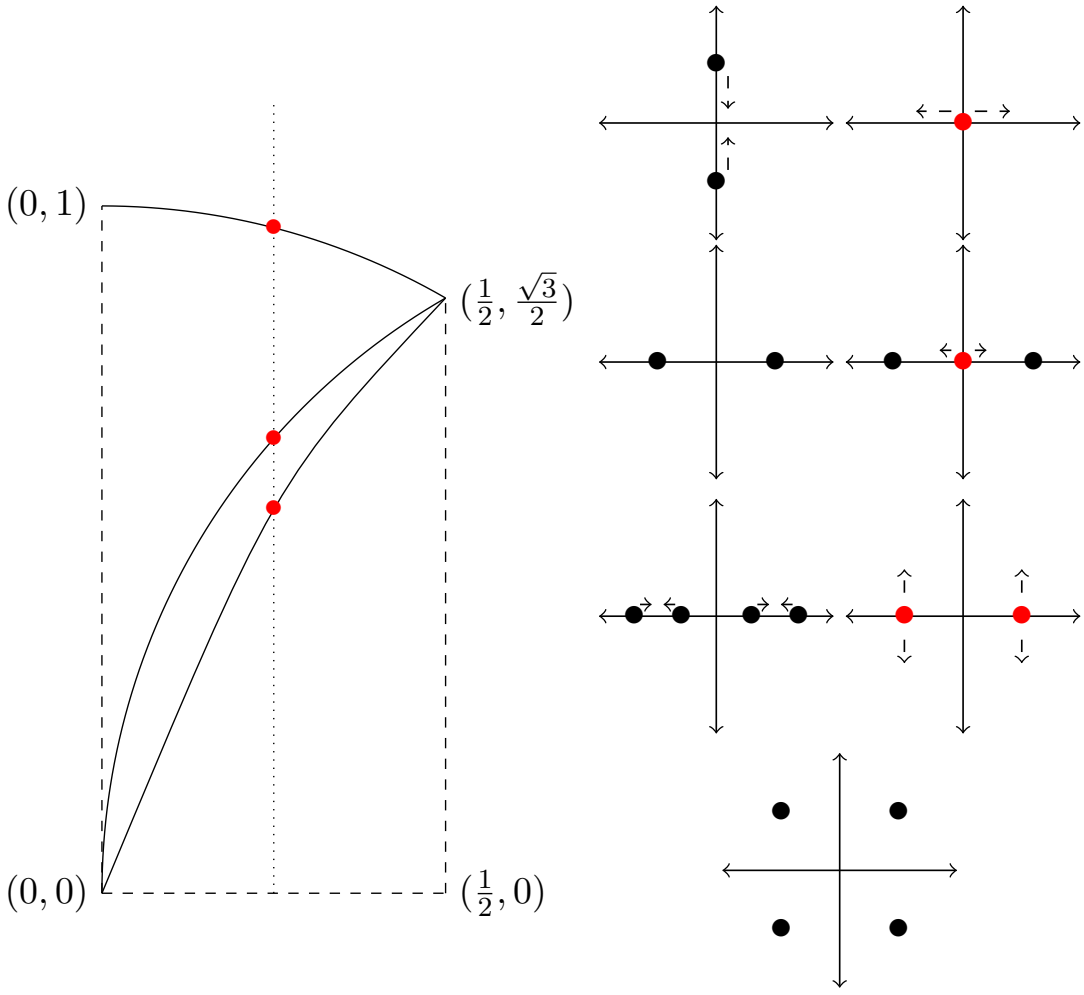

Figure 2.20 – The bifurcations that occur in the eigenvalues of M as a function of $\tilde{a}_x, \tilde{a}_y$. Left: an illustration of detail from 2.19, showing bifurcation curves. We only need to consider the range $0 \leq \tilde{a}_x \leq \frac{1}{2}$, $\tilde{a}_y \geq 0$. The other four quadrants are reflections of this one. Right: an illustration of how the eigenvalues change in the complex plane as $\tilde{a}_y$ changes along the dotted line $\tilde{a}_x = 0.25$ shown in the left figure, travelling from top to bottom. The figures are arranged from left to right, top to bottom. If $|\tilde{a}_y| > \sqrt{1 - \tilde{a}_x^2}$, there are no nonimaginary eigenvalues. When $|\tilde{a}_y| = \sqrt{1 - \tilde{a}_x^2}$ (the top red dot on the left figure), two imaginary eigenvalues collide at zero, and split off onto the real axis. Between this and the next bifurcation, there are two nonzero real eigenvalues. At the next bifurcation when $|\tilde{a}_y| = \sqrt{1 - (\tilde{a}_x - 1)^2}$ (the second red dot), another two imaginary eigenvalues collide at zero and split off onto the real axis. Then there are four nonzero real eigenvalues. At the final bifurcation (the third red dot), the two pairs of nonzero real eigenvalues collide, and travel into the complex plane. After this, there will be a complex quadruplet of eigenvalues.

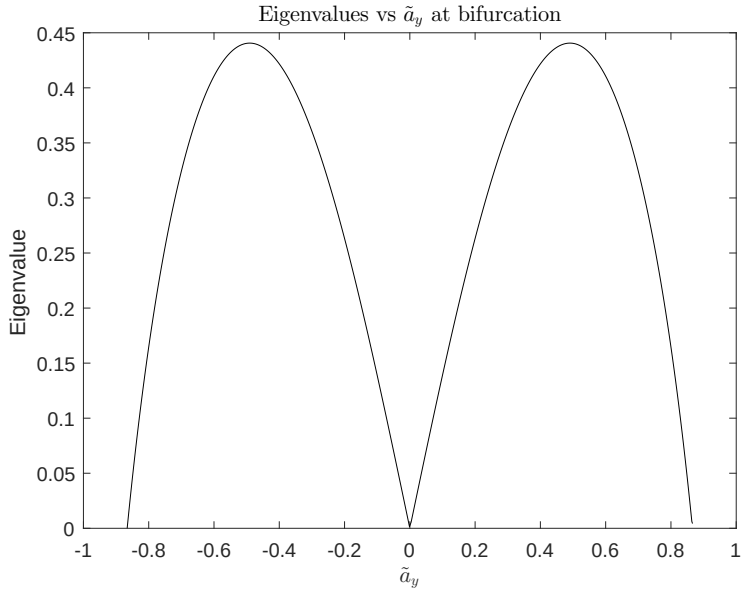

Figure 2.21 – The positive real eigenvalue of αM as a function of $\tilde{a}_y$ along the curve $(\tilde{a}_x - 1)^2 + \tilde{a}_y^2 = 1$. This occurs at the bifurcation between two and four real eigenvalues, as seen in Figure 2.19.

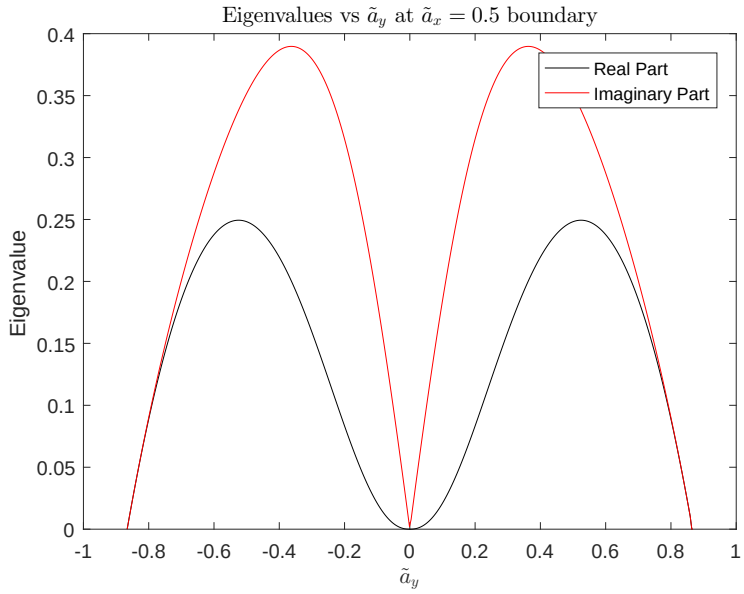

Figure 2.22 – The eigenvalue of αM as a function of $\tilde{a}_y$ at the boundary of the principal domain of modes $\mathcal{A}$ at $\tilde{a}_x = 1/2$. The eigenvalues here occur as a complex quadruplet $\pm\gamma \pm \delta i$; the positive real part is shown in black, and the positive imaginary part in red.

Jacobi operators are useful mathematical objects in a number of contexts. They arise in moment problems (see [**Akh65**]; that text refers to them as *infinite Jacobi matrices* or $\mathcal{J}$-matrices), as a discrete analogue of Sturm-Liouville operators, and as half of a Lax Pair for the Toda Lattice [**Tes00**]. Here we will recast our linearised system (2.4.22) in terms of a Jacobi operator and study the associated properties and how they translate back to the original problem.

For classes satisfying $\tilde{a}_x^2 + \tilde{a}_y^2 = 1$, or equivalently $\rho_0 = 0$, we split the problem into two "half-classes" which are semi-infinite rather than bi-infinite. We can therefore adjust our analysis for these special cases. We first present the equivalent stability result to Theorem 2.5.5 for the half-classes. We then derive a simple result giving an upper bound on eigenvalues of the associated matrix. The half-class is then studied from a Jacobi operator perspective.

2.9.1. The Associated Jacobi Operator. Consider the eigenvalue problem for (2.4.23)

$$\lambda v_n = \rho_{n+1} v_{n+1} - \rho_{n-1} v_{n-1}. \tag{2.9.1}$$

By using this recursion on v_{n+1} and v_{n-1} to expand the equation out further,

$$(\lambda^2 + \rho_n(\rho_{n+1} + \rho_{n-1}))v_n = \rho_{n+1}\rho_{n+2}v_{n+2} + \rho_{n-1}\rho_{n-2}v_{n-2}. \tag{2.9.2}$$

In the generic case $\rho_n \neq 0$ for all n, we define $\tilde{v}_k := \sqrt{\rho_{2n}} v_{2n}$ and $\bar{v}_k := \sqrt{\rho_{2n+1}} v_{2n+1}$. Then $\tilde{v}_k$ and $\bar{v}_k$ satisfy the second order difference equations

$$\begin{aligned} \lambda' \tilde{v}_n &= b_{n+1}\tilde{v}_{n+1} + a_n \tilde{v}_n + b_n \tilde{v}_{n-1} \\ \lambda' \bar{v}_n &= d_{n+1}\bar{v}_{n+1} + c_n \bar{v}_n + d_n \bar{v}_{n-1} \end{aligned} \tag{2.9.3}$$

where

$$\begin{aligned} a_n &= -\rho_{2n}(\rho_{2n+1} + \rho_{2n-1}), \quad b_n = \rho_{2n-1}\sqrt{\rho_{2n-2}\rho_{2n}}, \\ c_n &= -\rho_{2n+1}(\rho_{2n+2} + \rho_{2n}), \quad d_n = \rho_{2n}\sqrt{\rho_{2n-1}\rho_{2n+1}}, \end{aligned} \tag{2.9.4}$$

and the new eigenvalue is $\lambda' = \lambda^2$. These difference equations are the eigenvalue problems for the Jacobi operators

$$\begin{aligned} \tilde{J}\tilde{v}_n &:= b_{n+1}\tilde{v}_{n+1} + a_n \tilde{v}_n + b_n \tilde{v}_n, \\ \bar{J}\bar{v}_n &:= d_{n+1}\bar{v}_{n+1} + c_n \bar{v}_n + d_n \bar{v}_n. \end{aligned} \tag{2.9.5}$$

Note that a_n, b_n, c_n, d_n may not be real. If $\rho_n > 0$ for all n, then all the coefficients are real. In that case, the operators $\tilde{J}$ and $\bar{J}$ are Hermitian.

2.9.2. The Half-Class Operator. We now address the case $\rho_k = 0$ for some k. This allows for some simplifications, as we can decompose our Jacobi operator into two parts analogous to the approach in [**Li00**].

Working in the transformed system (2.8.6), we change the domain condition (2.8.7) from $\tilde{a}_x \in (-0.5, 0.5]$ to $\tilde{a}_x \in [-1, 0)$ for notational convenience. This means that ρ_0 is not always the minimum value of ρ_k, but we can now describe

any class with $\rho_k = 0$ for some k by $\tilde{a}_y = \pm\sqrt{1-\tilde{a}_x^2}$, so $\rho_0 = 0$. Then if $\rho_k \leq 0$ for any k, this must be ρ_1.

There are some special cases when we have a clearer idea of when these parameter values will actually be attained in the real problem. The case $\tilde{a}_x = 0$, $\tilde{a}_y = \pm 1$ (where $\rho_0 = 0$) translates to $\mathbf{a} = (\pm\kappa_x^{-1}p_y, \mp\kappa_y^{-1}p_x)^\mathsf{T}$ in the full problem; when κ_x^{-1} and κ_y^{-1} are integers this is always a lattice point, and so such a class exists. Furthermore, in the case $K = \mathbb{I}$, the classes $\mathbf{a} = \pm(p_y, p_x)$ will always lead to one of these cases. There are also the two classes $\mathbf{a} = \pm(-p_x, p_y)$. Other classes will occur across the parameter ranges of $\mathbf{p}$ and $\boldsymbol{\kappa}$, but one cannot make precise statements about when they will and will not occur.

There is also the exceptional case when $\rho_k = 0$ for two values of k. This occurs in the transformed coordinates when $\tilde{a}_x = 0$, $\tilde{a}_y = 0$ (so $\rho_{-1} = \rho_{+1} = 0$) or $\tilde{a}_x = -1/2$, $\tilde{a}_y = \pm\sqrt{3}/2$ (so $\rho_0 = 0$, $\rho_1 = 0$). The former case is singular, but occurs when $\alpha = 0$ and so can be safely ignored. As discussed in Section 2.7.1, the latter case can only occur in the untransformed problem for very specific values of K and $\mathbf{p}$ satisfying (2.7.2). It is not possible to have $\rho_k = 0$ for more than two values of k.

Whether there are one or two values of k such that $\rho_k = 0$, we can now split (2.9.2) into two Jacobi operators. Without loss of generality, assume that $\tilde{a}_y = \sqrt{1-\tilde{a}_x^2}$, so $\rho_0 = 0$. Then

$$\lambda v_{-1} = -\rho_{-2}v_{-2}, \quad \lambda v_{+1} = \rho_2 v_2 \tag{2.9.6}$$

and (2.9.1) holds for all $|n| > 1$.

Before proceeding to turn these into a Jacobi problem, we address the stable cases. This is Case (a) from Section 2.7.1.

Proposition 2.9.7 (Half-Class stability)**.** *If $\rho_i = 0$ for exactly one $i \in \mathbb{Z}$ and $\rho_k > 0$ for all $k \neq i$ (or equivalently, $\Sigma_\mathbf{a} \cap D_\mathbf{p} = \emptyset$ and $|\Sigma_\mathbf{a} \cap \partial D_\mathbf{p}| = 1$), the corresponding subsystem does not contribute linear instability to the full system.*

Proof. Without loss of generality, assume $\rho_0 = 0$. Then by the above, the dynamics of the associated system can be split into two parts and described by the matrices

$$M_1 = \begin{pmatrix} 0 & \rho_2 & 0 & 0 & \dots \\ -\rho_1 & 0 & \rho_3 & 0 & \dots \\ 0 & -\rho_2 & 0 & \rho_4 & \dots \\ 0 & 0 & -\rho_3 & 0 & \dots \\ \vdots & \vdots & \vdots & \vdots & \ddots \end{pmatrix} \tag{2.9.8}$$

and

$$M_2 = \begin{pmatrix} 0 & \rho_{-2} & 0 & 0 & \dots \\ -\rho_{-1} & 0 & \rho_{-3} & 0 & \dots \\ 0 & -\rho_{-2} & 0 & \rho_{-4} & \dots \\ 0 & 0 & -\rho_{-3} & 0 & \dots \\ \vdots & \vdots & \vdots & \vdots & \ddots \end{pmatrix}. \tag{2.9.9}$$

If $\rho_k > 0$ for all $k \neq 0$, these matrices are both similar to a skew-symmetric matrix by the transformation matrix

$$T = \begin{pmatrix} \rho_{\pm 1}^{-1/2} & 0 & 0 & \dots \\ 0 & \rho_{\pm 2}^{-1/2} & 0 & \dots \\ 0 & 0 & \rho_{\pm 3}^{-1/2} & \dots \\ \vdots & \vdots & \vdots & \ddots \end{pmatrix} \tag{2.9.10}$$

with positive choices of $\rho_{\pm k}$ for M_1 and negative for M_2. This condition is equivalent to the class $\Sigma_{\mathbf{a}}$ never intersecting the interior of the unstable ellipse. Thus, all the eigenvalues associated with such a class are imaginary and thus cannot contribute linear instability. □

Compare this with Theorem 2.5.5. Together, these prove that classes that do not intersect the *interior* of the unstable ellipse cannot contribute instability.

Return now to the Jacobi problem for the half-class with initial condition (2.9.6). Applying our recursion formula (2.9.2), we split the system into four Jacobi problems, which will now no longer be bi-infinite but have a boundary condition.

The four Jacobi operators associated with the problem have the form

$$\begin{aligned} \lambda' \tilde{v}_0 &= b_1 \tilde{v}_1 + a_0 \tilde{v}_0, \\ \lambda' \tilde{v}_n &= b_{n+1} \tilde{v}_{n+1} + a_n \tilde{v}_n + c_n \tilde{v}_{n-1} \quad \text{for } n \geq 1. \end{aligned} \tag{2.9.11}$$

There are two "odd" problems with $\delta = 1$ and $\delta = -1$ for the positive and negative directions respectively. In these problems, $\tilde{v}_n = v_{(2n+1)\delta}$, $\lambda' = \lambda^2$ and

$$\begin{aligned} a_n &= -\rho_{(2n+1)\delta}(\rho_{(2n+2)\delta} + \rho_{(2n)\delta}), \\ b_n &= \rho_{(2n)\delta}\rho_{(2n+1)\delta}, \\ c_n &= \rho_{(2n-1)\delta}\rho_{(2n)\delta}. \end{aligned} \tag{2.9.12}$$

For the "even" problems, $\delta = 1$ or $\delta = -1$, $\tilde{v}_n = v_{(2n+2)\delta}$, $\lambda' = \lambda^2$ and the coefficients are

$$\begin{aligned} a_n &= -\rho_{(2n+2)\delta}(\rho_{(2n+3)\delta} + \rho_{(2n+1)\delta}), \\ b_n &= \rho_{(2n+1)\delta}\rho_{(2n+2)\delta}, \\ c_n &= \rho_{(2n)\delta}\rho_{(2n+1)\delta}. \end{aligned} \tag{2.9.13}$$

In summary, there are four problems found by the following procedure: first squaring our original matrix (2.4.23) and splitting into an "even" and "odd" part, and then splitting each of these into two halves around the coefficient $\rho_0 = 0$.

The tridiagonal matrix associated with these problems is then

$$\mathcal{J}_1 = \begin{pmatrix} a_0 & b_1 & 0 & 0 & 0 & ... \\ c_1 & a_1 & b_2 & 0 & 0 & ... \\ 0 & c_2 & a_2 & b_3 & 0 & ... \\ 0 & 0 & c_3 & a_3 & b_4 & .... \\ 0 & 0 & 0 & c_4 & a_4 & ... \\ \vdots & \vdots & \vdots & \vdots & \vdots & \ddots \end{pmatrix}. \tag{2.9.14}$$

Note this is now infinite in one direction only, unlike most of the matrices we have seen so far.

We can transform any matrix of this form into a symmetric matrix by the transformation matrix

$$T_1 = \begin{pmatrix} 1 & 0 & 0 & 0 & 0 & ... \\ 0 & \sqrt{\frac{c_1}{b_1}} & 0 & 0 & 0 & ... \\ 0 & 0 & \sqrt{\frac{c_1 c_2}{b_1 b_2}} & 0 & 0 & ... \\ 0 & 0 & 0 & \sqrt{\frac{c_1 c_2 c_3}{b_1 b_2 b_3}} & 0 & ... \\ 0 & 0 & 0 & 0 & \sqrt{\frac{c_1 c_2 c_3 c_4}{b_1 b_2 b_3 b_4}} & ... \\ \vdots & \vdots & \vdots & \vdots & \vdots & \ddots \end{pmatrix} \tag{2.9.15}$$

to

$$\mathcal{J}_2 = \begin{pmatrix} a_0 & \sqrt{b_1 c_1} & 0 & 0 & 0 & ... \\ \sqrt{b_1 c_1} & a_1 & \sqrt{b_2 c_2} & 0 & 0 & ... \\ 0 & \sqrt{b_2 c_2} & a_2 & \sqrt{b_3 c_3} & 0 & ... \\ 0 & 0 & \sqrt{b_3 c_3} & a_3 & \sqrt{b_4 c_4} & .... \\ 0 & 0 & 0 & \sqrt{b_4 c_4} & a_4 & ... \\ \vdots & \vdots & \vdots & \vdots & \vdots & \ddots \end{pmatrix}. \tag{2.9.16}$$

Note this is in general not Hermitian, unless b_i and c_i are all positive. Also note that in our case the matrix T is bounded and invertible as the relevant ρ_k values are nonzero and have a finite limit. Note that this is one of two potentially Hermitian matrices related to (2.4.23). The matrix $i\tilde{M}$ where $\tilde{M}$ is (2.5.7) is also Hermitian if $\rho_k \geq 0$ for all k. Then if $\pm\lambda$ are in the spectrum of $i\tilde{M}$, then λ^2 is in the spectrum of $\mathcal{J}_2$.

The off-diagonal terms are now

$$\sqrt{b_i c_i} = \rho_{(2n)\delta}\sqrt{\rho_{(2n-1)\delta}\rho_{(2n+1)\delta}} \tag{2.9.17}$$

and

$$\sqrt{b_i c_i} = \rho_{(2n+1)\delta}\sqrt{\rho_{(2n)\delta}\rho_{(2n+2)\delta}}, \tag{2.9.18}$$

depending which of the four problems we are in. Thus if $\rho_k \geq 0$ for all $k \neq 0$, all four matrices $\mathcal{J}_2$ are Hermitian and thus have all real eigenvalues.

If $\rho_1 < 0$ and $\rho_k > 0$ for $k > 1$, then the positive odd problem with coefficients

$$\begin{aligned} a_n &= -\rho_{2n+1}(\rho_{2n+2} + \rho_{2n}), \\ b_n &= \rho_{2n}\rho_{2n+1}, \\ c_n &= \rho_{2n-1}\rho_{2n} \end{aligned} \tag{2.9.19}$$

satisfies $\sqrt{b_n c_n} \in \mathbb{R}$ for all $n > 1$, and $\sqrt{b_1 c_1} = \rho_2\sqrt{\rho_1\rho_3} \in i\mathbb{R}$. Thus is some sense the non-Hermitian part is "localised" to a small number of coefficients. This corresponds to the observation there are only ever one or two nonreal eigenvalues, and thus only two or four nonimaginary eigenvalues of the original problem.

2.9.3. Gershgorin Circle Theorem. The Jacobi matrix associated with (2.9.11) is (2.9.14) for the appropriate set of coefficients a_i, b_i, c_i. According to the definition in [**Akh65**], this is a Jacobi matrix if $b_i = c_i > 0$ and $a_i \in \mathbb{R}$ for all i. There are equivalent definitions in other texts, which can usually be transformed to this form. For an eigenvalue λ of $\mathcal{J}$, (2.9.11) has a bounded solution in $\tilde{v}_k$.

We can apply the Gershgorin circle theorem to this matrix to obtain some simple results. The Gershgorin circle theorem is as follows: given a matrix M with entries $M_{i,j} \in \mathbb{C}$, define $C_i = M_{i,i}$ and $R_i = \sum_{j\neq i} |M_{i,j}|$. Then all eigenvalues of M lie in at least one of the discs $|\lambda - C_i| \leq R_i$. Furthermore, if there is a set of k discs disjoint from the other discs, k of the eigenvalues of M lie in that set.

Applying this to (2.9.14), all the eigenvalues of J lie in the set of circles with centres $C_i = a_i$ and radii $R_i = |b_{i+1}| + |c_i|$ (setting $c_0 = 0$). We can also apply this to the transpose (as the eigenvalues are invariant under transposition), so the eigenvalues lie in the set of circles with centres a_i and radii $|b_i| + |c_{i+1}|$.

Substituting the coefficients (2.9.13), the eigenvalues must lie in the discs with centres $C_i = -\rho_{\delta(2i+1)}(\rho_{\delta(2i+2)} + \rho_{\delta(2i)})$ and radii $R_i = |\rho_{\delta(2i+1)}\rho_{\delta(2i+2)}| + |\rho_{\delta(2i+1)}\rho_{\delta(2i)})|$ for $i \geq 1$ and $C_0 = -\rho_1\rho_2$, $R_0 = |\rho_1\rho_2|$. In particular, as $\rho_n > 0$ for all $n > 1$, $C_i < 0$ and $C_i = -R_i$ for all $i > 1$. If $\rho_1 < 0$, $C_0 = R_0$, otherwise $C_0 = -R_0$.

As R_i is strictly increasing (as ρ_n is strictly increasing for positive n), this means the C_i, R_i generate a series of nested discs, all nested within the limiting disc $C_\infty = -2$, $R_\infty = 2$ (as $\lim_{n\to\infty} \rho_n = 1$ in the transformed system). Thus all eigenvalues lie in the set

$$\{|\lambda + 2|^2 \leq 2^2\} \cup \{ |\lambda + \rho_1\rho_2|^2 \leq (\rho_1\rho_2)^2\}. \tag{2.9.20}$$

In particular, $\mathrm{Re}(\lambda) \in [-2, -2\rho_1\rho_2]$ if $\rho_1 < 0$. Thus for an eigenvalue $\lambda' = \pm\sqrt{\lambda}$ of the corresponding matrix (2.9.8),

$$\mathrm{Re}(\lambda') \in [-2\sqrt{-\rho_1\rho_2}, 2\sqrt{-\rho_1\rho_2}]. \tag{2.9.21}$$

This is true for $\rho_0 = 0$. We will return to this in Section 6.1.5 and discuss a general bound on eigenvalues with positive real part.

2.9.4. Associated Properties of the Jacobi Operators. The Jacobi matrix $\mathcal{J}_2$ (2.9.16) has a number of associated objects of note. For $\mathcal{J}_2$ to be a Jacobi matrix per the definition in [**Akh65**], in our case we require $\rho_k > 0$ for all ρ_k in the coefficients given by (2.9.17), (2.9.18).

Associated with a Jacobi matrix is a set of orthogonal polynomials given by the recursion

$$\begin{aligned} (a_0 - x)P_0(x) + \sqrt{b_1c_1}P_1(x) &= 0, \\ \sqrt{b_kc_k}P_{k-1}(x) + a_kP_k(x) + \sqrt{b_{k+1}c_{k+1}}P_{k+1}(x) &= xP_k(x). \end{aligned} \tag{2.9.22}$$

With the initial condition $P_0(x) = 1$, this recursion generates the characteristic polynomials employed throughout Section 2.7 up to a scaling of x. This set of polynomials is called the *polynomials of the first kind*. Then $P_k(x)$ is of degree k and the polynomials $P_k(x)$ are orthonormal with respect to the *spectral density*. The spectral density is equivalent to the linear functional $\mathcal{S}$ which can be constructed via the orthogonality condition $\mathcal{S}(P_m, P_n) = \delta_{m,n}$ for all $m, n \in \mathbb{Z}$; see Chapter 1, Section 1.4 of [**Akh65**].

If we take (2.9.22) with the initial condition $Q_0(x) = 0$, this generates the *polynomials of the second kind*. Then the polynomials $P_k(x)$ and $Q_k(x)$ satisfy a number of properties:

- the roots of $P_k(x)$ are real and simple (that is, $P_k(x)$ has no double roots for any $k \in \mathbb{N}$);
- the roots of $Q_k(x)$ are real and simple;
- the roots of $P_k(x)$ and $P_{k-1}(x)$ interlace; between any two roots of $P_k(x)$ there is a root of $P_{k-1}(x)$ and vice versa;
- the roots of $P_k(x)$ and $Q_k(x)$ interlace; between any two roots of $P_k(x)$ there is a root of $Q_k(x)$ and vice versa.

Proofs for these statements can be found in Chapter 1, Section 2 of [**Akh65**].

We can also use this characterisation to calculate the spectral density of (2.9.16) as the limit of a series of functions. Denote the ordered roots of $P_n(x)$ as $\lambda_{n,k}$ for $k = 1, 2, 3, ..., n$ such that $\lambda_{n,k-1} < \lambda_{n,k}$. Then for fixed $n \in \mathbb{N}$ define the quadrature weights

$$\mu_k := \frac{1}{\sum_{i=0}^{n-1} P_i(\lambda_n, k)^2} \tag{2.9.23}$$

for $k = 1, 2, 3, ..., n$. These weights are useful in a number of way. They provide a quadrature formula for the linear functional $\mathcal{S}$; for any polynomial $R(\lambda)$ of degree $\leq 2n - 2$,

$$\mathcal{S}\{R\} = \sum_{k=1}^{n} \mu_k R(\lambda_k). \tag{2.9.24}$$

Additionally, they allow us to define the piecewise constant functions that approximate the spectral density. Define $\sigma_n(x)$ as a piecewise constant function with discontinuities at λ_i, so that

$$\lim_{\epsilon \to 0}(\sigma_n(\lambda_i + \epsilon) - \sigma_n(\lambda_i - \epsilon)) = \mu_i. \tag{2.9.25}$$

This function is defined up to an arbitrary constant. Then the limit

$$\sigma(x) := \lim_{n \to \infty} \sigma_n(x) \tag{2.9.26}$$

is the spectral density associated with the Jacobi Matrix (2.9.16). This is the weight with respect to which the polynomials $P_n(x)$ are orthonormal. It is also the solution to the associated *moment problem*, which is of much interest in the mathematical and physical sciences; see [**Akh65**] for more information.

This setting also provides a link between the approach of [**Li00**] to the linearised Euler equations and the study of the Jacobi operators. In Chapter 1, Section 4 of [**Akh65**] and Chapter 1 of [**Tes00**] a link is formed between the Jacobi Matrix (2.9.16) and the continued fraction

$$\cfrac{1}{z - a_0 - \cfrac{b_1 c_1}{z - a_1 - \cfrac{b_2 c_2}{z - a_2 - ...}}}. \tag{2.9.27}$$

For the coefficients (2.9.17), this is equivalent to the continued fractions studied in Section 5 of [**Li00**].

These links between the Euler equations, Jacobi operators, moment problems, and continued fractions run deep, and provide interesting and natural avenues for further research.

Chapter 3

Structure Preserving Truncation of the Two-Dimensional Euler Equations

In Chapter 2, we introduced a Poisson formulation for the Euler equations and discussed its advantages. We also studied a finite-mode truncation which led to the main instability result of Theorem 2.7.53. However, this truncation is only a Poisson structure for the *linearised* truncated equations. If we take a Galerkin-style finite mode truncation per Section 2.7.2 of the nonlinear system given by (2.3.2) and (2.3.7), the result will no longer be a Poisson system.

There is an alternative truncation for the nonlinear problem that does preserve the Poisson structure of the system. Thanks to a clever characterisation of the space of symplectomorphisms on $\mathbb{T}^2$ [**FFZ89**], Zeitlin [**Zei91**] defines a series of Poisson brackets that approximate the ideal fluid bracket (2.3.2). This is the *sine Poisson bracket*. This truncation is useful for a number of reasons. Studying a finite-dimensional problem has analytical advantages and makes a numerical study more tractable. Additionally, a structure-preserving truncation allows us to take full advantage of a Poisson system. The system has a family of Casimirs corresponding to the generalised enstrophy Casimirs (2.3.10). The finite-dimensional Poisson structure allows us to develop a robust Poisson integrator, which we here generalise from the integrator for the isotropic domain [**McL93**] to the anisotropic domain. There have also been results showing that systems with similar truncations are integrable for sufficiently low truncation values, for instance in Dullin [**Dul13**].

In this chapter, we introduce the sine-bracket truncated system, and linearise around shear flows. The technical details associated with the truncation are discussed, particularly with regards to the decomposition into subsystems. We then show that the same stability results as for the untruncated system hold in the truncated system. Under certain conditions, we can actually improve the stability results of Chapter 2.

3.1. The Sine-Bracket Truncation

Define the finite domain of Fourier Mode indices for a fixed $N \in \mathbb{N}$

$$\mathcal{D}_N := \{\mathbf{j} = (j_x, j_y) \in \mathbb{Z}^2 \mid |j_x|, |j_y| \leq N\}. \tag{3.1.1}$$

Then $\mathcal{D}_N \subset \mathbb{Z}^2$ is a "box" of Fourier modes with sufficiently small mode numbers. The size of this domain is $|\mathcal{D}_N| = (2N+1)^2$.

We wish to define a truncated approximation of (2.3.2) that is defined only on the modes

$$\omega_{\mathbf{k}}, \quad \mathbf{j} \in \mathcal{D}_N. \tag{3.1.2}$$

Such a truncation exists called the *sine-bracket truncation*. This truncation is based on an algebra developed by Fairlie, Fletcher and Zachos [**FZ89, FFZ89**] and developed for the two-dimensional Euler Equations by Zeitlin [**Zei91, Zei05**]. Further discussion of the theoretical background can be found in [**Hop89, PR90, BHSS91, AK98**].

The sine-bracket, as defined in those texts, is for the isotropic periodic domain with size $[0, 2\pi) \times [0, 2\pi)$. In our notation, this is the special case $K = \mathbb{I}$. We first present that definition, then the extension to the general case $\kappa_x, \kappa_y \in \mathbb{R}^+$. The bracket also has a set of Casimirs, which we will present and discuss.

3.1.1. The Sine-Bracket Truncation. Introduce the notation $\widehat{\mathbf{j}}$ such that $\widehat{\mathbf{j}} \in \mathcal{D}_N$ and $\mathbf{j} - \widehat{\mathbf{j}} = (2N+1)(a,b)^\mathsf{T}$ for some integers $a, b \in \mathbb{Z}$. This is equivalent to taking $\mathbf{j}$ modulo the lattice grid $\mathcal{D}$. For any $\mathbf{j} \in \mathbb{Z}^2$ there is a unique $\widehat{\mathbf{j}} \in \mathcal{D}_N$. This is not to be confused with the notation used for the cross product matrix in Chapters 4 and 5; this wrapping operation will be used in this chapter only.

Define the sine-bracket [**FZ89, Zei91**] on the domain of modes with mode number in $\mathcal{D}_N$:

$$\{f, g\} = \sum_{\mathbf{j},\mathbf{k} \in \mathcal{D}_N} \frac{\sin(\varepsilon \mathbf{j} \times \mathbf{k})}{\varepsilon} \frac{\partial f}{\partial \omega_{\mathbf{j}}} \frac{\partial g}{\partial \omega_{\mathbf{k}}} \omega_{\widehat{\mathbf{j}+\mathbf{k}}} \tag{3.1.3}$$

where $\mathbf{j}, \mathbf{k} \in \mathcal{D}_N$ and

$$\varepsilon = \frac{2\pi}{2N+1}. \tag{3.1.4}$$

Note that

$$\lim_{N\to\infty} \frac{\sin(\varepsilon \mathbf{j} \times \mathbf{k})}{\varepsilon} = \lim_{\varepsilon \to 0} \frac{\sin(\varepsilon \mathbf{j} \times \mathbf{k})}{\varepsilon} = \mathbf{j} \times \mathbf{k}. \tag{3.1.5}$$

This Poisson bracket has structure matrix J with entries

$$J_{\mathbf{j},\mathbf{k}} = \frac{1}{\varepsilon} \sin(\varepsilon \mathbf{j} \times \mathbf{k}) \omega_{\widehat{\mathbf{j}+\mathbf{k}}} \tag{3.1.6}$$

The bracket has limit (2.3.2) in the following sense. As there is a Poisson structure, ideal fluid flow is a symplectomorphism of the phase space $\mathbb{T}^2$ to itself [**AK98**]. It is known [**Hop89**] that the Poisson algebra of diffeomorphisms on the torus can be written as a limit of Lie algebras equivalent to $\mathrm{SU}(N)$, as $N \to \infty$. Thus this system is an approximation of the Euler equations. This concept is used to develop the bracket (3.1.3) in [**Zei91**]. Notably, there is a corresponding construction for symplectomorphisms on the sphere S^2 [**Hop89, Zei04**].

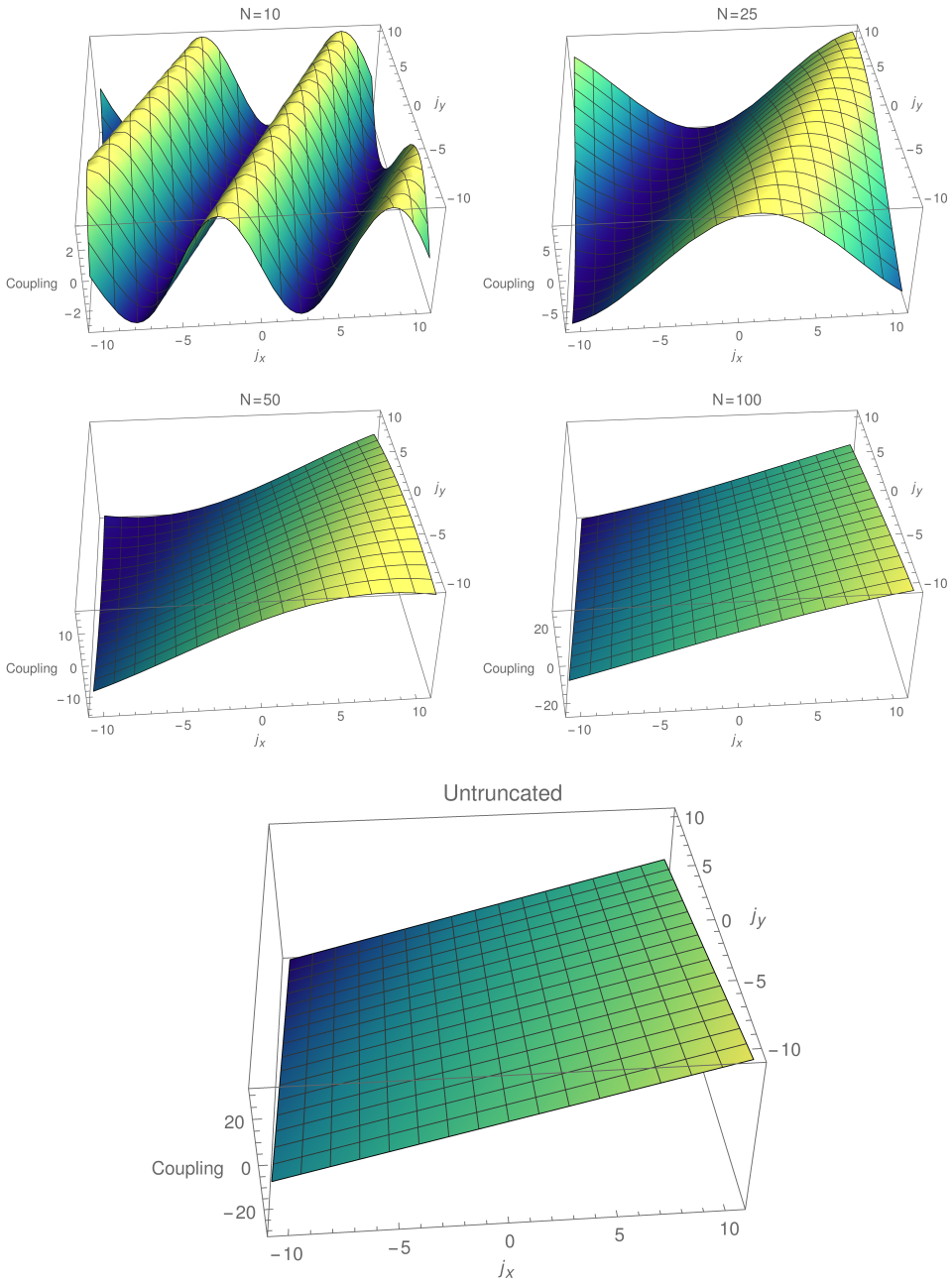

Figure 3.1 – The coupling coefficient $J_{\mathbf{j},\mathbf{k}}/\omega_{\widehat{\mathbf{j}+\mathbf{k}}} = \sin(\varepsilon \mathbf{j}\times\mathbf{k})/\varepsilon$ for a fixed $\mathbf{k}$ and N as a function of $\mathbf{j} = (j_x, j_y)$. Here $\mathbf{k} = (1, 2)$. The coupling coefficient is shown for $|j_x|, |j_y| \leq 10$. Top row: $N = 10$, $N = 25$. Middle row: $N = 50$, $N = 100$. Bottom row: the limiting coefficient for the untruncated case, $\mathbf{j}\times\mathbf{k}$. As N increases, the coupling approaches the untruncated case; this limit is reached more quickly for modes with a smaller perpendicular distance to the line through $\mathbf{k}$.

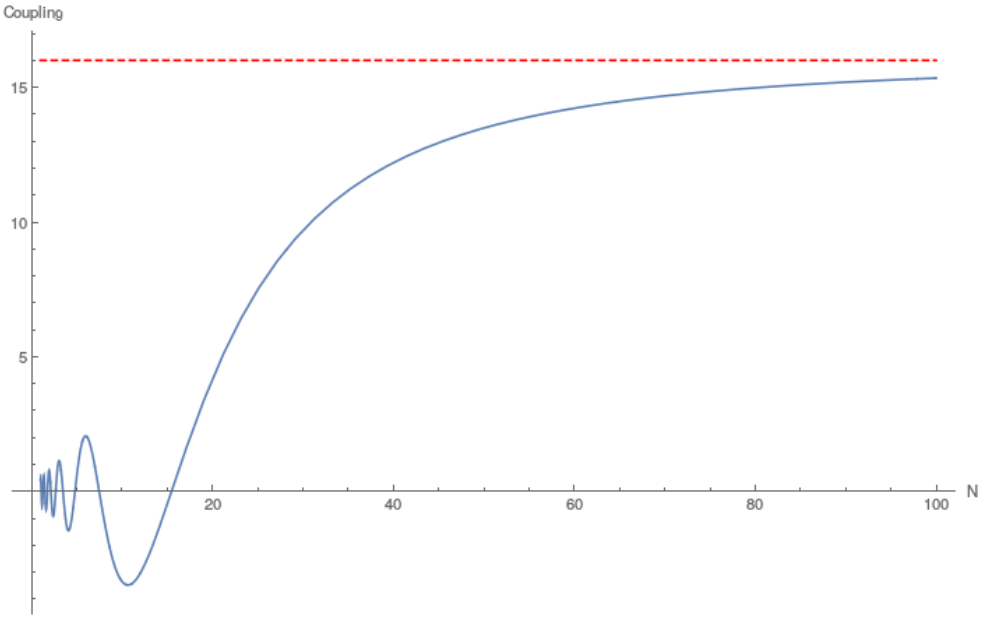

Figure 3.2 – The coupling coefficient of the sine-truncated bracket as a function of N. Solid blue curve: the coupling coefficient $\sin(\varepsilon \mathbf{j} \times \mathbf{k})/\varepsilon$ for $\mathbf{j} = (8, 0)$, $\mathbf{k} = (1, 2)$ as a function of the truncation value N. Dashed red line: constant value $\mathbf{j} \times \mathbf{k}$. As $N \to \infty$, the coupling coefficient approaches the limit. As $\mathbf{j} \times \mathbf{k} = 16$ is relatively large, it takes a larger value of N to approach the limiting value. Compare with Figure 3.1.

Figure 3.1 shows how the "coupling coefficient" between modes $\omega_{\mathbf{j}}$ and $\omega_{\mathbf{k}}$, $\mathbf{k}, \mathbf{j} \in \mathcal{D}_N$ in (3.1.3) evolves as the truncation size $N \in \mathbb{N}$ increases. As N increases the coefficient of $J_{\mathbf{j},\mathbf{k}}$ goes to the limiting value given by the structure matrix for the full system (2.3.3); the closer the vectors $\mathbf{j}$ and $\mathbf{k}$ are, the quicker this occurs. Figure 3.2 shows how the coupling coefficient between two particular modes evolves as N increases, approaching the limit given by (2.3.3).

The corresponding truncation of (2.3.7) is the Hamiltonian

$$\mathcal{H} = \frac{1}{2} \sum_{\mathbf{j} \in \mathcal{D}_N \setminus \{\mathbf{0}\}} \frac{\omega_{+\mathbf{j}} \omega_{-\mathbf{j}}}{|\mathbf{j}|^2}, \tag{3.1.7}$$

where only the domain of summation has changed. The vector field under the sine-bracket truncation is thus given by

$$\dot{\omega}_{\mathbf{j}} = (J \nabla \mathcal{H})_{\mathbf{j}} = \sum_{\mathbf{k} \in \mathcal{D}_N} J_{\mathbf{j},\mathbf{k}} \nabla H_{\mathbf{k}} \tag{3.1.8}$$

$$= \frac{1}{\varepsilon} \sum_{\mathbf{k} \in \mathcal{D}_N} \sin(\varepsilon \mathbf{j} \times \mathbf{k}) \omega_{\widehat{\mathbf{j}+\mathbf{k}}} \frac{\omega_{-\mathbf{k}}}{|\mathbf{k}|^2}. \tag{3.1.9}$$

3.1.2. Extension to General κ_x, κ_y. The above definitions are for the special case with domain $K = \mathbb{I}$. We now present a simple extension to the general anisotropic case.

Definition 3.1.10 (Generalised Sine-Bracket)**.** *For $\boldsymbol{\kappa} = (\kappa_x, \kappa_y)^\mathsf{T}$ with $\kappa_x, \kappa_y \in \mathbb{R}^+$, the generalised sine-bracket is*

$$\{f, g\} = \sum_{\mathbf{j},\mathbf{k}} \kappa_x \kappa_y \frac{\sin \varepsilon \mathbf{j} \times \mathbf{k}}{\varepsilon} \frac{\partial f}{\partial \omega_{\mathbf{j}}} \frac{\partial g}{\partial \omega_{\mathbf{k}}} \omega_{\widehat{\mathbf{j}+\mathbf{k}}}, \tag{3.1.11}$$

Define the equivalent Hamiltonian to (3.1.7) with the adjusted $\boldsymbol{\kappa}$ norm

$$H = \frac{1}{2} \sum_{\mathbf{j} \in \mathcal{D}_N \setminus \{\mathbf{0}\}} \frac{\omega_{+\mathbf{j}} \omega_{-\mathbf{j}}}{|\mathbf{j}|^2_{\boldsymbol{\kappa}}}, \tag{3.1.12}$$

Now the Poisson system (3.1.11), (3.1.12) approximates the ideal fluid system (2.3.2), (2.3.7). The vector field for the sine-bracket truncated Fourier modes is

$$\dot{\omega}_{\mathbf{j}} = \kappa_x \kappa_y \sum_{\mathbf{k} \in \mathcal{D}_N} \frac{1}{\varepsilon} \sin(\varepsilon \mathbf{j} \times \mathbf{k}) \omega_{\widehat{\mathbf{j}+\mathbf{k}}} \frac{\omega_{-\mathbf{k}}}{|\mathbf{k}|^2_{\boldsymbol{\kappa}}}. \tag{3.1.13}$$

As the bracket (3.1.11) differs from the isotropic sine-bracket (3.1.3) by a constant factor only, we are able to generalise some existing results for this new setting.

3.1.3. Casimirs of the Sine-Truncated Bracket. As discussed in Section 2.3.2 the full bracket (2.3.2) has infinitely many Casimirs, or conserved quantities. These are the generalised enstrophy constants $\mathcal{C}_M$ (2.3.10) for all $M \in \mathbb{N}$. These Casimirs are lost in a nonlinear Galerkin-style truncation, with the exception of the enstrophy $\mathcal{C}_2$. Due to the Poisson structure, our sine-bracket has a set of N Casimirs for truncation size N. As the truncation size is increased, the number and value of the Casimirs approaches those of the full system.

The bracket (3.1.11) has a family of Casimirs functions

$$\mathcal{C}_M = \sum_{\mathcal{I}_M} \omega_{\mathbf{i}_1} \omega_{\mathbf{i}_2} ... \omega_{\mathbf{i}_M} \cos\left(\varepsilon A(\mathbf{i}_1, \mathbf{i}_2, ... \mathbf{i}_M)\right) \tag{3.1.14}$$

for $M = 1, 2, ..., N$ where

$$\mathcal{I}_M = \left\{ (\mathbf{i}_1, \mathbf{i}_2, ..., \mathbf{i}_M) \mid \mathbf{i}_k \in \mathcal{D}_N, \ \widehat{\sum_{k=1}^{M}} \mathbf{i}_k = \mathbf{0} \right\} \tag{3.1.15}$$

and A is the area form

$$A(\mathbf{i}_1, \mathbf{i}_2, ..., \mathbf{i}_M) = \sum_{j<k} \mathbf{i}_k \times \mathbf{i}_j. \tag{3.1.16}$$

These Casimirs can be calculated from the algebraic structure of the Poisson bracket [**Zei05**]. In the limit $N \to \infty$, $\varepsilon \to 0$ these tend to the Casimirs for the full bracket (2.3.10).

In the case $M = 2$, this is equal to the usual enstrophy, calculated over the finite domain of modes

$$\mathcal{C}_2 = \sum_{\mathbf{j} \in \mathcal{D}_N} \omega_{-\mathbf{j}} \omega_{\mathbf{j}}. \tag{3.1.17}$$

3.2. Stability Theory for the Sine-Truncated System

We now show that many of the same stability results for shear flows developed in Chapter 2 for the full systems also exist in the sine-bracket truncated system. This has the advantage of allowing us to study a finite-dimensional Hamiltonian system. However, there are new technicalities to consider.

We begin by linearising, which leads to a class decomposition per the untruncated system. The nature of the sine-bracket truncation means that these classes are more complicated; they wrap around our finite domain of modes. This means the proofs in this case must be adjusted, as there is now a matching condition at this wrapping point.

We explicitly calculate a basis for a global canonical Poisson structure for this linearised system. This is due to the circulant structure of this system, which can be diagonalised by a discrete Fourier transform. This structure will be exploited again in Section 3.3 to develop an explicit Poisson integrator.

Having linearised, we prove that the two key results from Chapter 2 hold. Firstly, there is an unstable ellipse which classes must pass through to contribute linear instability. Secondly, there is instability for almost all choices of $\mathbf{p}$, $\boldsymbol{\kappa}$. However, the more complicated structure of classes in this truncation means there are additional considerations; specifically, the possibility that classes may intersect the unstable ellipse at multiple nonadjacent points. For a generic $\mathbf{p}$ we show that one can ignore this possibility and these results hold.

We also prove a new stability result akin to that of Section 2.6. For parallel shear flows with $\mathbf{p} = (p_x, 0)$ and appropriate values of κ_x, κ_y, the system is linearly stable. There is an interesting difference to the untruncated system; for certain truncation values N this stability can be extended to energy-Casimir stability, a much stronger result. There is an unbounded sequence of values of N for which the system exhibits energy-Casimir stability. This sensitivity to the choice of truncation size N is an interesting technical detail to the sine-bracket truncation, which was noted by McLachlan [**McL93**].

3.2.1. Linearisation and Class Decomposition. We linearise (3.1.13) around the shear flow equilibrium (2.4.6). As long as $\mathbf{p} \in \mathcal{D}_N$, this equilibrium persists. The Jacobian of the vector field (3.1.13) around the equilibrium

is

$$J_{\mathbf{a},\mathbf{b}} = \begin{cases} 0 \quad \text{if } \mathbf{a} = \mathbf{b} \text{ or } \mathbf{b} = \mathbf{0} \\ \kappa_x \kappa_y \frac{1}{\varepsilon} \left(\frac{1}{|\mathbf{b}|_{\boldsymbol{\kappa}}^2} \sin(\varepsilon \mathbf{b} \times \mathbf{a}) + \frac{1}{|\widehat{(\mathbf{b}-\mathbf{a})}|_{\boldsymbol{\kappa}}^2} \sin(\varepsilon \mathbf{a} \times \widehat{(\mathbf{b}-\mathbf{a})}) \right) \omega_{\widehat{(\mathbf{a}-\mathbf{b})}}. \end{cases} \tag{3.2.1}$$

Note that

$$\begin{aligned} \sin(\varepsilon \mathbf{a} \times \widehat{(\mathbf{b}-\mathbf{a})}) &= \sin\left(\varepsilon \mathbf{a} \times (\mathbf{b} - \mathbf{a} + (2N+1)\mathbf{k})\right) \\ &= \sin(\varepsilon \mathbf{a} \times \mathbf{b} - \varepsilon \mathbf{a} \times \mathbf{a} + 2\pi \mathbf{a} \times \mathbf{k}) \\ &= \sin(\varepsilon \mathbf{a} \times \mathbf{b}) \end{aligned} \tag{3.2.2}$$

for some $\mathbf{k} \in \mathbb{Z}^2$.

Thus the linearised differential equations are

$$\dot{\omega}_{\mathbf{j}} = \alpha \left(\rho_{\widehat{\mathbf{j}+\mathbf{p}}} \omega_{\widehat{\mathbf{j}+\mathbf{p}}} - \rho_{\widehat{\mathbf{j}-\mathbf{p}}} \omega_{\widehat{\mathbf{j}-\mathbf{p}}} \right) \tag{3.2.3}$$

where

$$\alpha = \kappa_x \kappa_y \frac{\Gamma}{\varepsilon} \sin(\varepsilon \mathbf{p} \times \mathbf{j}), \quad \rho_{\mathbf{j}} = \frac{1}{|\mathbf{p}|_{\boldsymbol{\kappa}}^2} - \frac{1}{|\mathbf{j}|_{\boldsymbol{\kappa}}^2}. \tag{3.2.4}$$

Compare this with the equivalent equations in Section 2.4.2 for the Galerkin truncation. For example,

$$\lim_{N \to \infty} \alpha = \lim_{\varepsilon \to 0} \alpha = \kappa_x \kappa_y \Gamma \mathbf{p} \times \mathbf{j}. \tag{3.2.5}$$

In addition, there is again a splitting into subsystems or "classes". However, such a splitting is more complicated in this truncation, due to the wrapping operation $\widehat{\mathbf{j}}$. For a fixed $\mathbf{a} \in \mathcal{D}_N$, define

$$\omega_n := \omega_{\widehat{\mathbf{a}+n\mathbf{p}}}, \quad \rho_n := \rho_{\mathbf{a}+n\mathbf{p}}. \tag{3.2.6}$$

By (3.2.3), the linearised dynamics of ω_n only depends on the values of ω_{n+1} and ω_{n-1}. Thus the set of modes ω_n form a subsystem.

The set of mode numbers in this class is a set of unique mode numbers

$$\Sigma_{\mathbf{a}} = \{\widehat{\mathbf{a} + n\mathbf{p}} \mid n \in \mathbb{Z}\} \tag{3.2.7}$$

As there is a finite lattice of modes, $|\Sigma_{\mathbf{a}}|$ will always be finite. By translation invariance, the number of modes in a class $|\Sigma_{\mathbf{a}}|$ is also independent of the starting mode $\mathbf{a}$. Now the modes ω_n are only defined modulo the size of the class; i.e. $\omega_{n+k|\Sigma_{\mathbf{a}}|} = \omega_n$ for all $k \in \mathbb{Z}$.

Here a key distinction emerges: as classes only have finitely many modes, for a fixed class led by $\mathbf{a} \in \mathbb{Z}^2$ there exists some $n \in \mathbb{N}$ such that $\omega_0 = \omega_n$. This value n will not depend on $\mathbf{a}$, only on $\mathbf{p}$ and N. The class "wraps around" upon itself on the lattice $\mathcal{D}_N$.

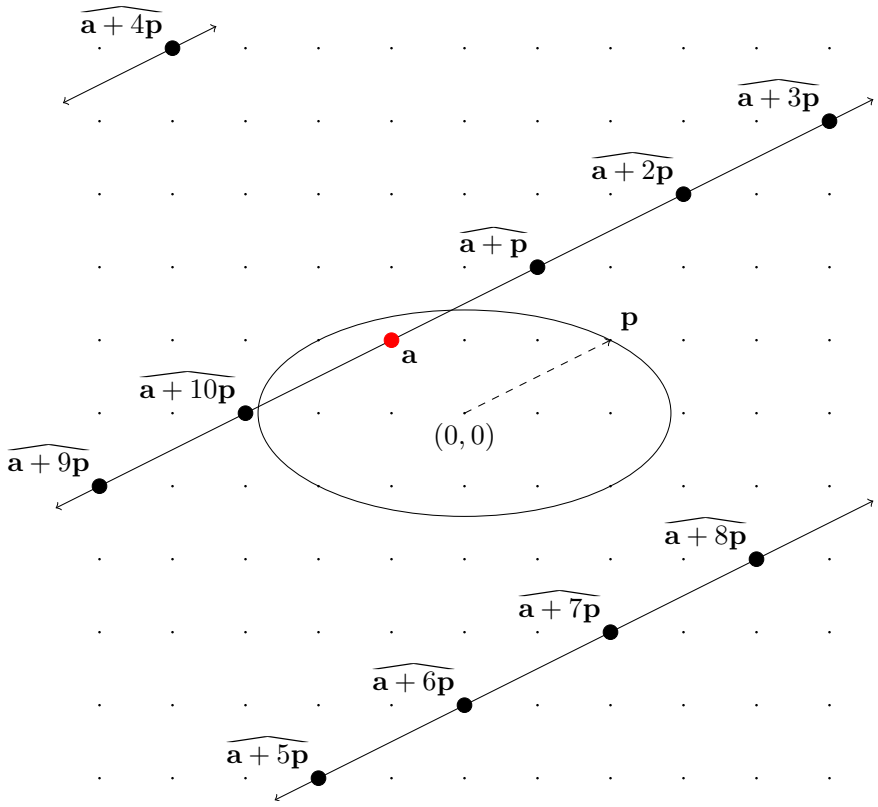

Figure 3.3 – Class decomposition for the linearised sine-bracket system. The dynamics of $\omega_{\mathbf{a}}$ depend only on $\omega_{\widehat{\mathbf{a}\pm\mathbf{p}}}$; extrapolating this, the modes $\omega_{\widehat{\mathbf{a}+n\mathbf{p}}}$ form a subsystem. These modes lie on lines parallel to $\mathbf{p}$ that "wrap" around the finite lattice $\mathcal{D}_N$. Note that $\widehat{\mathbf{a}+11\mathbf{p}} = \mathbf{a}$, as $|\Sigma_{\mathbf{a}}| = 11$. The unstable ellipse is also shown; it is the same as for the untruncated problem. For this figure, $\mathbf{p} = (2,1)$, $N = 5$, and the class led by $\mathbf{a} = (-1,1)$ is shown. Compare with Figure 2.4; unlike in that figure, here the class wraps around the domain.

We wish to find $n \in \mathbb{N}^+$ such that $\widehat{\mathbf{a}+n\mathbf{p}} = \mathbf{a}$, and $\widehat{\mathbf{a}+k\mathbf{p}} \neq \mathbf{a}$ for all $0 < k < n$. By translation invariance, $\widehat{n\mathbf{p}} = \mathbf{0}$. Thus, for some k_x, k_y,

$$np_x = (2N+1)k_x, \quad np_y = (2N+1)k_y. \tag{3.2.8}$$

For this to hold,

$$n = \frac{2N+1}{\gcd(2N+1, p_x)} j_x = \frac{2N+1}{\gcd(2N+1, p_y)} j_y \tag{3.2.9}$$

for some $j_x, j_y \in \mathbb{Z}$, as n must be an integer. Thus the smallest positive value of n is

$$\begin{aligned} n &= \operatorname{lcm}\left(\frac{2N+1}{\gcd(2N+1,p_x)}, \frac{2N+1}{\gcd(2N+1,p_y)}\right) \\ &= \frac{2N+1}{\gcd(2N+1,p_x,p_y)}. \end{aligned} \tag{3.2.10}$$

Thus

$$|\Sigma_{\mathbf{a}}| = \frac{2N+1}{\gcd(2N+1,p_x,p_y)}. \tag{3.2.11}$$

As N is an integer, $|\Sigma_{\mathbf{a}}|$ is always odd.

This suggests that the nature of these classes is highly dependent on the prime factorisation of $2N+1$ and $\mathbf{p}$; this will become evident in later sections. In the simplest case where $\gcd(2N+1,p_x,p_y)=1$, $\mathcal{D}_N$ splits into $2N+1$ classes of size $2N+1$. This is always true for choices of $\mathbf{p}$ with p_x, p_y coprime. By choosing N appropriately, we can treat this as a generic case.

Note that for our purposes, $\gcd(x,0)=x$ for all x. We also use the notation $\gcd(a,b,c)=\gcd(a,\gcd(b,c))$. In the special case $\mathbf{p}=(p_x,0)$ (or equivalently $\mathbf{p}=(0,p_y)$), $|\Sigma_{\mathbf{a}}| = \frac{2N+1}{\gcd(2N+1,p_x)}$.

Define $\mathcal{A} \subset \mathcal{D}_N$ such that $\mathbf{a} \in \mathcal{A}$ if and only if

$$\begin{aligned} &-\frac{1}{2}|\mathbf{p}|_{\boldsymbol{\kappa}}^2 < \frac{\gcd(p_x,p_y)}{\gcd(2N+1,p_x,p_y)}\langle \mathbf{a},\mathbf{p}\rangle \le \frac{1}{2}|\mathbf{p}|_{\boldsymbol{\kappa}}^2 \quad \text{and} \\ &-\frac{1}{2}(2N+1)\gcd(p_x,p_y) < \mathbf{a}\times\mathbf{p} \le \frac{1}{2}(2N+1)\gcd(p_x,p_y). \end{aligned} \tag{3.2.12}$$

Then for all $\mathbf{j} \in \mathcal{D}_N$, $\mathbf{j} = \widehat{\mathbf{a}+n\mathbf{p}}$ for a unique $\mathbf{a} \in \mathcal{A}$ and unique n modulo $|\Sigma_{\mathbf{a}}|$. $\mathcal{A}$ is illustrated in Figure 3.4. Compare this with the equivalent definition for the untruncated problem, (2.4.15). The size of $\mathcal{A}$ is

$$|\mathcal{A}| = {}^{|\mathcal{D}_N|}/_{|\Sigma_{\mathbf{a}}|} = (2N+1)\gcd(2N+1,p_x,p_y). \tag{3.2.13}$$

The choice of $\mathcal{A}$ ensures that, as in the untruncated problem, ρ_0 is the minimum value of ρ_n for $n \in \mathbb{Z}$. However, due to the wrapping, ρ_k is no longer monotonic (though it is locally monotonic near ρ_0 in the sense that it will be monotonic until the wrapping operation occurs).

The definition of $\mathcal{A}$ also suggests that there are issues when p_x, p_y, $2N+1$ are not coprime. This is illustrated in Figure 3.5, where translations of $\mathcal{A}$ by $\mathbf{p}$ are no longer adjacent. This will become an important consideration later. For instance, if p_x, p_y, and $2N+1$ are all mutually coprime and $\mathbf{a} \in \mathcal{A}$ but not in the unstable ellipse $D_{\mathbf{p}}$, $\widehat{\mathbf{a}+n\mathbf{p}} \notin D_{\mathbf{p}}$ unless n is a multiple of $|\Sigma_{\mathbf{a}}|$. This is not true if $\gcd(p_x,p_y,2N+1)>1$.

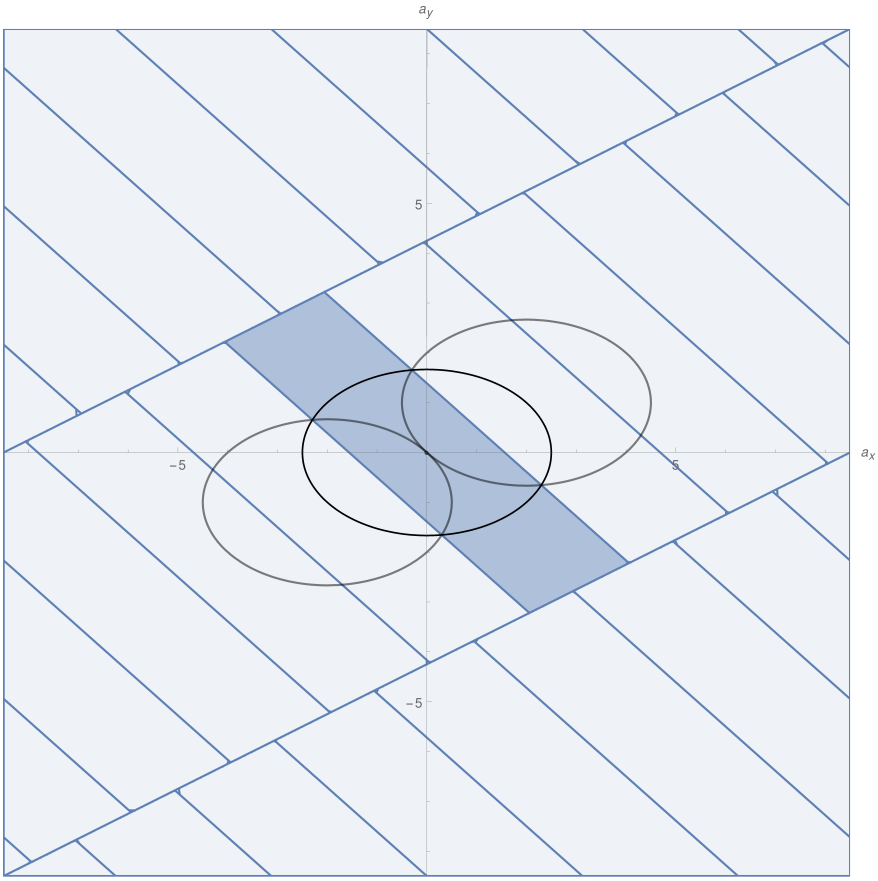

Figure 3.4 – The principal domain $\mathcal{A} \subset \mathcal{D}_N$ shown in dark blue, and translations of the principal domain $\mathcal{A} + n\mathbf{p}$ (modulo wrapping around $\mathcal{D}_N$) shown in light blue. For this figure, $\mathbf{p} = (2, 1)$, $\kappa_y/\kappa_x = 3/2$, and $N = 8$. The translations $A + n\mathbf{p}$ completely cover the lattice $\mathcal{D}_N$ for $0 \leq n < |\Sigma|_{\mathbf{a}}$. For a class $\Sigma_{\mathbf{a}}$, there is exactly one $\mathbf{j} \in \Sigma_{\mathbf{a}}$ in each translation $\mathcal{A} + n\mathbf{p}$. Also shown is the unstable ellipse, and the translations of such by $\pm\mathbf{p}$. Note that the intersections of the discs lie on the boundary of $\mathcal{A}$. Thus, if $\mathbf{a} \in \mathcal{A}$ is not in the unstable ellipse, $\mathbf{a} + n\mathbf{p}$ is not in the unstable ellipse for all $n \in \mathbb{Z}$.

Fix $\mathbf{a} \in \mathcal{A}$, and for brevity denote $n = |\Sigma_{\mathbf{a}}|$. Define the matrix

$$M_T = \begin{pmatrix} 0 & +\rho_1 & 0 & 0 & \cdots & 0 & -\rho_{n-1} \\ -\rho_0 & 0 & +\rho_2 & 0 & \cdots & 0 & 0 \\ 0 & -\rho_1 & 0 & +\rho_3 & \cdots & 0 & 0 \\ 0 & 0 & -\rho_2 & 0 & \cdots & 0 & 0 \\ \vdots & \vdots & \vdots & \vdots & \ddots & \vdots & \vdots \\ 0 & 0 & 0 & 0 & \cdots & 0 & +\rho_{n-1} \\ +\rho_0 & 0 & 0 & 0 & \cdots & -\rho_{n-2} & 0 \end{pmatrix}. \tag{3.2.14}$$

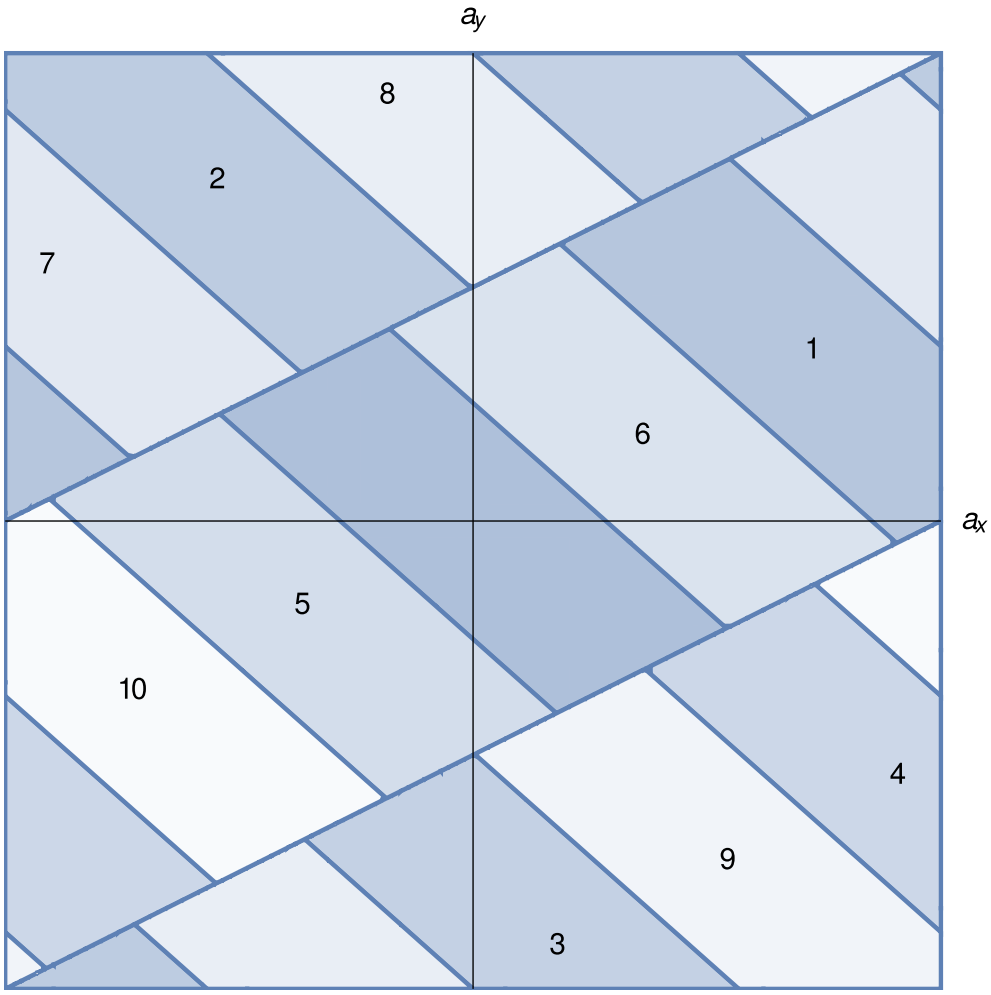

Figure 3.5 – The principal domain of the sine-bracket truncated system wraps around the domain of Fourier modes $\mathcal{D}_N$. If $\gcd(p_x, p_y) \neq 1$, the translations of $\mathcal{A}$ are no longer adjacent. The principal domain $\mathcal{A} \subset \mathcal{D}_N$ is at the centre in dark blue, and translations $\mathcal{A}+n\mathbf{p}$ are labelled with n and shown in gradually lightening shades of blue. Note that the translations "wrap around" the domain $D_{\mathbf{p}}$. For this figure, $\mathbf{p} = (4, 2)$, $\kappa_y/\kappa_x = 3/2$, and $N = 5$. As $\gcd(p_x, p_y) = 2 > 1$, the translations of $\mathcal{A}$ skip over one another, so $\mathcal{A} + n\mathbf{p}$ and $\mathcal{A} + (n + 1)\mathbf{p}$ are not adjacent. Also note that $\mathcal{A} + 11\mathbf{p} = \mathcal{A}$.

Compare this to (2.4.23). Here the matrix is finite, and the truncation operation introduces two extra nonzero elements in the top right and bottom left corners.

Now $\omega = (\omega_0, \omega_1, ..., \omega_{n-2}, \omega_{n-1})$ evolves as $\dot{\omega} = \alpha M_T \omega$. As for the truncated case, we can write M_T as a Poisson system, $M_T = JS$ with J antisymmetric and

S symmetric where

$$J = \begin{pmatrix} 0 & +1 & 0 & \cdots & 0 & -1 \\ -1 & 0 & +1 & \cdots & 0 & 0 \\ 0 & -1 & 0 & \cdots & 0 & 0 \\ \vdots & \vdots & \vdots & \ddots & \vdots & \vdots \\ 0 & 0 & 0 & \cdots & 0 & +1 \\ +1 & 0 & 0 & \cdots & -1 & 0 \end{pmatrix}, \quad S = \begin{pmatrix} \rho_0 & 0 & 0 & \cdots & 0 \\ 0 & \rho_1 & 0 & \cdots & 0 \\ 0 & 0 & \rho_2 & \cdots & 0 \\ \vdots & \vdots & \vdots & \ddots & \vdots \\ 0 & 0 & 0 & \cdots & \rho_{n-1} \end{pmatrix}. \quad (3.2.15)$$

3.2.2. Canonical Symplectic Structure. As noted above, the linearised system is Poisson, with structure matrix J and Hamiltonian $H = \omega^{\mathsf{T}} S\omega$. As J is not the canonical structure matrix, this is not a canonical structure. However, by Darboux's theorem [**dS01, Ste99**], there are local coordinates with canonical structure on the manifold created by fixing the values of the Casimirs (3.1.14). This manifold is known as a symplectic leaf. These symplectic leaves foliate the full Poisson manifold, which in this case is $\mathbb{R}^{|\Sigma_{\mathbf{a}}|}$. As J is constant, these coordinates can be defined globally on a symplectic leaf of the manifold. Additionally, we can use the simple structure of J to find a basis explicitly.

The matrix J has size n for some odd $n \in \mathbb{Z}$. As symplectic manifolds are even-dimensional, J has a kernel, which is one dimensional and spanned by the vector $(1, 1, 1, 1, ..., 1)$. Thus there is exactly one Casimir function of the linear subsystem, namely

$$\mathcal{C} = \sum_{k=0}^{n-1} \omega_k. \quad (3.2.16)$$

Thus the canonical structure has $2\tilde{n}$ basis vectors, where $2\tilde{n}+1 = n$. We can now find a canonical basis for J by the symplectic Gram-Schmidt theorem [**dG06**]. Additionally, J is *circulant* [**Gra06**]; each row is the previous row shifted one space to the right. Thus J is diagonalised by a discrete Fourier transform.

The eigenvalues of J are

$$\lambda_k = -2i \sin(\frac{2\pi k}{n}), \quad k = 0, 1, 2, ..., n-1. \quad (3.2.17)$$

Note that $\lambda_0 = 0$, and $\lambda_k = -\lambda_{n-k}$. Additionally, all eigenvalues are imaginary, as J is skew-symmetric. The corresponding eigenvectors of J are

$$\mathbf{v}_k = (\varphi^0, \varphi^k, \varphi^{2k}, ..., \varphi^{(n-1)k})^{\mathsf{T}} \quad (3.2.18)$$

where $\varphi = e^{\frac{2\pi i}{n}}$.

Now let

$$a_k = \sqrt{\frac{2}{n|\lambda_k|}}\mathrm{Im}(\mathbf{v}_k) = \sqrt{\frac{2}{n|\lambda_k|}}\begin{pmatrix} 0 \\ -\sin\left(\frac{2\pi}{n}k\right) \\ -\sin\left(\frac{2\pi}{n}2k\right) \\ \vdots \\ -\sin\left(\frac{2\pi}{n}(n-1)k\right) \end{pmatrix}, \tag{3.2.19}$$

$$b_k = \sqrt{\frac{2}{n|\lambda_k|}}\mathrm{Re}(\mathbf{v}_k) = \sqrt{\frac{2}{n|\lambda_k|}}\begin{pmatrix} 1 \\ \cos\left(\frac{2\pi}{n}k\right) \\ \cos\left(\frac{2\pi}{n}2k\right) \\ \vdots \\ \cos\left(\frac{2\pi}{n}(n-1)k\right) \end{pmatrix} \tag{3.2.20}$$

for $k = 1, 2, ..., \tilde{n}$. Finally, let $c = (1, 1, 1, ..., 1)^\mathsf{T}$.

Now

- a_1, a_2, ... , $a_{\tilde{n}}$, b_1, b_2, ... , $b_{\tilde{n}}$, c are linearly independent and span $\mathbb{R}^n$;
- $a_i^\mathsf{T} J a_j = 0$ for all i, j (that is, they are orthogonal with respect to the Poisson form);
- $b_i^\mathsf{T} J b_j = 0$ for all i, j;
- $b_i^\mathsf{T} J a_j = 0$ for all $i \neq j$;
- $b_i^\mathsf{T} J a_i = 1$ for all i;
- $x^\mathsf{T} J c = 0$ for any vector x.

Thus if we define $T := (a_1, a_2, ..., a_{\tilde{n}}, b_1, b_2, ..., b_{\tilde{n}}, c)$, T is an $n \times n$ matrix such that

$$T^\mathsf{T} J T = \begin{pmatrix} \mathbf{0} & \mathbb{I} & 0 \\ -\mathbb{I} & \mathbf{0} & 0 \\ 0 & 0 & 0 \end{pmatrix}. \tag{3.2.21}$$

This is block diagonal, with a block of canonical J and a 0 block. Restricting to a symplectic leaf means we consider only the dynamics on the manifold away from the 0 block. Thus this is an explicit basis for a canonical structure on the symplectic leaf. This is of limited utility, as the corresponding symmetric matrix S from (3.2.15) is dense rather than diagonal in this basis, but is still notable.

3.2.3. Stable Classes and Stable Cases. Taking a similar approach to Theorem 2.5.5, we now show that classes led by values of $\mathbf{a}$ outside the unstable ellipse do not contribute instability. The unstable ellipse

$$D_\mathbf{p} = \{\mathbf{x} \in \mathcal{D}_N \; ||\widehat{\mathbf{x}}|_{\boldsymbol{\kappa}} < |\mathbf{p}|_{\boldsymbol{\kappa}}\} \tag{3.2.22}$$

is not significantly altered from the definition (2.5.2) by the truncation. Stability is manifest for stable classes in this setting by the same argument as for the untruncated system: define the transformation matrix

$$T := \begin{pmatrix} \rho_0^{-1/2} & 0 & 0 & ... & 0 \\ 0 & \rho_1^{-1/2} & 0 & ... & 0 \\ 0 & 0 & \rho_2^{-1/2} & ... & 0 \\ \vdots & \vdots & \vdots & \ddots & \vdots \\ 0 & 0 & 0 & ... & \rho_{n-1}^{-1/2} \end{pmatrix}. \tag{3.2.23}$$

If $\rho_k > 0$ for all k, this is real. So $T^{-1}M_T T$ is real and antisymmetric, and thus only has imaginary eigenvalues. As this is similar to M_T, the class cannot contribute instability. Geometrically, the condition $\rho_k > 0$ for all k is equivalent to $\Sigma_{\mathbf{a}} \cap D_{\mathbf{p}} = \emptyset$, and therefore $\mathbf{a} \notin D_{\mathbf{p}}$.

We could also note that the Hamiltonian form corresponding to the symmetric matrix S, $H = \sum_{k=0}^{n-1} \rho_k \omega_k^2$, is positive definite if all $\rho_k > 0$. But by the properties of the Hamiltonian, $\frac{\mathrm{d}}{\mathrm{d}t}H = 0$. Thus H is a weak Lyapunov function for the flow as $\frac{\mathrm{d}}{\mathrm{d}t}H = 0$. This is discussed in [**AKN07**].

This theorem, together with the unstable ellipse being invariant under the truncation, means that the result of Theorem 2.6.1 holds in the truncated system. If $\mathbf{p} = (p_x, 0)$ and $\kappa_x |p_x| < \kappa_y$, the equilibrium is linearly stable in the truncated system. Equivalently, if $\mathbf{p} = (0, p_y)$ and $\kappa_y |p_y| < \kappa_x$, the equilibrium is linearly stable.

3.2.4. Energy-Casimir Stability. It was shown in Section 3.2.3 that if $\mathbf{p} = (p_x, 0)$ and $\kappa_x |p_x| < \kappa_y$, the parallel shear flow equilibrium $\omega_{\pm\mathbf{p}} = \Gamma$ is linearly stable. It is natural to ask if this linear stability can be extended to a stronger sense of stability. We can study the energy-Casimir stability as per Section 2.6.2 in the sine-bracket truncated system, as there is an analogous set of Casimirs (3.1.14). In most cases, the result will be the same; the linear stability cannot be extended to energy-Casimir stability. The only case where energy-Casimir stability can always be concluded is if $\mathbf{p} = (1, 0)$ and $\kappa_x < \kappa_y$. Thus the result from [**AK98**] is also true in the sine-bracket truncated system. However, we will see that under some conditions on N other parallel shear flows are also energy-Casimir stable.

We calculate the linear approximation of the invariant subspace with fixed Casimirs. The derivatives are given by

$$\frac{\partial \mathcal{C}_M}{\partial \omega_{\mathbf{k}}} = \sum \omega_{\mathbf{i}_1} \omega_{\mathbf{i}_2} \omega_{\mathbf{i}_{M-1}} \cos\left(\varepsilon A \left(\mathbf{i}_1, \mathbf{i}_2, ..., \mathbf{i}_{M-1}, -\sum_{j=1}^{M-1} \mathbf{i}_j \right) \right) \tag{3.2.24}$$

where the summation is over all sets of modes $\{\mathbf{i}_j\}$ such that $\sum_{j=1}^{M-1} \mathbf{i}_j = -\mathbf{k}$.

Consider $\mathbf{p} = (p_x, 0)$, and evaluate (3.2.24) at the equilibrium Ω^*. The only nonzero terms remaining will be when $\mathbf{i}_j = \pm\mathbf{p}$ for all j. Thus

$$A\left(\mathbf{i}_1, \mathbf{i}_2, ..., \mathbf{i}_{M-1}, -\sum_{j=1}^{M-1} \mathbf{i}_j\right) = A\left(\pm\mathbf{p}, \pm\mathbf{p}, ..., \pm\mathbf{p}, \xi\mathbf{p}\right) = 0 \tag{3.2.25}$$

for some ξ (as $\mathbf{p} \times \mathbf{p} = 0$). Thus, writing the derivative in vector form,

$$\nabla \mathcal{C}_M|_{\Omega^*} = \Gamma^{M-1} \sum_{a=0}^{M-1} \binom{M-1}{a} \mathbf{e}_{\widehat{(2a-M+1)\mathbf{p}}} \tag{3.2.26}$$

where $\mathbf{e}_{\mathbf{k}}$ is the unit vector in the direction $\mathbf{k}$.

This is only nonzero in directions that are multiples of $\mathbf{p}$, and the coefficients there are always nonzero. Thus (recalling that $\mathcal{C}_1 = \omega_{\mathbf{0}}$)

$$\begin{aligned} &\operatorname{span}\left(\nabla \mathcal{C}_1|_{\Omega^*}, \nabla \mathcal{C}_2|_{\Omega^*}, ...\nabla \mathcal{C}_N|_{\Omega^*}\right) \\ &\quad = \operatorname{span}\left(\mathbf{e}_{0\mathbf{p}}, (\mathbf{e}_{\widehat{\mathbf{p}}} + \mathbf{e}_{-\widehat{\mathbf{p}}}), (\mathbf{e}_{\widehat{2\mathbf{p}}} + \mathbf{e}_{-\widehat{2\mathbf{p}}}), ..., (\mathbf{e}_{\widehat{N\mathbf{p}}} + \mathbf{e}_{-\widehat{N\mathbf{p}}})\right). \end{aligned} \tag{3.2.27}$$

This, along with the reality condition on $\omega_{\pm\mathbf{k}}$ fixes $\frac{2N+1}{\gcd(2N+1,p_x)}$ of the modes: exactly those that can be written in the form $\widehat{a\mathbf{p}}$. If $\gcd(2N+1, p_x) > 1$, then the equivalent result as for the untruncated system applies; as fixing the Casimirs does not fix the value of $(a_x, 0)$ for at least one value of $0 < a_x < p_x$, the energy remains indefinite, and so there is not energy-Casimir stability.

However, if $\gcd(2N+1, p_x) = 1$ this leads to a surprising result.

Proposition 3.2.28 (Energy-Casimir Stable Flows)**.** *If $\mathbf{p} = (p_x, 0)$, $\kappa_x|p_x| < \kappa_y$, and $2N+1$ and p_x are coprime, then the sine-bracket truncated system is energy-Casimir stable around the parallel shear flow equilibrium $\omega_{\pm\mathbf{p}} = \Gamma$.*

Proof. As in Section 2.4.2, define

$$H = \mathcal{H} - \frac{1}{2|\mathbf{p}|^2_{\boldsymbol{\kappa}}}\mathcal{C}_2 = -\frac{1}{2}\sum_{\mathbf{j}\in\mathcal{D}_N \setminus \{\mathbf{0}\}} \rho_{\mathbf{j}}|\omega_{\mathbf{j}}|^2. \tag{3.2.29}$$

Then, as $\mathcal{C}_2$ is a Casimir of the sine-bracket, H and $\mathcal{H}$ generate the same dynamics. The gradient of H is

$$\nabla H = -\sum_{\mathbf{j}\in\mathcal{D}_N \setminus \{\mathbf{0}\}} \rho_{\mathbf{j}}\omega_{\mathbf{j}}\mathbf{e}_{\mathbf{j}} \tag{3.2.30}$$

and the Jacobian is

$$(D^2H)_{i,j} = \rho_{\mathbf{i}}\delta(\mathbf{j} + \mathbf{i}) \tag{3.2.31}$$

where δ is the Dirac delta function centred at zero. Additionally, note that

$$H|_{\Omega^*} = 0, \quad \nabla H|_{\Omega^*} = 0. \tag{3.2.32}$$

If $\mathbf{p} = (p_x, 0)$ and $\gcd(2N+1, p_x) = 1$, by the above the span of the gradient of the Casimirs $\mathcal{C}_M$ is $\text{span}(\mathbf{e}_{\widehat{a\mathbf{p}}} + \mathbf{e}_{\widehat{-a\mathbf{p}}})$ for $a = 0, 1, ..., N$. Additionally, $\omega_{\mathbf{j}} = \omega_{-\mathbf{j}}$. Thus upon restricting to the complement of the gradient of the Casimirs projects D^2H to the basis $\mathbf{e}_{\mathbf{j}}$ for all $\mathbf{j} \in \mathcal{D}_N$ such that $\mathbf{j} \neq a\mathbf{p}$ for all $a \in \mathbb{Z}$. However, as $\kappa_x|p_x| < \kappa_y$, $\rho_{\mathbf{j}} > 0$ for all $\mathbf{j} \neq a\mathbf{p}$ (as $|\mathbf{j}|_{\boldsymbol{\kappa}} > |\mathbf{p}|_{\boldsymbol{\kappa}}$ for all $\mathbf{j} \neq a\mathbf{p}$). Thus D^2H is negative definite on the subspace fixed by the Casimirs, and therefore we conclude the parallel shear flow is energy-Casimir stable. □

This is based on the algorithm presented in [**HMRW85**], which is based on the approach used in [**AK98, Arn66b**]. As H is quadratic, the procedure is simpler here, and equivalent to showing that H is a Lyapunov function for the flow after restricting to the subspace fixed by the Casimirs.

As shown in Section 2.6.2, there is not energy-Casimir stability for the untruncated system at the corresponding equilibria. For the truncated system, there are arbitrarily large values of N for which energy-Casimir stability occurs, and also arbitrarily large values for which it does not occur. If p_x is even, there is energy-Casimir stability for *all* choices of N. Compare this to Lemma 3.2.42, where it is shown that when $\gcd(p_x, p_y)$ is even there are issues with the instability arguments.

The importance of $\gcd(2N+1, p_x)$ in the above proof demonstrates that the question of energy-Casimir stability is very sensitive to choice of truncation, and care must be taken when selecting the truncation size N for the finite-dimensional truncation. There is also the surprising result that parallel shear flows of the form $\cos(2n\kappa_x x)$ are energy-Casimir stable for all $n \in \mathbb{N}$ and $2n\kappa_x < \kappa_y$ regardless of truncation size. This is in contrast to the untruncated system, where they are not energy-Casimir stable.

3.2.5. Unstable Classes. For classes that intersect the unstable ellipse and therefore contribute instability, we prove the same two results as for the Galerkin-truncated system: if $\rho_0 < 0$ and $\rho_k > 0$ for all $k \neq 0$, nonimaginary eigenvalues exist, and there is a lower bound for a real eigenvalue under certain conditions. To prove this, we study the characteristic polynomial and use the intermediate value theorem on the real axis. This characteristic polynomial can be written as a function of the characteristic polynomials of the Galerkin-truncated matrices defined in Section 2.7.4. This can be used to show that there is some lower bond λ^* on a root of the characteristic polynomial. When this lower bound is real, there is a positive real eigenvalue. We then discuss values of $\mathbf{p}$ and N such that there exists an $\mathbf{a} \in \mathbb{Z}^2$ such that the lower bound is real. This requires a careful selection of N to make sure the class of Fourier modes satisfies the condition $\rho_k > 0$ for all $k \neq 0$. We show that such an N can be found for all $\mathbf{p}$ with p_x, p_y not both even, and for almost all such $\mathbf{p}$ we conclude linear instability.

Introduce the characteristic polynomial of M_T

$$\mathcal{M}_T(x) = \det(x\mathbb{I} - M_T). \tag{3.2.33}$$

This can be expressed in terms of the characteristic polynomials $\mathcal{M}_m^n$ of the Galerkin-truncated matrices (2.7.7). Note that we consider the ρ_k in that definition to be our new, wrapped ρ_k (3.2.4) rather than the ρ_k corresponding to the untruncated system (2.4.10). As the ρ_k are treated symbolically throughout much of Section 2.7, this discrepancy does not affect the recurrence relations or the lower bound λ^*.

Expand by minors along the final row and column of $x\mathbb{I} - M_T$ to calculate the determinant $\mathcal{M}_T(x)$:

$$\begin{aligned}\mathcal{M}_T(x) &= x\mathcal{M}_0^{n-2}(x) + \rho_{n-1}\rho_{n-2}\mathcal{M}_0^{n-3}(x) + \rho_{n-1}\rho_0\mathcal{M}_1^{n-2}(x)\\ &= \mathcal{M}_0^{n-1}(x) + \rho_0\rho_{n-1}\mathcal{M}_1^{n-2}(x).\end{aligned} \tag{3.2.34}$$

Here $n = |\Sigma_{\mathbf{a}}|$ is the size of the class, and $\mathcal{M}_a^b$ are the characteristic polynomials of the Galerkin-truncated system. This calculation uses the fact that n is odd.

Proposition 3.2.35 (Existence of a real eigenvalue (sine-truncated system))**.** *If $\rho_0 < 0$, and $\rho_k \geq 0$ for all $k = 1, 2, ..., n-1$, $\rho_k = 0$ for at most one of $k = 1, 2, ..., n-1$, and sufficiently large N, M_T has a nonzero real eigenvalue.*

Proof. The characteristic polynomial $\mathcal{M}_T$ for odd n has leading term x^n and constant term 0. By combining (3.2.34) and (2.7.13) (noting that n is odd, so $n-1$ and $n-3$ are even), the linear coefficient is given by

$$\begin{aligned}\left.\frac{\mathrm{d}\mathcal{M}_T}{\mathrm{d}x}\right|_{x=0} &= \left.\frac{\mathrm{d}}{\mathrm{d}x}\mathcal{M}_0^{n-1}(x)\right|_0 + \rho_0\rho_{n-1}\left.\mathcal{M}_1^{n-2}(x)\right|_0\\ &= \sum_{k=0}^{\frac{n-1}{2}}\left(\prod_{j=0;\, j\neq 2k}^{n-1}\rho_j\right) + \sum_{k=0}^{\frac{n-3}{2}}\left(\prod_{j=1;\, j\neq 1+2k}^{n-2}\rho_j\right)\\ &= \sum_{k=0}^{n-1}\left(\prod_{j=0;\, j\neq k}^{n-1}\rho_j\right) \qquad (3.2.36)\\ &= \left(\prod_{j=0}^{n-1}\rho_j\right)\left(\sum_{k=0}^{n-1}\frac{1}{\rho_k}\right). \qquad (3.2.37)\end{aligned}$$

Note that (3.2.37) is only valid for $\rho_k \neq 0$ for all k, but (3.2.36) is always valid[1]. Assume $\rho_k > 0$ for all $k \neq 0$. As $\rho_k \to \frac{1}{|\mathbf{p}|^2} > 0$ as $|\widehat{\mathbf{a} + k\mathbf{p}}| \to \infty$ and the size n of the classes grows linearly with N, $\sum_{j=0}^{n-1}\frac{1}{\rho_j} > 0$ for sufficiently large N.

[1]The expression in equation (3.2.36) is the so-called $n-1^{\text{th}}$ *elementary symmetric polynomial* in the variables $\rho_0, \rho_1, ..., \rho_{n-1}$.

However $\prod_{j=0}^{n-1} \rho_j < 0$ as $\rho_0 < 0$, $\rho_j > 0$ for all $j = 1, .., n-1$, and hence the linear coefficient of the characteristic polynomial is less than zero.

If $\rho_k = 0$ for exactly one k, then (3.2.36) consists of only one term, $\prod_{j=0;\, j\neq k}^{n-1} \rho_j$. This is less than zero as $\rho_0 < 0$ and $\rho_j > 0$ for all $j \neq 0, k$. If $\rho_k = 0$ for more than one value of k, then the linear term is zero and this argument breaks down.

As the constant term is zero, and the linear term is nonzero, then the lowest order nonzero coefficient of the polynomial is negative.

We now argue by contradiction, as per the proof of Proposition 2.7.15. Assume all roots of the polynomial are imaginary (say $i\omega_k$) or complex ($\gamma_j + i\delta_j$) or zero. Then the lowest order nonzero coefficient (of x^{n_1}) is $\prod_{k=1}^{n_2}(\omega_k^2) \prod_{j=1}^{n_3} \left((\gamma_j^2 + \delta_j^2)^2\right) > 0$. Thus by contradiction there must be some real eigenvalue, which will occur in a positive and negative pair by the Hamiltonian property of the spectrum. □

The lower bound in Lemma 2.7.20 is also a lower bound on a real eigenvalue of M_T by a similar argument.

Lemma 3.2.38 (Lower Bound for a Real Eigenvalue (sine-truncated))**.** *If* $\mathbf{a} \in D_{\mathbf{p}}$, $\widehat{\mathbf{a} + k\mathbf{p}} \notin D_{\mathbf{p}}$ *for all* $k \neq 0$,

$$\lambda^* = \sqrt{-\rho_1(\rho_0 + \rho_2)} \tag{3.2.39}$$

is real and nonzero, and N *is sufficiently large, there is some real eigenvalue* $\lambda > \lambda^*$ *of* M_T.

Proof. By expanding (3.2.34) using (2.7.8), (2.7.9)

$$\begin{aligned} \mathcal{M}_T(x) =& (x^3 + (\rho_0\rho_1 + \rho_1\rho_2)x)\mathcal{M}_3^{n-1}(x) \\ &+ (x^2 + \rho_0\rho_1)\rho_2\rho_3\mathcal{M}_4^{n-1}(x) \\ &+ \rho_0\rho_{n-1}\mathcal{M}_1^{n-2}(x). \end{aligned} \tag{3.2.40}$$

Thus

$$\begin{aligned} \mathcal{M}_T(\sqrt{-\rho_1(\rho_0 + \rho_2)}) =& -\rho_1\rho_2^2\rho_3\mathcal{M}_4^{n-1}(\sqrt{-\rho_1(\rho_0 + \rho_2)}) \\ &+ \rho_0\rho_{n-1}\mathcal{M}_1^{n-2}(\sqrt{-\rho_2(\rho_1 + \rho_3)}). \end{aligned} \tag{3.2.41}$$

As $\rho_1, \rho_2, \rho_3, \rho_{n-1} > 0$, $\rho_0 < 0$ and the $\mathcal{M}_m^n$ terms are positive by Lemma 2.7.10, $\mathcal{M}_T(\lambda^*) < 0$.

However, as the leading term of $\mathcal{M}_T$ is x^n, $\lim_{x\to\infty} \mathcal{M}_T(x) > 0$. Thus, by the intermediate value theorem, there exists some $\lambda > \lambda^*$ such that $\mathcal{M}_T(\lambda) = 0$ and therefore λ is a positive real eigenvalue of M_T. □

All that remains is to clarify when the lower bound (3.2.39) is real in terms of $\mathbf{a}$, $\mathbf{p}$, K. This is a more difficult task for the sine-bracket truncation than for the Galerkin style truncation, due to the wrapping operation. For poor choices of truncation size N, the class of modes $\Sigma_{\mathbf{a}}$ may intersect the unstable ellipse more

than once. This can happen in two ways. If N is particularly small, the modes in the classes may lie on two line segments which both intersect the unstable ellipse. This can be remedied by selecting sufficiently large N. This scenario is illustrated in Figure 3.6.

A more difficult problem is classes that wrap onto themselves. If $\mathbf{p} = (p_x, p_y)$ and $\eta = \gcd(p_x, p_y) > 1$, there may be integer lattice points in the class $\Sigma_{\mathbf{a}}$ of the form $\mathbf{a} + k\mathbf{p} + (p_x/\eta, p_y/\eta)$ for $k \in \mathbb{Z}$. In particular, if $\mathbf{a} \in D_{\mathbf{p}}$ in the Galerkin-truncated we can conclude that if $\mathbf{a} \pm \mathbf{p} \notin D_{\mathbf{p}}$, then $\mathbf{a} + k\mathbf{p} \notin D_{\mathbf{p}}$ for all $k \neq 0$. In the sine-bracket truncated system $\mathbf{a} + (p_x/\eta, p_y/\eta)$ may still be in $D_{\mathbf{p}}$, which will break the assumptions of Lemma 2.7.27. If η is odd, this can be avoided by making appropriate choices of N.

Lemma 3.2.42 (Appropriate choices of N for the sine-bracket truncation)**.** *For all $\mathbf{p} = (p_x, p_y)$ such that $\eta = \gcd(p_x, p_y)$ is not even, there exists a sequence of N which increases without bound such that for all choices of $\mathbf{a}$ any two nonconsecutive lattice points in $\Sigma_{\mathbf{a}}$ cannot both be in the unstable ellipse.*

Proof. Choose N such that

$$N = \frac{(2\tilde{N} + 1)\eta - 1}{2} \tag{3.2.43}$$

for some $\tilde{N} \in \mathbb{N}$. Thus $2N + 1 = (2\tilde{N} + 1)\eta$. If η is not even, then such an N is a positive integer and thus a valid lattice size.

Select as a lower bound $\tilde{N} > \frac{2|\mathbf{p}|_{\boldsymbol{\kappa}}^2 - \eta\kappa_x\kappa_y}{2\eta\kappa_x\kappa_y}$ so that $N > \frac{2|\mathbf{p}|_{\boldsymbol{\kappa}}^2 - \kappa_x\kappa_y}{2\kappa_x\kappa_y}$. Both $\mathbf{p}$ and $\boldsymbol{\kappa}$ are fixed and finite and $\kappa_x, \kappa_y \neq 0$ so this lower bound is always finite. We can thus find an infinite sequence of N that increases without bound by letting $\tilde{N}$ increase without bound.

If $\mathbf{x} \in \Sigma_{\mathbf{a}}$ then $\mathbf{x} = \widehat{\mathbf{a} + k\mathbf{p}}$ for some $k \in \mathbb{N}$. Thus $\mathbf{x}$ lies on the line parallel to the vector $\mathbf{p}$ that passes through the point $\mathbf{a} + \boldsymbol{\Delta}_{\mathbf{x}}(2N + 1)$ for some $\boldsymbol{\Delta}_{\mathbf{x}} \in \mathbb{Z}^2$ (note that this point may be outside the domain $\mathcal{D}_N$).

Similarly if $\mathbf{y} \in \Sigma_{\mathbf{a}}$ then it lies on the line parallel to $\mathbf{p}$ that passes through $\mathbf{a} + \boldsymbol{\Delta}_{\mathbf{y}}(2N + 1)$ for some $\boldsymbol{\Delta}_{\mathbf{y}} \in \mathbb{Z}^2$. Then the distance between these two lines is

$$\begin{aligned} d &= \frac{|[(\mathbf{a} + \boldsymbol{\Delta}_{\mathbf{x}}(2N + 1)) - (\mathbf{a} + \boldsymbol{\Delta}_{\mathbf{y}}(2N + 1))] \times \mathbf{p}|}{|\mathbf{p}|} \\ &= \frac{(2N + 1)|(\boldsymbol{\Delta}_{\mathbf{x}} - \boldsymbol{\Delta}_{\mathbf{y}}) \times \mathbf{p}|}{|\mathbf{p}|}. \end{aligned} \tag{3.2.44}$$

The value $(\boldsymbol{\Delta}_{\mathbf{x}} - \boldsymbol{\Delta}_{\mathbf{y}}) \times \mathbf{p} \in \mathbb{Z}^2$, so $d = 0$ or $d \geq \frac{2N+1}{|\mathbf{p}|}$. If $d \geq \frac{2N+1}{|\mathbf{p}|}$, this corresponds to $\mathbf{x}$ and $\mathbf{y}$ lying on different line segments, as in Figure 3.6. Thus the distance between two points on different line segments is at least $\frac{2N+1}{|\mathbf{p}|} > \frac{2|\mathbf{p}|_{\boldsymbol{\kappa}}^2}{\kappa_x\kappa_y|\mathbf{p}|}$ for our choice of N.

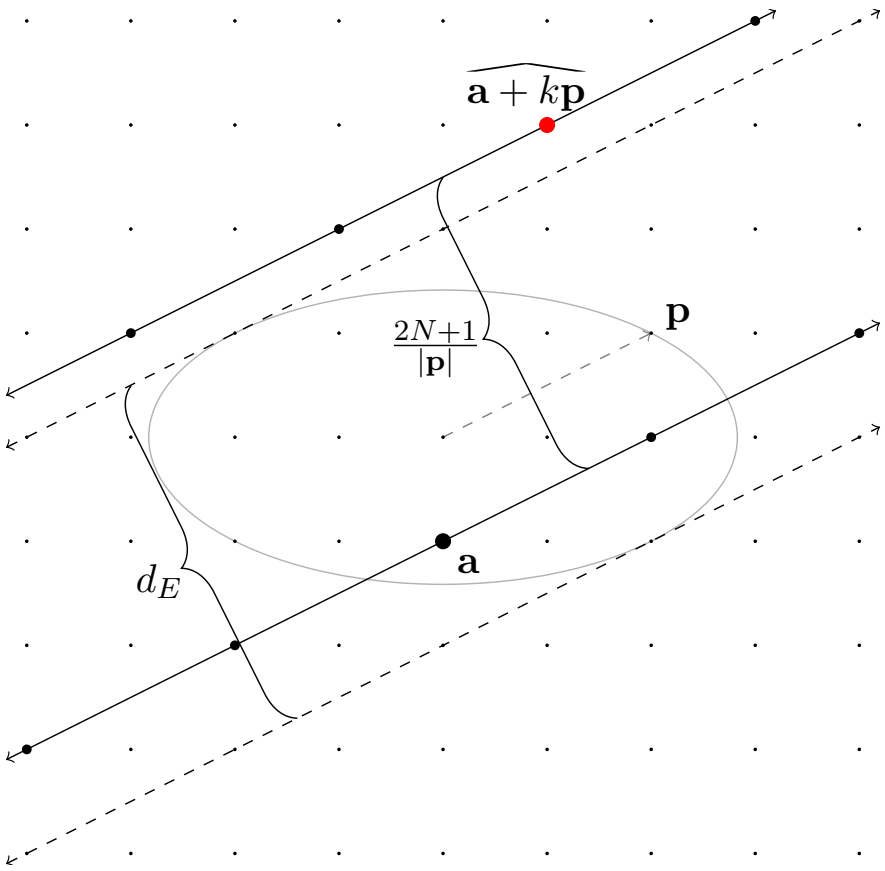

Figure 3.6 – A possible issue in the linearised sine-bracket truncated system. For poor choices of N, a class of modes $\widehat{\mathbf{a}+k\mathbf{p}}$ may intersect the unstable ellipse at multiple nonadjacent values of k. This would cause issues for our stability arguments. The minimum distance between modes in the same class that do *not* lie on the same line segment (ie, the class has wrapped around $\mathcal{D}_p$) is $\frac{2N+1}{|\mathbf{p}|}$. If this is sufficiently large, the class cannot intersect the ellipse on more than one line segment. Therefore nonadjacent modes in the class cannot both lie in the unstable ellipse for sufficiently large N.

Now, d_E, as indicated in Figure 3.6, is the distance between the two tangents to the unstable ellipse parallel to the vector $\mathbf{p}$. We calculate that

$$d_E = \frac{2|\mathbf{p}|_{\boldsymbol{\kappa}}^2}{\kappa_x \kappa_y |\mathbf{p}|}. \tag{3.2.45}$$

Note that this expression involves both the $\boldsymbol{\kappa}$-norm and the usual Euclidean norm. We have shown that the distance between the line segments that contain modes in the same class on two different line segments is greater than d_E for sufficiently large N; thus, they cannot both intersect the unstable ellipse. Thus,

if two modes $\mathbf{a}$ and $\widehat{\mathbf{a}+k\mathbf{p}}$ are in the unstable ellipse, they both lie on the line segment through $\mathbf{a}$ parallel to $\mathbf{p}$.

If $d = 0$, by the above, $\mathbf{y}$ lies on the line parallel to $\mathbf{p}$ passing through $\mathbf{x}$. We thus need to show that $\mathbf{y} = \mathbf{x} \pm \mathbf{p}$. This is not possible for all choices of $\mathbf{p}$, N; see Figure 3.5. For poor choices of $\mathbf{p}$ and N, $\mathbf{x}$ and $\mathbf{y}$ can lie in adjacent translations of $A + n\mathbf{p}$ and therefore possibly both be in the unstable ellipse, but not satisfy $\mathbf{y} = \mathbf{x} \pm \mathbf{p}$.

Define $\mathbf{q} := (q_x, q_y)$ such that $\mathbf{p} = \eta\mathbf{q}$ and $\gcd(q_x, q_y) = 1$. Then as $\mathbf{x}, \mathbf{y} \in \mathbb{Z}^2$, $\mathbf{y} = \mathbf{x} + k\mathbf{q}$ for some $k \in \mathbb{Z}$. But $\mathbf{x}, \mathbf{y} \in \Sigma_{\mathbf{a}}$ so $\mathbf{y} = \mathbf{x} + j\mathbf{p} + (2N+1)\boldsymbol{\Delta}$ for some $\boldsymbol{\Delta} \in \mathbb{Z}^2$. Thus $k\mathbf{q} = j\mathbf{p} + (2N+1)\boldsymbol{\Delta}$. So

$$k\mathbf{q} = j\eta\mathbf{q} + (2\tilde{N}+1)\eta\boldsymbol{\Delta} = \eta(j\mathbf{q} + (2\tilde{N}+1)\boldsymbol{\Delta}). \tag{3.2.46}$$

Thus $k\mathbf{q}$ is divisible by η, but the elements of $\mathbf{q}$ cannot both be divisible by η as $\gcd(q_1, q_2) = 1$, so $\eta | k$. Thus $\mathbf{y} = \mathbf{x} + \eta\beta\mathbf{q}$ for some $\beta \in \mathbb{Z}$, and so $\mathbf{y} = \mathbf{x} + \beta\mathbf{p}$. Then if $|\mathbf{y} - \mathbf{x}|_{\boldsymbol{\kappa}} < 2|\mathbf{p}|_{\boldsymbol{\kappa}}$ (a necessary condition for $\mathbf{x}, \mathbf{y}$ to both be in $D_{\mathbf{p}}$) this implies $\beta = 0$ or $\beta = \pm 1$.

Thus if there are two values $\mathbf{x}, \mathbf{y} \in \Sigma_{\mathbf{a}} \cap D_{\mathbf{p}}$, then $\mathbf{x} = \mathbf{y} \pm \mathbf{p}$, and the result follows. □

An outstanding issue with the sine-bracket truncation is that there is no appropriate choice of N when $\gcd(p_x, p_y)$ is even. If $\eta > 1$ and $\gcd(\eta, 2N+1) = 1$, then $\mathbf{p}$ will generate all multiples of $\mathbf{q}$ due to the wrapping operation. Thus classes that intersect the ellipse can return after leaving the ellipse and intersect the ellipse again, breaking the assumption of 3.2.38 that $\rho_k < 0$ for only one value of k. This behaviour continues for all values of N with $\gcd(2N+1, \eta) = 1$. If η is even, this is true for any N; if η is odd, we select appropriate N to avoid this.

Theorem 3.2.47 (Linear Instability in the Sine-Bracket Truncated system)**.** *Choose* $\mathbf{p}$ *such that* p_x*,* p_y *are not both even and*

$$|\mathbf{p}|_{\boldsymbol{\kappa}} > \frac{3 + 2\sqrt{3}}{2}, \tag{3.2.48}$$

and N *such that* $2N+1$ *is a multiple of* $\gcd(p_x, p_y)$ *and* $2N+1 > \frac{2|\mathbf{p}|^2_{\boldsymbol{\kappa}}}{\kappa_x \kappa_y}$*. Then in the sine-bracket truncated system with truncation size* N*, the shear flow equilibrium* $\omega_{\pm\mathbf{p}}$ *is linearly unstable.*

Proof. By Lemma 2.7.30, under the above conditions there is at least one value of $\mathbf{a} \in \mathcal{D}_N$ such that $\lambda^* = \sqrt{-\rho_1(\rho_0 + \rho_2)}$ is real and positive and $\rho_0 < 0$, $\rho_{\pm 1} > 0$. This result is not affected by the truncation, as it only depends on the sign of values of ρ_k near $k = 0$. By Lemma 3.2.42, this implies $\rho_k > 0$ for all $k \neq 0$.

Thus by Lemma 3.2.38, there is some eigenvalue of M_T with positive real part, and we conclude linear instability. □

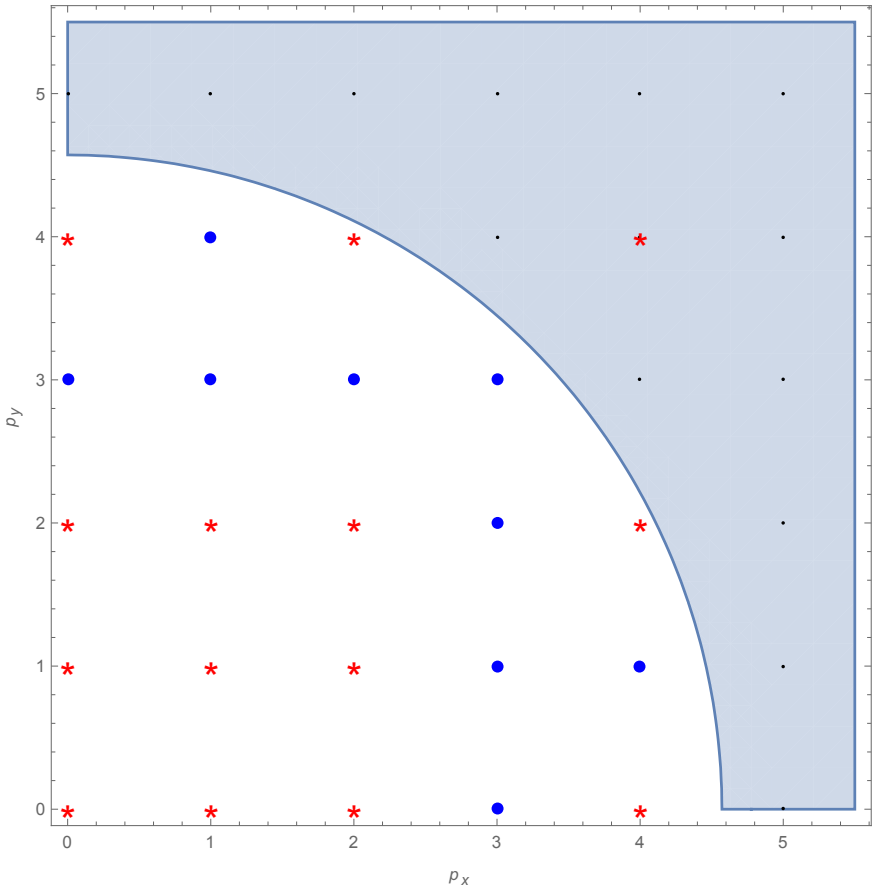

Figure 3.7 – Valid values of $\mathbf{p}$ for Theorem 3.2.47. Values of $\mathbf{p}$ in the shaded region satisfy (3.2.48). For the values of $\mathbf{p}$ indicated by blue dots, there exists at least one values of $\mathbf{a} \in \mathbb{Z}^2$ such that the conditions of Lemma 3.2.38 hold and we can conclude linear instability. At the points indicated by red asterisks, we cannot apply Theorem 3.2.47 to conclude instability because either there are no values of $\mathbf{a}$ such that Lemma 3.2.38 holds or $\gcd(p_x, p_y)$ is even. Note that this includes values of $\mathbf{p}$ that satisfy (3.2.48) but have $\gcd(p_x, p_y)$ even. We cannot prove instability in this case, though numerical evidence suggests instability in all cases except those shown to be stable in Section 3.2.3. Compare this to Figure 2.13; this figure is the same except at the points with $\gcd(p_x, p_y)$ even.

Note that for a given value of $\mathbf{p}$ there is an unbounded sequence appropriate choices of N such that the equilibrium is linearly unstable in the N-truncated system. If $\gcd(p_x, p_y) \neq 1$ there are also infinitely many choices of N for which our proof breaks down as $2N + 1$ is not a multiple of $\gcd(p_x, p_y)$. However, this does not mean there is not instability for these values of N; merely that our current method is not sufficient to deal with these cases.

3.3. Poisson Integrator for the Truncated Euler Equations

A practical application of identifying the Poisson structure associated with a manifold is the development of a *Poisson integrator* [**Rut83, HLW06**]. For a Hamiltonian flow $\dot{\mathbf{x}} = X_H(\mathbf{x})$, the flow can be approximated by a function Φ_t that integrates $\mathbf{x}(t_0 + t) \approx \Phi_t(\mathbf{x}(t_0))$. The flow Φ_t is called a Poisson integrator if $\mathbf{x} \to \Phi_t(\mathbf{x})$ is a Poisson transformation. In our notation, a Poisson transformation is one that preserves the Poisson bracket; a set of coordinates $\mathbf{y} = F(\mathbf{x})$ such that $\{y_i, y_j\} = \{x_i, x_j\}$ for all i, j. Thus a Poisson integrator is an integrator that preserves the Poisson structure.

In the case of canonically conjugate coordinates q_i p_i with $\{q_i, p_i\} = 1$, $\{q_i, p_j\} = 0$ for $i \neq j$ and $\{q_i, q_j\} = \{p_i, p_j\} = 0$ for all i, j, a Poisson integrator called a *symplectic integrator* often exists in the form of a *splitting integrator* [**HLW06**]. If the Hamiltonian in question is of the form $H = T(p) + V(q)$, one can generate a symplectic integrator $\Phi_t = \Phi_t^T \circ \Phi_t^V$, where Φ_t^T is the flow generated by T and Φ_t^V is the flow generated by V. This is the *symplectic Euler method*. One can design more sophisticated and accurate symplectic integrators by composing smaller timesteps of Φ_τ^T and Φ_τ^V in particular combinations, including the *symplectic Runge-Kutta method*. Recently, new methods have been developed to construct symplectic integrators for general Hamiltonians by introducing an "extended phase space" that essentially binds two copies of the phase space together [**Tao16**].

For a noncanonical system, Poisson integrators are more difficult to construct. For a large class of Poisson systems, an explicit integrator can be developed [**CS91, McL93**]. We now summarise the method described by McLachlan [**McL93**]. Define a Poisson bracket on the phase space with coordinates $\mathbf{x} = (x_1, x_2, ..., x_N)$ with structure matrix linear in the coordinates $J_{i,j} = \sum_{k=1}^N c_{i,j}^k x_k$ for structure constants $c_{i,j}^k$. Then let

$$\Sigma = \{\sigma \subset \{1, 2, ..., N\} \mid J_{i,j} = 0 \; \forall \; i, j \in \sigma\} \tag{3.3.1}$$

ie, the collection of sets of commuting coordinates (that is, $\{x_i, x_j\} = 0$ for all $i, j \in \sigma$ for some $\sigma \in \Sigma$).

Consider a Hamiltonian $H(\sigma)$ that only depends on some set of variables x_i for $i \in \sigma$ for some $\sigma \in \Sigma$. Then the dynamics of the Poisson system with Hamiltonian $H(\sigma)$ are linear, with constant coefficients. This is because for any $i \in \sigma$, x_i is constant under the flow of $H(\sigma)$ as $\{x_i, H(\sigma)\} = 0$ because $H(\sigma)$ only depends on coordinates x_j for which $\{x_i, x_j\}$. Thus $\nabla H(\sigma)$ is constant, so the dynamics of the full system are at most linear as J is linear in the coordinates. We can think of the dynamics of x_i for $i \notin \sigma$ as depending on x_j for $j \in \sigma$ as parameters.

Now, for a system given by the sum of such Hamiltonians, we can construct a Poisson integrator. Say $H = \sum_{i=1}^{n} H_i(\sigma_i)$. Then the flow map

$$\Phi_H^t(\mathbf{x}_0) = \Phi_{H_1}^t(\mathbf{x}_0) \circ \Phi_{H_2}(t)^t(\mathbf{x}_0) \circ \Phi_{H_3}^t(\mathbf{x}_0) \circ ... \circ \Phi_{H_n}^t(\mathbf{x}_0) \tag{3.3.2}$$

where $\Phi_{H_i}^t(\mathbf{x}_0)$ is the flow map for the dynamics of H_i is a first order Poisson integrator for the dynamics of H. However, as we know the dynamics of H_i are linear, we can write this explicitly as

$$\Phi_H^t(\mathbf{x}_0) = \exp(tJD^2H_1)\exp(tJD^2H_2)\exp(tJD^2H_3)...\exp(tJD^2H_n)\mathbf{x}_0. \tag{3.3.3}$$

One can improve this and generate higher order methods by combining the integrators in other configurations [**BGS93**].

In the case of the sine-truncated Euler equations, such a Poisson integrator exists, by the same mechanism that allows the class decomposition in the linearised system. This was developed in [**McL93**] for the isotropic case $\kappa_y/\kappa_y = 1$ and $2N+1$ prime. We here present the generalisation to general $\kappa_x, \kappa_y \in \mathbb{R}^+$ and $N \in \mathbb{N}$. As we have seen in Section 3.2.4, there is qualitatively different nonlinear behaviour for cases where $2N + 1$ is nonprime. Thus it is useful to be able to apply this Poisson integrator for all truncation values N.

For a fixed $\mathbf{j} \in \mathcal{D}_N$, $\{\omega_{\mathbf{j}}, \omega_{\widehat{k}\mathbf{j}}\} = 0$ for any $k \in \mathbb{Z}$. Thus define

$$\sigma_{\mathbf{j}} := \{\widehat{n\mathbf{j}} \mid n \in \mathbb{Z}\}. \tag{3.3.4}$$

Choose any subset $K \subset \mathcal{D}_N$ such that

$$\bigcup_{\mathbf{k}\in K} \sigma_{\mathbf{k}} = \mathcal{D}_N. \tag{3.3.5}$$

Then define

$$\mu(\mathbf{j}) := \text{number of } \mathbf{k} \in K \text{ such that } \mathbf{j} = \widehat{n\mathbf{k}} \text{ for some } n \in \mathbb{Z}. \tag{3.3.6}$$

If $2N + 1$ is prime, there is a choice of K such that $\mu(\mathbf{j}) = 1$ for all $\mathbf{j} \neq \mathbf{0}$, given in [**McL93**] as $K = \{(0, 1)\} \cup \{(1, m) \mid -N \leq m \leq N\}$. Otherwise, for $\mathbf{j}$ such that $\gcd(2N + 1, j_x, j_y) > 1$, $\mu(\mathbf{j}) > 1$. In this case, we can generate K algorithmically and calculate $\mu(\mathbf{j})$ directly.

Now split the Hamiltonian (3.1.12) as

$$H = \sum_{\mathbf{k}\in K} H_{\mathbf{k}}, \quad H_{\mathbf{k}} = \frac{1}{2} \sum_{n\neq 0} \frac{1}{\mu(\widehat{n\mathbf{k}})} \frac{\omega_{+\widehat{n\mathbf{k}}}\omega_{-\widehat{n\mathbf{k}}}}{|\widehat{n\mathbf{k}}|^2_{\boldsymbol{\kappa}}}. \tag{3.3.7}$$

Now this satisfies our requirements; each $H_{\mathbf{k}}$ only depends on a set of commuting coordinates, and so generates linear dynamics. Note that the sets $\sigma_{\mathbf{k}}$ are not necessarily disjoint, so the same mode $\omega_{\mathbf{j}}$ may appear in multiple Hamiltonians $H_{\mathbf{k}}$. This does not happen in the case $2N + 1$ prime. The integrator still operates correctly with this overlap between the modes.

Now the Poisson integrator for this system is

$$\Phi_H^t(\mathbf{x}_0) = \left(\prod_{\mathbf{k} \in K} \exp(tJD^2 H_{\mathbf{k}}) \right) \mathbf{x}_0. \tag{3.3.8}$$

This is explicit. Furthermore we can calculate $\exp(tJD^2 H_{\mathbf{k}})$ efficiently by exploiting the structure of the problem (the same structure that allows the class decomposition in the linearised problem).

Under the dynamics of $H_{\mathbf{k}}$, the evolution of a mode $\omega_{\mathbf{j}}$ is

$$\dot{\omega}_{\mathbf{j}} = \sum_n \left(\kappa_x \kappa_y \frac{\sin(\varepsilon n \mathbf{j} \times \mathbf{k})}{\varepsilon} \frac{1}{\mu(\widehat{n\mathbf{k}}) |\widehat{n\mathbf{k}}|^2} \omega_{\widehat{n\mathbf{k}}} \right) \omega_{\widehat{\mathbf{j}-n\mathbf{k}}} \tag{3.3.9}$$

where the summation is over all unique values of $\widehat{n\mathbf{k}} \in \mathcal{D}_N$, $n \neq 0$. If $\mathbf{j} = \widehat{n\mathbf{k}}$ for some $n \in \mathbb{Z}$, the term in brackets above is zero, and so as expected the modes in $\sigma_{\mathbf{k}}$ are constant under the dynamics of $H_{\mathbf{k}}$. Thus the term in brackets is constant, and so this system has linear dynamics, with the $\omega_{\widehat{n\mathbf{k}}}$ entering as parameters only.

Note that the dynamics of $\omega_{\mathbf{j}}$ depend only on the values of $\omega_{\widehat{n\mathbf{k}}}$ (which are constant) and $\omega_{\widehat{\mathbf{j}+n\mathbf{k}}}$. Thus the dynamics generated by $H_{\mathbf{k}}$ can be split into subsystems of modes $\omega_{\widehat{\mathbf{j}+n\mathbf{k}}}$. These subsystems are analogous to those in Section 3.2.1, illustrated in Figure 3.3. Let $\omega_m := \omega_{\widehat{\mathbf{j}+m\mathbf{p}}}$, per (2.4.10). Then

$$\dot{\omega}_m = \sum_n a_n \omega_{m-n} \tag{3.3.10}$$

where

$$a_n = \kappa_x \kappa_y \frac{\sin(\varepsilon n \mathbf{j} \times \mathbf{k})}{\varepsilon} \frac{1}{\mu(\widehat{n\mathbf{k}}) |\widehat{n\mathbf{k}}|^2} \omega_{\widehat{n\mathbf{k}}} \tag{3.3.11}$$

which is constant.

If $\omega = (\omega_0, \omega_1, \omega_2, ...)$, the dynamics are given by

$$\dot{\omega} = M\omega, \quad M = \begin{pmatrix} a_0 & a_{-1} & a_{-2} & ... \\ a_1 & a_0 & a_{-1} & ... \\ a_2 & a_1 & a_0 & ... \\ \vdots & \vdots & \vdots & \ddots \end{pmatrix}. \tag{3.3.12}$$

Now M is circulant (as in Section 3.2.2), and so can be diagonalised by a Discrete Fourier transform. This allows us to efficiently compute the exponential of M and thus the dynamics of $H_{\mathbf{k}}$. Multiplying these together for all $\mathbf{k} \in K$ gives the full Poisson integrator (3.3.8).

The existence of this integrator is very useful. In this thesis, it will be used to generate numerical results in Section 6.3 to corroborate and analyse our stability

results. More generally, an efficient integrator allows for a deeper numerical study of the Euler equations without high computation cost.

Chapter 4

Stability Theory in the Three-Dimensional Euler Equations

In Chapter 2, we discussed shear flows, stability, and Poisson structure in the Euler equations on a periodic two-dimensional domain. A natural extension is to consider a domain with three spatial dimensions and study shear flows there. The dynamics of the Euler equations on a three-dimensional domain are qualitatively different and more complex than the dynamics on a two-dimensional domain, and it is correspondingly more challenging to complete stability analysis.

The examples of Section 1.3.1 guide our study of shear flows in the three-dimensional domain. Figures 1.4 and 1.6 show that for particular domain sizes, the spectrum of a linearised shear flow in three dimensions is the same as the spectrum of a linearised shear flow in two dimensions. This observation leads to our key result: the linearised three-dimensional Euler equations split into subsystems which generically have the same spectrum as a corresponding subsystem of the linearised two-dimensional Euler equations. Thus the full spectrum of the three-dimensional system can be described in terms of the spectrum of classes of the linearised two-dimensional system. This allows us to identify linearly stable and unstable shear flows on the three-dimensional domain. There is also a dense set of parameters for which there exist subsystems with nontrivial nilpotent part; such cases lead to linear instabilities which are not caused by the instability of a related two-dimensional class.

We begin this chapter with a broad overview of the Euler equations in three-dimensional domain and the associated considerations. We then derive a formulation of the dynamics on a periodic domain in terms of the vorticity Fourier modes and linearise around a family of shear flows. The linearised system has a decomposition analogous to the two-dimensional problem, which can be significantly simplified. We then show that a subset of the shear flows are linearly stable, and another subset are linearly unstable. We also discuss the nonnormality of the linearised dynamics, and the connection to transition to turbulence.

4.1. The Three-Dimensional Euler Equations

The Euler equations on a three-dimensional domain present a large number of unanswered questions, despite centuries of research [**Gib08**]. Many results known

for the two-dimensional domain either do not hold or are open problems in the three-dimensional domain. For instance, the question of *finite-time blowup* is a popular area of research in dynamics. In both the Euler equations and the Navier-Stokes equations, it is in general unknown whether a smooth initial condition can lead to a singularity in finite time. This forms part of the Clay Millennium Prize question on the Navier Stokes Problem [**Fef06**]. In the Euler equations in two dimensions, assuming an initial condition with smooth, finite kinetic energy it is known that solutions do not blow up [**Bar72**]. For a three-dimensional domain the same question is an open problem [**Con07**]. With this in mind we study the linearisation and stability of shear flows and develop results analogous to those studied in Chapter 2.

We begin by deriving a formulation of the Euler equations in terms of the vorticity Fourier coefficients only. This relies on the divergence-free property which restricts the possible vorticities that can occur. We then discuss the helicity, a constant of motion in the three-dimensional Euler equations and its relationship to the enstrophy in the two-dimensional domain problem.

We then introduce three-dimensional shear flows, which are complicated by the fact that vorticity is vector-valued rather than scalar. Linearising around these shear flows gives a class decomposition, though the governing differential equations are significantly more complex than those for the corresponding two-dimensional equations.

4.1.1. Vorticity Formulation of the Three-Dimensional Euler Equations. As per the two-dimensional Euler equations in Section 2.2.3, the three-dimensional Euler equations on a general domain $\mathcal{D} \subset \mathbb{R}^3$ can be formulated in terms of the *velocity* vector field $V : \mathcal{D}\times\mathbb{R} \to \mathbb{R}^3$ and the *vorticity* $\Omega : \mathcal{D}\times\mathbb{R} \to \mathbb{R}^3$. The velocity field $V(\mathbf{x}; t)$ describes the instantaneous velocity of a fluid element at position $\mathbf{x} = (x, y, z) \in \mathcal{D}$ at time t, and the vorticity $\Omega(\mathbf{x}; t)$ measures the local rotational motion of a fluid element at $\mathbf{x} = (x, y, z) \in \mathcal{D}$. Note that unlike in the two-dimensional case, Ω is vector-valued. One can think of each component of Ω corresponding to the rotation of the fluid around the axis parallel to the corresponding coordinate. One can consider the two-dimensional vorticity as a special case where the z-dimension has trivial dynamics; then $V = (v_x, v_y, 0)$, and the vorticity $\Omega = (0, 0, \Omega_z)$ can be reduced to the scalar vorticity Ω_z.

The three-dimensional Euler equations for an incompressible, inviscid flow are given in terms of the vorticity and velocity by

$$\Omega = \nabla \times V \tag{4.1.1}$$

$$\frac{\partial \Omega}{\partial t} = (\Omega \cdot \nabla)V - (V \cdot \nabla)\Omega. \tag{4.1.2}$$

See e.g. Constantin [**Con07**] for a discussion of these equations.

We also have the *divergence free conditions*

$$\nabla \cdot V = 0, \quad \nabla \cdot \Omega = 0. \tag{4.1.3}$$

For the velocity field, this is a consequence of the incompressibility; for the vorticity, it follows from the formula $\Omega = \nabla \times V$ and the fact that the divergence of the curl of any vector must be zero.

We will consider these equations on the periodic domain

$$\mathcal{D} = \left[-\frac{\pi}{\kappa_x}, \frac{\pi}{\kappa_x}\right) \times \left[-\frac{\pi}{\kappa_y}, \frac{\pi}{\kappa_y}\right) \times \left[-\frac{\pi}{\kappa_z}, \frac{\pi}{\kappa_z}\right) \tag{4.1.4}$$

for some $\kappa_x, \kappa_y, \kappa_z \in \mathbb{R}^+$.

Write $\boldsymbol{\kappa} = (\kappa_x, \kappa_y, \kappa_z)$, and introduce the *anisotropy matrix*

$$K := \begin{pmatrix} \kappa_x & 0 & 0 \\ 0 & \kappa_y & 0 \\ 0 & 0 & \kappa_z \end{pmatrix}. \tag{4.1.5}$$

This matrix is diagonal, positive definite, and invertible. For the isotropic domain $\kappa_x = \kappa_y = \kappa_z = 1$, $K = \mathbb{I}_3$. We rescale our domain and normalise $|\boldsymbol{\kappa}| = 1$ so $\kappa_x^2 + \kappa_y^2 + \kappa_z^2 = 1$.

Define the weighted inner product

$$\langle \mathbf{a}, \mathbf{b} \rangle := (K\mathbf{a})^\mathsf{T}(K\mathbf{b}). \tag{4.1.6}$$

For the domain size $K = \mathbb{I}$ this reduces to the usual Euclidean dot product. The induced norm is

$$|\mathbf{a}|_{\boldsymbol{\kappa}} := \sqrt{\langle \mathbf{a}, \mathbf{a} \rangle} = \sqrt{\mathbf{a}^\mathsf{T} K^2 \mathbf{a}}. \tag{4.1.7}$$

As K is positive definite, this norm is positive for all $\mathbf{a} \neq \mathbf{0}$. Note the identity $|K\mathbf{a}| = |\mathbf{a}|_{\boldsymbol{\kappa}}$ relates this weighted norm to the usual Euclidean norm.

Define the *cross product matrix* of a vector $\mathbf{a}$

$$\widehat{\mathbf{a}} := \begin{pmatrix} 0 & -a_z & a_y \\ a_z & 0 & -a_x \\ -a_y & a_x & 0 \end{pmatrix} \tag{4.1.8}$$

where $\mathbf{a} = (a_x, a_y, a_z)$. Then for any $\mathbf{b} \in \mathbb{R}^3$, $\widehat{\mathbf{a}}\mathbf{b} = \mathbf{a} \times \mathbf{b}$. Note that $\widehat{\mathbf{a}}$ is antisymmetric. This is not to be confused with the notation use for the wrapping operation in Chapter 3; as there is no such wrapping for the three-dimensional problem, there is no overlap in the use of the notation.

For any invertible three by three matrix M, by the properties of the cross product it can be shown that $M\mathbf{a} \times M\mathbf{b} = \det(M) M^{-\mathsf{T}}(\mathbf{a} \times \mathbf{b})$. Thus we have the identities $\widehat{M\mathbf{a}} = \det(M) M^{-\mathsf{T}} \widehat{\mathbf{a}} M^{-1}$. In the special case of a rotation matrix $R \in SO(3)$, $\widehat{R\mathbf{a}} = R\widehat{\mathbf{a}}R^\mathsf{T}$.

Per the two-dimensional equations in Section 2.2.3, we expand V and Ω in terms of Fourier expansions. Defining the Fourier coefficients with wavenumber $\mathbf{j} \in \mathbb{Z}^3$ by

$$\mathbf{v}_\mathbf{j} := \int_\mathcal{D} V(\mathbf{x}, t) e^{-i\langle \mathbf{j}, K^{-1}\mathbf{x}\rangle} d\mathbf{x}, \tag{4.1.9}$$

$$\boldsymbol{\omega}_\mathbf{j} := \int_\mathcal{D} \Omega(\mathbf{x}, t) e^{-i\langle \mathbf{j}, K^{-1}\mathbf{x}\rangle} d\mathbf{x} \tag{4.1.10}$$

where the spatial variable $\mathbf{x} \in \mathcal{D}$. Note that $\mathbf{v}_\mathbf{j}(t), \boldsymbol{\omega}_\mathbf{j}(t) \in \mathbb{C}^3$. Then

$$\begin{aligned} V &= \sum_{\mathbf{j}\in\mathbb{Z}^3} \mathbf{v}_\mathbf{j}(t) e^{i\langle \mathbf{j}, K^{-1}\mathbf{x}\rangle}, \\ \Omega &= \sum_{\mathbf{j}\in\mathbb{Z}^3} \boldsymbol{\omega}_\mathbf{j}(t) e^{i\langle \mathbf{j}, K^{-1}\mathbf{x}\rangle}. \end{aligned} \tag{4.1.11}$$

As V and Ω are real, $\mathbf{v}_{-\mathbf{j}} = \bar{\mathbf{v}}_\mathbf{j}$ and $\boldsymbol{\omega}_{-\mathbf{j}} = \bar{\boldsymbol{\omega}}_\mathbf{j}$.

The divergence free conditions imply

$$\begin{aligned} \langle \mathbf{j}, K^{-1}\mathbf{v}_\mathbf{j}\rangle &= \mathbf{j}^\mathsf{T} K \mathbf{v}_\mathbf{j} = 0, \\ \langle \mathbf{j}, K^{-1}\boldsymbol{\omega}_\mathbf{j}\rangle &= \mathbf{j}^\mathsf{T} K \boldsymbol{\omega}_\mathbf{j} = 0 \end{aligned} \tag{4.1.12}$$

for all $\mathbf{j}$. This implies that all dynamics of the Euler equations occur on the *divergence-free subspace*

$$\{\boldsymbol{\omega}_\mathbf{j} \mid \langle \mathbf{j}, K^{-1}\boldsymbol{\omega}_\mathbf{j}\rangle = 0\}. \tag{4.1.13}$$

We wish to write the system as a set of differential equations for the dynamics of the vorticity modes $\boldsymbol{\omega}_\mathbf{j}$ only. The condition $\Omega = \nabla \times V$ implies

$$\boldsymbol{\omega}_\mathbf{j} = i(K\mathbf{j}) \times \mathbf{v}_\mathbf{j}. \tag{4.1.14}$$

Combining (4.1.12) and (4.1.14) implies

$$(K\mathbf{j}) \times \boldsymbol{\omega}_\mathbf{j} = -i|\mathbf{j}|_{\boldsymbol{\kappa}}^2 \mathbf{v}_\mathbf{j}. \tag{4.1.15}$$

Thus for all $\mathbf{j} \neq \mathbf{0}$, we can take the divergence-free inverse to the curl

$$\mathbf{v}_\mathbf{j} = i\frac{(K\mathbf{j}) \times \boldsymbol{\omega}_\mathbf{j}}{|\mathbf{j}|_{\boldsymbol{\kappa}}^2}. \tag{4.1.16}$$

This allows us to invert the relationship (4.1.1) and formally write $V = (\nabla\times)^{-1}\Omega$ on the divergence-free subspace.

Now

$$\begin{aligned} (\Omega \cdot \nabla)V &= \sum_{\mathbf{j},\mathbf{k}\in\mathbb{Z}^3} i\mathbf{j}^\mathsf{T} K \boldsymbol{\omega}_\mathbf{k} \mathbf{v}_\mathbf{j} e^{i(\mathbf{j}+\mathbf{k})^\mathsf{T} K\mathbf{x}} \\ &= -\sum_{\mathbf{j},\mathbf{k}\in\mathbb{Z}^3} \mathbf{j}^\mathsf{T} K \boldsymbol{\omega}_\mathbf{j} \frac{(K\mathbf{j}) \times \boldsymbol{\omega}_\mathbf{j}}{|\mathbf{j}|_{\boldsymbol{\kappa}}^2} e^{i(\mathbf{j}+\mathbf{k})^\mathsf{T} K\mathbf{x}} \end{aligned} \tag{4.1.17}$$

by reordering the summation. Similarly

$$\begin{aligned}(V\cdot\nabla)\Omega &= \sum_{\mathbf{j},\mathbf{k}\in\mathbb{Z}^3} i\mathbf{j}^{\mathsf{T}}K\mathbf{v}_{\mathbf{k}}\boldsymbol{\omega}_{\mathbf{j}}e^{i(\mathbf{j}+\mathbf{k})^{\mathsf{T}}K\mathbf{x}}\\ &= -\sum_{\mathbf{j},\mathbf{k}\in\mathbb{Z}^3}\frac{1}{|\mathbf{k}|_{\boldsymbol{\kappa}}^2}\mathbf{j}^{\mathsf{T}}K(K\mathbf{k}\times\boldsymbol{\omega}_{\mathbf{j}})\boldsymbol{\omega}_{\mathbf{j}}e^{i(\mathbf{j}+\mathbf{k})^{\mathsf{T}}K\mathbf{x}}.\end{aligned} \tag{4.1.18}$$

Rewriting the partial differential equation $\Omega_t = (\Omega\cdot\nabla)V - (V\cdot\nabla)\Omega$ in Fourier space now leads to the ordinary differential equations

$$\begin{aligned}\dot{\boldsymbol{\omega}}_{\mathbf{j}} &= \sum_{\mathbf{k}+\mathbf{l}=\mathbf{j}}\frac{1}{|\mathbf{k}|_{\boldsymbol{\kappa}}^2}\left(\mathbf{l}^{\mathsf{T}}K((K\mathbf{k})\times\boldsymbol{\omega}_{\mathbf{k}})\boldsymbol{\omega}_{\mathbf{l}} - \mathbf{k}^{\mathsf{T}}K\boldsymbol{\omega}_{\mathbf{l}}(K\mathbf{k})\times\boldsymbol{\omega}_{\mathbf{k}}\right)\\ &= \sum_{\mathbf{k}\in\mathbb{Z}^3\setminus\mathbf{0}}\left(\boldsymbol{\omega}_{\mathbf{j}+\mathbf{k}}[(K\mathbf{k})\times(K\mathbf{j})]^{\mathsf{T}} - \langle\mathbf{k},K^{-1}\boldsymbol{\omega}_{\mathbf{j}+\mathbf{k}}\rangle\widehat{K\mathbf{k}}\right)\frac{\boldsymbol{\omega}_{-\mathbf{k}}}{|\mathbf{k}|_{\boldsymbol{\kappa}}^2}\end{aligned} \tag{4.1.19}$$

This is a differential equation for the vorticity modes that does not depend on velocity. Note that $\boldsymbol{\omega}_{\mathbf{0}} = 0$ by (4.1.14), and therefore can be omitted in the summation so there is no singularity in (4.1.19).

The dynamics governed by the differential equations (4.1.19) reduce to the two-dimensional equivalent (2.2.26) under the assumption that $\boldsymbol{\omega}_{\mathbf{a}} = (0,0,\boldsymbol{\omega}_{\mathbf{a}})$ and $\mathbf{a} = (a_1,a_2,0)$ for all relevant modes $\boldsymbol{\omega}_{\mathbf{a}}$, and vectors $\mathbf{a}$.

Define

$$A(\mathbf{j},\mathbf{k}) := \left(\boldsymbol{\omega}_{\mathbf{j}+\mathbf{k}}[(K\mathbf{k})\times(K\mathbf{j})]^{\mathsf{T}} - \langle\mathbf{k},K^{-1}\boldsymbol{\omega}_{\mathbf{j}+\mathbf{k}}\rangle\widehat{K\mathbf{k}}\right) \tag{4.1.20}$$

so

$$\dot{\boldsymbol{\omega}}_{\mathbf{j}} = \sum_{\mathbf{k}} A(\mathbf{j},\mathbf{k})\frac{\boldsymbol{\omega}_{-\mathbf{k}}}{|\mathbf{k}|_{\boldsymbol{\kappa}}^2}. \tag{4.1.21}$$

This simplifies for the isotropic domain $K = \mathbb{I}_3$ to

$$\dot{\boldsymbol{\omega}}_{\mathbf{j}} = \sum_{\mathbf{k}\in\mathbb{Z}^3}\left(\boldsymbol{\omega}_{\mathbf{j}+\mathbf{k}}\,(\mathbf{k}\times\mathbf{j})^{\mathsf{T}} - (\mathbf{k}\cdot\boldsymbol{\omega}_{\mathbf{j}+\mathbf{k}})\widehat{\mathbf{k}}\right)\frac{\boldsymbol{\omega}_{-\mathbf{k}}}{|\mathbf{k}|^2}. \tag{4.1.22}$$

4.1.2. Helicity. The three-dimensional Euler equations (4.1.1) and (4.1.2) have a constant of motion called the *helicity* [**Gib08**]. The helicity is given by

$$\begin{aligned}C &= \int_{\mathcal{D}} V\cdot(\nabla\times V)\,\mathrm{d}x\\ &= \int_{\mathcal{D}} V\cdot\Omega\,\mathrm{d}x\end{aligned} \tag{4.1.23}$$

By substituting the expansions (4.1.11) and the relation (4.1.16),

$$\begin{aligned} C &= i \int \left(\sum_{\mathbf{j}\neq\mathbf{0}} \frac{(K\mathbf{j}) \times \boldsymbol{\omega}_{\mathbf{j}}}{|\mathbf{j}|^2_{\boldsymbol{\kappa}}} e^{-i\mathbf{j}\cdot\mathbf{x}} \right) \cdot \left(\sum_{\mathbf{k}} \boldsymbol{\omega}_{\mathbf{k}} e^{-i\mathbf{k}\cdot\mathbf{x}} \right) \mathrm{d}x \\ &= i \int \left(\sum_{\mathbf{j}\neq\mathbf{0},\mathbf{k}} \frac{(K\mathbf{j}) \times \boldsymbol{\omega}_{\mathbf{j}}}{|\mathbf{j}|^2_{\boldsymbol{\kappa}}} \cdot \boldsymbol{\omega}_{\mathbf{k}} e^{-i(\mathbf{j}+\mathbf{k})\mathbf{x}} \right) \cdot \mathrm{d}x \\ &= i \frac{(2\pi)^3}{\kappa_x\kappa_y\kappa_z} \sum_{\mathbf{j}\neq\mathbf{0}} \frac{(K\mathbf{j}) \times \boldsymbol{\omega}_{\mathbf{j}}}{|\mathbf{j}|^2_{\boldsymbol{\kappa}}} \cdot \boldsymbol{\omega}_{-\mathbf{j}} \end{aligned} \tag{4.1.24}$$

This can be rewritten as a quadratic form

$$C = i \frac{(2\pi)^3}{\kappa_x\kappa_y\kappa_z} \sum_{\mathbf{j}\neq\mathbf{0}} \boldsymbol{\omega}_{-\mathbf{j}}^{\mathsf{T}} Q(\mathbf{j}) \boldsymbol{\omega}_{\mathbf{j}} \tag{4.1.25}$$

where

$$Q(\mathbf{j}) = \frac{1}{|\mathbf{j}|^2_{\boldsymbol{\kappa}}} \widehat{K\mathbf{j}}. \tag{4.1.26}$$

It should be noted that the helicity is always zero in the two-dimensional domain and does not provide any insight into the dynamics there. Conversely the three-dimensional equations do not conserve the generalised enstrophy constants discussed in Section 2.3.2. As there are infinitely many generalised enstrophy constants, one can infer that the two-dimensional problem is more geometrically constrained, reflecting a fundamental difference between the two cases [**YM16**]. Dynamical observations of two-dimensional flow are generically less turbulent, which accounts for observable coherent structures such as typhoons, jet streams and polar vortices.

A class of flows called *epi-two-dimensional* flows was introduced in Yoshida and Morrison [**YM16**] as a sort of intermediate state between two- and three-dimensional flows. These flows are defined on a three-dimensional domain and have zero helicity. They also have constants of motion analogous to the generalised enstrophies. This is very recent work and may be a fruitful model for future study of the Euler equations and turbulence, with many constants of motion but more complexity than two-dimensional flow.

4.1.3. Shear Flows. In the three-dimensional Euler equations with a periodic domain there is a family of shear flow steady states

$$\begin{aligned} V^* &= \boldsymbol{\alpha} f(\langle \mathbf{p}, K\mathbf{x} \rangle), \\ \Omega^* &= (K\mathbf{p}) \times \boldsymbol{\alpha} f'(\langle \mathbf{p}, K\mathbf{x} \rangle) \end{aligned} \tag{4.1.27}$$

for a 2π-periodic function $f : \mathbb{R} \to \mathbb{R}$ and a vector $\boldsymbol{\alpha} \in \mathbb{R}^3$ satisfying the divergence free condition $\langle \mathbf{p}, K^{-1}\boldsymbol{\alpha} \rangle = 0$. Then $V = V^*$, $\Omega = \Omega^*$ satisfies (4.1.1)

and is a steady state for (4.1.2) by a similar calculation to the analogous two-dimensional shear flows in Section 2.4.1.

Now consider (4.1.27) in the particular case

$$f(x) = \alpha \sin(x) + \beta \cos(x), \quad \boldsymbol{\alpha} = \frac{2\boldsymbol{\Gamma} \times (K\mathbf{p})}{|\mathbf{p}|_{\boldsymbol{\kappa}}^2}. \tag{4.1.28}$$

By the same reasoning as in Section 2.4.1, we can simplify this to consider $f(x) = \sin(x)$ by redefining our coordinate frame and taking a time rescaling. The divergence-free condition implies that $(K\mathbf{p}) \times \boldsymbol{\alpha} = 2\boldsymbol{\Gamma}$. Then the steady state is

$$\begin{aligned} V^* &= \frac{2\boldsymbol{\Gamma} \times (K\mathbf{p})}{|\mathbf{p}|_{\boldsymbol{\kappa}}^2} \sin(\langle \mathbf{p}, K^{-1}\mathbf{x} \rangle), \\ \Omega^* &= 2\boldsymbol{\Gamma} \cos(\langle \mathbf{p}, K^{-1}\mathbf{x} \rangle). \end{aligned} \tag{4.1.29}$$

In terms of vorticity Fourier coefficients, (4.1.29) is represented by the equilibrium

$$\boldsymbol{\omega}_{\mathbf{k}}^* = \begin{cases} \boldsymbol{\Gamma} \text{ if } \mathbf{k} = \pm\mathbf{p}; \\ \mathbf{0} \text{ otherwise.} \end{cases} \tag{4.1.30}$$

For the divergence-free condition on $\boldsymbol{\omega}_{\mathbf{p}}$ to be satisfied, the parameter $\boldsymbol{\Gamma}$ must satisfy $\langle \mathbf{p}, K^{-1}\boldsymbol{\Gamma} \rangle = 0$.

4.1.4. Linearisation. We now linearise the vector field (4.1.21) around the steady state (4.1.30) to study linear stability. We first calculate the Jacobian:

$$\frac{\partial}{\partial \boldsymbol{\omega}_{\mathbf{k}}} \dot{\boldsymbol{\omega}}_{\mathbf{j}} = \frac{1}{|\mathbf{k}|_{\boldsymbol{\kappa}}^2} A(\mathbf{j}, -\mathbf{k}) + \frac{\partial}{\partial \boldsymbol{\omega}_{\mathbf{k}}} (A(\mathbf{j}, \mathbf{k} - \mathbf{j})) \frac{\boldsymbol{\omega}_{\mathbf{j}-\mathbf{k}}}{|\mathbf{j} - \mathbf{k}|_{\boldsymbol{\kappa}}^2}. \tag{4.1.31}$$

where

$$\frac{\partial}{\partial \boldsymbol{\omega}_{\mathbf{k}}} \dot{\boldsymbol{\omega}}_{\mathbf{j}} = \begin{pmatrix} \frac{\partial}{\partial (\boldsymbol{\omega}_{\mathbf{k}})_x} (\dot{\boldsymbol{\omega}}_{\mathbf{j}})_x & \frac{\partial}{\partial (\boldsymbol{\omega}_{\mathbf{k}})_x} (\dot{\boldsymbol{\omega}}_{\mathbf{j}})_y & \frac{\partial}{\partial (\boldsymbol{\omega}_{\mathbf{k}})_x} (\dot{\boldsymbol{\omega}}_{\mathbf{j}})_z \\ \frac{\partial}{\partial (\boldsymbol{\omega}_{\mathbf{k}})_y} (\dot{\boldsymbol{\omega}}_{\mathbf{j}})_x & \frac{\partial}{\partial (\boldsymbol{\omega}_{\mathbf{k}})_y} (\dot{\boldsymbol{\omega}}_{\mathbf{j}})_y & \frac{\partial}{\partial (\boldsymbol{\omega}_{\mathbf{k}})_y} (\dot{\boldsymbol{\omega}}_{\mathbf{j}})_z \\ \frac{\partial}{\partial (\boldsymbol{\omega}_{\mathbf{k}})_z} (\dot{\boldsymbol{\omega}}_{\mathbf{j}})_x & \frac{\partial}{\partial (\boldsymbol{\omega}_{\mathbf{k}})_z} (\dot{\boldsymbol{\omega}}_{\mathbf{j}})_y & \frac{\partial}{\partial (\boldsymbol{\omega}_{\mathbf{k}})_z} (\dot{\boldsymbol{\omega}}_{\mathbf{j}})_z \end{pmatrix} \tag{4.1.32}$$

is the $(\mathbf{j}, \mathbf{k})$ three-by-three block of the Jacobian.

Evaluating this at the equilibrium,

$$\frac{\partial}{\partial \boldsymbol{\omega}_{\mathbf{k}}} \dot{\boldsymbol{\omega}}_{\mathbf{j}}|_{\Omega^*} = \begin{cases} \frac{1}{|\mathbf{j}-\mathbf{p}|_{\boldsymbol{\kappa}}^2} A(\mathbf{j}, \mathbf{p} - \mathbf{j})|_{\Omega^*} + \frac{1}{|\mathbf{p}|_{\boldsymbol{\kappa}}^2} \frac{\partial}{\partial \boldsymbol{\omega}_{\mathbf{j}-\mathbf{p}}} (A(\mathbf{j}, -\mathbf{p})\boldsymbol{\Gamma}) & \text{if } \mathbf{k} = \mathbf{j} - \mathbf{p}; \\ \frac{1}{|\mathbf{j}+\mathbf{p}|_{\boldsymbol{\kappa}}^2} A(\mathbf{j}, -\mathbf{p} - \mathbf{j})|_{\Omega^*} + \frac{1}{|\mathbf{p}|_{\boldsymbol{\kappa}}^2} \frac{\partial}{\partial \boldsymbol{\omega}_{\mathbf{j}+\mathbf{p}}} (A(\mathbf{j}, \mathbf{p})\boldsymbol{\Gamma}) & \text{if } \mathbf{k} = \mathbf{j} + \mathbf{p}; \\ 0 \text{ otherwise.} \end{cases} \tag{4.1.33}$$

Then the linearised system about Ω^* is

$$\dot{\mathbf{z}}_{\mathbf{j}} = \chi_1(\mathbf{j} + \mathbf{p})\mathbf{z}_{\mathbf{j}+\mathbf{p}} + \chi_2(\mathbf{j} - \mathbf{p})\mathbf{z}_{\mathbf{j}-\mathbf{p}} \tag{4.1.34}$$

where $\mathbf{z_j} = \boldsymbol{\omega_j} - \boldsymbol{\omega_j^*}$ and

$$\begin{aligned}\chi_1(\mathbf{j}) &= \frac{1}{|\mathbf{j}|^2_{\boldsymbol{\kappa}}} A(\mathbf{j}-\mathbf{p},-\mathbf{j})|_{\Omega^*} + \frac{1}{|\mathbf{p}|^2_{\boldsymbol{\kappa}}}\frac{\partial}{\partial \boldsymbol{\omega_j}}(A(\mathbf{j}-\mathbf{p},\mathbf{p})\boldsymbol{\Gamma}),\\ \chi_2(\mathbf{j}) &= \frac{1}{|\mathbf{j}|^2_{\boldsymbol{\kappa}}} A(\mathbf{j}+\mathbf{p},-\mathbf{j})|_{\Omega^*} + \frac{1}{|\mathbf{p}|^2_{\boldsymbol{\kappa}}}\frac{\partial}{\partial \boldsymbol{\omega_j}}(A(\mathbf{j}+\mathbf{p},-\mathbf{p})\boldsymbol{\Gamma}).\end{aligned} \tag{4.1.35}$$

We have written the coefficients in the form above in analogy with the differential equations (2.4.13), where $\rho_{\mathbf{k}}$ appears as a coefficient of $\omega_{\mathbf{k}}$. Unlike the $\rho_{\mathbf{k}}$ coefficients, $\chi_1(\mathbf{j})$ and $\chi_2(\mathbf{j})$ are not the same function.

Now

$$A(\mathbf{j}-\mathbf{p},-\mathbf{j})|_{\Omega^*} = \boldsymbol{\Gamma}[(K\mathbf{j})\times(K\mathbf{p})]^{\mathsf{T}} - \langle \mathbf{j}, K^{-1}\boldsymbol{\Gamma}\rangle \widehat{K\mathbf{j}} \tag{4.1.36}$$

$$A(\mathbf{j}+\mathbf{p},-\mathbf{j})|_{\Omega^*} = -\boldsymbol{\Gamma}[(K\mathbf{j})\times(K\mathbf{p})]^{\mathsf{T}} - \langle \mathbf{j}, K^{-1}\boldsymbol{\Gamma}\rangle \widehat{K\mathbf{j}} \tag{4.1.37}$$

$$\frac{\partial}{\partial \boldsymbol{\omega_j}}(A(\mathbf{j}-\mathbf{p},\mathbf{p})\boldsymbol{\Gamma}) = \boldsymbol{\Gamma}^{\mathsf{T}}\left[(K\mathbf{p})\times(K\mathbf{j})\right]\mathbb{I}_3 - \left[(K\mathbf{p})\times\boldsymbol{\Gamma}\right](K\mathbf{p})^{\mathsf{T}} \tag{4.1.38}$$

$$\frac{\partial}{\partial \boldsymbol{\omega_j}}(A(\mathbf{j}+\mathbf{p},-\mathbf{p})\boldsymbol{\Gamma}) = -\boldsymbol{\Gamma}^{\mathsf{T}}\left[(K\mathbf{p})\times(K\mathbf{j})\right]\mathbb{I}_3 - \left[(K\mathbf{p})\times\boldsymbol{\Gamma}\right](K\mathbf{p})^{\mathsf{T}} \tag{4.1.39}$$

so χ_1, χ_2 can be written as

$$\chi_1(\mathbf{j}) = \chi_a(\mathbf{j}) + \chi_b(\mathbf{j}), \quad \chi_2(\mathbf{j}) = \chi_a(\mathbf{j}) - \chi_b(\mathbf{j}) \tag{4.1.40}$$

where

$$\chi_a(\mathbf{j}) = -\frac{1}{|\mathbf{j}|^2_{\boldsymbol{\kappa}}}\langle \mathbf{j}, K^{-1}\boldsymbol{\Gamma}\rangle \widehat{K\mathbf{j}} - \frac{1}{|\mathbf{p}|^2_{\boldsymbol{\kappa}}}\left[(K\mathbf{p})\times\boldsymbol{\Gamma}\right](K\mathbf{p})^{\mathsf{T}} \tag{4.1.41}$$

and

$$\chi_b(\mathbf{j}) = \frac{1}{|\mathbf{j}|^2_{\boldsymbol{\kappa}}}\boldsymbol{\Gamma}[(K\mathbf{j})\times(K\mathbf{p})]^{\mathsf{T}} + \frac{1}{|\mathbf{p}|^2_{\boldsymbol{\kappa}}}\boldsymbol{\Gamma}^{\mathsf{T}}\left[(K\mathbf{p})\times(K\mathbf{j})\right]\mathbb{I}_3. \tag{4.1.42}$$

The differential equations (4.1.34) can now be written as

$$\begin{aligned}\dot{\mathbf{z}}_{\mathbf{j}} =& (\chi_a(\mathbf{j}+\mathbf{p})\mathbf{z}_{\mathbf{j}+\mathbf{p}} + \chi_a(\mathbf{j}-\mathbf{p})\mathbf{z}_{\mathbf{j}-\mathbf{p}})\\ &+ (\chi_b(\mathbf{j}+\mathbf{p})\mathbf{z}_{\mathbf{j}+\mathbf{p}} - \chi_b(\mathbf{j}-\mathbf{p})\mathbf{z}_{\mathbf{j}-\mathbf{p}}).\end{aligned} \tag{4.1.43}$$

One can think of these equations as having a symmetric part with coefficients χ_a and an antisymmetric part with coefficients χ_b. Note the similarity to the differential equations for the two-dimensional system, where $\dot{\omega}_{\mathbf{j}} = \rho_{\mathbf{j}+\mathbf{p}}\omega_{\mathbf{j}+\mathbf{p}} - \rho_{\mathbf{j}-\mathbf{p}}\omega_{\mathbf{j}-\mathbf{p}}$. There there is only the antisymmetric part, corresponding to the χ_b coefficients.

Note that the divergence-free subspace (4.1.13) is still invariant under the linearised dynamics. The differential equations defining the dynamics on this subspace are only unique on the divergence-free subspace, and therefore can be defined up to the addition of terms of the form $g(\mathbf{j},\mathbf{p},\boldsymbol{\Gamma})(K\mathbf{j})^{\mathsf{T}}$ to $\chi_a(\mathbf{j})$ and $\chi_b(\mathbf{j})$ for any function g. We can also add or subtract any multiple of $\langle \mathbf{p}, K^{-1}\boldsymbol{\Gamma}\rangle$ as $\langle \mathbf{p}, K^{-1}\boldsymbol{\Gamma}\rangle = 0$.

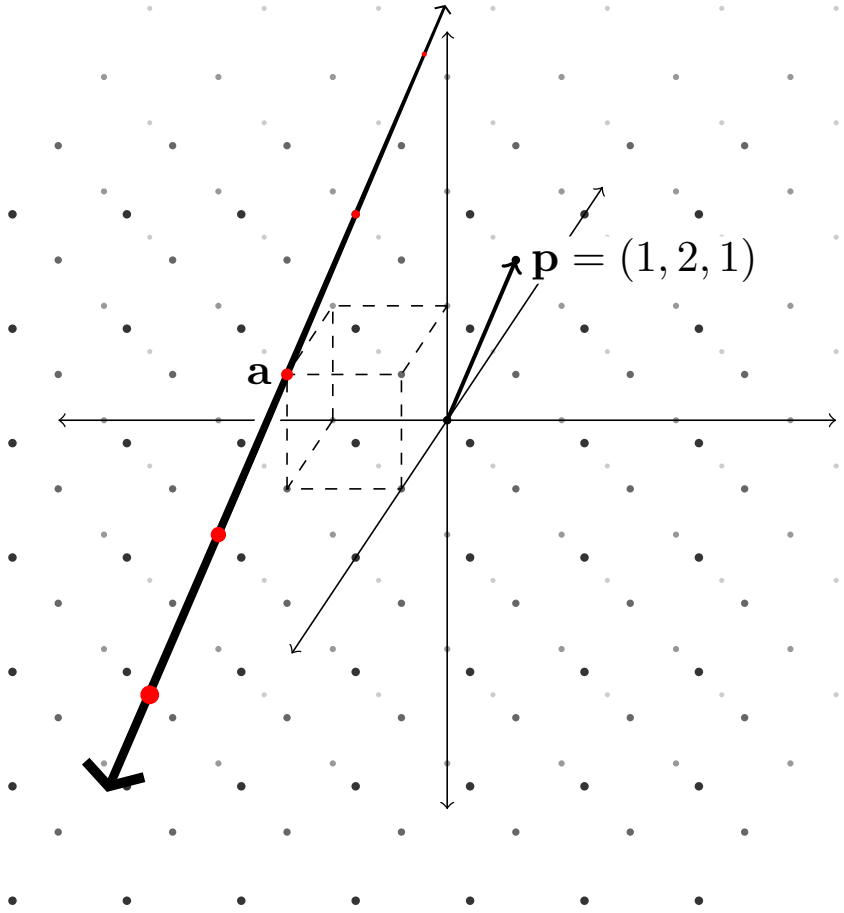

Figure 4.1 – The class decomposition into subsystems for the linearised three-dimensional Euler equations. The steady state is defined by $\mathbf{p} \in \mathbb{Z}^3$. The lattice points on the line parallel to $\mathbf{p}$ passing through $\mathbf{a} \in \mathbb{Z}^3$ all belong to one class of modes. The linearised dynamics of the modes in a class only depend on other modes in the same class. For this figure, $\mathbf{p} = (1, 2, 1)$ and the class led by $\mathbf{a} = (-1, 1, 1)$ is shown.

4.1.5. Class Decomposition of the Linearised System. The differential equations (4.1.43) have a clear class decomposition; the dynamics of mode $\mathbf{z}_\mathbf{a}$ depends only on the modes $\mathbf{z}_{\mathbf{a}\pm\mathbf{p}}$, which in turn depend only on $\mathbf{z}_\mathbf{a}$ and $\mathbf{z}_{\mathbf{a}\pm2\mathbf{p}}$, and so on. Thus the subset of modes with indices of the form $\mathbf{a} + n\mathbf{p}$ for $n \in \mathbb{Z}$ are a decoupled subsystem for any $\mathbf{a} \in \mathbb{Z}^3$. This is illustrated in Figure 4.1, and works much the same as the class decomposition for the two-dimensional case in Section 2.4.2.

In the linearised system, any mode of the form $\mathbf{z}_{q\mathbf{p}}$ for $q \in \mathbb{Q}$ such that $q\mathbf{p} \in \mathbb{Z}^3$ is constant. This is less obvious here than in the two-dimensional case. Calculating $\chi_1(q\mathbf{p})$ and $\chi_2(q\mathbf{p})$,

$$\chi_1(q\mathbf{p}) = \chi_2(q\mathbf{p}) = -\frac{1}{|\mathbf{p}|_{\boldsymbol{\kappa}}^2} \left(K\mathbf{p} \times \boldsymbol{\Gamma}\right) \left(K\mathbf{p}\right)^{\mathsf{T}}. \tag{4.1.44}$$

So the dynamics are given by

$$\dot{\mathbf{z}}_{q\mathbf{p}} = -\frac{1}{|\mathbf{p}|_{\boldsymbol{\kappa}}^2} \left(K\mathbf{p} \times \boldsymbol{\Gamma}\right) \left[\left(K\mathbf{p}\right)^{\mathsf{T}} \mathbf{z}_{(q+1)\mathbf{p}} + \left(K\mathbf{p}\right)^{\mathsf{T}} \mathbf{z}_{(q-1)\mathbf{p}}\right]. \tag{4.1.45}$$

But $(K\mathbf{p})^{\mathsf{T}}\mathbf{z}_{m\mathbf{p}} = \frac{1}{m}\langle m\mathbf{p}, K^{-1}\mathbf{z}_{m\mathbf{p}}\rangle = 0$ by the divergence-free condition, and thus $\dot{\mathbf{z}}_{q\mathbf{p}} = 0$.

We define the *principal domain* of mode numbers

$$\mathcal{A} := \{\mathbf{a} \in \mathbb{Z}^3 \mid -\frac{1}{2}|\mathbf{p}|_{\boldsymbol{\kappa}}^2 < \langle \mathbf{a}, \mathbf{p}\rangle \leq \frac{1}{2}|\mathbf{p}|_{\boldsymbol{\kappa}}^2\}. \tag{4.1.46}$$

Then for all $\mathbf{j} \in \mathbb{Z}^3$, $\mathbf{j} = \mathbf{a} + n\mathbf{p}$ for a unique $\mathbf{a} \in \mathcal{A}$ and $n \in \mathbb{Z}$.

Now when studying the linearised system, we can study each class of modes with indices $\mathbf{a} + n\mathbf{p}$ for a fixed $\mathbf{a}$ one at a time. We thus introduce the following notation: for a fixed $\mathbf{a} \in \mathcal{A}$, define

$$\mathbf{z}_n := \mathbf{z}_{\mathbf{a}+n\mathbf{p}}, \quad \chi_i(n) := \chi_i(\mathbf{a} + n\mathbf{p}). \tag{4.1.47}$$

We have reused the variables $\mathbf{z}$ and χ_i; the definition depends on whether we consider the variables a function of an integer n or a vector $\mathbf{v}$. In the former case, we are considering the dynamics of a single class only. This is equivalent to the use of ρ_k vs $\rho_{\mathbf{j}}$ in Section 2.4.2.

The differential equations for a single class are now

$$\dot{\mathbf{z}}_n = \chi_1(n+1)\mathbf{z}_{n+1} + \chi_2(n-1)\mathbf{z}_{n-1}. \tag{4.1.48}$$

4.2. Simplifying the Class Dynamics

In the previous section, it was shown that the linearised Euler equations around a shear flow decouple into "classes" of modes. In this section, we further simplify the dynamics of these classes and relate them to classes of the two-dimensional problem. To do so, we make a number of transformations: remove the influence of the anisotropic domain size $\boldsymbol{\kappa}$; rotate and scale $\mathbf{p}$ to a unit vector parallel to the x-axis; use the divergence-free property to simplify $\boldsymbol{\Gamma}$; and finally project down to the divergence-free subspace (4.1.13). The dynamics of the resulting system split into a part isomorphic to the dynamics of a corresponding class in the two-dimensional problem, and another part with simple dynamics. There are exceptional cases when $\boldsymbol{\Gamma}$ and $K\mathbf{a}$ are coplanar, which induce qualitatively different dynamics.

4.2.1. Motivating Examples. To illustrate how the dynamics of a class in the linearised three-dimensional problem relate to the classes of the two-dimensional problem, consider the class with $\mathbf{p} = (2,0,0)$, $\mathbf{a} = (0,1,0)$, and $K = \mathbb{I}_3$.

If $\mathbf{\Gamma} = (0,0,1)$, we calculate the eigenvalues of the differential equations (4.1.48) using a large Galerkin truncation. The associated spectrum consists of all imaginary eigenvalues on the interval $i[-2,2]$ and two real eigenvalues $\lambda = \pm 0.5225...$. This is exactly the spectrum of the linearised class in the two-dimensional problem with $\mathbf{p} = (2,0)$, $\mathbf{a} = (0,1)$ from (2.4.22). It should be noted that the spectrum at any finite truncation is not exactly the same in the two- and three-dimensional classes; the eigenvalues on the imaginary axis will not coincide. In the untruncated limit, they fill out the same interval.

If $\mathbf{\Gamma} = (0, \sqrt{3}/2, 1/2)$ (normalised so $|\mathbf{\Gamma}| = 1$) we again calculate the eigenvalues. There are imaginary eigenvalues in the interval $i[-1,1] = \frac{1}{2}i[-2,2]$, and real eigenvalues at $\lambda = \pm 0.2612... = \pm 1/2 \times 0.5225...$. These values are the eigenvalues of the two-dimensional class with $\mathbf{p} = (2,0)$, $\mathbf{a} = (0,1)$ as above, up to a factor of $1/2$. It seems reasonable to hypothesise that the spectrum of any class of the three-dimensional problem can be written in terms of a class of the two-dimensional problem up to a factor. We will show that the appropriate factor is the length of the vector rejection of $\mathbf{a}$ onto $\mathbf{\Gamma}$ in a weighted norm.

Finally, consider $\mathbf{\Gamma} = (0,1,0)$. In this case the operator associated with (4.1.48) is nilpotent. Therefore all eigenvalues are zero. This accords with the hypothesis of the previous paragraph, as $\mathbf{a}$ and $\mathbf{\Gamma}$ are parallel and so the length of the vector rejection is zero. Unlike the cases with $\cos\theta \neq 0$, there are unstable linear dynamics due to the nontrivial nilpotent part. We study this case and its implications for stability in Section 4.2.9.

To show that any class of the three-dimensional linearised problem can be written in terms of a class of the two-dimensional linearised Euler equations, we will first rewrite the problem in terms of simplified parameters. We then use these parameters to show that the system decomposes into a part with stable dynamics and another part isomorphic to a class of the two-dimensional problem.

4.2.2. Rescaling and Rotation. Define $\tilde{\mathbf{a}} := K\mathbf{a}$, $\tilde{\mathbf{p}} := K\mathbf{p}$. The condition (4.1.12) now implies $\tilde{\mathbf{p}}^{\mathsf{T}}\mathbf{\Gamma} = 0$. Written in terms of these new variables,

$$\chi_a(n) = -\frac{1}{|\tilde{\mathbf{a}} + n\tilde{\mathbf{p}}|^2}\tilde{\mathbf{a}}^{\mathsf{T}}\mathbf{\Gamma}\widehat{(\tilde{\mathbf{a}} + n\tilde{\mathbf{p}})} - \frac{1}{|\mathbf{p}|^2}\left[\tilde{\mathbf{p}} \times \mathbf{\Gamma}\right]\tilde{\mathbf{p}}^{\mathsf{T}} \tag{4.2.1}$$

and

$$\chi_b(n) = \frac{1}{|\tilde{\mathbf{a}} + n\tilde{\mathbf{p}}|^2}\mathbf{\Gamma}[\tilde{\mathbf{a}} \times \tilde{\mathbf{p}}]^{\mathsf{T}} + \frac{1}{|\tilde{\mathbf{p}}|^2}\mathbf{\Gamma}^{\mathsf{T}}\left[\tilde{\mathbf{p}} \times \tilde{\mathbf{a}}\right]\mathbb{I}_3. \tag{4.2.2}$$

Note that $|\mathbf{x}| = \sqrt{\mathbf{x}^{\mathsf{T}}\mathbf{x}}$ is the usual Euclidean norm, rather than the $\boldsymbol{\kappa}$-norm.

There is no explicit $\boldsymbol{\kappa}$ dependence in the differential equations now. Due to the transformation $\tilde{\mathbf{a}}$ and $\tilde{\mathbf{p}}$ are no longer integer lattice points. The same will be true throughout this chapter, unless stated otherwise. Thus we must consider $\tilde{\mathbf{a}}, \tilde{\mathbf{p}}$ as general parameters in $\mathbb{R}^3$. When considering the full stability problem for a shear flow, the final step will be to transform back to the original $\mathbf{a}$, $\mathbf{p}$ variables and surmise which values actually occur on the lattice $\mathbb{Z}^3$. We must keep this in mind throughout this section. Compare this to the equivalent transformation in two-dimensions, discussed in Section 2.8.1 and depicted in Figure 2.16.

Next consider the rotation matrix that rotates a given vector $\mathbf{v} = (v_x, v_y, v_z)$ to the positive x-axis

$$R_1(\mathbf{v}) := \frac{1}{|\mathbf{v}|} \begin{pmatrix} v_x & v_y & p_z \\ 0 & \frac{-v_z|\mathbf{v}|}{\sqrt{v_y^2+v_z^2}} & \frac{v_y|\mathbf{v}|}{\sqrt{v_y^2+v_z^2}} \\ \sqrt{v_y^2+v_z^2} & \frac{-v_x v_y}{\sqrt{v_y^2+v_z^2}} & \frac{-v_x v_z}{\sqrt{v_y^2+v_z^2}} \end{pmatrix}. \tag{4.2.3}$$

Similarly, define the rotation matrix $R_2(\mathbf{v})$ which rotates $\mathbf{v}$ to align it with the x-y plane

$$R_2(\mathbf{v}) := \frac{1}{\sqrt{v_y^2+v_z^2}} \begin{pmatrix} \sqrt{v_y^2+v_z^2} & 0 & 0 \\ 0 & v_y & v_z \\ 0 & -v_z & v_y \end{pmatrix}. \tag{4.2.4}$$

Note the special cases for these rotation matrices. If $\mathbf{v} = (v_x, 0, 0)$, we can define $R_1(v_x, 0, 0) := \lim_{v_y, v_z \to 0} R_1(v_x, v_y, v_z) = \mathbb{I}_3$, and similarly if $v_z = 0$ we can define $R_2(v_x, v_y, 0) := \mathbb{I}_3$.

Now the product

$$R = R_2(R_1(\tilde{\mathbf{p}})\tilde{\mathbf{a}})R_1(\tilde{\mathbf{p}}) \tag{4.2.5}$$

is a rotation matrix that satisfies $\det(R) = 1$ and

$$RR^{\mathsf{T}} = R^{\mathsf{T}}R = \mathbb{I}_3, \quad R\tilde{\mathbf{p}} = \begin{pmatrix} |\tilde{\mathbf{p}}| \\ 0 \\ 0 \end{pmatrix}, \quad R\tilde{\mathbf{a}} = \begin{pmatrix} \bar{a}_x \\ \bar{a}_y \\ 0 \end{pmatrix} \tag{4.2.6}$$

for some $\bar{a}_x, \bar{a}_y \in \mathbb{R}$. Then define

$$\bar{\mathbf{p}} := R\tilde{\mathbf{p}}, \quad \bar{\mathbf{a}} := R\tilde{\mathbf{a}}, \quad \bar{\boldsymbol{\Gamma}} := R\boldsymbol{\Gamma}. \tag{4.2.7}$$

For any n, $\bar{\mathbf{a}} + n\bar{\mathbf{p}}$ lies in the x-y plane. The condition $\tilde{\mathbf{p}}^{\mathsf{T}}\boldsymbol{\Gamma} = 0$ implies $\bar{\mathbf{p}}^{\mathsf{T}}\bar{\boldsymbol{\Gamma}} = 0$, and so

$$\bar{\boldsymbol{\Gamma}} = \begin{pmatrix} 0 \\ \Gamma_y \\ \Gamma_z \end{pmatrix} = \Gamma \begin{pmatrix} 0 \\ \cos\theta \\ \sin\theta \end{pmatrix} \tag{4.2.8}$$

for some $\Gamma \in \mathbb{R}^+$, $\theta \in (-\pi, \pi]$. Note the exceptional cases $\theta = \frac{\pi}{2}, -\frac{\pi}{2}$ where $\Gamma_y = 0$ and $\theta = 0, \pi$ where $\Gamma_z = 0$. These cases will be very important in Sections 4.2.7 and 4.2.9.

Now define $\bar{\mathbf{z}}_n := R\mathbf{z}_n$, so

$$\dot{\bar{\mathbf{z}}}_n = R\chi_1(n+1)R^{\mathsf{T}}\bar{\mathbf{z}}_{n+1} + R\chi_2(n-1)R^{\mathsf{T}}\bar{\mathbf{z}}_{n-1}. \tag{4.2.9}$$

Note that $|\mathbf{j}| = |R\mathbf{j}|$ and $\widehat{R\mathbf{j}} = R\hat{\mathbf{j}}R^{\mathsf{T}}$ for all $\mathbf{j} \in \mathbb{R}^3$, as $R \in SO(3)$. So

$$\begin{aligned} R\chi_a(n)R^{\mathsf{T}} = &\frac{1}{|\bar{\mathbf{a}} + n\bar{\mathbf{p}}|^2}\left(-(\bar{\mathbf{a}} + n\bar{\mathbf{p}})^{\mathsf{T}}\bar{\mathbf{\Gamma}}\widehat{(\bar{\mathbf{a}} + n\bar{\mathbf{p}})} - \frac{1}{2}\bar{\mathbf{p}}^{\mathsf{T}}\mathbf{\Gamma}\hat{\bar{\mathbf{p}}}\right) \\ &+ \frac{1}{|\bar{\mathbf{p}}|^2}\left(-\left[\bar{\mathbf{p}} \times \bar{\mathbf{\Gamma}}\right]\bar{\mathbf{p}}^{\mathsf{T}} - \frac{1}{2}\left[(\bar{\mathbf{a}} + n\bar{\mathbf{p}}) \times \bar{\mathbf{\Gamma}}\right](\bar{\mathbf{a}} + n\bar{\mathbf{p}})^{\mathsf{T}}\right), \end{aligned} \tag{4.2.10}$$

$$\begin{aligned} R\chi_b(n)R^{\mathsf{T}} = &\frac{1}{|\bar{\mathbf{a}} + n\bar{\mathbf{p}}|^2}\left(\mathbf{\Gamma}[(\bar{\mathbf{a}} + n\bar{\mathbf{p}}) \times \bar{\mathbf{p}}]^{\mathsf{T}} + \bar{\mathbf{p}}^{\mathsf{T}}\mathbf{\Gamma}\widehat{(\bar{\mathbf{a}} + n\bar{\mathbf{p}})}\right) \\ &+ \frac{1}{|\bar{\mathbf{p}}|^2}\left(\mathbf{\Gamma}^{\mathsf{T}}\left[\bar{\mathbf{p}} \times (\bar{\mathbf{a}} + n\bar{\mathbf{p}})\right]I_3 + \left[\bar{\mathbf{p}} \times \mathbf{\Gamma}\right](\bar{\mathbf{a}} + n\bar{\mathbf{p}})^{\mathsf{T}}\right). \end{aligned} \tag{4.2.11}$$

These are equivalent to the matrices that give the dynamics of the system with the parameters $\bar{\mathbf{a}}$, $\bar{\mathbf{p}}$, $K = \mathbb{I}$ and $\mathbf{\Gamma}$, so the differential equations are invariant under these transformations.

A final rescaling by $|\bar{\mathbf{p}}|$ transforms to a new $\mathbf{p} = (1,0,0)$, $\mathbf{a} = \frac{1}{|\bar{\mathbf{p}}|}(\bar{a}_x, \bar{a}_y, 0) = (\tilde{a}_x, \tilde{a}_y, 0)$. A time rescaling $t \to \Gamma t$ scales $\mathbf{\Gamma} = (0, \cos\theta, \sin\theta)$ to be a unit vector. We can specialise to this set of classes with $\mathbf{p} = (1,0,0)$, $\mathbf{a} = (\tilde{a}_x, \tilde{a}_y, 0)$, and $\mathbf{\Gamma} = (0, \cos\theta, \sin\theta)$ and infer the dynamics of any other class from the dynamics of a class of this form by inverting the above transformations. Note that we consider $\tilde{a}_x, \tilde{a}_y \in \mathbb{R}$ rather than $\mathbb{Z}$, due to the transformations required to put a class in this form. To make this clear, we denote the parameters $\tilde{a}_x, \tilde{a}_y$ and $\tilde{\mathbf{a}} = (\tilde{a}_x, \tilde{a}_y, 0)$ rather than $a_x, a_y, a_z, \mathbf{a}$. We also write $\tilde{\mathbf{p}} = (1,0,0)$. We will also use $\boldsymbol{\omega}$ as the linearised variable in place of $\mathbf{z}$ for consistency with the notation in Chapter 2. The dynamics of such a class are given by

$$\dot{\boldsymbol{\omega}}_n = \chi_1(n+1)\boldsymbol{\omega}_{n+1} + \chi_2(n-1)\boldsymbol{\omega}_{n-1} \tag{4.2.12}$$

where

$$\chi_1(n) := \chi_a(n) + \chi_b(n), \quad \chi_2(n) := \chi_a(n) - \chi_b(n) \tag{4.2.13}$$

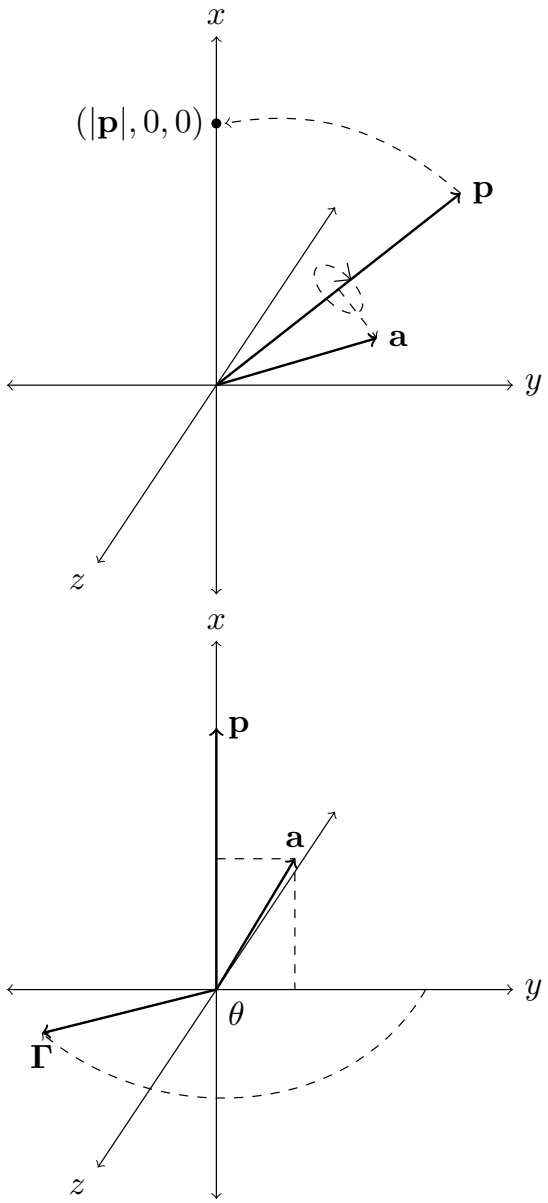

Figure 4.2 – Simplifying transformations for the linearised classes. The dynamics of the classes (4.1.48) can be simplified significantly by a change of coordinates. First, the vector $\mathbf{p}$ is rotated to the x axis. An additional rotation around the x-axis aligns $\mathbf{a}$ with the x-y plane. As $\mathbf{\Gamma}$ is perpendicular to $\mathbf{p}$, it lies in the y-z plane, and we can describe it by its length $|\mathbf{\Gamma}|$ and angle to the positive y-axis θ. The dynamics are invariant under these transformations, so we only need to consider classes with these parameters. Compare this to the Section 2.8.1.

for

$$\begin{aligned}\chi_a(n) = &\begin{pmatrix} -\frac{1}{2}(\tilde{a}_x+n)\tilde{a}_y & -\frac{1}{2}\tilde{a}_y^2 & 0 \\ \frac{1}{2}(2+(\tilde{a}_x+n)^2) & \frac{1}{2}(\tilde{a}_x+n)\tilde{a}_y & 0 \\ 0 & 0 & 0 \end{pmatrix}\sin\theta \\ &+\begin{pmatrix} 0 & 0 & -\frac{\tilde{a}_y^2}{|\tilde{\mathbf{a}}+n\tilde{\mathbf{p}}|^2} \\ 0 & 0 & \frac{(\tilde{a}_x+n)\tilde{a}_y}{|\tilde{\mathbf{a}}+n\tilde{\mathbf{p}}|^2} \\ \frac{(-2-(\tilde{a}_x+n)^2)|\tilde{\mathbf{a}}+n\tilde{\mathbf{p}}|^2+2\tilde{a}_y^2}{2|\tilde{\mathbf{a}}+n\tilde{\mathbf{p}}|^2} & \frac{-(\tilde{a}_x+n)\tilde{a}_y(|\tilde{\mathbf{a}}+n\tilde{\mathbf{p}}|^2+2)}{2|\tilde{\mathbf{a}}+n\tilde{\mathbf{p}}|^2} & 0 \end{pmatrix}\cos\theta,\end{aligned} \tag{4.2.14}$$

$$\begin{aligned}\chi_b(n) = &\begin{pmatrix} \tilde{a}_y & 0 & 0 \\ -(\tilde{a}_x+n) & 0 & 0 \\ 0 & 0 & \tilde{a}_y\left(1-\frac{1}{|\tilde{\mathbf{a}}+n\tilde{\mathbf{p}}|^2}\right) \end{pmatrix}\sin\theta \\ &+\begin{pmatrix} 0 & 0 & 0 \\ 0 & 0 & \frac{-\tilde{a}_y}{|\tilde{\mathbf{a}}+n\tilde{\mathbf{p}}|^2} \\ (\tilde{a}_x+n) & \tilde{a}_y & 0 \end{pmatrix}\cos\theta.\end{aligned} \tag{4.2.15}$$

The next step is to show that this class has quantitatively the same dynamics as the corresponding class in the two-dimensional problem; that is, there is limited dependence on the parameter θ.

4.2.3. Calculating the Reduced Parameters. We have shown that the original parameters $\mathbf{a} \in \mathbb{Z}^3$, $\mathbf{p} \in \mathbb{Z}^3$, $\mathbf{\Gamma} \in \mathbb{R}^3$ can be reduced to three parameters $\tilde{a}_x, \tilde{a}_y \in \mathbb{R}$ and $\theta \in [0, 2\pi)$. The reduced parameters are related to the original parameters by the transformation $\mathbf{a} \to \frac{1}{|\mathbf{p}|_{\boldsymbol{\kappa}}} RK\mathbf{a} = (\tilde{a}_x, \tilde{a}_y, 0)$, with the rotation matrix R defined by (4.2.5). Explicitly, we can write $\tilde{a}_x, \tilde{a}_y$ in terms of the original parameters $\mathbf{a}, \mathbf{p}$ as

$$\tilde{a}_x = \frac{\langle \mathbf{a}, \mathbf{p}\rangle}{|\mathbf{p}|_{\boldsymbol{\kappa}}^2}, \quad \tilde{a}_y = \frac{|K\mathbf{a} \times K\mathbf{p}|}{|\mathbf{p}|_{\boldsymbol{\kappa}}^2}. \tag{4.2.16}$$

We can also calculate the angle θ that defines the reduced $\mathbf{\Gamma}$ parameter $(0, \cos\theta, \sin\theta)$ by the formula

$$\tan\theta = \frac{\mathbf{\Gamma}^{\mathsf{T}}(K\mathbf{p} \times K\mathbf{a})}{\langle \mathbf{a}, K^{-1}\mathbf{\Gamma}\rangle |\mathbf{p}|_{\boldsymbol{\kappa}}} \tag{4.2.17}$$

directly from the definition (4.2.8). One can see this by noting that Γ_y and Γ_z are the magnitude of the vector projection and vector rejection respectively of $\mathbf{\Gamma}$ onto the plane spanned by $\mathbf{p}$, $\mathbf{a}$. Note that θ is zero if $\mathbf{\Gamma}^{\mathsf{T}}(K\mathbf{p} \times K\mathbf{a}) = 0$, so the associated reduced parameter $\mathbf{\Gamma} = (0, 1, 0)$. Also, $\tan\theta$ is singular if $\langle \mathbf{a}, K^{-1}\mathbf{\Gamma}\rangle = 0$, so $\mathbf{\Gamma} = (0, 0, 1)$. Compare this to the illustration of the angle θ in Figure 4.2, noting the relationship between $\mathbf{a}$, $\mathbf{\Gamma}$ and the angle θ.

4.2.4. Verifying a Linear Constraint. It is necessary to confirm that the divergence-free subspace (4.1.13) is invariant under the linearised differential equations (4.1.48), so that we can study the dynamics on that subspace. Note that the divergence is generally not a constant of motion of the differential equations; an initial condition off the divergence-free subspace can have a varying divergence. However, an initial condition with zero divergence will always have zero divergence.

In general, the procedure for verifying that a linear constraint is preserved by a linear differential equation is as follows. Given a linear system of differential equations

$$\dot{\mathbf{x}} = D\mathbf{x} \tag{4.2.18}$$

one may need to check whether the linear subspace given by the constraint $C\mathbf{x} = \mathbf{0}$ for some C is invariant. For a nondegenerate constraint, CC^{T} is invertible. Define the projector

$$P := \mathbb{I} - C^{\mathsf{T}}(CC^{\mathsf{T}})^{-1}C. \tag{4.2.19}$$

This satisfies two properties:

- $CP = C - CC^{\mathsf{T}}(CC^{\mathsf{T}})^{-1}C = 0$;
- for all $\mathbf{x}$ such that $C\mathbf{x} = 0$, $P\mathbf{x} = \mathbf{x}$.

So now we wish to verify that the subspace is invariant, i.e. $\frac{\mathrm{d}}{\mathrm{d}t}(C\mathbf{x}) = \mathbf{0}$. But

$$\frac{\mathrm{d}}{\mathrm{d}t}(C\mathbf{x}) = CD\mathbf{x} = CDP\mathbf{x} \tag{4.2.20}$$

for an initial condition $\mathbf{x}$ in the subspace satisfying $\mathbf{x} = P\mathbf{x}$. Therefore, if $CDP = 0$, the subspace is invariant.

4.2.5. Divergence Free Condition in the Linearised Subsystem. Using the method described in Section 4.2.4, we now confirm the divergence-free subspace is invariant in the linearised subsystem. The condition $(\tilde{\mathbf{a}}+n\tilde{\mathbf{p}})^{\mathsf{T}}\boldsymbol{\omega}_n = 0$ for all n can be encoded as

$$C\boldsymbol{\omega} = 0, \quad \boldsymbol{\omega} = (..., \boldsymbol{\omega}_{-1}, \boldsymbol{\omega}_0, \boldsymbol{\omega}_1, \boldsymbol{\omega}_2, ...)^{\mathsf{T}}, \tag{4.2.21}$$

$$C = \begin{pmatrix} \ddots & \vdots & \vdots & \vdots & \vdots & \ddots \\ \dots & (\tilde{\mathbf{a}} - \tilde{\mathbf{p}})^{\mathsf{T}} & 0 & 0 & 0 & \vdots \\ \dots & 0 & (\tilde{\mathbf{a}})^{\mathsf{T}} & 0 & 0 & \vdots \\ \dots & 0 & 0 & (\tilde{\mathbf{a}} + \tilde{\mathbf{p}})^{\mathsf{T}} & 0 & \vdots \\ \dots & 0 & 0 & 0 & (\tilde{\mathbf{a}} + 2\tilde{\mathbf{p}})^{\mathsf{T}} & \vdots \\ \ddots & \vdots & \vdots & \vdots & \vdots & \ddots \end{pmatrix}. \tag{4.2.22}$$

Now $CC^{\mathsf{T}} = \mathrm{diag}(..., |\tilde{\mathbf{a}}-\tilde{\mathbf{p}}|^2, |\tilde{\mathbf{a}}|^2, |\tilde{\mathbf{a}}+\tilde{\mathbf{p}}|^2, |\tilde{\mathbf{a}}+2\tilde{\mathbf{p}}|^2, ..)$, so P is block diagonal and can be written as

$$\begin{aligned} P &= \mathrm{diag}(.., P_{-1}, P_0, P_1, P_2, ...), \\ P_n &= \mathbb{I}_3 - \frac{1}{|\tilde{\mathbf{a}} + n\tilde{\mathbf{p}}|^2}(\tilde{\mathbf{a}} + n\tilde{\mathbf{p}})(\tilde{\mathbf{a}} + n\tilde{\mathbf{p}})^{\mathsf{T}}. \end{aligned} \tag{4.2.23}$$

The dynamics of $\boldsymbol{\omega}$ are given by $\dot{\boldsymbol{\omega}} = M\boldsymbol{\omega}$ where

$$M = \begin{pmatrix} \ddots & \vdots & \vdots & \vdots & \vdots & \ddots \\ \dots & 0 & \chi_1(0) & 0 & 0 & \vdots \\ \dots & \chi_2(-1) & 0 & \chi_1(1) & 0 & \vdots \\ \dots & 0 & \chi_2(0) & 0 & \chi_1(2) & \vdots \\ \dots & 0 & 0 & \chi_2(1) & 0 & \vdots \\ \ddots & \vdots & \vdots & \vdots & \vdots & \ddots \end{pmatrix}. \tag{4.2.24}$$

So

$$CMP = \begin{pmatrix} \ddots & \vdots & \vdots & \vdots & \vdots & \ddots \\ \dots & 0 & \mu_0 & 0 & 0 & \vdots \\ \dots & \nu_{-1} & 0 & \mu_1 & 0 & \vdots \\ \dots & 0 & \nu_0 & 0 & \mu_2 & \vdots \\ \dots & 0 & 0 & \nu_1 & 0 & \vdots \\ \ddots & \vdots & \vdots & \vdots & \vdots & \ddots \end{pmatrix} \tag{4.2.25}$$

where

$$\begin{aligned} \mu_k &= (\tilde{\mathbf{a}} + (k-1)\tilde{\mathbf{p}})^{\mathsf{T}}\chi_1(k)P(k), \\ \nu_k &= (\tilde{\mathbf{a}} + (k+1)\tilde{\mathbf{p}})^{\mathsf{T}}\chi_2(k)P(k). \end{aligned} \tag{4.2.26}$$

By substituting the definition (4.2.13) we can directly confirm that $\mu_k = 0$, $\nu_k = 0$ for all $k \in \mathbb{Z}$. Thus the divergence-free subspace is invariant under the linearised dynamics.

4.2.6. Projecting to the Divergence-Free Subspace. Having confirmed that the divergence-free subspace is invariant, we project down to this space to find the true dynamics of the linearised Euler equations by disallowing perturbations off this subspace. For each $n \in \mathbb{Z}$, define the matrix

$$R_n := \frac{1}{|\tilde{\mathbf{a}} + n\tilde{\mathbf{p}}|} \begin{pmatrix} \tilde{a}_x + n & -\tilde{a}_y & 0 \\ \tilde{a}_y & \tilde{a}_x + n & 0 \\ 0 & 0 & |\tilde{\mathbf{a}} + n\tilde{\mathbf{p}}| \end{pmatrix}. \tag{4.2.27}$$

One can confirm this is a rotation matrix $R_n \in SO(3)$ and satisfies

$$R_n^{\mathsf{T}}(\tilde{\mathbf{a}} + n\tilde{\mathbf{p}}) = |\tilde{\mathbf{a}} + n\tilde{\mathbf{p}}|(1,0,0)^{\mathsf{T}}. \tag{4.2.28}$$

Define $\tilde{\boldsymbol{\omega}}_n := R_n^{\mathsf{T}}\boldsymbol{\omega}_n$ and write $\tilde{\boldsymbol{\omega}} = (\tilde{\omega}_{n,x}, \tilde{\omega}_{n,y}\tilde{\omega}_{n,z})$. Then the divergence-free condition $(\tilde{\mathbf{a}} + n\tilde{\mathbf{p}})^{\mathsf{T}}\boldsymbol{\omega}_n = 0$ implies

$$\begin{aligned} 0 &= (\tilde{\mathbf{a}} + n\tilde{\mathbf{p}})^{\mathsf{T}} R_n \tilde{\boldsymbol{\omega}}_n \\ &= (R_n^{\mathsf{T}}(\tilde{\mathbf{a}} + n\tilde{\mathbf{p}}))^{\mathsf{T}} \tilde{\boldsymbol{\omega}}_n \\ &= |\tilde{\mathbf{a}} + n\tilde{\mathbf{p}}|(1,0,0)^{\mathsf{T}} \tilde{\boldsymbol{\omega}}_n \\ &= |\tilde{\mathbf{a}} + n\tilde{\mathbf{p}}|\tilde{\omega}_{n,x}. \end{aligned} \tag{4.2.29}$$

As we discard the zero class as explained in Section 4.1.5, $|\tilde{\mathbf{a}}+n\tilde{\mathbf{p}}| \neq 0$, so $\tilde{\omega}_{n,x} = 0$ and $\tilde{\boldsymbol{\omega}}_n = (0, \tilde{\omega}_{n,y}, \tilde{\omega}_{n,z})^{\mathsf{T}}$. We can thus consider the dynamics of $\tilde{\omega}_{n,y}, \tilde{\omega}_{n,z}$ only.

The differential equations for $\tilde{\boldsymbol{\omega}}_n = (\tilde{\omega}_{n,y}, \tilde{\omega}_{n,z})$ are

$$\dot{\tilde{\boldsymbol{\omega}}}_n = R_n^{\mathsf{T}}\chi_1(n+1)R_{n+1}\tilde{\boldsymbol{\omega}}_{n+1} + R_n^{\mathsf{T}}\chi_2(n-1)R_{n-1}\tilde{\boldsymbol{\omega}}_{n-1} \tag{4.2.30}$$

where the coefficient matrices are projected down to the y, z coordinates. The new projected coefficients

$$\tilde{\chi}_1(n) := R_{n-1}^{\mathsf{T}}\chi_1(n)R_n|_{\text{projected}}, \quad \tilde{\chi}_2(n) := R_{n-1}^{\mathsf{T}}\chi_2(n)R_n|_{\text{projected}} \tag{4.2.31}$$

are

$$\begin{aligned} \tilde{\chi}_1(n) =& \frac{\tilde{a}_y}{|\tilde{\mathbf{a}} + n\tilde{\mathbf{p}}|^2}\Bigg[\begin{pmatrix} |\tilde{\mathbf{a}} + n\tilde{\mathbf{p}}||\tilde{\mathbf{a}} + (n-1)\tilde{\mathbf{p}}| & 0 \\ 0 & (|\tilde{\mathbf{a}} + n\tilde{\mathbf{p}}|^2 - 1) \end{pmatrix}\sin\theta \\ &+ \begin{pmatrix} 0 & |\tilde{\mathbf{a}} + (n-1)\tilde{\mathbf{p}}| \\ 0 & 0 \end{pmatrix}\cos\theta\Bigg], \end{aligned} \tag{4.2.32}$$

$$\begin{aligned} \tilde{\chi}_2(n) =& \frac{\tilde{a}_y}{|\tilde{\mathbf{a}} + n\tilde{\mathbf{p}}|^2}\Bigg[\begin{pmatrix} -|\tilde{\mathbf{a}} + n\mathbf{p}||\tilde{\mathbf{a}} + (n+1)\mathbf{p}| & 0 \\ 0 & -(|\tilde{\mathbf{a}} + n\mathbf{p}|^2 - 1) \end{pmatrix}\sin\theta \\ &+ \begin{pmatrix} 0 & |\tilde{\mathbf{a}} + (n+1)\mathbf{p}| \\ 0 & 0 \end{pmatrix}\cos\theta\Bigg]. \end{aligned} \tag{4.2.33}$$

By a reordering of the coordinates to

$$\boldsymbol{\omega} = (..., \omega_{-1,y}, \omega_{0,y}, \omega_{1,y}, ..., \omega_{-1,z}, \omega_{0,z}, \omega_{1,z}, ...), \tag{4.2.34}$$

the system (4.1.43) can be written as

$$\dot{\boldsymbol{\omega}} = \tilde{a}_y \mathcal{M}\boldsymbol{\omega}, \tag{4.2.35}$$

$$\mathcal{M} = \left(\begin{pmatrix} M_1 & 0 \\ 0 & M_2 \end{pmatrix}\sin\theta + \begin{pmatrix} 0 & M_3 \\ 0 & 0 \end{pmatrix}\cos\theta\right) \tag{4.2.36}$$

where

$$M_1 = \begin{pmatrix} \ddots & \vdots & \vdots & \vdots & \vdots & \vdots & \ddots \\ \dots & 0 & \frac{|\tilde{\mathbf{a}}-2\tilde{\mathbf{p}}|}{|\tilde{\mathbf{a}}-\tilde{\mathbf{p}}|} & 0 & 0 & 0 & \vdots \\ \dots & -\frac{|\tilde{\mathbf{a}}-\tilde{\mathbf{p}}|}{|\tilde{\mathbf{a}}-2\tilde{\mathbf{p}}|} & 0 & \frac{|\tilde{\mathbf{a}}-\tilde{\mathbf{p}}|}{|\tilde{\mathbf{a}}|} & 0 & 0 & \vdots \\ \dots & 0 & -\frac{|\tilde{\mathbf{a}}|}{|\tilde{\mathbf{a}}-\tilde{\mathbf{p}}|} & 0 & \frac{|\tilde{\mathbf{a}}|}{|\tilde{\mathbf{a}}+\tilde{\mathbf{p}}|} & 0 & \vdots \\ \dots & 0 & 0 & -\frac{|\tilde{\mathbf{a}}+\tilde{\mathbf{p}}|}{|\tilde{\mathbf{a}}|} & 0 & \frac{|\tilde{\mathbf{a}}+\tilde{\mathbf{p}}|}{|\tilde{\mathbf{a}}+2\tilde{\mathbf{p}}|} & \vdots \\ \dots & 0 & 0 & 0 & -\frac{|\tilde{\mathbf{a}}+2\tilde{\mathbf{p}}|}{|\tilde{\mathbf{a}}+\tilde{\mathbf{p}}|} & 0 & \vdots \\ \ddots & \vdots & \vdots & \vdots & \vdots & \ddots & \end{pmatrix}, \tag{4.2.37}$$

$$M_2 = \begin{pmatrix} \ddots & \vdots & \vdots & \vdots & \vdots & \vdots & \ddots \\ \dots & 0 & \frac{|\tilde{\mathbf{a}}-\tilde{\mathbf{p}}|^2-1}{|\tilde{\mathbf{a}}-\tilde{\mathbf{p}}|^2} & 0 & 0 & 0 & \vdots \\ \dots & \frac{-|\tilde{\mathbf{a}}-2\tilde{\mathbf{p}}|^2+1}{|\tilde{\mathbf{a}}-2\tilde{\mathbf{p}}|^2} & 0 & \frac{|\tilde{\mathbf{a}}|^2-1}{|\tilde{\mathbf{a}}|^2} & 0 & 0 & \vdots \\ \dots & 0 & \frac{-|\tilde{\mathbf{a}}-\tilde{\mathbf{p}}|^2+1}{|\tilde{\mathbf{a}}-\tilde{\mathbf{p}}|^2} & 0 & \frac{|\tilde{\mathbf{a}}+\tilde{\mathbf{p}}|^2-1}{|\tilde{\mathbf{a}}+\tilde{\mathbf{p}}|^2} & 0 & \vdots \\ \dots & 0 & 0 & \frac{-|\tilde{\mathbf{a}}|^2+1}{|\tilde{\mathbf{a}}|^2} & 0 & \frac{|\tilde{\mathbf{a}}+2\tilde{\mathbf{p}}|^2-1}{|\tilde{\mathbf{a}}+2\tilde{\mathbf{p}}|^2} & \vdots \\ \dots & 0 & 0 & 0 & \frac{-|\tilde{\mathbf{a}}+\tilde{\mathbf{p}}|^2+1}{|\tilde{\mathbf{a}}+\tilde{\mathbf{p}}|^2} & 0 & \vdots \\ \ddots & \vdots & \vdots & \vdots & \vdots & \ddots & \end{pmatrix}, \tag{4.2.38}$$

and

$$M_3 = \begin{pmatrix} \ddots & \vdots & \vdots & \vdots & \vdots & \vdots & \ddots \\ \dots & 0 & \frac{|\tilde{\mathbf{a}}-2\tilde{\mathbf{p}}|}{|\tilde{\mathbf{a}}-\tilde{\mathbf{p}}|^2} & 0 & 0 & 0 & \vdots \\ \dots & \frac{|\tilde{\mathbf{a}}-\tilde{\mathbf{p}}|}{|\tilde{\mathbf{a}}-2\tilde{\mathbf{p}}|^2} & 0 & \frac{|\tilde{\mathbf{a}}-\tilde{\mathbf{p}}|}{|\tilde{\mathbf{a}}|^2} & 0 & 0 & \vdots \\ \dots & 0 & \frac{|\tilde{\mathbf{a}}|}{|\tilde{\mathbf{a}}-\tilde{\mathbf{p}}|^2} & 0 & \frac{|\tilde{\mathbf{a}}|}{|\tilde{\mathbf{a}}+\tilde{\mathbf{p}}|^2} & 0 & \vdots \\ \dots & 0 & 0 & \frac{|\tilde{\mathbf{a}}+\tilde{\mathbf{p}}|}{|\tilde{\mathbf{a}}|^2} & 0 & \frac{|\tilde{\mathbf{a}}+\tilde{\mathbf{p}}|}{|\tilde{\mathbf{a}}+2\tilde{\mathbf{p}}|^2} & \vdots \\ \dots & 0 & 0 & 0 & \frac{|\tilde{\mathbf{a}}+2\tilde{\mathbf{p}}|}{|\tilde{\mathbf{a}}+\tilde{\mathbf{p}}|^2} & 0 & \vdots \\ \ddots & \vdots & \vdots & \vdots & \vdots & \ddots & \end{pmatrix}. \tag{4.2.39}$$

This reduction is a key result. We have shown that the dynamics of the linearisation are block upper-triangular, and can thus make conclusions about spectral stability or instability in terms of the spectrum of blocks on the diagonal. In the next section this is further improved by transforming to a block diagonal matrix; one can then conclude that the system is diagonalisable and therefore discuss linear stability or instability.

4.2.7. Further Simplifications and Lax Pair Reduction. The dynamics of a class can be simplified further by transforming to split (4.2.35) into two subsystems. This will result in a subsystem with very simple dynamics and another subsystem isomorphic to a corresponding class of the two-dimensional linearised Euler equations. Both these subsystems are diagonalisable, so we can make more precise claims about stability. Define the transformation matrix

$$T := \operatorname{diag}(..., |\tilde{\mathbf{a}} - 2\tilde{\mathbf{p}}|, |\tilde{\mathbf{a}} - \tilde{\mathbf{p}}|, |\tilde{\mathbf{a}}|, |\tilde{\mathbf{a}} + \tilde{\mathbf{p}}|, |\tilde{\mathbf{a}} + 2\tilde{\mathbf{p}}|, ...). \tag{4.2.40}$$

As $\tilde{\mathbf{a}} + n\tilde{\mathbf{p}} \neq \mathbf{0}$ for all n, T is invertible. Then for all $\theta \neq 0, \pi$, $\cot(\theta)$ is nonsingular so we can define

$$\mathcal{T} := \begin{pmatrix} T & \cot(\theta)T \\ 0 & \mathbb{I} \end{pmatrix} \tag{4.2.41}$$

so

$$\mathcal{T}^{-1} = \begin{pmatrix} T^{-1} & -\cot(\theta)\mathbb{I} \\ 0 & \mathbb{I} \end{pmatrix}. \tag{4.2.42}$$

We will discuss the singular case $\theta = 0, \pi$ in Section 4.2.9 and consider the possible dynamical implications in Section 4.3.3. Then for $\theta \neq 0, \pi$, define

$$\begin{aligned} \tilde{\mathcal{M}} &:= \operatorname{cosec}\theta\, \mathcal{T}^{-1}\mathcal{M}\mathcal{T} \\ &= \begin{pmatrix} \tilde{M}_1 & 0 \\ 0 & \tilde{M}_2 \end{pmatrix} + \begin{pmatrix} 0 & \tilde{M}_3 \\ 0 & 0 \end{pmatrix} \cot\theta \\ &= \begin{pmatrix} \tilde{M}_1 & \eta\tilde{M}_3 \\ 0 & \tilde{M}_2 \end{pmatrix} \end{aligned} \tag{4.2.43}$$

where

$$\begin{aligned} \tilde{M}_1 &= \tilde{T}^{-1} M_1 \tilde{T} \\ &= \begin{pmatrix} \ddots & \vdots & \vdots & \vdots & \vdots & \vdots & \ddots \\ \dots & 0 & 1 & 0 & 0 & 0 & \vdots \\ \dots & -1 & 0 & 1 & 0 & 0 & \vdots \\ \dots & 0 & -1 & 0 & 1 & 0 & \vdots \\ \dots & 0 & 0 & -1 & 0 & 1 & \vdots \\ \dots & 0 & 0 & 0 & -1 & 0 & \vdots \\ \ddots & \vdots & \vdots & \vdots & \vdots & \ddots & \end{pmatrix}, \end{aligned} \tag{4.2.44}$$

$$\tilde{M}_3 = \tilde{T}^{-1} M_1 \tilde{T} - \tilde{T}^{-1} M_3 - M_2$$

$$= \begin{pmatrix} \ddots & \vdots & \vdots & \vdots & \vdots & \vdots & \ddots \\ \dots & 0 & \frac{2}{|\tilde{\mathbf{a}}-\tilde{\mathbf{p}}|^2} & 0 & 0 & 0 & \vdots \\ \dots & 0 & 0 & \frac{2}{|\tilde{\mathbf{a}}|^2} & 0 & 0 & \vdots \\ \dots & 0 & 0 & 0 & \frac{2}{|\tilde{\mathbf{a}}+\tilde{\mathbf{p}}|^2} & 0 & \vdots \\ \dots & 0 & 0 & 0 & 0 & \frac{2}{|\tilde{\mathbf{a}}+2\tilde{\mathbf{p}}|^2} & \vdots \\ \dots & 0 & 0 & 0 & 0 & 0 & \vdots \\ \ddots & \vdots & \vdots & \vdots & \vdots & \ddots & \end{pmatrix}, \tag{4.2.45}$$

$\tilde{M}_2 = M_2$, and $\eta = \cot\theta$. Now $\tilde{\mathcal{M}}$ and $\mathcal{M}$ are similar up to a constant factor of $1/\mathrm{cosec}\theta = \sin\theta$. The parameter η captures the effect of the choice of $\mathbf{\Gamma}$, and can have a extreme impact on the dynamics of the system.

Note that $\tilde{M}_2$ is equal to the governing matrix for a two-dimensional class (2.4.23) with $\mathbf{p} = (1, 0, 0)$. Also note that $\tilde{M}_1$ is antisymmetric and equivalent to the constant matrix M_∞ defined by (2.5.10) with $\rho_\infty = 1$.

The dynamics have been split into two parts; a subsystem driven by $\tilde{M}_3$ equivalent to the dynamics of the two-dimensional linearised system, and another driven by those dynamics through $\tilde{M}_2$ with constant coefficient feedback given by $\tilde{M}_1$. The coupling between the two subsystems depends on the value of η. If $\eta = 0$, there is no coupling and the matrix is block diagonal. We will show that $\tilde{\mathcal{M}}$ is always similar to the block diagonal matrix with $\eta = 0$.

Note that with ρ_k in the reduced coordinates defined as

$$\rho_k := 1 - \frac{1}{(\tilde{a}_x + k)^2 + \tilde{a}_y^2} \tag{4.2.46}$$

we can write $\tilde{M}_3$ (4.2.45) as

$$\tilde{M}_3 = \begin{pmatrix} \ddots & \vdots & \vdots & \vdots & \vdots & \vdots & \ddots \\ \dots & 0 & 2(1-\rho_{-1}) & 0 & 0 & 0 & \vdots \\ \dots & 0 & 0 & 2(1-\rho_0) & 0 & 0 & \vdots \\ \dots & 0 & 0 & 0 & 2(1-\rho_1) & 0 & \vdots \\ \dots & 0 & 0 & 0 & 0 & 2(1-\rho_2) & \vdots \\ \dots & 0 & 0 & 0 & 0 & 0 & \vdots \\ \ddots & \vdots & \vdots & \vdots & \vdots & \ddots & \end{pmatrix} \tag{4.2.47}$$

and $\tilde{M}_2$ the same as the matrix for the dynamics of the two-dimensional linearised Euler equations (2.4.23). Now define the matrix

$$B := \begin{pmatrix} \ddots & \vdots & \vdots & \vdots & \vdots & \vdots & \ddots & \\ \dots & -1 & 0 & +1 & 0 & +1 & 0 & \vdots \\ \dots & 0 & -1 & 0 & +1 & 0 & +1 & \vdots \\ \dots & -1 & 0 & -1 & 0 & +1 & 0 & \vdots \\ \dots & 0 & -1 & 0 & -1 & 0 & +1 & \vdots \\ \dots & -1 & 0 & -1 & 0 & -1 & 0 & \vdots \\ \ddots & \vdots & \vdots & \vdots & \vdots & \vdots & \ddots & \end{pmatrix}. \tag{4.2.48}$$

This is a Toeplitz operator [**Gra06**] composed of shifted copies of the row

$$(..., b_{-3}, b_{-2}, b_{-1}, b_0, b_1, b_2, b_3, ...) \tag{4.2.49}$$

where

$$b_i = \begin{cases} +1 \text{ if } i = 2k \text{ for some } k > 0 \\ -1 \text{ if } i = 2k \text{ for some } k \leq 0 \\ 0 \text{ otherwise.} \end{cases} \tag{4.2.50}$$

Now we can confirm that

$$\tilde{M}_3 = \tilde{M}_1 B - B\tilde{M}_2. \tag{4.2.51}$$

Thus if we define

$$\mathcal{B} := \begin{pmatrix} 0 & B \\ 0 & 0 \end{pmatrix} \tag{4.2.52}$$

then

$$\frac{\mathrm{d}}{\mathrm{d}\eta}\tilde{\mathcal{M}} = [\mathcal{B}, \tilde{\mathcal{M}}]. \tag{4.2.53}$$

Thus $\mathcal{B}$, $\tilde{\mathcal{M}}$ are a Lax Pair for $\tilde{\mathcal{M}}$. Note also that $\mathcal{B}\frac{\mathrm{d}}{\mathrm{d}\eta}(\tilde{\mathcal{M}}) = \frac{\mathrm{d}}{\mathrm{d}\eta}(\tilde{\mathcal{M}})\mathcal{B} = 0$. Form the transformation $\tilde{\mathcal{T}}$ satisfying

$$\frac{\mathrm{d}}{\mathrm{d}\eta}\left(\tilde{\mathcal{T}}^{-1}\right) = \mathcal{B}\tilde{\mathcal{T}}^{-1} \tag{4.2.54}$$

with $\tilde{\mathcal{T}}(0) = \mathbb{I}$. This has solution

$$\tilde{\mathcal{T}} = \mathbb{I} - \eta\mathcal{B} = \begin{pmatrix} \mathbb{I} & -\eta B \\ 0 & \mathbb{I} \end{pmatrix}, \quad \tilde{\mathcal{T}}^{-1} = \begin{pmatrix} \mathbb{I} & \eta B \\ 0 & \mathbb{I} \end{pmatrix}. \tag{4.2.55}$$

Now by (4.2.53)

$$\begin{aligned}
\frac{\mathrm{d}}{\mathrm{d}\eta}(\tilde{\mathcal{M}}) &= \mathcal{B}\tilde{\mathcal{M}} - \tilde{\mathcal{M}}\mathcal{B} \\
\eta\frac{\mathrm{d}}{\mathrm{d}\eta}(\tilde{\mathcal{M}}) &= \eta\mathcal{B}\tilde{\mathcal{M}} - \eta\tilde{\mathcal{M}}\mathcal{B} \\
\tilde{\mathcal{M}} + \eta\tilde{\mathcal{M}}\mathcal{B} &= \tilde{\mathcal{M}} + \eta\mathcal{B}\tilde{\mathcal{M}} - \eta\frac{\mathrm{d}}{\mathrm{d}\eta}(\tilde{\mathcal{M}}) - \eta\mathcal{B}\frac{\mathrm{d}}{\mathrm{d}\eta}(\tilde{\mathcal{M}}) \qquad (4.2.56) \\
\tilde{\mathcal{M}}(\mathbb{I} + \eta\mathcal{B}) &= (\mathbb{I} + \eta\mathcal{B})(\tilde{\mathcal{M}} - \eta\frac{\mathrm{d}}{\mathrm{d}\eta}(\tilde{\mathcal{M}})) \\
\tilde{\mathcal{M}} &= \tilde{\mathcal{T}}\left(\tilde{\mathcal{M}} - \eta\frac{\mathrm{d}}{\mathrm{d}\eta}(\tilde{\mathcal{M}})\right)\tilde{\mathcal{T}}^{-1}.
\end{aligned}$$

But $\tilde{\mathcal{M}} - \eta\frac{\mathrm{d}}{\mathrm{d}\eta}(\tilde{\mathcal{M}})$ does not depend on η as $\tilde{\mathcal{M}}$ is linear in η. Thus the spectrum of $\tilde{\mathcal{M}}$ is independent of the parameter η. This is a very simple case of the general theory of Lax pairs and isospectral operators [**Lax68**].

Thus we define

$$\bar{\mathcal{M}} := \tilde{\mathcal{M}} - \eta\frac{\mathrm{d}}{\mathrm{d}\eta}(\tilde{\mathcal{M}}) = \begin{pmatrix} \tilde{M}_1 & 0 \\ 0 & \tilde{M}_2 \end{pmatrix} \qquad (4.2.57)$$

so

$$\tilde{\mathcal{M}} = \tilde{\mathcal{T}}\bar{\mathcal{M}}\tilde{\mathcal{T}}^{-1}. \qquad (4.2.58)$$

Then $\bar{\mathcal{M}}$ and $\tilde{\mathcal{M}}$ are similar operators.

The new operator $\bar{\mathcal{M}}$ is independent of η and block diagonal with blocks $\tilde{M}_1$, $\tilde{M}_2$. The matrix $\tilde{M}_1$ is diagonalisable by a discrete Fourier transform per Section 3.2.2 and $\tilde{M}_2$ is diagonalisable by the results of Chapter 2. We thus arrive at the following conclusion.

Theorem 4.2.59 (Equating two- and three-dimensional classes)**.** *Assume that* $\mathbf{\Gamma}^{\mathsf{T}}(K\mathbf{a}\times K\mathbf{p}) \neq 0$*. Then the linear stability and spectrum of the three-dimensional class with parameters* $\mathbf{a}$*,* $\mathbf{p}$*,* $\mathbf{\Gamma}$ *is equivalent to the linear stability of the two-dimensional class with parameters* $\tilde{\mathbf{a}} = (\tilde{a}_x, \tilde{a}_y)$*,* $\tilde{\mathbf{p}} = (1, 0)$*,* $\Gamma = \tilde{a}_y \sin\theta$*, where*

$$\tilde{a}_x = \frac{\langle \mathbf{a}, \mathbf{p}\rangle}{|\mathbf{p}|_{\boldsymbol{\kappa}}^2}, \quad \tilde{a}_y = \frac{|K\mathbf{a} \times K\mathbf{p}|}{|\mathbf{p}|_{\boldsymbol{\kappa}}^2}. \qquad (4.2.60)$$

and

$$\tan\theta = \frac{\mathbf{\Gamma}^{\mathsf{T}}(K\mathbf{p} \times K\mathbf{a})}{\langle \mathbf{a}, K^{-1}\mathbf{\Gamma}\rangle |\mathbf{p}|_{\boldsymbol{\kappa}}}. \qquad (4.2.61)$$

Proof. By Section 4.2, the dynamics of a class with parameters $\mathbf{a}$, $\mathbf{p}$ and $\mathbf{\Gamma}$ are isomorphic to the dynamics of a class with parameters $\tilde{\mathbf{a}} = (\tilde{a}_x, \tilde{a}_y, 0)$, $\mathbf{p} = (1, 0, 0)$ and $\mathbf{\Gamma} = (0, \cos\theta, \sin\theta)$ given in Section 4.2.3. As $\mathbf{\Gamma}^{\mathsf{T}}(K\mathbf{a} \times K\mathbf{p}) \neq 0$, $\sin\theta \neq 0$.

Now the dynamics of this class can be reduced by the divergence-free condition and are given by the matrix $\mathcal{M}$ (4.2.36). As $\sin\theta \neq 0$, by the transformation in Section 4.2.7 the dynamics are governed by the matrix $\tilde{\mathcal{M}}$ (4.2.57). The matrix $\tilde{\mathcal{M}}$ is block diagonal with a constant antisymmetric block $\tilde{M}_1$ (4.2.44) and a block equal to the matrix giving the dynamics of the equivalent two-dimensional problem $\tilde{M}_2$ (2.4.23). The spectrum of $\tilde{M}_1$ is purely imaginary and covers the interval $2i[-1,1]$ by Proposition 2.5.8. This is also the continuous spectrum of $\tilde{M}_2$ by Proposition 2.5.8, and thus the full spectrum of $\tilde{\mathcal{M}}$ is the same as the spectrum of $\tilde{M}_2$. This is the same as the spectrum of the corresponding two-dimensional class with parameters $\tilde{\mathbf{a}} = (\tilde{a}_x, \tilde{a}_y)$, $\mathbf{p} = (1,0)$, and $\Gamma = \sin\theta$. □

Note that even though the imaginary spectrum of the two-dimensional and three-dimensional classes are the same, the spectral density may be different, as there is a contribution to the imaginary spectrum from $\tilde{M}_1$ in addition to the contribution from $\tilde{M}_2$. This is clear when looking at truncations of the system, where the continuous spectrum is approximated by a finite set of values. Then the spectrum of the two- and three-dimensional problems will be different, though they have the same limit.

4.2.8. Continuous Spectrum. Note that $\bar{\mathcal{M}}$ is block diagonal by (4.2.57) with blocks $\tilde{M}_1$ and $\tilde{M}_2$. It was shown in Proposition 2.5.8 that the continuous spectrum of $\tilde{M}_2$ is $\sigma_{\text{ess}}(\tilde{M}_2) = [-2,2]i$. The same argument shows that the continuous spectrum of $\tilde{M}_1$ is also $\sigma_{\text{ess}}(\tilde{M}_1) = [-2,2]i$. Thus the continuous spectrum of $\mathcal{M}$, including the scaling factor of $\sin\theta$ from Theorem 4.2.59, is

$$\sigma_{\text{ess}}(\mathcal{M}) = 2|\sin\theta|[-1,1] \tag{4.2.62}$$

In the case $\theta = 0, \pi$, the operator is nilpotent, and so the continuous spectrum is degenerate [**HN01**].

4.2.9. Linear Growth Classes. The matrix $\tilde{\mathcal{M}}$ is singular when $\theta = 0, \pi$ as $\cot\theta$ is singular. In that case, $\mathcal{M}$ is nilpotent of degree 2 as $\mathcal{M}^2 = 0$. Thus the associated solutions to (4.2.35) are linear and given by

$$\boldsymbol{\omega}(t) = (\mathbb{I} + \tilde{a}_y \begin{pmatrix} 0 & M_3 \\ 0 & 0 \end{pmatrix} t)\boldsymbol{\omega}(0). \tag{4.2.63}$$

These constant dynamics cause the steady state to be linearly unstable.

We thus need to determine when the reduced parameter $\theta = 0$ or π and thus $\sin\theta = 0$ in terms of the original parameters $\mathbf{a}, \mathbf{p} \in \mathbb{Z}^3$, $\boldsymbol{\Gamma} \in \mathbb{R}^3$ and $\boldsymbol{\kappa} \in \mathbb{R}^{+3}$. Such classes occur when $\sin\theta = 0$, so $\boldsymbol{\Gamma}^{\mathsf{T}}(K\mathbf{p} \times K\mathbf{a}) = 0$ or equivalently $(K^{-1}\boldsymbol{\Gamma})^{\mathsf{T}}(\mathbf{a} \times \mathbf{p}) = 0$, by the properties of the cross product and the fact that K is invertible. Geometrically, this implies that $\mathbf{a}$, $\mathbf{p}$, and $K^{-1}\boldsymbol{\Gamma}$ are all coplanar. One can see this from Figure 4.2 by considering when the angle θ is 0 or π.

An important question is whether given $\mathbf{p}$, $\mathbf{\Gamma}$ and $\boldsymbol{\kappa}$, there exist any actual lattice points $\mathbf{a} \in \mathbb{Z}^3$ such that $\sin\theta = 0$. If $\mathbf{a} = k\mathbf{p}$ for some $k \in \mathbb{R}$, then the condition is automatically satisfied, but these classes only consist of constant modes by the argument in Section 4.1.5 and cannot contribute instability. If $\mathbf{a}$ and $\mathbf{p}$ are not parallel, we have the following condition.

Proposition 4.2.64. *If and only if $\mathbf{\Gamma}$ can be expressed in the form*

$$\mathbf{\Gamma} = \alpha K \left(\mathbf{b} - \frac{\langle \mathbf{b}, \mathbf{p} \rangle}{\langle \mathbf{p}, \mathbf{p} \rangle} \mathbf{p} \right) \tag{4.2.65}$$

for some nonzero $\alpha \in \mathbb{R}$ and $\mathbf{b} \in \mathbb{Z}^3$, then there exist classes with linear growth given by (4.2.63)*. Specifically, any class led by $\mathbf{a} = k\mathbf{b}$ for $k \in \mathbb{Z}$ has linear dynamics.*

Proof. Assume we have some $\mathbf{b}, \mathbf{p} \in \mathbb{Z}^3$, $\mathbf{\Gamma} \in \mathbb{R}^3$ such that $\theta = 0, \pi$. Then $K^{-1}\mathbf{\Gamma}$, $\mathbf{b}$, and $\mathbf{p}$ are all coplanar, so for some constants $\alpha, \beta \in \mathbb{R}$

$$K^{-1}\mathbf{\Gamma} = \alpha\mathbf{b} + \beta\mathbf{p}. \tag{4.2.66}$$

But $\mathbf{\Gamma}$ also satisfies the divergence-free condition $\mathbf{\Gamma}^\mathsf{T} K\mathbf{p} = 0$, so

$$\begin{aligned} (\alpha K\mathbf{b} + \beta K\mathbf{p})^\mathsf{T} K\mathbf{p} &= 0 \\ \alpha\langle \mathbf{b}, \mathbf{p} \rangle + \beta\langle \mathbf{p}, \mathbf{p} \rangle &= 0. \end{aligned} \tag{4.2.67}$$

As $\langle \mathbf{p}, \mathbf{p} \rangle = |\mathbf{p}|_{\boldsymbol{\kappa}}^2 \neq 0$ as $\mathbf{p} \neq \mathbf{0}$ by definition,

$$\beta = \frac{-\alpha\langle \mathbf{b}, \mathbf{p} \rangle}{\langle \mathbf{p}, \mathbf{p} \rangle} \tag{4.2.68}$$

and the result follows.

We should also note that the above implies that $\mathbf{b}$ and $\mathbf{p}$ are not parallel. If $\mathbf{b}$ and $\mathbf{p}$ are parallel, for some $\nu \in \mathbb{R}$

$$\begin{aligned} \mathbf{\Gamma} &= \alpha K \left(\nu\mathbf{p} - \frac{\langle \nu\mathbf{p}, \mathbf{p} \rangle}{\langle \mathbf{p}, \mathbf{p} \rangle} \mathbf{p} \right) \\ &= \mathbf{0} \end{aligned} \tag{4.2.69}$$

by the linearity of the inner product. But $\mathbf{\Gamma} \neq \mathbf{0}$ by definition, so by contradiction $\mathbf{b}$ and $\mathbf{p}$ must not be parallel.

Conversely, if $\mathbf{\Gamma}$ cannot be written in the form (4.2.65), then no $\mathbf{b} \in \mathbb{Z}^3$ coplanar with $K^{-1}\mathbf{\Gamma}$ and $\mathbf{p}$ and not parallel with $\mathbf{p}$ would exist, or the above construction would be possible for that value of $\mathbf{b}$. □

Note that their are either zero linear growth classes, or infinitely many.

In particular cases we can sharpen the above to make more specific claims about the form of $\mathbf{\Gamma}$.

Proposition 4.2.70. *Assume only one of p_x, p_y, p_z is nonzero. Without loss of generality, let $\mathbf{p} = (p_x, 0, 0)$ with $p_x \neq 0$. Then there exists $\mathbf{a} \in \mathbb{Z}^3$ not parallel to $\mathbf{p}$ such that the reduced parameter $\theta = 0$ or π if and only if $\Gamma_z = 0$ or*

$$\frac{\kappa_z \Gamma_y}{\kappa_y \Gamma_z} \in \mathbb{Q}. \tag{4.2.71}$$

Proof. By the divergence free theorem $\mathbf{\Gamma}^\mathsf{T} K \mathbf{p} = 0$. If $\mathbf{\Gamma} = (\Gamma_x, \Gamma_y, \Gamma_z)$, this implies $\Gamma_x = 0$ as $\kappa_x > 0$.

Assume there exists some $\mathbf{a} \in \mathbb{Z}^3$ not parallel to $\mathbf{p}$ such that $\mathbf{\Gamma}$, $\mathbf{p}$ and $\mathbf{a}$ are coplanar. Then $K^{-1}\mathbf{\Gamma} = \alpha(0, a_y, a_z)$ by (4.2.65). If $a_z = 0$, then $\Gamma_z = 0$ as $\kappa_z, \alpha \neq 0$. Otherwise

$$\begin{aligned} \frac{\kappa_y^{-1}\Gamma_y}{\kappa_z^{-1}\Gamma_z} &= \frac{\alpha a_y}{\alpha a_z}, \\ \frac{\kappa_z \Gamma_y}{\kappa_y \Gamma_z} &= \frac{a_y}{a_z} \in \mathbb{Q}. \end{aligned} \tag{4.2.72}$$

Conversely, assume either $\Gamma_z = 0$ or ${}^{\kappa_z\Gamma_y}/_{\kappa_y\Gamma_z} \in \mathbb{Q}$. Then there exist $q, r \in \mathbb{Z}$ and $c \in \mathbb{R}$ such that q, r are not both zero, $c \neq 0$ and $\kappa_y^{-1}\Gamma_y = cq$ and $\kappa_z^{-1}\Gamma_z = cr$. Then consider $\mathbf{a} = (0, q, r) \in \mathbb{Z}^3$. Then $\mathbf{\Gamma}, \mathbf{p}, \mathbf{a}$ satisfy (4.2.65), and $\mathbf{a}$ is not parallel to $\mathbf{p}$ by construction. □

It is clear from the above Proposition that for a dense set of values of $\mathbf{\Gamma}$, there exist corresponding $\mathbf{a}$ with $\theta = 0, \pi$. We will discuss an interpretation of these classes in Section 4.3.3.

4.3. Stable Shear Flows

In Theorem 4.2.59 it was shown that the dynamics of a three-dimensional linearised class can almost always be reduced to the dynamics of a two-dimensional linearised class. Thus we can form similar stability results to those in Chapter 2. We begin by showing that all but finitely many classes do not contribute linear instability. By carefully controlling the domain size $\boldsymbol{\kappa}$, we identify parallel shear flows that are linearly stable.

4.3.1. Stable Classes.

Define the *unstable ellipsoid*.

Definition 4.3.1 (The Unstable Ellipsoid)**.** *Define the unstable ellipsoid*

$$D_{\mathbf{p}} := \{\mathbf{x} \in \mathbb{R}^3 \mid |\mathbf{x}|_{\boldsymbol{\kappa}} < |\mathbf{p}|_{\boldsymbol{\kappa}}\}. \tag{4.3.2}$$

The unstable ellipsoid is illustrated in Figure 4.3. This object will serve the same purpose as the unstable ellipse (2.5.2), delineating linearly stable and unstable classes. We shall now prove that classes that do not intersect the unstable

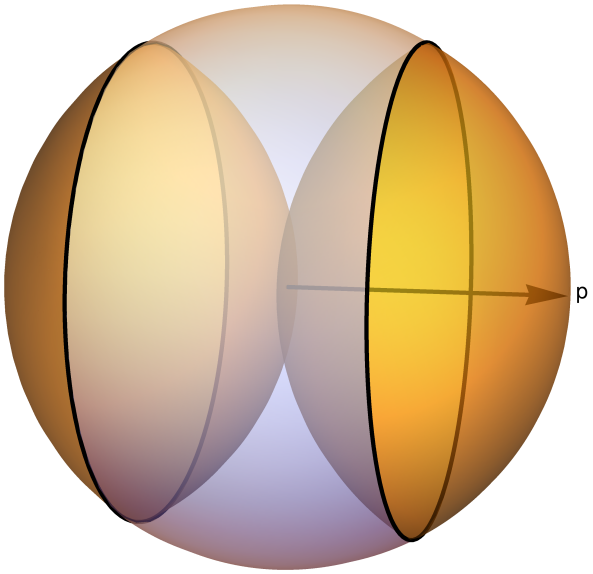

Figure 4.3 – The unstable ellipsoid per Definition 4.3.1. This is the three-dimensional equivalent of the unstable ellipse. Classes led by values of $\mathbf{a}$ inside the unstable ellipsoid will contribute instability, classes with $\mathbf{a}$ outside the unstable ellipsoid will not. This can be split into the regions shown in Figures 4.4 and 4.5 which further delineate the eigenvalues of the class led by $\mathbf{a}$. This figure uses the parameters $\mathbf{p} = (1, 0, 0)$ and $\boldsymbol{\kappa} = (1, 1, 1)$; for other parameter values, the region will change by an affine transformation according to the scaling and rotations in Section 4.2.

ellipsoid at a lattice point and do not satisfy $\theta = 0$ or π cannot contribute linear instability.

Begin by noting that for general $\mathbf{a}, \mathbf{p} \in \mathbb{Z}^3$ with associated reduced parameters $\tilde{a}_x, \tilde{a}_y$ defined by (4.2.60), $|\mathbf{a}|_{\boldsymbol{\kappa}}|\mathbf{p}|_{\boldsymbol{\kappa}} = \sqrt{\tilde{a}_x^2 + \tilde{a}_y^2}$. Thus the definition of ρ_k as used in (4.2.46) is

$$\begin{aligned} \rho_k &:= 1 - \frac{1}{\tilde{a}_x^2 + \tilde{a}_y^2} \\ &= |\mathbf{p}|_{\boldsymbol{\kappa}}^2 \left(\frac{1}{|\mathbf{p}|_{\boldsymbol{\kappa}}^2} - \frac{1}{|\mathbf{a}|_{\boldsymbol{\kappa}}^2} \right). \end{aligned} \tag{4.3.3}$$

This matches the original definition for ρ_k in (2.4.10) up to the constant factor of $|\mathbf{p}|_{\boldsymbol{\kappa}}^2$. This factor can be removed by a time rescaling and ignored. Also note that for $\mathbf{a} \in \mathcal{A}$, the principal domain, $\mathbf{a} \notin D_{\mathbf{p}} \implies \mathbf{a} + k\mathbf{p} \notin D_{\mathbf{p}}$ for all $k \in \mathbb{Z}$.

Proposition 4.3.4. *If and only if* $\mathbf{a} + k\mathbf{p} \in D_{\mathbf{p}}$, *then* $\rho_k < 0$.

Proof. By definition, $\mathbf{a} + k\mathbf{p} \in D_{\mathbf{p}} \iff |\mathbf{a}|_{\boldsymbol{\kappa}} < |\mathbf{p}|_{\boldsymbol{\kappa}}$. Therefore, $\rho_k < 0$ by (4.3.3). □

Proposition 4.3.5 (Stable Classes)**.** *If* $(K^{-1}\boldsymbol{\Gamma})^{\mathsf{T}}(\mathbf{a} \times \mathbf{p}) \neq 0$ *and* $\mathbf{a} \notin D_{\mathbf{p}}$*, the associated class is linearly stable and cannot contribute instability.*

Proof. If $(K^{-1}\boldsymbol{\Gamma})^{\mathsf{T}}(\mathbf{a} \times \mathbf{p}) \neq 0$, then $\theta \neq 0, \pi$ per Proposition 4.2.64. Thus by Theorem 4.2.59, the system is diagonalisable and the spectrum is that of the associated two-dimensional problem. If $\mathbf{a} \notin D_{\mathbf{p}}$ and $\mathbf{a}$ is in the principal domain (4.1.46) then $\mathbf{a} + k\mathbf{p} \notin D_{\mathbf{p}}$ for all $k \in \mathbb{Z}$. Thus by Proposition 4.3.4 $\rho_k \geq 0$ for all $k \in \mathbb{Z}$. Then by Theorem 2.5.5 and Proposition 2.9.7, the spectrum does not have any nonimaginary eigenvalues and is diagonalisable, and the result follows. □

Thus if $\theta \neq 0, \pi$ only finitely many classes can contribute linear instability; those that intersect the unstable ellipsoid at one of its finite interior lattice points. We therefore limit our search for instability to this finite collection of classes. If $\theta = 0, \pi$ these are the only classes that contribute spectral instability, but other classes may contribute linear instability.

4.3.2. Stable Flows. We have shown that under the conditions in Propositions 4.2.64 and 4.2.70 on $\boldsymbol{\Gamma}$ and $\boldsymbol{\kappa}$ all but finitely many classes cannot contribute linear instability. The classes that can contribute instability are exactly those that are led by $\mathbf{a}$ that lie in the unstable ellipsoid. As the shape of this ellipsoid is determined by the size of the domain $\boldsymbol{\kappa}$, it is possible make the unstable ellipsoid sufficiently small to ensure there are no classes that contribute spectral instability. This is analogous to Theorem 2.6.1; however, the existence of the nilpotent classes discussed in Section 4.2.9 means there is an additional condition on $\boldsymbol{\Gamma}, \boldsymbol{\kappa}$ to ensure there is not linear instability.

Theorem 4.3.6 (Stable Shear Flows)**.** *If* $\mathbf{p} = (p_x, 0, 0)$*,* $\kappa_y, \kappa_z > \kappa_x |p_x|$*, and* $\frac{\kappa_z \Gamma_y}{\kappa_y \Gamma_z} \notin \mathbb{Q}$*, the parallel shear flow of the Euler equations* (4.1.1)*,* (4.1.2)

$$\Omega^* = 2\boldsymbol{\Gamma} \cos(\kappa_x p_x x) \tag{4.3.7}$$

is linearly stable.

Proof. If $\mathbf{a} = (a_x, a_y, a_z)$, and $a_z \in \mathbb{Z}$ is nonzero, then

$$|\mathbf{a}|_{\boldsymbol{\kappa}}^2 \geq \kappa_z^2 a_z^2 > \kappa_z^2 > \kappa_x^2 |p_x|^2 = |\mathbf{p}|_{\boldsymbol{\kappa}}^2. \tag{4.3.8}$$

Thus if a_z is nonzero, the class has $|\mathbf{a}|_{\boldsymbol{\kappa}} > |\mathbf{p}|_{\boldsymbol{\kappa}}$ and thus cannot contribute spectral instability by Proposition 4.3.5 (as $a_z \neq 0$ means $\mathbf{a}$ cannot be parallel to $\mathbf{p} = (p_x, 0, 0)$). Similarly, if a_y is nonzero $|\mathbf{a}|_{\boldsymbol{\kappa}} > |\mathbf{p}|_{\boldsymbol{\kappa}}$ and the class cannot contribute linear instability. As the conditions of Proposition 4.2.70 are satisfied, the class also does not contribute linear instability. Thus the only classes that can contribute linear instability are of the form $\mathbf{a} = (a_x, 0, 0) = {}^{a_x}\!/_{p_x}\mathbf{p}$. But then the class dynamics cannot contribute instability as $\mathbf{a}$ and $\mathbf{p}$ are parallel, per Section

4.1.5. Thus there are no classes that contribute linear instability, and the shear flow is linearly stable. □

This proof can be adjusted for shear flows with $\mathbf{p} = (0, p_y, 0)$ or $\mathbf{p} = (0, 0, p_z)$ and the corresponding condition on $\boldsymbol{\kappa}$.

If we relax the condition that $(K^{-1}\boldsymbol{\Gamma})^{\mathsf{T}}(\mathbf{a} \times \mathbf{p}) \neq 0$ for all $\mathbf{a} \in \mathbb{Z}^3$, then there exist nilpotent classes with unstable linear dynamics per Section 4.2.9. However, all classes are still spectrally stable as all other classes are block diagonal and all blocks have only imaginary spectrum. Then the parallel shear flow is spectrally stable, but not linearly stable.

The condition on $\boldsymbol{\Gamma}$ for stability can be interpreted as precluding the possibility of *strong stability* with respect to $\boldsymbol{\Gamma}$. Adjusting the definition in [**Arn78**], the equilibrium of a linear Hamiltonian system is strongly stable if it is stable and the corresponding equilibria of all linear Hamiltonian systems with sufficiently close parameter values are also stable.

We observe that this is not true for the parallel shear flows in Theorem 4.3.6. The values of $\boldsymbol{\Gamma}$ satisfying ${}^{\kappa_z \Gamma_y}/_{\kappa_y \Gamma_z} \in \mathbb{Q}$ are dense on the plane of admissible $\boldsymbol{\Gamma}$ values perpendicular to $K\mathbf{p}$. Thus there is always a Hamiltonian system a small perturbation away in $\boldsymbol{\Gamma}$ for which Theorem 4.3.6 does not hold. Therefore these shear flows are unstable, as there exist classes with nilpotent dynamics which are linearly unstable. Thus the shear flows are not strongly stable with respect to $\boldsymbol{\Gamma}$. In the next section, we explore how this weaker linear stability can allow for nonlinear instability.

4.3.3. Nonnormality and Transition to Turbulence. In Proposition 4.3.5 it was shown that if $(K^{-1}\boldsymbol{\Gamma})^{\mathsf{T}}(\mathbf{a} \times \mathbf{p}) \neq 0$ the class led by $\mathbf{a}$ is not nilpotent and does not contribute linear growth terms. Furthermore, in Propositions 4.2.64 and 4.2.70 it was shown that there exist appropriate choices of the parameters $\mathbf{p}, \boldsymbol{\Gamma}, \boldsymbol{\kappa}$ such that for all $\mathbf{a} \in \mathbb{Z}^3$ not parallel with $\mathbf{p}$, $(K^{-1}\boldsymbol{\Gamma})^{\mathsf{T}}(\mathbf{a} \times \mathbf{p}) \neq 0$. However, for any $\mathbf{p}, \boldsymbol{\Gamma}, \boldsymbol{\kappa}$ there exist values of $\mathbf{a} \in \mathbb{Z}^3$ such that $(K^{-1}\boldsymbol{\Gamma})^{\mathsf{T}}(\mathbf{a} \times \mathbf{p})$ is arbitrarily small. On a superficial level, this does not affect our analysis. We can still apply the transformation per (4.2.57), remove the influence of the $\mathcal{M}_3$ term, and make conclusions about spectral stability or instability. However, if we take a broader view, there is an important point to be made with implications for the dynamics of the full nonlinear system.

For small values of $(K^{-1}\mathbf{\Gamma})^{\mathsf{T}}(\mathbf{a}\times\mathbf{p})$ the parameter η is correspondingly large. For all nonzero values of η, the matrix $\tilde{\mathcal{M}}$ is nonnormal [**TE05**], as the commutator of $\tilde{\mathcal{M}}$ and its conjugate transpose is

$$\begin{aligned}[\tilde{\mathcal{M}},\tilde{\mathcal{M}}^{\mathsf{T}}] &= \tilde{\mathcal{M}}\tilde{\mathcal{M}}^{\mathsf{T}} - \tilde{\mathcal{M}}^{\mathsf{T}}\tilde{\mathcal{M}} \\ &= \begin{pmatrix} \eta^2\tilde{M}_3\tilde{M}_3^{\mathsf{T}} & \eta(\tilde{M}_3\tilde{M}_2^{\mathsf{T}} - \tilde{M}_1^{\mathsf{T}}\tilde{M}_3) \\ \eta(\tilde{M}_2\tilde{M}_3^{\mathsf{T}} - \tilde{M}_3^{\mathsf{T}}\tilde{M}_1) & (\tilde{M}_2^{\mathsf{T}}\tilde{M}_2 - \tilde{M}_2\tilde{M}_2^{\mathsf{T}}) - \eta^2\tilde{M}_3^{\mathsf{T}}\tilde{M}_3 \end{pmatrix} \\ &\neq 0. \end{aligned} \tag{4.3.9}$$

One can think of $\tilde{\mathcal{M}}$ as becoming "more nonnormal" for larger values of η. The concept of a measure of nonnormality is discussed in [**EP87**]. A nonnormal matrix may be linearly stable, but have dramatic transient behaviour that can cause instability in the full nonlinear system. In Boberg and Brosa [**BB88**], it is shown how turbulence can arise from shear flows in the Navier-Stokes equation in a pipe. They showed that small transient instabilities that occur in the linearised problem can propagate into larger instabilities in the nonlinear problem, leading to turbulence. This instability is attributed to the degeneracy or near-degeneracy of eigenvalues; if two eigenvalues are very close, the transient dynamics on a short timescale may grow dramatically due to near-parallel eigenfunctions. In Trefethen, Trefethen, Reddy, and Driscoll [**TTRD93**] (see also [**TE05**]) it was shown that this behaviour can more generally be attributed to the nonnormality of the associated operator or matrix. This transition from laminar to turbulent flow is of much physical interest, and has been well-studied [**ESHW07**].

Following the very lucid explanation by Grossmann [**Gro00**], we briefly sketch how this can occur in our system. Say we have an eigenvalue $\lambda \in \sigma(\tilde{M}_2)$. As $\tilde{\mathcal{M}}$ is block diagonal with $\tilde{M}_2$ as a block, $\lambda \in \sigma(\tilde{\mathcal{M}})$. Say the eigenvector associated with λ is $(v_1, v_2)^{\mathsf{T}}$, so $\tilde{M}_1 v_1 + \eta\tilde{M}_3 v_2 = \lambda v_1$ and $\tilde{M}_2 v_2 = \lambda v_2$. So v_2 is the eigenvector of $\tilde{M}_2$ associated with λ. As this does not involve η, $v_2 = \mathcal{O}(1)$ with respect to η. But $\tilde{M}_1$ and $\tilde{M}_3$ are also $\mathcal{O}(1)$, so $v_1 = \mathcal{O}(\eta)$. Thus for large values of η, the eigenvector (v_1, v_2) is dominated by v_1.

However, for all $\mu \in \sigma(\tilde{M}_1)$, $\mu \in \sigma(\tilde{\mathcal{M}})$ with an eigenvector of the form $(\nu, 0)$. As $\tilde{M}_1$ is diagonalisable, there is a full set of eigenvectors for $\tilde{M}_1$. Therefore there is a set of eigenvectors of $\tilde{\mathcal{M}}$ that span the space of vectors of the form $(\nu, 0)$. For large values of η, the eigenvector of λ $(v_1, v_2) = (\mathcal{O}(\eta), \mathcal{O}(1))$ lies nearly parallel to this subspace. Thus all eigenvectors of $\tilde{\mathcal{M}}$ are of the form $(\mathcal{O}(\eta), \mathcal{O}(1))$.

Therefore for a perturbation of the form $(0, v_2)$, the dynamics will take some time to reach the limiting dynamics along the eigenvectors which are of the form $(\mathcal{O}(\eta), \mathcal{O}(1))$. In the linearised system, these transients will not affect stability. However, the short term transient behaviour can be very dramatic before the stable dynamics occur. This transient behaviour can lead to turbulent instability in the nonlinear system, per [**Gro00**]. Additional detail is required to formalise

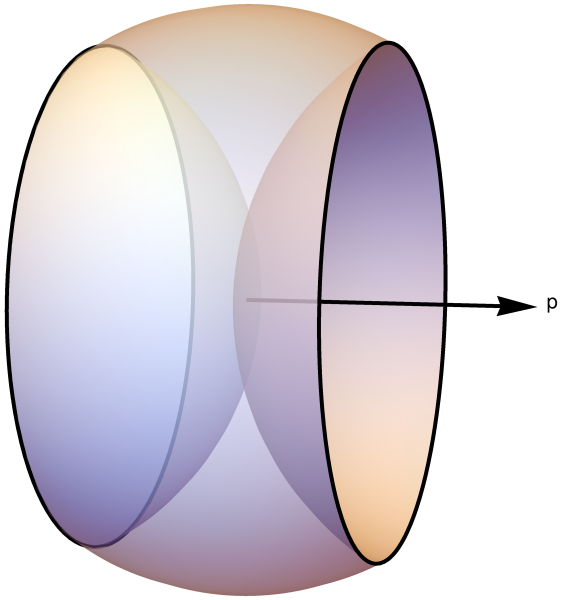

Figure 4.4 – The region containing values $\mathbf{a} \in \mathbb{R}^3$ such that $\mathbf{a} \in D_{\mathbf{p}}$ (the unstable ellipsoid) but $\mathbf{a} \pm \mathbf{p} \notin D_{\mathbf{p}}$. Classes with $\mathbf{a}$ in this region will contribute two nonzero real eigenvalues. Compare this to shape of Figure 2.19; this region is the solid of revolution obtained by rotating the "two real eigenvalues" region around the vector $\mathbf{p}$.

such an argument, but numerical evidence shows that eigenvectors become very close to parallel for large η.

Thus for classes that are spectrally stable as in Proposition 4.3.5, nonnormality can cause transient dynamics that are stable in the linearised problem, but are harbingers of nonlinear instability. Note that this occurs for sufficiently small values of $(K^{-1}\mathbf{\Gamma})^{\mathsf{T}}(\mathbf{a} \times \mathbf{p})$; as $\mathbf{a}$ must take all values in $\mathbb{Z}^3$, this quantity can be made arbitrarily small by selecting appropriate $\mathbf{a}$ for any $\mathbf{p}, \mathbf{\Gamma}, \boldsymbol{\kappa}$. Studying this in the context of nonlinear transition to turbulence from shear flows in a three-dimensional domain is a promising future direction for this research.

4.4. Unstable Shear Flows

4.4.1. Classifying Nonimaginary Eigenvalues. Having discussed in Section 4.3 the range of parameters for which a stable shear flow occurs, we now look at the larger set of parameters for which the shear flow is unstable. Based on numerical observations, we can classify the number and type of nonimaginary eigenvalues in these cases. Assume that $(K^{-1}\mathbf{\Gamma})^{\mathsf{T}}(\mathbf{a} \times \mathbf{p}) \neq 0$, so we are not in a nilpotent class with linear instability. Then we make the following observations:

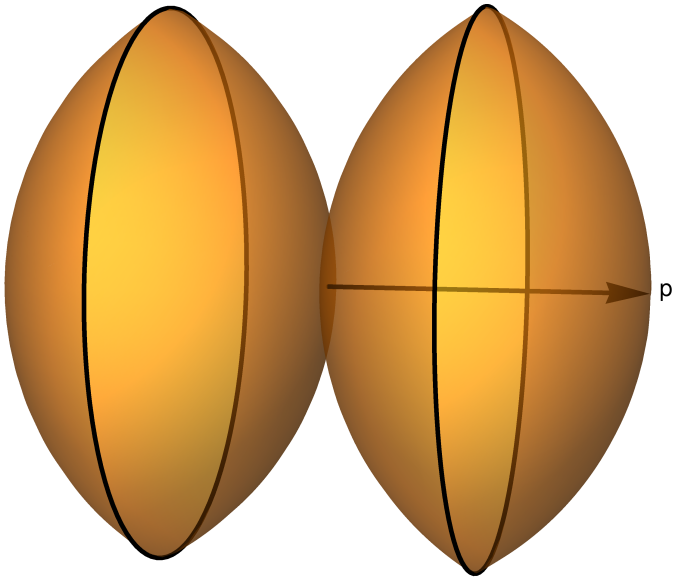

Figure 4.5 – Region showing values of $\mathbf{a} \in \mathbb{R}^3$ such that $\mathbf{a} \in D_{\mathbf{p}}$ (the unstable ellipsoid) and $\mathbf{a}+\mathbf{p} \in D_{\mathbf{p}}$ or $\mathbf{a}-\mathbf{p} \in D_{\mathbf{p}}$. Classes with $\mathbf{a}$ in this region will contribute four nonimaginary eigenvalues; either two real pairs, or a complex quadruplet. Compare this to the regions in Figure 2.19; this region is the "four real eigenvalues" and "four complex eigenvalues" regions rotated around the vector $\mathbf{p}$. The union of this figure and Figure 4.4 make up the full unstable ellipsoid in Figure 4.3.

- If $\mathbf{a} \in D_{\mathbf{p}}$ but $\mathbf{a} + k\mathbf{p} \notin D_{\mathbf{p}}$ for all nonzero $k \in \mathbb{Z}$ the associated class has two real nonzero eigenvalues. The values of $\mathbf{a}$ for which this is true are illustrated in Figure 4.4.
- if $\mathbf{a} \in D_{\mathbf{p}}$ and $\mathbf{a} + \mathbf{p} \in D_{\mathbf{p}}$ or $\mathbf{a} - \mathbf{p} \in D_{\mathbf{p}}$, but $\mathbf{a} + k\mathbf{p} \notin D_{\mathbf{p}}$ for all other values of k, the associated class has either four real nonzero eigenvalues or a nonzero complex quadruplet of eigenvalues. The values of $\mathbf{a}$ for which this is true are illustrated in Figure 4.5.

These observations are in direct analogy to the observations of Section 2.7.1. We shall formulate this as Conjecture 6.1.10 in Chapter 6. Under particular conditions on $\mathbf{p}$ we can prove in the first case that there is a class with a positive real eigenvalue, leading to linear instability.

4.4.2. Unstable Shear Flows. We now prove that, under a simple condition on $\mathbf{p}$ we can find a corresponding $\mathbf{a}$ such that the class led by $\mathbf{a}$ has a positive real eigenvalue. This then implies linear instability.

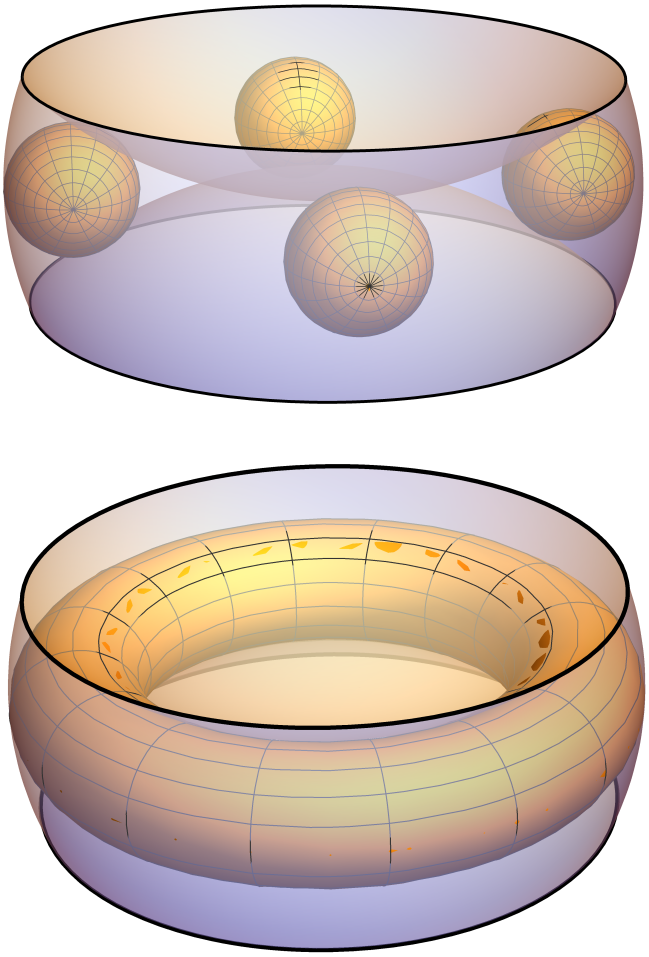

Figure 4.6 – The condition for a lower bound for a real eigenvalue and therefore linear instability. The curved outer surfaces in both figures are $|\mathbf{a}|_{\boldsymbol{\kappa}} = (\sqrt{3}-1)|\mathbf{p}|_{\boldsymbol{\kappa}}$ and $|\mathbf{a} \pm \mathbf{p}|_{\boldsymbol{\kappa}} = |\mathbf{p}|_{\boldsymbol{\kappa}}$. If $\mathbf{a}$ lies within the region enclosed by these surfaces, a lower bound exists. This region is a subset of Figure 4.4. If a lattice point $\mathbf{a}$ lies within the region enclosed by the surfaces, it satisfies the conditions of Lemma 2.7.27 and therefore there is an explicit lower bound for a positive real eigenvalue in the associated class. In Theorem 4.4.1, we show that under a condition on $\mathbf{p}$, such an $\mathbf{a}$ exists. Top: the ellipsoids E_ϕ for $\phi = 0, \frac{\pi}{2}, \pi, \frac{3\pi}{2}$. E_ϕ is enclosed by the surfaces for all ϕ, and thus any $\mathbf{a} \in E_\phi$ satisfies the condition of Lemma 2.7.27. Bottom: the union $\cup_\phi E_\phi$ gives a torus. For this figure, $\mathbf{p} = (1,0,0)$ and $\boldsymbol{\kappa} = (1,1,1)$; for other values, the region is identical up to an affine transformation composed of rotations and scaling.

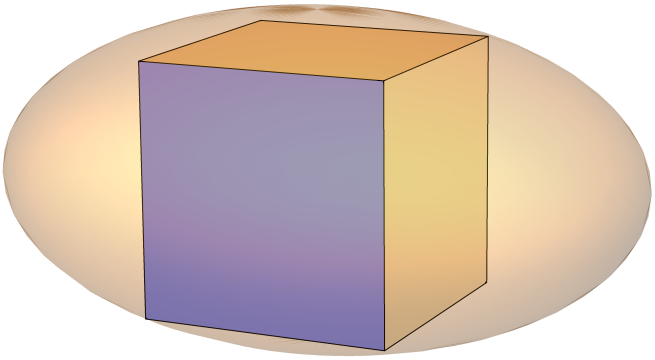

Figure 4.7 – The largest cube contained wholly within the ellipsoid $\frac{x^2}{a^2}+\frac{y^2}{b^2}+\frac{z^2}{c^2} \leq 1$ has side length $d = 2\left(\frac{1}{a^2}+\frac{1}{b^2}+\frac{1}{c^2}\right)^{-1/2}$. If $d > 1$, this cube contains some lattice point $\mathbf{a} \in \mathbb{Z}^3$. This is used to find a lower bound on a positive real eigenvalue in Theorem 4.4.1.

Theorem 4.4.1 (Unstable Shear Flows)**.** *The shear flow steady state*

$$\Omega^* = 2\mathbf{\Gamma}\cos(\langle \mathbf{p}, K^{-1}\mathbf{x}\rangle) \tag{4.4.2}$$

is linearly unstable for all $\mathbf{p}$ *such that*

$$|\mathbf{p}|_{\boldsymbol{\kappa}} > \sqrt{3}+\frac{3}{2}. \tag{4.4.3}$$

Proof. According to Theorem 4.2.59, the spectrum of the class with parameters $\mathbf{a}$, $\mathbf{p}$, $\mathbf{\Gamma}$ is equivalent to the spectrum of a two-dimensional class with parameters $\tilde{a}_x$, $\tilde{a}_y$ given by (4.2.60). The parameters ρ_k in this two-dimensional problem are then given by (4.3.3). According to Lemma 2.7.27, if $\rho_0 < 0$, $\rho_k > 0$ for all $k \neq 0$, and $\rho_0 + \rho_2 < 0$ (or equivalently $\rho_0 + \rho_{-2} < 0$) then there is a real eigenvalue λ of $\tilde{M}_2$ and therefore of $\tilde{\mathcal{M}}$ satisfying

$$\lambda \geq \lambda^* = \sqrt{-\rho_1(\rho_0+\rho_2)}. \tag{4.4.4}$$

The region of $\mathbf{a} \in \mathbb{R}^3$ where these conditions on ρ_k are satisfied is shown in Figure 4.6. We now wish to prove there is a lattice point $\mathbf{a} \in \mathbb{Z}^3$ such that $\rho_0 < 0$, $\rho_k > 0$ for all $k \neq 0$ and $\rho_0 + \rho_2 < 0$. We do so by showing there is a sufficiently large ellipsoid contained within the region in Figure 4.6 that it must contain some integer lattice point.

Consider the family of ellipsoids E_ϕ given by

$$E_\phi = \{\mathbf{x} \in \mathbb{R}^3 \mid |\mathbf{x}-\mathbf{c}(\phi)|_{\boldsymbol{\kappa}} < \left(\frac{2}{\sqrt{3}}-1\right)|\mathbf{p}|_{\boldsymbol{\kappa}}\} \tag{4.4.5}$$

where the centres are given by

$$\mathbf{c}(\phi) = \frac{1}{\sqrt{3}} K^{-1} \left(\frac{\boldsymbol{\Gamma}}{|\boldsymbol{\Gamma}|} |\mathbf{p}|_{\boldsymbol{\kappa}} \cos\phi + (\boldsymbol{\Gamma} \times K\mathbf{p}) \sin\phi \right). \tag{4.4.6}$$

Note that $\langle \mathbf{c}(\phi), \mathbf{p} \rangle = 0$ for all ϕ, and $|\mathbf{c}(\phi)|_{\boldsymbol{\kappa}} = \frac{1}{\sqrt{3}} |\mathbf{p}|_{\boldsymbol{\kappa}}$ as $\boldsymbol{\Gamma}$, $\boldsymbol{\Gamma} \times K\mathbf{p}$ are perpendicular.

If $\mathbf{a} \in E_\phi$, then by the triangle inequality with the $\boldsymbol{\kappa}$-norm

$$\begin{aligned} |\mathbf{a}|_{\boldsymbol{\kappa}} &< |\mathbf{a} - \mathbf{c}(\phi)|_{\boldsymbol{\kappa}} + |\mathbf{c}(\phi)|_{\boldsymbol{\kappa}} \\ &< \left(\frac{2}{\sqrt{3}} - 1 \right) |\mathbf{p}|_{\boldsymbol{\kappa}} + \frac{1}{\sqrt{3}} |\mathbf{p}|_{\boldsymbol{\kappa}} \\ &= (\sqrt{3} - 1) |\mathbf{p}|_{\boldsymbol{\kappa}}. \end{aligned} \tag{4.4.7}$$

So $|\mathbf{a}|_{\boldsymbol{\kappa}} < |\mathbf{p}|_{\boldsymbol{\kappa}}$ and therefore $\rho_0 < 0$. Also,

$$\begin{aligned} |\mathbf{a} + \mathbf{p}|_{\boldsymbol{\kappa}} &\geq |(\mathbf{a} + \mathbf{p}) - (\mathbf{a} - \mathbf{c}(\phi))|_{\boldsymbol{\kappa}} - |\mathbf{a} - \mathbf{c}(\phi)|_{\boldsymbol{\kappa}} \\ &= |\mathbf{p} + \mathbf{c}(\phi)|_{\boldsymbol{\kappa}} - |\mathbf{a} - \mathbf{c}(\phi)|_{\boldsymbol{\kappa}}. \end{aligned} \tag{4.4.8}$$

As $\langle \mathbf{c}(\phi), \mathbf{p} \rangle = 0$, $|\mathbf{p} + \mathbf{c}(\phi)|_{\boldsymbol{\kappa}}^2 = |\mathbf{p}|_{\boldsymbol{\kappa}}^2 + |\mathbf{c}(\phi)|_{\boldsymbol{\kappa}}^2 = \frac{4}{3} |\mathbf{p}|_{\boldsymbol{\kappa}}^2$ and so

$$\begin{aligned} |\mathbf{a} + \mathbf{p}|_{\boldsymbol{\kappa}} &> \frac{2}{\sqrt{3}} |\mathbf{p}|_{\boldsymbol{\kappa}} - \left(\frac{2}{\sqrt{3}} - 1 \right) |\mathbf{p}|_{\boldsymbol{\kappa}} \\ &= |\mathbf{p}|_{\boldsymbol{\kappa}}. \end{aligned} \tag{4.4.9}$$

But $|\mathbf{a} + \mathbf{p}|_{\boldsymbol{\kappa}} > |\mathbf{p}|_{\boldsymbol{\kappa}}$ implies $\rho_1 > 0$. By the same argument on $\mathbf{a} - \mathbf{p}$, $\rho_{-1} > 0$. As $\mathbf{a}$ is in the principal domain $\mathcal{A}$, ρ_k is monotonically increasing for $k > 0$ and monotonically decreasing for $k < 0$. Thus $\rho_k > 0$ for all integers $k \neq 0$.

Also by the triangle inequality, $|\mathbf{a} \pm 2\mathbf{p}|_{\boldsymbol{\kappa}} \leq |\mathbf{a}|_{\boldsymbol{\kappa}} + 2|\mathbf{p}|_{\boldsymbol{\kappa}} < (\sqrt{3} + 1) |\mathbf{p}|_{\boldsymbol{\kappa}}$. By the same argument as Lemma 2.7.30,

$$\begin{aligned} \rho_0 + \rho_2 &= \frac{2}{|\mathbf{p}|_{\boldsymbol{\kappa}}^2} - \frac{1}{|\mathbf{a}|_{\boldsymbol{\kappa}}^2} - \frac{1}{|\mathbf{a} + 2\mathbf{p}|_{\boldsymbol{\kappa}}^2} \\ &< \frac{1}{|\mathbf{p}|_{\boldsymbol{\kappa}}^2} \left(2 - \frac{1}{(\sqrt{3} - 1)^2} - \frac{1}{(\sqrt{3} + 1)^2} \right) \\ &= 0 \end{aligned} \tag{4.4.10}$$

and similarly $\rho_0 + \rho_{-2} < 0$.

Thus if there is an integer lattice point $\mathbf{a} \in E_\phi \cap \mathbb{Z}^3$ for any $\phi \in \mathbb{R}$, then $\rho_0 < 0$, $\rho_k > 0$ for all $k \neq 0$ and $\rho_0 + \rho_{\pm 2} < 0$. We now show that if $|\mathbf{p}|_{\boldsymbol{\kappa}} > \sqrt{3} + \frac{3}{2}$, such an $\mathbf{a}$ exists.

The region inside an ellipsoid

$$\frac{(x - x_0)^2}{a^2} + \frac{(y - y_0)^2}{b^2} + \frac{(z - z_0)^2}{c^2} \leq 1 \tag{4.4.11}$$

contains a cube with side length

$$d = \frac{2}{\sqrt{\frac{1}{a^2} + \frac{1}{b^2} + \frac{1}{c^2}}}. \tag{4.4.12}$$

This is illustrated in Figure 4.7.

For E_ϕ,

$$a = \frac{(2/\sqrt{3} - 1)|\mathbf{p}|_{\boldsymbol{\kappa}}}{\kappa_x}, \quad b = \frac{(2/\sqrt{3} - 1)|\mathbf{p}|_{\boldsymbol{\kappa}}}{\kappa_y}, \quad c = \frac{(2/\sqrt{3} - 1)|\mathbf{p}|_{\boldsymbol{\kappa}}}{\kappa_z}. \tag{4.4.13}$$

so

$$\sqrt{\frac{1}{a^2} + \frac{1}{b^2} + \frac{1}{c^2}} = \frac{1}{(2/\sqrt{3} - 1)\,|\mathbf{p}|_{\boldsymbol{\kappa}}} \sqrt{\kappa_x^2 + \kappa_y^2 + \kappa_z^2} \tag{4.4.14}$$

and so

$$d = 2\left(\frac{2}{\sqrt{3}} - 1\right)|\mathbf{p}|_{\boldsymbol{\kappa}} \tag{4.4.15}$$

as we have normalised $\kappa_x^2 + \kappa_y^2 + \kappa_z^2 = 1$.

If $d > 1$, the cube is guaranteed to contain some integer lattice point, which we can select as our $\mathbf{a}$. Thus a sufficient condition for such an $\mathbf{a}$ to exist is

$$|\mathbf{p}|_{\boldsymbol{\kappa}} > \frac{1}{2\left(\frac{2}{\sqrt{3}} - 1\right)} = \sqrt{3} + \frac{3}{2}. \tag{4.4.16}$$

If such an $\mathbf{a}$ exists, by Theorem 4.2.59 and Lemma 2.7.27, the associated class has a positive real eigenvalue with an explicit lower bound $\lambda^* = \sqrt{-\rho_1(\rho_0 + \rho_2)}$. Including the scaling factor due to the reduced parameter θ, the linearised class has a real eigenvalue larger than $\tilde{a}_y|\sin\theta|\lambda^*$.

As ϕ is arbitrary, we can select ϕ and therefore $\mathbf{a}$ such that $\theta \neq 0, \pi$ and $\sin\theta \neq 0$. This also means the class is not of the nilpotent form described in Section 4.2.9. For instance, we can select $\phi = \frac{\pi}{2}$ and find a corresponding value of $\mathbf{a}$ which cannot be coplanar with $K^{-1}\boldsymbol{\Gamma}, \mathbf{p}$ and $\mathbf{0}$, so $\theta \neq 0, \pi$.

Therefore the class has a positive real eigenvalue and is diagonalisable, and therefore is linearly unstable. □

The region containing lattice points $\mathbf{a}$ with lower bound on a positive real eigenvalue and the ellipsoids E_ϕ are illustrated in Figure 4.6. This figure also shows the union of E_ϕ for all ϕ; this gives a toroidal region. If there is any lattice point $\mathbf{a}$ in this torus, the previous theorem is valid.

It is important to stress here that the condition $|\mathbf{p}|_{\boldsymbol{\kappa}} > \sqrt{3} + 3/2$ is sufficient, but not necessary. In fact, numerical experiments suggests that all flows not of the form described in Theorem 4.3.6 will be unstable. This statement is discussed in Conjecture 6.1.10. However, for a fixed domain size $\boldsymbol{\kappa}$ Theorem 4.4.1 proves instability for all but finitely many values of the parameter $\mathbf{p}$. Figure 4.8 shows all

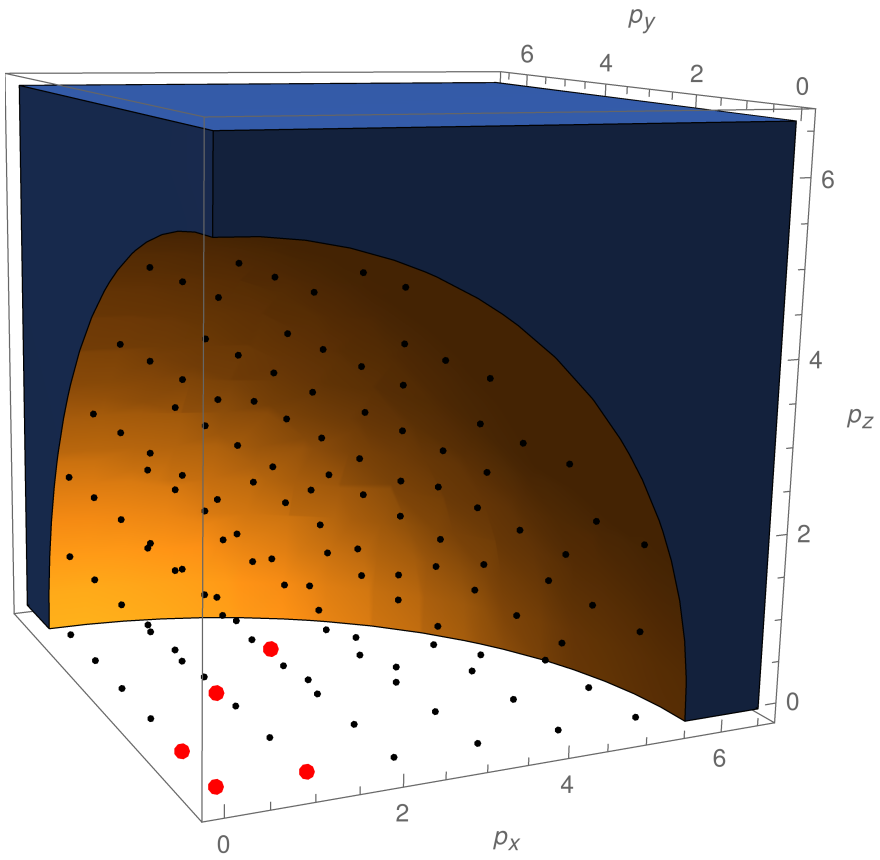

Figure 4.8 – Valid values of $\mathbf{p}$ for the sufficient condition for instability in Theorem 4.4.1. In this figure, the isotropic case $\boldsymbol{\kappa} = (1, 1, 1)$ is used. If $\mathbf{p}$ is in the solid region indicated, $\mathbf{p}$ satisfies (4.4.16) and so there is instability. For the values of $\mathbf{p}$ outside this region indicated by small black dots, there is still a corresponding $\mathbf{a} \in \mathbb{Z}^3$ such that we can guarantee the class contains a positive real eigenvalue and thus conclude instability. For values of $\mathbf{p}$ indicated as large red points, there are no valid values of $\mathbf{a}$ such that the lower bound is real, so we cannot use the proof for instability. Note that there are only a small number of these points: $\mathbf{p} = (1, 00), (0, 1, 0), (0, 0, 1), (1, 1, 1)$. This is likely due to the high probability of a lattice point existing in the larger region in Figure 4.6 that is not captured by the argument showing a lattice point in E_ϕ. For other values of $\boldsymbol{\kappa}$, the size of the region will change.

$\mathbf{p}$ satisfying the sufficient condition for a fixed $\boldsymbol{\kappa}$. Note that there is no required condition on $\boldsymbol{\Gamma}$ beyond $\theta \neq 0, \pi$, reflecting the idea that $\boldsymbol{\Gamma}$ has limited influence on the stability of the shear flow.

To summarise the stability results of this chapter, we have shown analytically that

- if $\mathbf{p} = (p_x, 0, 0)$, $\kappa_y, \kappa_z > \kappa_x |p_x|$ and $\frac{\kappa_z \Gamma_y}{\kappa_y \Gamma_z} \notin \mathbb{Q}$, the flow is linearly stable (Theorem 4.3.6);
- if $\mathbf{p} = (p_x, 0, 0)$ and $\Gamma_z = 0$ or $\frac{\kappa_z \Gamma_y}{\kappa_y \Gamma_z} \in \mathbb{Q}$, there is at least one class with linear growth which contributes instability (Proposition 4.2.70);
- if $|\mathbf{p}|_{\boldsymbol{\kappa}} > \sqrt{3} + 3/2$, the flow is linearly unstable (Theorem 4.4.1);
- if $\boldsymbol{\Gamma}$ can be expressed in the form in Proposition 4.2.64, there are classes with linear growth which contribute linear instability.

A discussion of the full spectrum of the linearised problem is included in Chapter 6 and formulated as Conjecture 6.1.10.

Chapter 5

Poisson Structure of the Three-Dimensional Euler Equations in Fourier Space

In Chapter 2, we formulated the Euler equations on a two-dimensional domain as a Poisson system (2.3.2), (2.3.7). This is a well-known result based on the observation that the dynamics of the Euler equations can be described by geodesics on the group of volume preserving diffeomorphisms [**AK98, Zha08**]. In this chapter we prove that the Euler equations on a three-dimensional periodic domain can also be formulated as a Poisson system in terms of the vorticity Fourier coefficients. This is a significant new result, as a Poisson structure means we have access to the theory of Poisson dynamics and the associated ideas such as energy-Casimir stability.

We first show that the Poisson structure exists by writing the system in terms of ordinary differential equations on the Fourier coefficients of the vorticity, and show that this is a Poisson structure. To do so we prove that the structure satisfies the properties of a Poisson bracket per Section 2.1. We then calculate the same structure on the divergence-free subspace. This is a simpler Poisson manifold, so for instance stability analysis of this system is mechanically simpler. However, the Poisson structure on the divergence-free subspace is significantly more complicated algebraically.

5.1. Poisson Structure on a Three-Dimensional Periodic Domain

In Section 4.1.1 the Euler equations on a periodic domain are written in terms of the vorticity Fourier coefficients as

$$\dot{\boldsymbol{\omega}}_{\mathbf{j}} = \sum_{\mathbf{k}} A(\mathbf{j},\mathbf{k}) \frac{\boldsymbol{\omega}_{-\mathbf{k}}}{|\mathbf{k}|_{\boldsymbol{\kappa}}^2} \tag{5.1.1}$$

where

$$A(\mathbf{j},\mathbf{k}) = \left(\boldsymbol{\omega}_{\mathbf{j}+\mathbf{k}} [(K\mathbf{k}) \times (K\mathbf{j})]^{\mathsf{T}} - \langle \mathbf{k}, K^{-1}\boldsymbol{\omega}_{\mathbf{j}+\mathbf{k}} \rangle \widehat{K\mathbf{k}} \right). \tag{5.1.2}$$

However, the dynamics of the Euler equations only occur on the divergence free subspace given by the constraint $\langle \mathbf{j}, K^{-1}\boldsymbol{\omega}_{\mathbf{j}} \rangle = 0$ for all $\mathbf{j} \in \mathbb{Z}^3$. Thus we

define

$$\begin{aligned} B(\mathbf{j},\mathbf{k}) &:= A(\mathbf{j},\mathbf{k}) - \frac{1}{2}\langle \mathbf{j}+\mathbf{k}, K^{-1}\boldsymbol{\omega}_{\mathbf{k}+\mathbf{j}}\rangle \widehat{K(\mathbf{j}-\mathbf{k})} \\ &= \boldsymbol{\omega}_{\mathbf{j}+\mathbf{k}}[(K\mathbf{k})\times(K\mathbf{j})]^{\mathsf{T}} + \frac{1}{2}\langle \mathbf{j}-\mathbf{k}, K^{-1}\boldsymbol{\omega}_{\mathbf{j}+\mathbf{k}}\rangle \widehat{K\mathbf{k}} \\ &\quad - \frac{1}{2}\langle \mathbf{j}+\mathbf{k}, K^{-1}\boldsymbol{\omega}_{\mathbf{j}+\mathbf{k}}\rangle \widehat{K\mathbf{j}}. \end{aligned} \tag{5.1.3}$$

On the divergence-free subspace (4.1.13), $A(\mathbf{j},\mathbf{k}) = B(\mathbf{j},\mathbf{k})$ and so the Euler equations (4.1.21) can be written as

$$\dot{\boldsymbol{\omega}}_{\mathbf{j}} = \sum_{\mathbf{k}} B(\mathbf{j},\mathbf{k})\frac{\boldsymbol{\omega}_{-\mathbf{k}}}{|\mathbf{k}|^2_{\boldsymbol{\kappa}}}. \tag{5.1.4}$$

We now show that by writing the differential equations in this form, the Euler equations on a three-dimensional periodic domain are a Poisson system.

Theorem 5.1.5 (Poisson Structure for Three-Dimensional Euler Equations)**.** *The dynamics of the three-dimensional Euler equations for an incompressible, inviscid flow are given by the Poisson system with Poisson bracket*

$$\{f,g\} = \sum_{\mathbf{j},\mathbf{k}\in\mathbb{Z}^3} (\frac{\partial f}{\partial \boldsymbol{\omega}_{\mathbf{j}}})^{\mathsf{T}} B(\mathbf{j},\mathbf{k})(\frac{\partial g}{\partial \boldsymbol{\omega}_{\mathbf{k}}}) \tag{5.1.6}$$

where $B(\mathbf{j},\mathbf{k})$ *is given by* (5.1.3) *and the Hamiltonian*

$$H = \frac{1}{2}\sum_{\mathbf{j}\in\mathbb{Z}^3\setminus\{\mathbf{0}\}} \frac{\boldsymbol{\omega}_{-\mathbf{j}}^{\mathsf{T}}\boldsymbol{\omega}_{\mathbf{j}}}{|\mathbf{j}|^2_{\boldsymbol{\kappa}}} \tag{5.1.7}$$

on the Poisson manifold

$$\mathcal{M} = \{\boldsymbol{\omega}_{\mathbf{j}} \in \mathbb{R}^3 \ \mid \ \mathbf{j}\in\mathbb{Z}^3,\ \mathbf{j}^{\mathsf{T}}K\boldsymbol{\omega}_{\mathbf{j}} = 0\}. \tag{5.1.8}$$

Proof. The manifold $\mathcal{M}$ is the divergence-free subspace (4.1.13) on which our dynamics are defined. The dynamics are

$$\begin{aligned} \dot{\boldsymbol{\omega}}_{\mathbf{j}} &= \{\boldsymbol{\omega}_{\mathbf{j}}, H\} \\ &= \sum_{\mathbf{k}\neq\mathbf{0}} B(\mathbf{j},\mathbf{k})\frac{\boldsymbol{\omega}_{-\mathbf{k}}}{|\mathbf{k}|^2_{\boldsymbol{\kappa}}}, \end{aligned} \tag{5.1.9}$$

which are the dynamics of the Euler equations by (5.1.4).

We now confirm that the bracket (5.1.6) satisfies the properties in Definition 2.1.1. One can check

$$\begin{aligned}\{g,f\} &= \sum_{\mathbf{k},\mathbf{j}\in\mathbb{Z}^3} (\frac{\partial g}{\partial \boldsymbol{\omega}_\mathbf{k}})^\mathsf{T} B(\mathbf{k},\mathbf{j})(\frac{\partial f}{\partial \boldsymbol{\omega}_\mathbf{j}}) \\ &= -\sum_{\mathbf{k},\mathbf{j}\in\mathbb{Z}^3} (\frac{\partial g}{\partial \boldsymbol{\omega}_\mathbf{k}})^\mathsf{T} B(\mathbf{j},\mathbf{k})^\mathsf{T} (\frac{\partial f}{\partial \boldsymbol{\omega}_\mathbf{j}}) \\ &= -\sum_{\mathbf{k},\mathbf{j}\in\mathbb{Z}^3} \left((\frac{\partial f}{\partial \boldsymbol{\omega}_\mathbf{j}})^\mathsf{T} B(\mathbf{j},\mathbf{k}) (\frac{\partial g}{\partial \boldsymbol{\omega}_\mathbf{k}}) \right)^\mathsf{T} \\ &= -\{f,g\}\end{aligned} \tag{5.1.10}$$

as $B(\mathbf{j},\mathbf{k})+B(\mathbf{k},\mathbf{j})^\mathsf{T}=0$ and so the bracket satisfies antisymmetry. It also satisfies bilinearity as the bracket is linear in the partial derivatives.

We must also check the bracket satisfies the Jacobi property via the condition (2.1.5). In this case the condition is

$$\begin{aligned} 0 &= \sum_{\delta\in\{x,y,z\},\mathbf{l}\in\mathbb{Z}^3} \Bigg(B(\mathbf{i},\mathbf{l})_{\alpha,\delta} \frac{\partial B(\mathbf{j},\mathbf{k})_{\beta,\gamma}}{\partial \omega_{\mathbf{l},\delta}} \\ &\qquad + B(\mathbf{j},\mathbf{l})_{\alpha,\delta} \frac{\partial B(\mathbf{j},\mathbf{k})_{\beta,\gamma}}{\partial \omega_{\mathbf{l},\delta}} + B(\mathbf{k},\mathbf{l})_{\alpha,\delta} \frac{\partial B(\mathbf{j},\mathbf{k})_{\beta,\gamma}}{\partial \omega_{\mathbf{l},\delta}} \Bigg) \\ &= \sum_{\delta\in\{x,y,z\}} \Bigg(B(\mathbf{i},\mathbf{j}+\mathbf{k})_{\alpha,\delta} \frac{\partial B(\mathbf{j},\mathbf{k})_{\beta,\gamma}}{\partial \omega_{\mathbf{j}+\mathbf{k},\delta}} \\ &\qquad + B(\mathbf{j},\mathbf{k}+\mathbf{i})_{\beta,\delta} \frac{\partial B(\mathbf{k},\mathbf{i})_{\gamma,\alpha}}{\partial \omega_{\mathbf{j}+\mathbf{k},\delta}} + B(\mathbf{k},\mathbf{i}+\mathbf{j})_{\gamma,\delta} \frac{\partial B(\mathbf{i},\mathbf{j})_{\alpha,\beta}}{\partial \omega_{\mathbf{j}+\mathbf{k},\delta}} \Bigg) \end{aligned} \tag{5.1.11}$$

for all $\alpha,\beta,\gamma \in \{x,y,z\}$ and $\mathbf{i},\mathbf{j},\mathbf{k} \in \mathbb{Z}^3$. We have used the notation $\boldsymbol{\omega}_\mathbf{j} = (\omega_{\mathbf{j},x}, \omega_{\mathbf{j},y}, \omega_{\mathbf{j},z})$ and similar notation for the matrix $B(\mathbf{j},\mathbf{k})$. This can be directly verified from the definition of $B(\mathbf{j},\mathbf{k})$. Although physically relevant dynamics only occur on the manifold $\mathcal{M}$, the Jacobi property and antisymmetry are both satisfied for all $\boldsymbol{\omega}_\mathbf{j} \in \mathbb{R}^3$. We can thus consider the Poisson system on the manifold $\mathcal{M}$ an invariant subsystem of a larger system without the divergence-free restriction.

Thus the system given by (5.1.6), (5.1.7) and (5.1.8) is a Poisson system, and generates the dynamics of the Euler equations on a three-dimensional periodic domain. □

Note that the extension of the structure from the divergence-free subspace to the full space of $\boldsymbol{\omega}_\mathbf{j} \in \mathbb{R}^3$ is not always possible for a generic Poisson system; see

for instance [**Egi95**]. The existence of this extension means we can avoid some technical difficulties.

Having a Poisson formulation of our system is very useful as it allows us to utilise the ideas and language of Hamiltonian mechanics. However, analysing the system is hindered by the fact that we are on the manifold $\mathcal{M}$ so any study of stability is restricted to perturbations on this manifold. Fortunately, $\mathcal{M}$ is a simple manifold topologically equivalent to $\mathbb{R}^{2n}$ so we can rewrite the system in a more convenient way.

5.2. Poisson Structure on the Divergence-Free Subspace

We wish to explicitly restrict our system to the manifold $\mathcal{M}$ defined by the divergence free subspace $\mathbf{j}^\mathsf{T} K\boldsymbol{\omega}_\mathbf{j} = 0$ for all $\mathbf{j}$. Then we can write the Poisson system as a lower-dimensional system on a simpler manifold.

To do so, for each $\mathbf{j} \in \mathbb{Z}^3$ introduce the rotation matrix $R_\mathbf{j} \in SO(3)$ that rotates $K\mathbf{j}$ parallel to the x-axis. As $R_\mathbf{j}$ is a rotation matrix, $\det(R_\mathbf{j}) = 1$ and $R_\mathbf{j}^\mathsf{T} R_\mathbf{j} = R_\mathbf{j} R_\mathbf{j}^\mathsf{T} = \mathbb{I}$. We also wish to ensure that $R_\mathbf{j}(K\mathbf{j}) = -R_{-\mathbf{j}}(-K\mathbf{j})$ so $R_\mathbf{j} = R_{-\mathbf{j}}$ and the same rotation is applied to both $\pm K\mathbf{j}$. This means that

$$R_\mathbf{j} K\mathbf{j} = \begin{pmatrix} \pm|\mathbf{j}|_{\boldsymbol{\kappa}} \\ 0 \\ 0 \end{pmatrix}, \quad R_{-\mathbf{j}}(-K\mathbf{j}) = \begin{pmatrix} \mp|\mathbf{j}|_{\boldsymbol{\kappa}} \\ 0 \\ 0 \end{pmatrix}. \tag{5.2.1}$$

To do so, we need some concept of "positive" vectors in $\mathbb{R}^3$. Define a function $\Delta_\mathbf{j} : \mathbb{R}^3 \setminus \{\mathbf{0}\} \to \{+1, -1\}$ such that $\Delta_\mathbf{j} + \Delta_{-\mathbf{j}} = 0$ for all $\mathbf{j}$ in the domain. Note that $\Delta_\mathbf{j}^2 = 1$ for all $\mathbf{j} \neq \mathbf{0}$. We do not need to worry about the specific form of the function as long as it partitions the domain into a "positive" half and "negative" half. A particular choice of $\Delta_\mathbf{j}$ where $\mathbf{j} = (j_x, j_y, j_z)$ is

$$\Delta_\mathbf{j} = \begin{cases} 1 \text{ if } (j_x > 0) \text{ or } (j_x = 0,\ j_y > 0) \\ \qquad \text{or } (j_x = 0,\ j_y = 0,\ j_z > 0), \\ -1 \text{ if } (j_x < 0) \text{ or } (j_x = 0,\ j_y < 0) \\ \qquad \text{or } (j_x = 0,\ j_y = 0,\ j_z < 0). \end{cases} \tag{5.2.2}$$

Having made some choice of function $\Delta_\mathbf{j}$, we can now define the required rotation matrix. Define the norm on the y and z components

$$|\mathbf{j}|_{y-z} := \sqrt{j_y^2 + j_z^2}. \tag{5.2.3}$$

Then let

$$\tilde{R}(\mathbf{j}) := \frac{1}{|\mathbf{j}||\mathbf{j}|_{y-z}} \begin{pmatrix} j_x|\mathbf{j}|_{y-z} & j_x|\mathbf{j}|_{y-z} & j_x|\mathbf{j}|_{y-z} \\ 0 & -j_z|\mathbf{j}|^2 & j_y|\mathbf{j}|^2 \\ |\mathbf{j}|_{y-z}^2 & -j_x j_y & -j_x j_z \end{pmatrix} \tag{5.2.4}$$

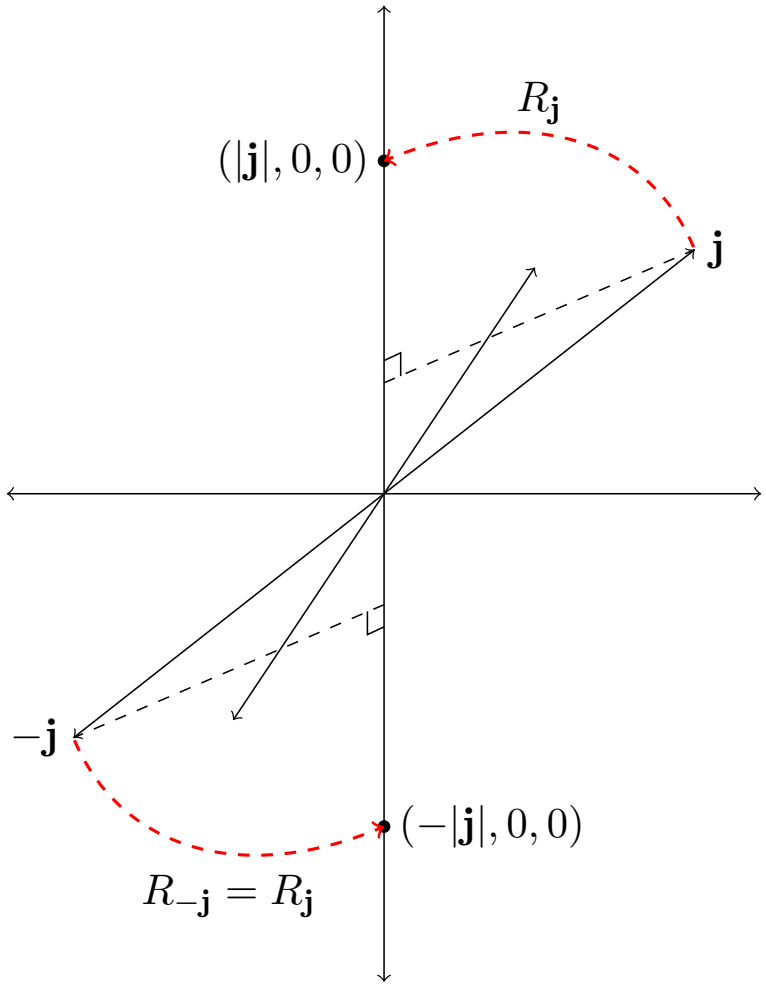

Figure 5.1 – To project the Poisson system onto the divergence-free manifold, introduce new coordinates $\tilde{\boldsymbol{\omega}}_{\mathbf{j}} = R_{\mathbf{j}}\boldsymbol{\omega}_{\mathbf{j}}$ where $R_{\mathbf{j}}$ is a rotation matrix such that $R_{\mathbf{j}}\mathbf{j}$ is parallel to the x-axis. For the resulting system to be Poisson, we also need $R_{\mathbf{j}} = R_{-\mathbf{j}}$. To do so, we need to "cut" $\mathbb{R}^3 \setminus \{\mathbf{0}\}$ in half, to rotate half of the vectors $\mathbf{j}$ to the positive x-axis, and the other half to the negative x-axis. Here we have shown $K = \mathbb{I}$; otherwise, we rotate $K\mathbf{j}$ rather than $\mathbf{j}$.

so $\tilde{R}(\mathbf{j})$ is a rotation matrix such that

$$\tilde{R}(\mathbf{j})\mathbf{j} = \begin{pmatrix} |\mathbf{j}| \\ 0 \\ 0 \end{pmatrix} \tag{5.2.5}$$

for all $\mathbf{j}$. To adjust for both $\Delta_{\mathbf{j}}$ and $K \neq \mathbb{I}$, define

$$R_{\mathbf{j}} := \tilde{R}(\Delta_{\mathbf{j}} K\mathbf{j}) \tag{5.2.6}$$

so $R_{\mathbf{j}} K\mathbf{j} = (\Delta_{\mathbf{j}}|\mathbf{j}|_{\boldsymbol{\kappa}}, 0, 0)$ for all $\mathbf{j} \neq \mathbf{0}$, as required. The action of this rotation is illustrated in Figure 5.1.

Compare this to the rotation matrix (4.2.3). Although both matrices rotate a given vector to align with the x-axis, the use is different in each case. In Section 4.2.2, the linearised modes were all rotated by the same matrix, to align the $\mathbf{p}$ parameter that defines the equilibrium with the x-axis. In the nonlinear system here, each mode is separately rotated by a different rotation matrix to align the mode so the divergence-free condition implies that one of the coordinates is zero.

Now the divergence-free condition becomes

$$\begin{aligned} 0 &= \mathbf{j}^{\mathsf{T}} K \boldsymbol{\omega}_{\mathbf{j}} \\ &= \mathbf{j}^{\mathsf{T}} K R_{\mathbf{j}}^{\mathsf{T}} R_{\mathbf{j}} \boldsymbol{\omega}_{\mathbf{j}} \\ &= (R_{\mathbf{j}} K \mathbf{j})^{\mathsf{T}} (R_{\mathbf{j}} \boldsymbol{\omega}_{\mathbf{j}}). \end{aligned} \tag{5.2.7}$$

Thus if we define $\bar{\boldsymbol{\omega}}_{\mathbf{j}} := R_{\mathbf{j}} \boldsymbol{\omega}_{\mathbf{j}}$,

$$(\Delta_{\mathbf{j}}|K\mathbf{j}|, 0, 0)^{\mathsf{T}} \bar{\boldsymbol{\omega}}_{\mathbf{j}} = 0 \tag{5.2.8}$$

and thus the first element of $\bar{\boldsymbol{\omega}}_{\mathbf{j}}$ must be zero and have trivial constant dynamics. This allows us to project down to the divergence-free subspace and still capture the full dynamics.

Proposition 5.2.9 (Reduced Poisson structure of three-dimensional Euler equations)**.** *The Poisson structure given by* (5.1.6), (5.1.7) *and* (5.1.8) *can be written as*

$$\{f, g\} = \sum_{\mathbf{j},\mathbf{k} \in \mathbb{Z}^3} \left(\frac{\partial f}{\partial \tilde{\boldsymbol{\omega}}_{\mathbf{j}}}\right)^{\mathsf{T}} \tilde{B}(\mathbf{j}, \mathbf{k}) \left(\frac{\partial g}{\partial \tilde{\boldsymbol{\omega}}_{\mathbf{k}}}\right) \tag{5.2.10}$$

for a function $\tilde{B}(\mathbf{j}, \mathbf{k}) : \mathbb{Z}^3 \times \mathbb{Z}^3 \to \mathbb{R}^{2\times 2}$

$$\tilde{H} = \frac{1}{2} \sum_{\mathbf{j} \in \mathbb{Z}^3 \setminus \{\mathbf{0}\}} \frac{\tilde{\boldsymbol{\omega}}_{-\mathbf{j}}^{\mathsf{T}} \tilde{\boldsymbol{\omega}}_{\mathbf{j}}}{|\mathbf{j}|_{\boldsymbol{\kappa}}^2} \tag{5.2.11}$$

on the phase space manifold

$$\tilde{\mathcal{M}} = \{\tilde{\boldsymbol{\omega}}_{\mathbf{j}} \in \mathbb{R}^2 \mid \mathbf{j} \in \mathbb{Z}^3\}. \tag{5.2.12}$$

Then the dynamics of the Poisson system

$$\dot{\tilde{\boldsymbol{\omega}}}_{\mathbf{j}} = \{\tilde{\boldsymbol{\omega}}_{\mathbf{j}}, \tilde{H}\} \tag{5.2.13}$$

are equivalent to the dynamics of (5.1.4)*, the Euler ideal fluid equations.*

Proof. Define $\bar{\boldsymbol{\omega}}_{\mathbf{j}} = R_{\mathbf{j}} \boldsymbol{\omega}_{\mathbf{j}}$ with $R_{\mathbf{j}}$ as above. Then if $\bar{\boldsymbol{\omega}}_{\mathbf{j}} = (\bar{\omega}_{\mathbf{j},x}, \bar{\omega}_{\mathbf{j},z}, \bar{\omega}_{\mathbf{j},y})$, the divergence-free condition implies that $\bar{\omega}_{\mathbf{j},x}$ is constant and zero for all $\mathbf{j}$.

Define

$$\begin{aligned}\bar{B}(\mathbf{j},\mathbf{k}) &:= R_{\mathbf{j}} B(\mathbf{j},\mathbf{k}) R_{-\mathbf{k}}^{\mathsf{T}} \\ &= R_{\mathbf{j}}\Big[(R_{\mathbf{j}+\mathbf{k}}^{\mathsf{T}}\bar{\boldsymbol{\omega}}_{\mathbf{j}+\mathbf{k}})(K\mathbf{k}\times K\mathbf{j})^{\mathsf{T}} \\ &\quad - \langle \mathbf{k}, K^{-1}R_{\mathbf{j}+\mathbf{k}}^{\mathsf{T}}\bar{\boldsymbol{\omega}}_{\mathbf{j}+\mathbf{k}}\rangle \widehat{K\mathbf{k}} \\ &\quad - \frac{1}{2}\langle \mathbf{j}+\mathbf{k}, K^{-1}R_{\mathbf{j}+\mathbf{k}}^{\mathsf{T}}\bar{\boldsymbol{\omega}}_{\mathbf{j}+\mathbf{k}}\rangle \widehat{K(\mathbf{j}-\mathbf{k})}\Big] R_{-\mathbf{k}}^{\mathsf{T}}.\end{aligned} \tag{5.2.14}$$

Then the dynamics of $\bar{\boldsymbol{\omega}}_{\mathbf{j}}$ are

$$\dot{\bar{\boldsymbol{\omega}}}_{\mathbf{j}} = \sum_{\mathbf{j},\mathbf{k}} \bar{B}(\mathbf{j},\mathbf{k})\frac{\bar{\boldsymbol{\omega}}_{-\mathbf{k}}}{|\mathbf{k}|_{\boldsymbol{\kappa}}^2}. \tag{5.2.15}$$

By direct calculation,

$$\bar{B}(\mathbf{j},\mathbf{k})_{x,y} = \bar{B}(\mathbf{j},\mathbf{k})_{x,z} = 0 \tag{5.2.16}$$

if $\bar{\omega}_{\mathbf{j},x} = 0$. Thus the divergence-free subspace is invariant, as expected.

Thus we can ignore the coordinate $\bar{\omega}_{\mathbf{j},x}$ and define $\tilde{\boldsymbol{\omega}}_{\mathbf{j}} = (\bar{\omega}_{\mathbf{j},y}, \bar{\omega}_{\mathbf{j},z})$. Similarly, define

$$\tilde{B}(\mathbf{j},\mathbf{k}) = \begin{pmatrix} \bar{B}(\mathbf{j},\mathbf{k})_{y,y} & \bar{B}(\mathbf{j},\mathbf{k})_{y,z} \\ \bar{B}(\mathbf{j},\mathbf{k})_{z,y} & \bar{B}(\mathbf{j},\mathbf{k})_{z,z}\end{pmatrix}. \tag{5.2.17}$$

The form of $\tilde{B}(\mathbf{j},\mathbf{k}) : \mathbb{Z}^3\times\mathbb{Z}^3 \to \mathbb{R}^{2\times 2}$ is quite complicated. It can be directly confirmed that this satisfies the antisymmetry and Jacobi identity conditions for a Poisson structure matrix, due to the form of the rotation matrices $R_{\mathbf{j}}$ and the property $R_{\mathbf{j}} = R_{-\mathbf{j}}$. The Hamiltonian on the new coordinates is

$$\tilde{H} = \frac{1}{2}\sum_{\mathbf{j}\in\mathbb{Z}^3\setminus\{\mathbf{0}\}} \frac{\tilde{\boldsymbol{\omega}}_{-\mathbf{j}}^{\mathsf{T}}\tilde{\boldsymbol{\omega}}_{\mathbf{j}}}{|\mathbf{j}|_{\boldsymbol{\kappa}}^2}. \tag{5.2.18}$$

As the coordinates $\tilde{\boldsymbol{\omega}}_{\mathbf{j}}$ are no longer restricted by the divergence-free condition, the Poisson manifold is the full space of $\tilde{\boldsymbol{\omega}}_{\mathbf{j}} \in \mathbb{R}^2$ for all $\mathbf{j}\in\mathbb{Z}^2$. Then the Poisson bracket (5.2.10) with structure matrix $\tilde{B}(\mathbf{j},\mathbf{k})$ and the Hamiltonian $\tilde{H}$ generate the dynamics of the Euler equations in the new coordinates $\tilde{\boldsymbol{\omega}}_{\mathbf{j}}$. □

We now explicitly calculate

$$\begin{aligned}\tilde{B}(\mathbf{j},\mathbf{k}) &= \begin{pmatrix} \tilde{B}_y(\mathbf{j},\mathbf{k})_{y,y} & \tilde{B}_y(\mathbf{j},\mathbf{k})_{y,z} \\ \tilde{B}_y(\mathbf{j},\mathbf{k})_{z,y} & \tilde{B}_y(\mathbf{j},\mathbf{k})_{z,z}\end{pmatrix}\bar{\omega}_{\mathbf{j}+\mathbf{k},y} \\ &\quad + \begin{pmatrix} \tilde{B}_z(\mathbf{j},\mathbf{k})_{y,y} & \tilde{B}_z(\mathbf{j},\mathbf{k})_{y,z} \\ \tilde{B}_z(\mathbf{j},\mathbf{k})_{z,y} & \tilde{B}_z(\mathbf{j},\mathbf{k})_{z,z}\end{pmatrix}\bar{\omega}_{\mathbf{j}+\mathbf{k},z}\end{aligned} \tag{5.2.19}$$

where $\tilde{B}_y(\mathbf{j},\mathbf{k})_{i,j}$, $\tilde{B}_z(\mathbf{j},\mathbf{k})_{i,j}$ are constant as $\tilde{B}(\mathbf{j},\mathbf{k})$ is linear in $\tilde{\boldsymbol{\omega}}_{\mathbf{j}+\mathbf{k}}$.

Define $\langle \mathbf{j},\mathbf{k}\rangle_{y-z} := \kappa_y^2 j_y k_y + \kappa_z^2 j_z k_z$ and $|\mathbf{j}|_{\boldsymbol{\kappa},y-z} := \sqrt{\langle \mathbf{j},\mathbf{j}\rangle_{y-z}}$. Now

$$\begin{aligned}\tilde{B}_y(\mathbf{j},\mathbf{k})_{y,y} =& \Big(\kappa_x j_x |\mathbf{k}|^2_{\boldsymbol{\kappa},y-z} \langle \mathbf{j},\mathbf{j}+\mathbf{k}\rangle_{y-z} \\ &- \kappa_x k_x |\mathbf{j}|^2_{\boldsymbol{\kappa},y-z} \langle \mathbf{k},\mathbf{j}+\mathbf{k}\rangle_{y-z} \Big) \\ &\times \frac{|\mathbf{j}|_{\boldsymbol{\kappa}}|\mathbf{k}|_{\boldsymbol{\kappa}}|\mathbf{j}+\mathbf{k}|_{\boldsymbol{\kappa}}\Delta_{\mathbf{j}}\Delta_{-\mathbf{k}}\Delta_{\mathbf{j}+\mathbf{k}}}{|\mathbf{j}|_{\boldsymbol{\kappa},y-z}|\mathbf{k}|_{\boldsymbol{\kappa},y-z}|\mathbf{j}+\mathbf{k}|_{\boldsymbol{\kappa},y-z}}.\end{aligned} \tag{5.2.20}$$

$$\tilde{B}_y(\mathbf{j},\mathbf{k})_{y,z} = ((K\mathbf{k})\times(K\mathbf{j}))_x \frac{|\mathbf{j}|_{\boldsymbol{\kappa},y-z}|\mathbf{j}|_{\boldsymbol{\kappa}}|\mathbf{k}|_{\boldsymbol{\kappa}}|\mathbf{j}+\mathbf{k}|_{\boldsymbol{\kappa}}\Delta_{\mathbf{j}}\Delta_{\mathbf{j}+\mathbf{k}}}{|\mathbf{k}|_{\boldsymbol{\kappa},y-z}|\mathbf{j}+\mathbf{k}|_{\boldsymbol{\kappa},y-z}}, \tag{5.2.21}$$

$$\tilde{B}_y(\mathbf{j},\mathbf{k})_{z,y} = -\tilde{B}_y(\mathbf{k},\mathbf{j})_{y,z}, \tag{5.2.22}$$

$$\tilde{B}_y(\mathbf{j},\mathbf{k})_{z,z} = 0. \tag{5.2.23}$$

$$\begin{aligned}\tilde{B}_z(\mathbf{j},\mathbf{k})_{y,y} =& (K\mathbf{j}\times K\mathbf{k})_x \left((K\mathbf{j}\times K\mathbf{k})_y^2 + (K\mathbf{j}\times K\mathbf{k})_z^2 \right) \\ &\times \frac{|\mathbf{j}|_{\boldsymbol{\kappa}}|\mathbf{k}|_{\boldsymbol{\kappa}}\Delta_{\mathbf{j}}\Delta_{\mathbf{k}}}{|\mathbf{j}|_{\boldsymbol{\kappa},y-z}|\mathbf{k}|_{\boldsymbol{\kappa},y-z}|\mathbf{j}+\mathbf{k}|_{\boldsymbol{\kappa},y-z}|\mathbf{j}+\mathbf{k}|_{\boldsymbol{\kappa}}}\end{aligned} \tag{5.2.24}$$

$$\begin{aligned}\tilde{B}_z(\mathbf{j},\mathbf{k})_{y,z} =& \big[\kappa_y j_y \kappa_y k_y (\kappa_y j_y + \kappa_y k_y)(K\mathbf{k}\times K\mathbf{j})_z \\ &- \kappa_z j_z \kappa_z k_z (\kappa_z j_z + \kappa_z k_z)(K\mathbf{k}\times K\mathbf{j})_y \\ &+ (K\mathbf{j}\times K\mathbf{k})_x \big((K\mathbf{j}\times K\mathbf{k})_x (\kappa_x j_x + \kappa_x k_x) \\ &- (\kappa_x k_x \kappa_y j_y \kappa_z j_z + \kappa_x j_x \kappa_y k_y \kappa_z k_z) \big) \\ &- 2(K\mathbf{j}\times K\mathbf{k})_z \kappa_z j_z \kappa_z k_z (\kappa_y j_y + \kappa_y k_y) \big] \\ &\times \frac{|\mathbf{j}|_{\boldsymbol{\kappa}}|\mathbf{k}|_{\boldsymbol{\kappa}}\Delta_{\mathbf{j}}}{|\mathbf{j}|_{\boldsymbol{\kappa},y-z}|\mathbf{k}|_{\boldsymbol{\kappa},y-z}|\mathbf{j}+\mathbf{k}|_{\boldsymbol{\kappa},y-z}|\mathbf{j}+\mathbf{k}|_{\boldsymbol{\kappa}}},\end{aligned} \tag{5.2.25}$$

$$\tilde{B}_z(\mathbf{j},\mathbf{k})_{z,y} = -\tilde{B}_z(\mathbf{k},\mathbf{j})_{y,z}. \tag{5.2.26}$$

$$\tilde{B}_z(\mathbf{j},\mathbf{k})_{z,z} = (K\mathbf{j}\times K\mathbf{k})_x \frac{|\mathbf{j}|_{\boldsymbol{\kappa}}|\mathbf{k}|_{\boldsymbol{\kappa}}|\mathbf{j}+\mathbf{k}|_{\boldsymbol{\kappa},y-z}}{|\mathbf{j}|_{\boldsymbol{\kappa},y-z}|\mathbf{k}|_{\boldsymbol{\kappa},y-z}|\mathbf{j}+\mathbf{k}|_{\boldsymbol{\kappa}}} \tag{5.2.27}$$

One can confirm the conditions for antisymmetry

$$\begin{aligned}\tilde{B}_y(\mathbf{j},\mathbf{k})_{y,y}+\tilde{B}_y(\mathbf{k},\mathbf{j})_{y,y}&=0,\\ \tilde{B}_y(\mathbf{j},\mathbf{k})_{z,z}+\tilde{B}_y(\mathbf{k},\mathbf{j})_{z,z}&=0,\\ \tilde{B}_z(\mathbf{j},\mathbf{k})_{y,y}+\tilde{B}_z(\mathbf{k},\mathbf{j})_{y,y}&=0,\\ \tilde{B}_z(\mathbf{j},\mathbf{k})_{z,z}+\tilde{B}_z(\mathbf{k},\mathbf{j})_{z,z}&=0\end{aligned} \tag{5.2.28}$$

by the property $\Delta_{-\mathbf{j}}=-\Delta_{\mathbf{j}}$.

The Jacobi property is also satisfied, which can be verified using (2.1.5) but is omitted here for brevity as it provides no particular insight.

This Poisson structure is quite complex and resists much algebraic traction. However, for stability theory we are no longer restricted to a subset of all possible perturbations. Thus this form can be very useful.

Chapter 6

Detailed Numerical Results

In this chapter, we present a number of numerical experiments verifying and exploring the analytical results of the previous chapters. These provide additional context for those results and a clearer idea of many aspects of the stability problem, such as the linearised spectrum and flow evolution. This also presents an opportunity to demonstrate the efficacy of the Poisson integrator described in Section 3.3 by computing flows of the Euler equations.

In Section 6.1 we discuss the spectrum of the Euler equations in two- and three-dimensional domains. In Section 6.2 we consider extreme values of the domain sizes κ_x, κ_y, κ_z. The nonimaginary spectrum approaches continuous curves as these sizes become large or small. In Section 6.3 some flows are calculated using the Poisson integrator. These numerical results allow us to make conjectures suggesting possible avenues for future research.

6.1. Spectrum of the Linearised Euler Equations

In Sections 2.4.2 and 4.1.5 it was shown that the Euler equations linearised around a sinusoidal shear flow decompose into subsystems or classes in both two- and three-dimensional periodic domains. Additionally, only finitely many of these classes contribute nonimaginary eigenvalues by Theorem 2.5.5 and Proposition 4.3.5. We need only check the classes led by modes that are both in the principal domain $\mathcal{A}$ and the unstable ellipse/ellipsoid $D_{\mathbf{p}}$ for nonimaginary eigenvalues.

We can explicitly reduce the parameter space for those classes, significantly simplifying numerical analysis across a wide range of parameters $\mathbf{p}$ and $\boldsymbol{\kappa}$. The nonimaginary eigenvalues for classes in this reduced parameter space are calculated which allows us to discuss how the type and number of nonimaginary eigenvalues depends on the parameters. This allows us to verify the observations made in Section 2.7.1.

We then calculate the set of nonimaginary eigenvalues for the full system, by combining all classes for which nonimaginary spectra occur. A conjecture on the number of nonimaginary eigenvalues occurring for a specific flow is explored that would sharpen the upper bound on the number of nonimaginary eigenvalues calculated by Latushkin, Li, and Stanislavova [**LLS04**]. Extensions are conjectured

for the anisotropic and three-dimensional domains. We also describe the imaginary spectrum for the sine-bracket truncated system, and see how this relates to the spectral density.

6.1.1. Simplified Dynamics of Linearised Euler Equations (Two Dimensions). Consider the linearised Euler equations on a two-dimensional periodic domain, as studied in Chapter 2. This splits into subsystems or classes. We wish to consider the spectrum of a class, which is given by eigenvalues of

$$M = \begin{pmatrix} \ddots & \vdots & \vdots & \vdots & \vdots & \vdots & \ddots \\ \cdots & 0 & \rho_{-1} & 0 & 0 & 0 & \cdots \\ \cdots & -\rho_{-2} & 0 & +\rho_0 & 0 & 0 & \cdots \\ \cdots & 0 & -\rho_{-1} & 0 & +\rho_1 & 0 & \cdots \\ \cdots & 0 & 0 & -\rho_0 & 0 & \rho_2 & \cdots \\ \cdots & 0 & 0 & 0 & -\rho_1 & 0 & \cdots \\ \ddots & \vdots & \vdots & \vdots & \vdots & \vdots & \ddots \end{pmatrix}. \tag{6.1.1}$$

This is the matrix (2.4.23) which governs the dynamics of a class of Fourier modes. In the full problem, this is premultiplied by the factor $\alpha \in \mathbb{R}$. In this chapter, we will assume that $\Gamma = 1$ unless otherwise noted. For $\alpha \neq 0$ these factors will not change the nature of the eigenvalues, and in particular whether or not there is an eigenvalue with positive real part. As all eigenvalues occur in pairs $\pm\lambda$, even if $\alpha < 0$ there is still a positive real eigenvalue after including the factor of α.

Our goal is to demonstrate how the eigenvalues of M depend on the parameters $\mathbf{a}$, $\mathbf{p}$, and $\boldsymbol{\kappa}$ that appear in the ρ_k coefficients. This allows us to generate figures such as Figure 6.10 showing the relationship between the parameters and the nonimaginary eigenvalues, and describe the full nonimaginary spectrum in Conjecture 6.1.8. That conjecture is an extension of Lemma 2.7.42, which showed that for certain parameter values we can prove the existence of a pair of real eigenvalues.

In Section 2.8.1 a transformation was calculated that reduces a linearised class to the form

$$\dot{\omega}_k = \Gamma \tilde{a}_y(\rho_{k+1}\omega_{k+1} - \rho_{k-1}\omega_{k-1}) \tag{6.1.2}$$

where

$$\rho_k = 1 - \frac{1}{(\tilde{a}_x + k)^2 + \tilde{a}_y^2} \tag{6.1.3}$$

for $(\tilde{a}_x, \tilde{a}_y)$ in the principal domain

$$\mathcal{A} = \{(\tilde{a}_x, \tilde{a}_y) \in \mathbb{R}^2 \mid -\frac{1}{2} < \tilde{a}_x \leq \frac{1}{2}\}. \tag{6.1.4}$$

Note the symmetry of ρ_k under $\tilde{a}_y \to -\tilde{a}_y$, so we need only consider $\tilde{a}_y > 0$. Although $\tilde{a}_y$ may be negative, this does not affect the spectrum due to the Hamiltonian symmetry of eigenvalues $\pm\lambda$. There is also a symmetry in $\tilde{a}_x$; if the ρ_k values are renumbered as $\rho_k \to \rho_{-k}$, this is equivalent to $\tilde{a}_x \to -\tilde{a}_x$. We thus observe symmetry in the $\tilde{a}_x$ parameter as well.

These reduced parameters $\tilde{\mathbf{a}} = (\tilde{a}_x, \tilde{a}_y)$ are related to the original parameter $\mathbf{a}$ by $\tilde{\mathbf{a}} = \frac{1}{|\mathbf{p}|_{\boldsymbol{\kappa}}} R_{\mathbf{p}} K \mathbf{a}$ for the matrices $R_{\mathbf{p}}$, K defined in Section 2.8.1. Explicitly we can write

$$\tilde{a}_x = \frac{\langle \mathbf{a}, \mathbf{p} \rangle}{|\mathbf{p}|^2_{\boldsymbol{\kappa}}}, \quad \tilde{a}_y = \frac{|K\mathbf{a} \times K\mathbf{p}|}{|\mathbf{p}|^2_{\boldsymbol{\kappa}}}. \tag{6.1.5}$$

One must recall that although the original parameter $\mathbf{a} \in \mathbb{Z}^2$, the reduced parameters $\tilde{a}_x, \tilde{a}_y \in \mathbb{R}$ are not necessarily integers. One can interpret $\tilde{a}_x$ and $\tilde{a}_y$ as the projection of $\mathbf{a}$ in the directions parallel to and orthogonal to $\mathbf{p}$ with respect to the $\boldsymbol{\kappa}$ norm (2.2.13) respectively. This was illustrated in Figure 2.17. This reduction is computationally useful as we can study the two-dimensional parameter range in the principal domain $\mathcal{A}$ and translate this for our original choice of parameters $\mathbf{a}$, $\mathbf{p}$ and $\boldsymbol{\kappa}$, rather than considering the six-dimensional space of parameters $\mathbf{a}$, $\mathbf{p}$, $\boldsymbol{\kappa}$.

6.1.2. Describing the Linearised Spectrum (Two Dimensions). Having reduced the linearised two-dimensional problem to subsystems with two parameters $\tilde{a}_x$ and $\tilde{a}_y$, we can describe the full spectrum by considering the eigenvalues in the class corresponding to those parameters. By Theorem 2.5.5, all classes with $(\tilde{a}_x, \tilde{a}_y) \in \mathcal{A}$ satisfying $\tilde{a}_x^2 + \tilde{a}_y^2 \geq 1$ have only imaginary eigenvalues. Thus to describe the nonimaginary spectrum we need only consider the parameter values satisfying $\tilde{a}_x^2 + \tilde{a}_y^2 < 1$. To do so, we numerically calculate the nonimaginary eigenvalues for the range $\tilde{a}_x \in [-0.5, 0.5]$ and $\tilde{a}_y \in (-\sqrt{1-\tilde{a}_x^2}, \sqrt{1-\tilde{a}_x^2})$ on a grid with a step size of 0.001. We calculate the eigenvalues using the sine-bracket truncated matrix (3.2.14) with a truncation size $N = 500$. These eigenvalues are calculated using the default MATLAB eigenvalue solver. All the figures in this chapter are then computed using these values, with the appropriate transformations when the original $\mathbf{a}$, $\mathbf{p}$, $\boldsymbol{\kappa}$ parameters are used. The advantage of using the sine-bracket truncated system is illustrated in Figure 6.1; the spectrum of a sine-bracket truncated system converges faster than the equivalent Galerkin truncated system.

Figure 6.2 shows how the real and imaginary parts of the nonimaginary eigenvalues of (6.1.1) change as a function of $\tilde{a}_x$, $\tilde{a}_y$. In Figure 6.3, the same contours as Figure 6.2 are shown with the factor of $\tilde{a}_y$ included. When translating back to the original parameters and considering the spectrum of the full linearised system, this factor is used. Compare the shape of these figures to Figure 2.19, where the number and type of nonimaginary eigenvalues were described in terms of $\tilde{a}_x$, $\tilde{a}_y$. For a small range of parameter values, there are two sets of real eigenvalues

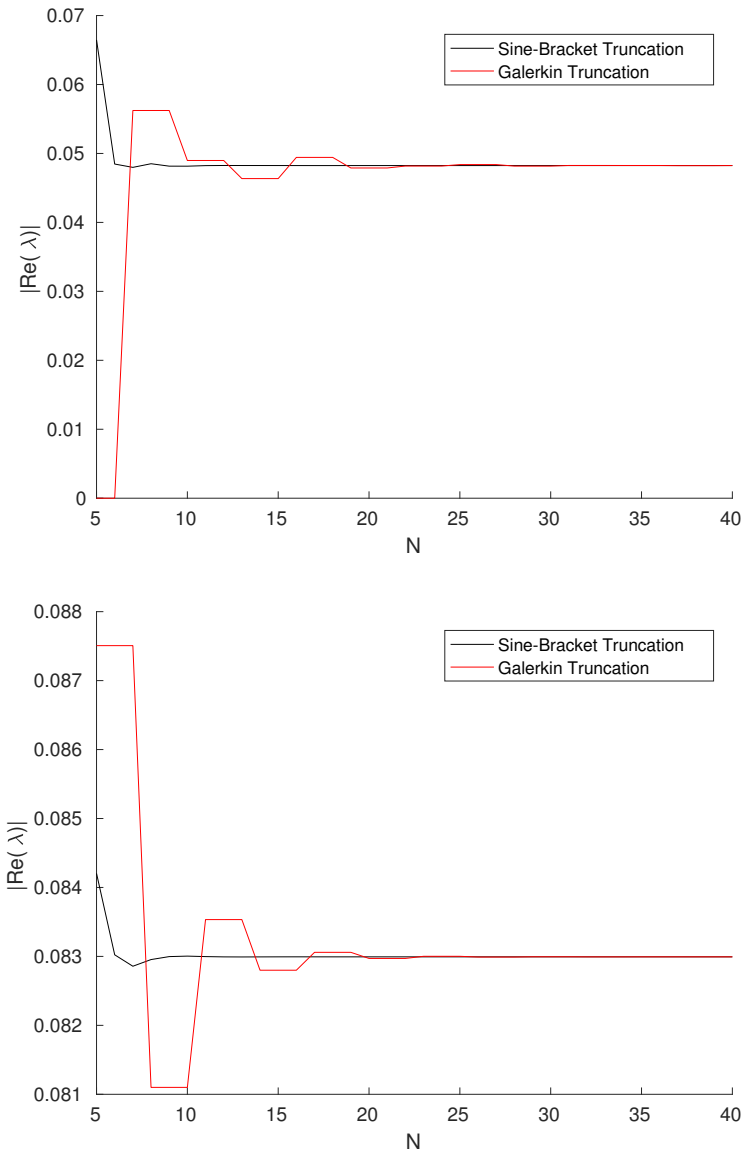

Figure 6.1 – Eigenvalues vs truncation size N for the sine-bracket truncated system vs the Galerkin truncated system. The Fourier modes $\omega_{\mathbf{k}}$ with $\mathbf{k} = (k_x, k_y)$ for $-N \leq k_x, k_y \leq N$ are used in the calculation. For both figures, $\mathbf{p} = (3, 2)$. Top: the convergence of the positive real part of the eigenvalue in the class $\mathbf{a} = (3, 1)$. Bottom: the convergence of the positive real part of the eigenvalue in the class $\mathbf{a} = (-1, 1)$. In both cases, the convergence of the eigenvalues of the sine-bracket truncated system (shown as a black line) is faster than the convergence of the eigenvalues of the Galerkin truncated system.

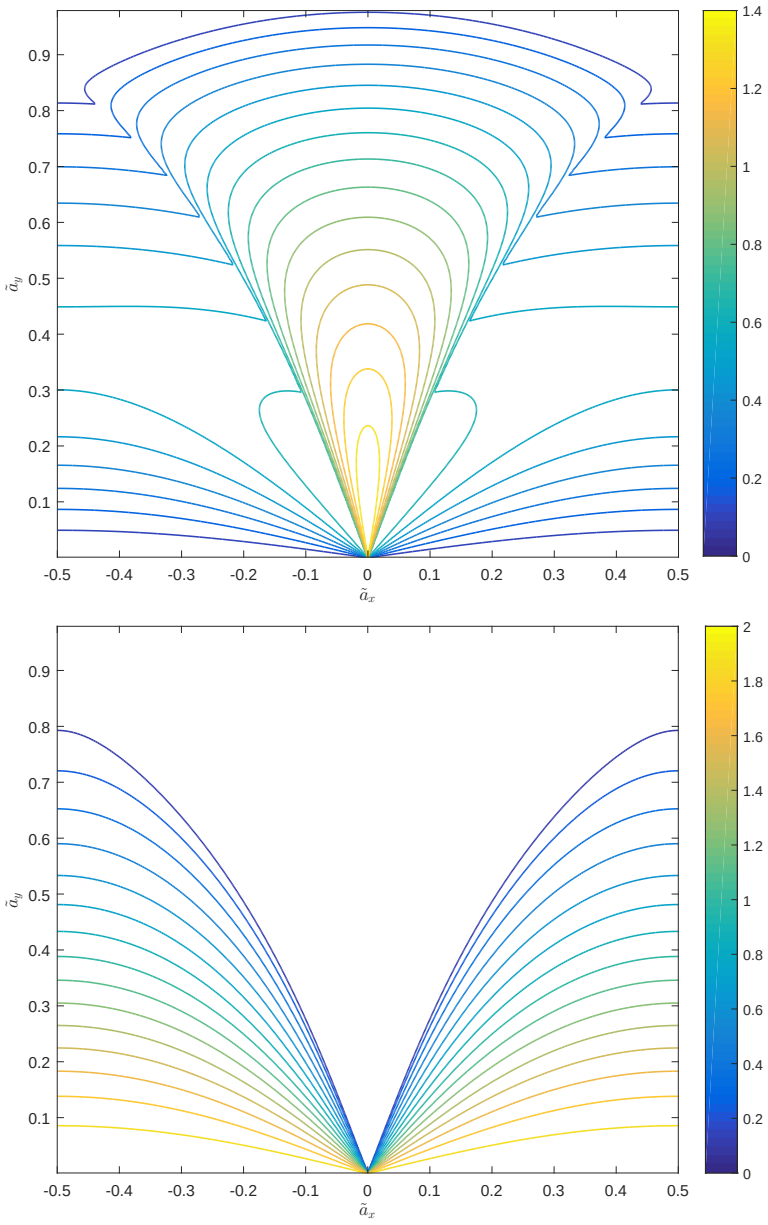

Figure 6.2 – Contours of nonimaginary eigenvalues of (6.1.1). Given parameters $\tilde{a}_x, \tilde{a}_y$ satisfying $\tilde{a}_x^2 + \tilde{a}_y^2 < 1$, there are nonimaginary eigenvalues of (6.1.1) $\lambda = \pm u \pm iv$ with $u \neq 0$. For some parameter values, there are two sets of real eigenvalues $\pm u_1$ and $\pm u_2$; for these, this figure shows the eigenvalues with larger absolute value. Top: contour lines showing constant values of $u = |\mathrm{Re}(\lambda)|$ as a function of $\tilde{a}_x$, $\tilde{a}_y$. Bottom: contour lines showing constant values of $v = |\mathrm{Im}(\lambda)|$ as a function of $\tilde{a}_x$, $\tilde{a}_y$. The region where there are no contour lines in the lower figure corresponds to the area where all nonimaginary eigenvalues are real as indicated in Figure 2.19. As there is a symmetry $\tilde{a}_y \leftrightarrow -\tilde{a}_y$, we only show $\tilde{a}_y > 0$.

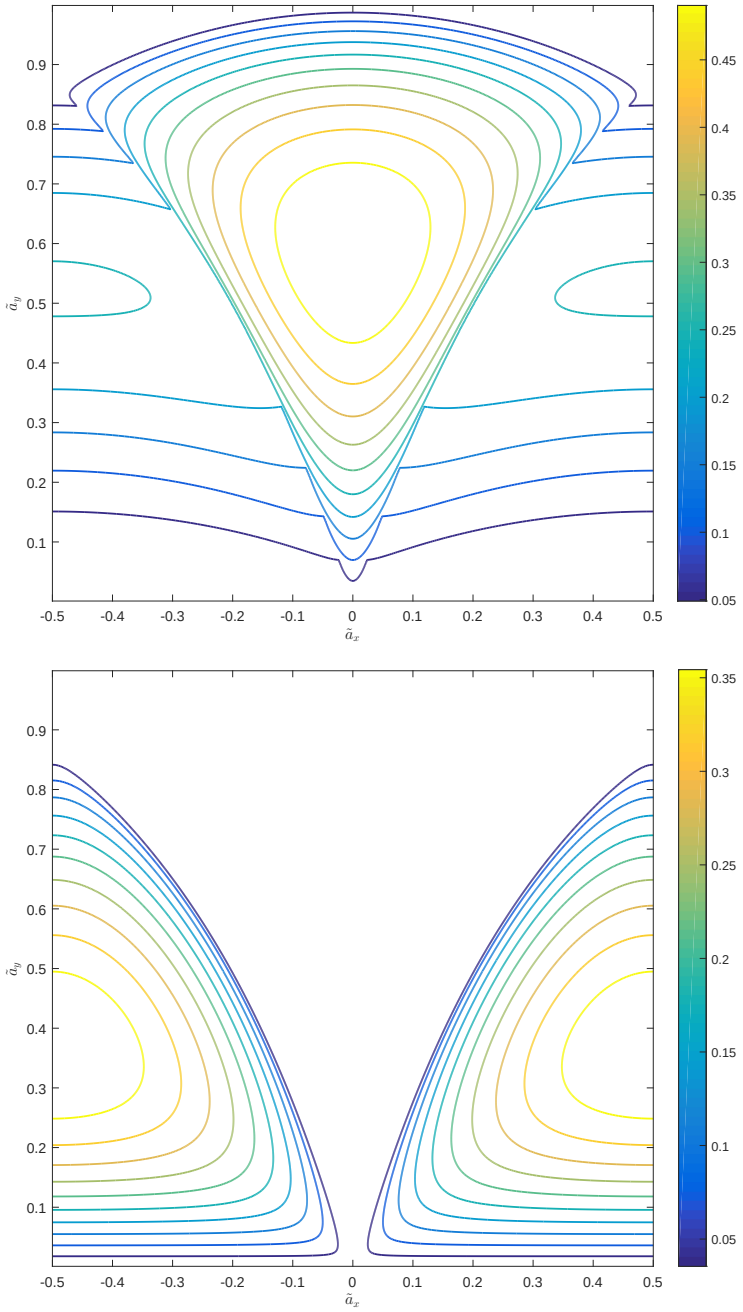

Figure 6.3 – Contours of constant real (top) and imaginary (bottom) parts of nonimaginary eigenvalues of $\tilde{a}_y M$. This is the same as Figure 6.2, except the factor of $\tilde{a}_y$ is included. Compare the top figure with the lower bound in Figure 2.18, which was proven to be a lower bound for a real eigenvalue in Theorem 2.7.53. Only the larger of the two eigenvalues is shown for the parameter ranges where there are two positive real eigenvalues.

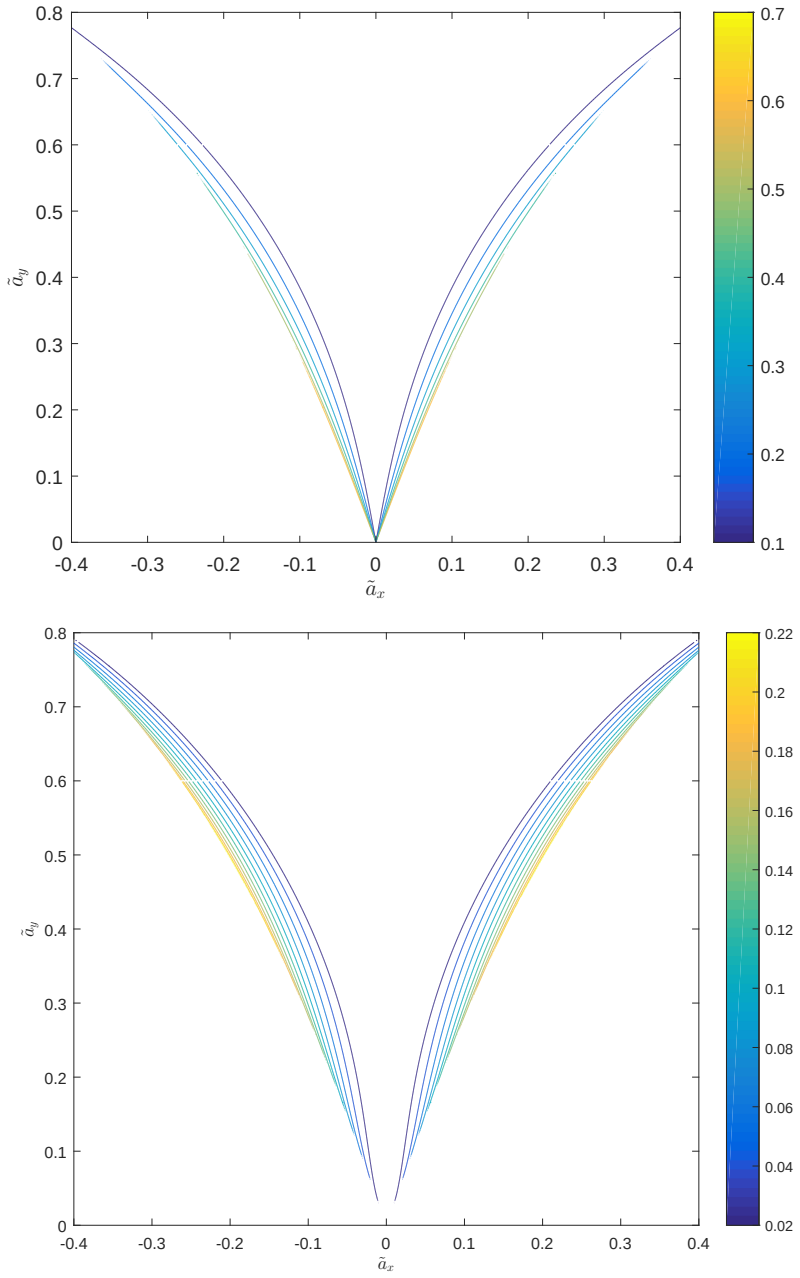

Figure 6.4 – Contours of the smaller real eigenvalues of (6.1.1). For some parameter values $\tilde{a}_x, \tilde{a}_y$, there are two pairs of real eigenvalues. For such values, the smaller of the two real eigenvalues are shown in these contour plots. Top: contours of equal eigenvalues of M, corresponding to Figure 6.2. Bottom: contours of equal eigenvalues of $\tilde{a}_y M$ corresponding to Figure 6.3. Compare the shape of the region where this eigenvalue exists to the "four real eigenvalues" region in Figure 2.19.

as noted in Section 2.7.1 and Figure 2.19. For these parameters the smaller of the real eigenvalues is shown in Figure 6.4.

Figures 6.5 and 6.6 show which complex numbers occur as eigenvalues occur across all parameter values $(\tilde{a}_x, \tilde{a}_y) \in \mathcal{A}$ with and without the factor of $\tilde{a}_y$ respectively. This corroborates the observation that there is a fixed upper bound on the size of any nonimaginary eigenvalue that can occur, as proven in Section 2.7.3. Figures 6.7 and 6.8 show curves of complex eigenvalues of M and $\tilde{a}_y M$ respectively for a finite number of fixed values of $\tilde{a}_x$ as $\tilde{a}_y$ is varied. This shows how the eigenvalues depend on the value of $\tilde{a}_x$. Figures 6.5 and 6.6 are the limits of these figures calculated by taking all possible values of $\tilde{a}_x$ rather than just finitely many values.

Figure 6.9 shows the full nonimaginary spectrum for a linearised problem with $\mathbf{p} = (5, 3)$ on an isotropic domain. As this is not of the linearly stable form discussed in Theorem 2.6.1, we observe eigenvalues with a positive real part, indicating linear instability. We also observe that there are only finitely many discrete nonimaginary eigenvalues, corresponding to the observation that there is a bijection between lattice points inside the unstable ellipse and pairs of nonimaginary eigenvalues.

In Figures 6.10 and 6.11, values of $\mathbf{a}$ that lead classes that contribute nonimaginary eigenvalues are shown, and the corresponding eigenvalues. This shows how the position of $\mathbf{a}$ relative to the unstable ellipse affects the type of eigenvalues that occur, corroborating the hypothesis of Section 2.7.1 which is illustrated in Figure 2.10. We will formulate this observation as Conjecture 6.1.8, and use this to make a further conjecture on the number of nonimaginary eigenvalues in the spectrum of the linearised Euler equations.

6.1.3. Describing the Linearised Spectrum (Three Dimensions). In Section 4.2.3, the explicit expression for the reduced parameters in the three-dimensional problem was calculated as

$$\tilde{a}_x = \frac{\langle \mathbf{a}, \mathbf{p} \rangle}{|\mathbf{p}|_{\boldsymbol{\kappa}}^2}, \quad \tilde{a}_y = \frac{|K\mathbf{a} \times K\mathbf{p}|}{|\mathbf{p}|_{\boldsymbol{\kappa}}^2}, \tag{6.1.6}$$

$$\tan\theta = \frac{\boldsymbol{\Gamma}^{\mathsf{T}}(K\mathbf{p} \times K\mathbf{a})}{\langle \mathbf{a}, K^{-1}\boldsymbol{\Gamma} \rangle |\mathbf{p}|_{\boldsymbol{\kappa}}} \tag{6.1.7}$$

The parameter space $\mathbf{a}, \mathbf{p} \in \mathbb{Z}^3$, $\boldsymbol{\Gamma} \in \mathbb{R}^3$, $\boldsymbol{\kappa} \in \mathbb{R}^{+3}$ can then be reduced to the parameters $\tilde{a}_x, \tilde{a}_y, \theta \in \mathbb{R}$. Only a discrete set of these parameter values actually occur for any shear flow corresponding to the $\mathbf{a}$ that occur at integer lattice points. The reduced parameters can be used to calculate the spectrum of the associated matrix for the three-dimensional linearised problem, which can then be related back to the original parameters. Recall that the spectrum is given by the union of the spectrum of the two-dimensional linearised class (6.1.1) and the spectrum of the constant matrix (4.2.44) multiplied through by $\tilde{a}_y |\sin\theta|$, except

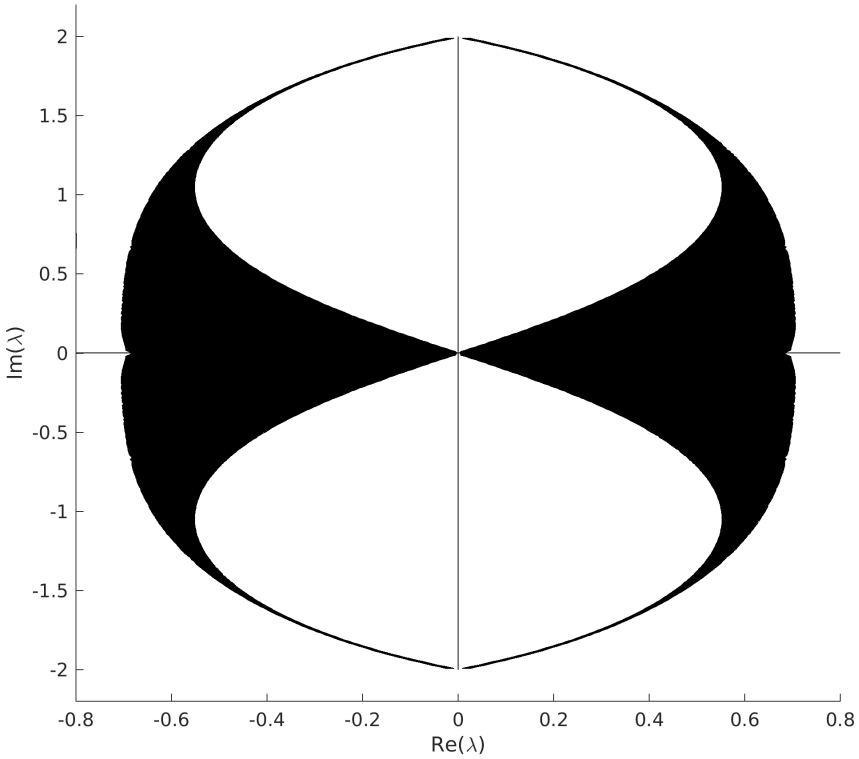

Figure 6.5 – A plot of all possible eigenvalues of M across parameter values $-\frac{1}{2} \leq \tilde{a}_x \leq \frac{1}{2}$, $\tilde{a}_y \in \mathbb{R}$ is shown in the shaded region. The real eigenvalues lie in the interval $[-\sqrt{2}, \sqrt{2}]$ and the imaginary eigenvalues lie in the interval $[-2, 2]i$. Note that all eigenvalues lie in a closed set and satisfy $|\lambda| \leq 2$.

in the special cases $\theta = 0, \pi$. An example of all nonimaginary eigenvalues for a linearised shear flow in a three-dimensional domain is shown in Figure 6.13.

For the three-dimensional problem, across all values of the parameters $\tilde{a}_x, \tilde{a}_y, \theta$ the eigenvalues must lie in the same region as in Figures 6.5 and 6.6. This is because the only difference in the spectrum will be a multiplicative factor of $|\sin\theta|$, and $0 \leq |\sin\theta| \leq 1$ so no eigenvalues can occur except those that also occur in the two-dimensional problem. This is illustrated in Figure 6.12, which also shows the dependence on the parameter θ.

We must note that the linearised spectrum does not tell the full story in the case of the three-dimensional problem. As discussed in Section 4.2.9, there may be classes that are nilpotent and therefore do not contribute any nonimaginary eigenvalues. However, these nilpotent classes lead to linear growth and therefore linear instability. Thus observing spectral stability is not sufficient for linear

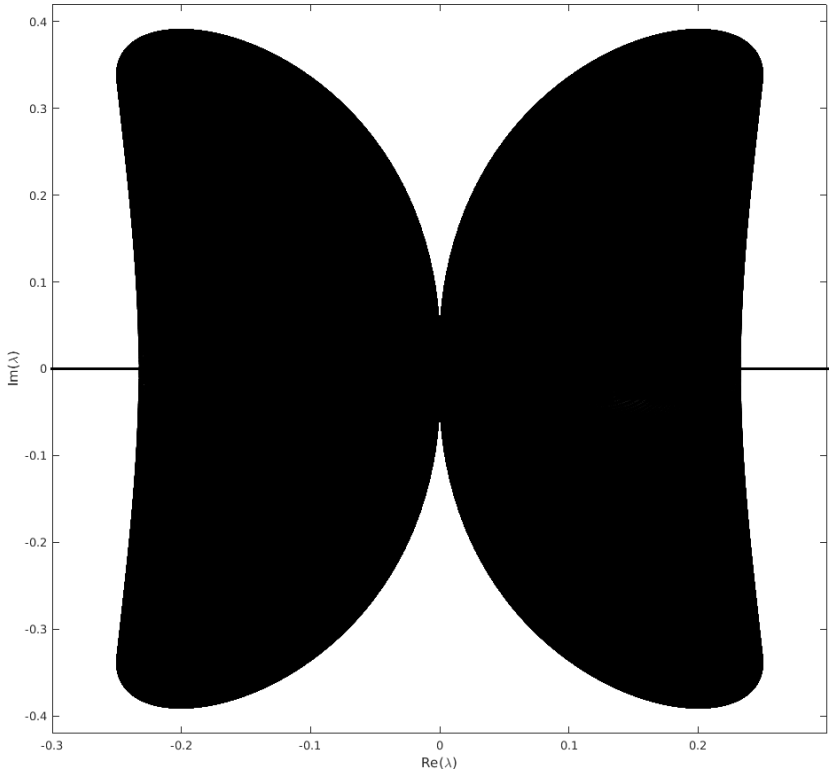

Figure 6.6 – All possible nonimaginary eigenvalues of $\tilde{a}_y M$ for all parameter values $-\frac{1}{2} \leq \tilde{a}_x \leq \frac{1}{2}$, $\tilde{a}_y \in \mathbb{R}$. These are the same eigenvalues as Figure 6.5, but including the scaling factor of $\tilde{a}_y$ that appears in the matrix in the context of the full problem. For the three-dimensional problem, across all parameter values of $\tilde{a}_x, \tilde{a}_y, \theta$, the same set of eigenvalues as illustrated above will occur, as the θ parameter only scales the eigenvalues by $|\sin\theta| \leq 1$. Also note that across all parameter values, every value on the imaginary axis will occur in the spectrum. Numerically, purely real eigenvalues occur in the range $[-0.54, 0.54]$, the real part of the complex eigenvalues occur in the range $[-0.25, 0.25]$ and the imaginary part of complex eigenvalues occur in the range $[-0.39, 0.39]$ to two decimal places.

stability in the three-dimensional class. Propositions 4.2.64 and 4.2.70 discus the additional requirement for linear stability. One must also keep in mind the possibility of nonlinear instability due to nonnormality in the linearly stable cases, which was discussed in Section 4.3.3.

6.1.4. The Full Nonimaginary Spectrum. The numerical evidence in this chapter presents a convincing argument that the number and nature of the nonimaginary eigenvalues of a class can be surmised from the location of the parameters $\tilde{a}_x$, $\tilde{a}_y$ in relation to the unstable ellipse. This was presented as an observation in Section 2.8 and can be seen here in Figures 6.2, 6.4. Based on this we make the following conjecture.

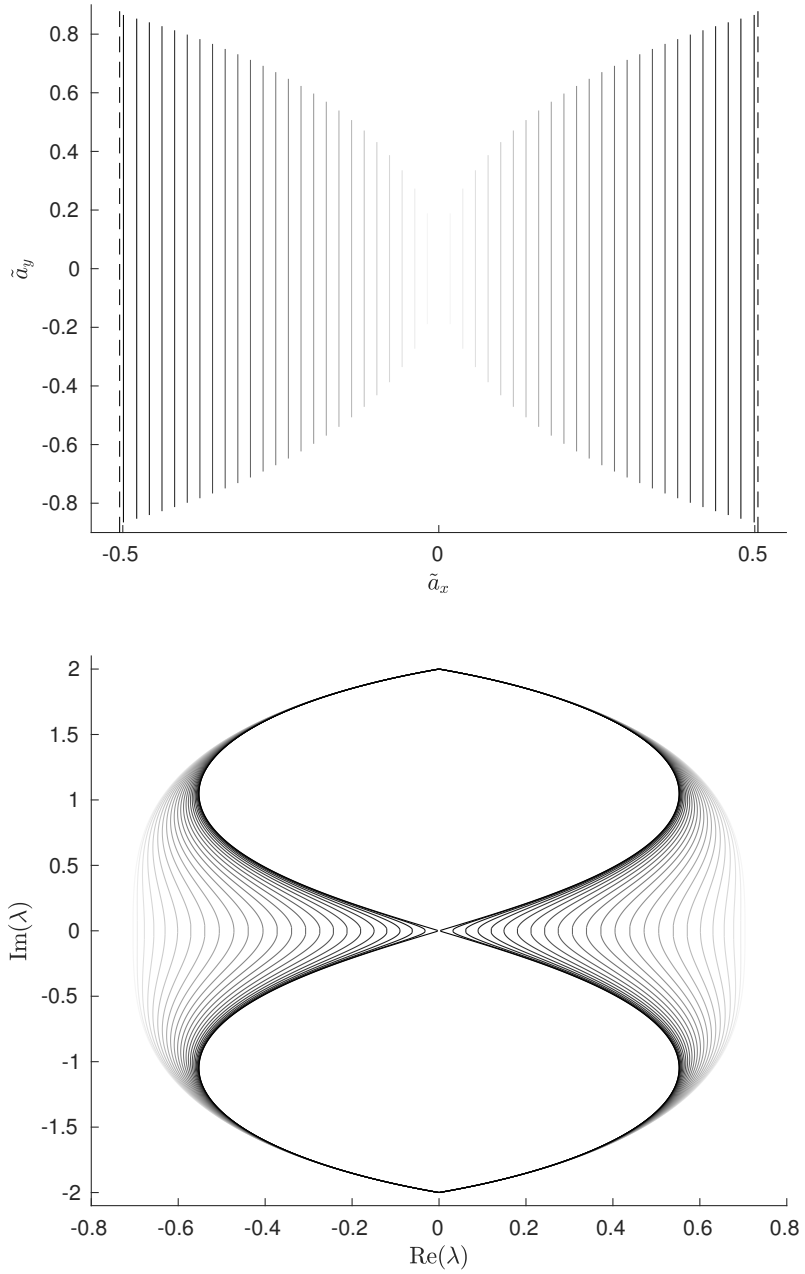

Figure 6.7 – Complex eigenvalues of M along contours of constant $\tilde{a}_x$. Top: for discrete values of $\tilde{a}_x$, the values in $\tilde{a}_x$-$\tilde{a}_y$ space for which there is an associated complex eigenvalue. The dashed lines show the edges of the principal domain $-1/2 \leq \tilde{a}_x \leq 1/2$. Bottom: for each of these lines of constant $\tilde{a}_x$, the associated complex eigenvalues of M as $\tilde{a}_y$ is varied are plotted in the same colour as for the top figure. Figure 6.5 is the superposition of these contours for all values of $\tilde{a}_x$.

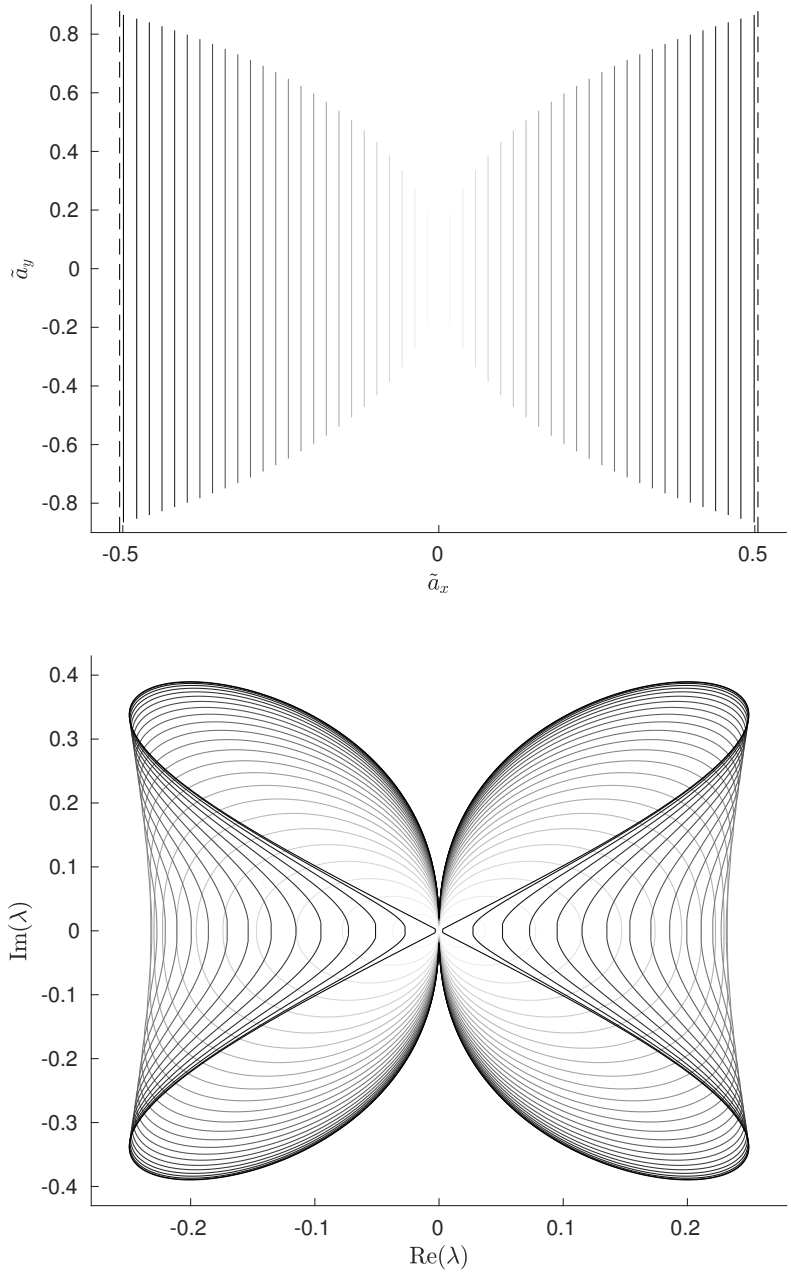

Figure 6.8 – Complex eigenvalues of $\tilde{a}_y M$ along contours of constant $\tilde{a}_x$. Top: for discrete values of $\tilde{a}_x$, lines for which there is an associated complex eigenvalue. The dashed lines show the edges of the principal domain $-1/2 \leq \tilde{a}_x \leq 1/2$. Bottom: for each of these lines, the associated complex eigenvalues of $\tilde{a}_y M$ are plotted in the same colour as for the top figure. Figure 6.6 is the superposition of these contours for all $\tilde{a}_x$. Compare with Figure 6.8; here the factor of $\tilde{a}_y$ is included.

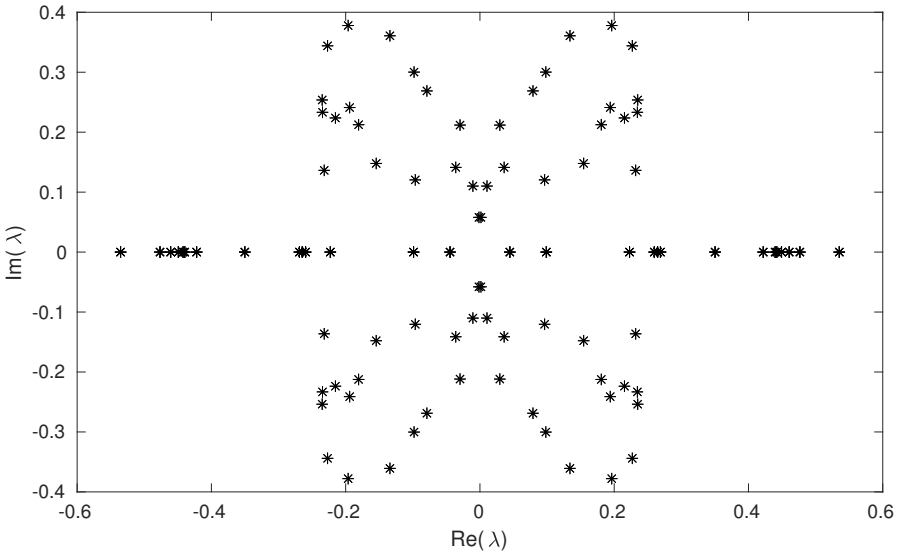

Figure 6.9 – All nonimaginary eigenvalues of the full linearised two-dimensional system with parameters $\mathbf{p} = (5, 3)$, $\kappa_y/\kappa_x = 1$. Compare the shape with Figure 6.6; all eigenvalues lie within the region indicated in that figure.

Conjecture 6.1.8 (Nonimaginary spectrum of linearised equations in two dimensions)**.** *Consider the linearised system in two dimensions with* $\mathbf{p} \in \mathbb{Z}^2$*. Then for the class led by* $\mathbf{a} \in \mathcal{A} \cap D_{\mathbf{p}}$ *such that* $\mathbf{a}$ *and* $\mathbf{p}$ *are not parallel,*

- *if* $\mathbf{a} \pm \mathbf{p} \notin D_{\mathbf{p}}$ *(the unstable ellipse), the nonimaginary spectrum of the class led by* $\mathbf{a}$ *is a pair of nonzero real eigenvalues* $\pm\lambda$*;*
- *if* $\mathbf{a} + \mathbf{p} \in D_{\mathbf{p}}$ *or* $\mathbf{a} - \mathbf{p} \in D_{\mathbf{p}}$*, the nonimaginary spectrum of the class led by* $\mathbf{a}$ *is either two pairs of nonzero real eigenvalues* $\pm\lambda_1$*,* $\pm\lambda_2$ *or four complex eigenvalues* $\pm u \pm iv$ *for nonzero* $u, v \in \mathbb{R}$*.*

Therefore, if there exists any $\mathbf{a} \in \mathcal{A} \cap D_{\mathbf{p}}$ *not parallel to* $\mathbf{p}$*, the linearised shear flow is linearly unstable. We can therefore conclude that it is nonlinearly unstable, by* [**FSV97**] *and* [**SL03**]*.*

Furthermore, if $\nu \in \mathbb{N}$ *is the number of lattice points in* $D_{\mathbf{p}}$*, the above implies that the number of nonimaginary eigenvalues counting multiplicity in the linearised system is given by*

$$|\sigma_{\text{discrete}}| = 2(\nu - 2\gcd(p_x, p_y) + 1). \tag{6.1.9}$$

This conjecture is based on the observations of Section 2.8 and the numerical evidence illustrated in Figures 2.19, 6.2, 6.3.

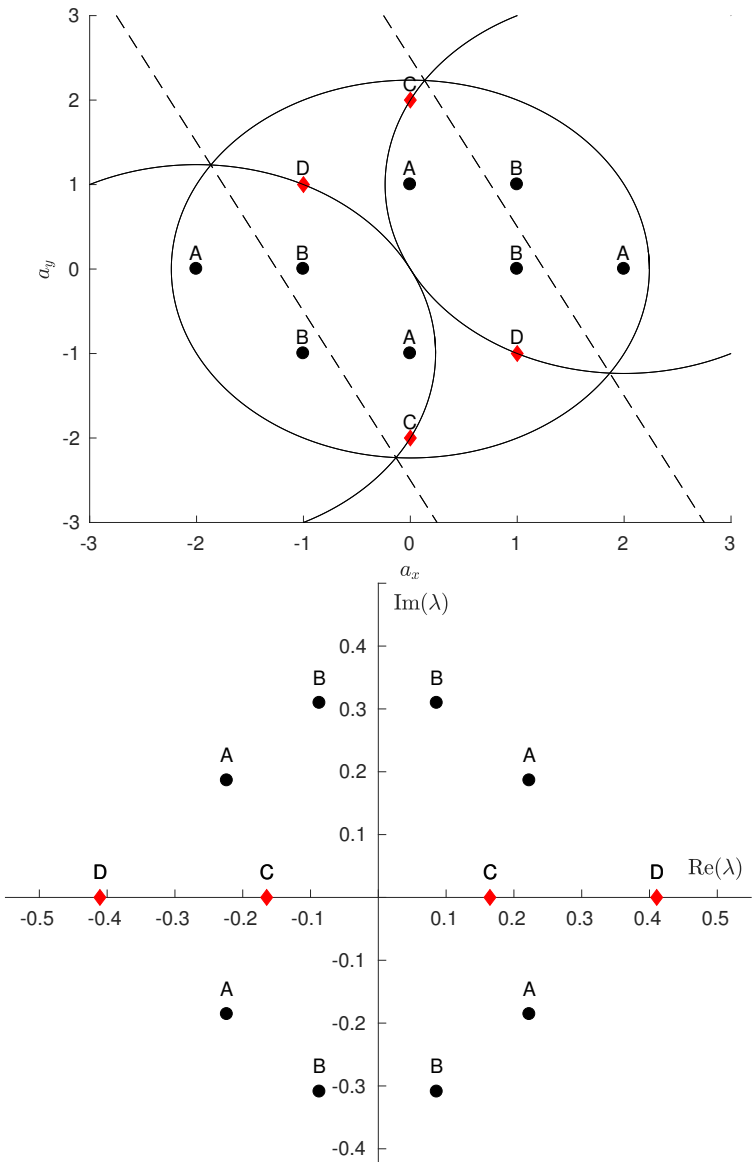

Figure 6.10 – Eigenvalues and their locations for $\mathbf{p} = (2, 1)$, $\kappa_y/\kappa_x = 1$. Top: all lattice points $\mathbf{a}$ in the unstable ellipse $D_{\mathbf{p}}$. Values with $\rho_{\pm 1} \notin D_{\mathbf{p}}$ are shown as red diamonds, other points are shown as black circles. The dashed lines are the edges of the principal domain $\mathcal{A}$. Bottom: all nonimaginary eigenvalues of αM, marked with the symbols of the corresponding values of $\mathbf{a}$. For each lattice point in the top figure, the corresponding eigenvalues in the bottom figure are labelled with the same letter. Note that the values of $\mathbf{a}$ such that $\rho_{\pm 1} \notin D_{\mathbf{p}}$ correspond to real eigenvalues, and all others to complex eigenvalues. This corroborates the observation in Section 2.7.1. Note also that any pair $\mathbf{a}$ and $-\mathbf{a}$ correspond to the same eigenvalues. Thus all eigenvalues have multiplicity 2.

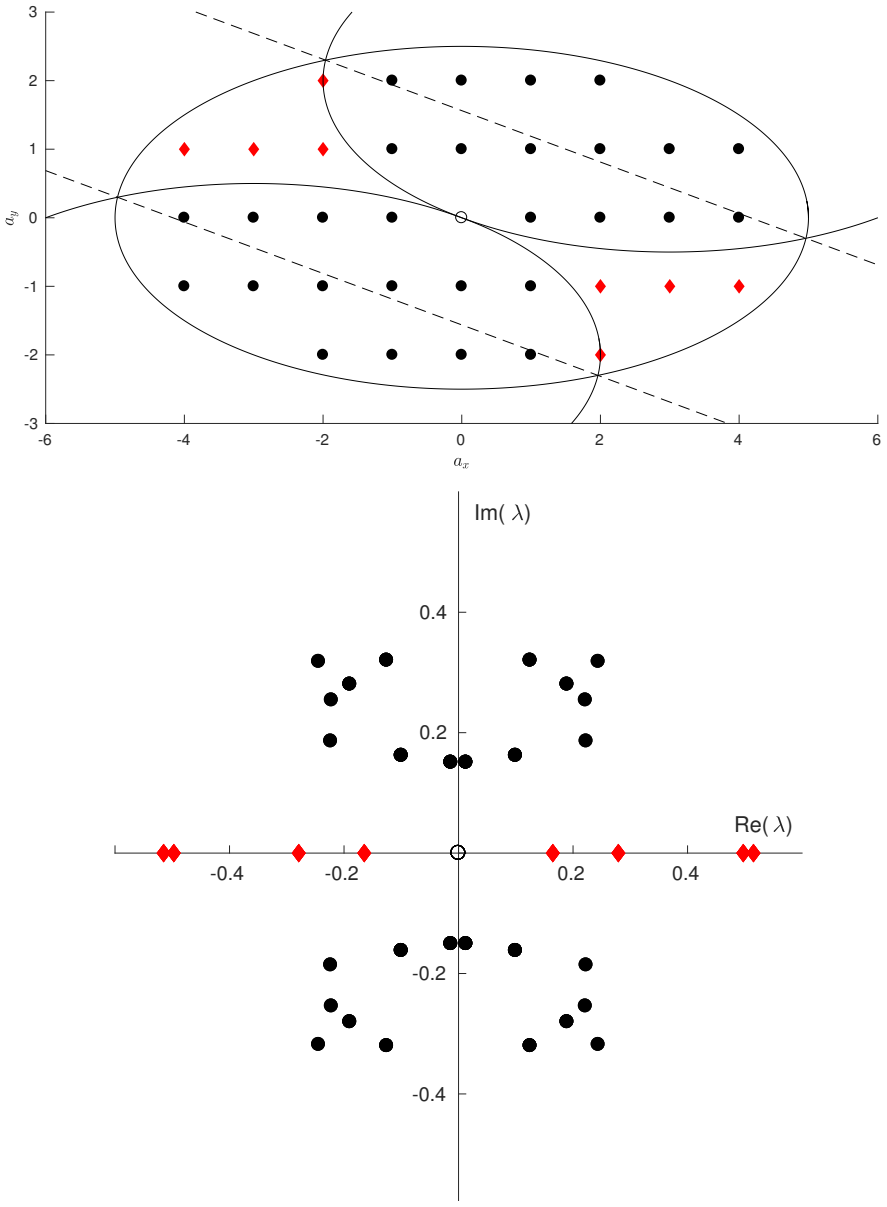

Figure 6.11 – As per Figure 6.10, with parameters $\mathbf{p} = (3, 2)$ and $\kappa_y/\kappa_x = 2$. In both figures, the number of lattice points in the unstable ellipse is exactly the number of discrete nonimaginary eigenvalues, each of which has multiplicity 2. This corresponds to a natural extension of the result in [**LLS04**], presented here as Conjecture 6.1.8. The principal domain of modes $\mathcal{A}$ is between the dashed lines. Note the points that lie in the unstable ellipse but not the principal domain. These are in the same class as some other point that is in the intersection of the unstable ellipse and the principal domain.

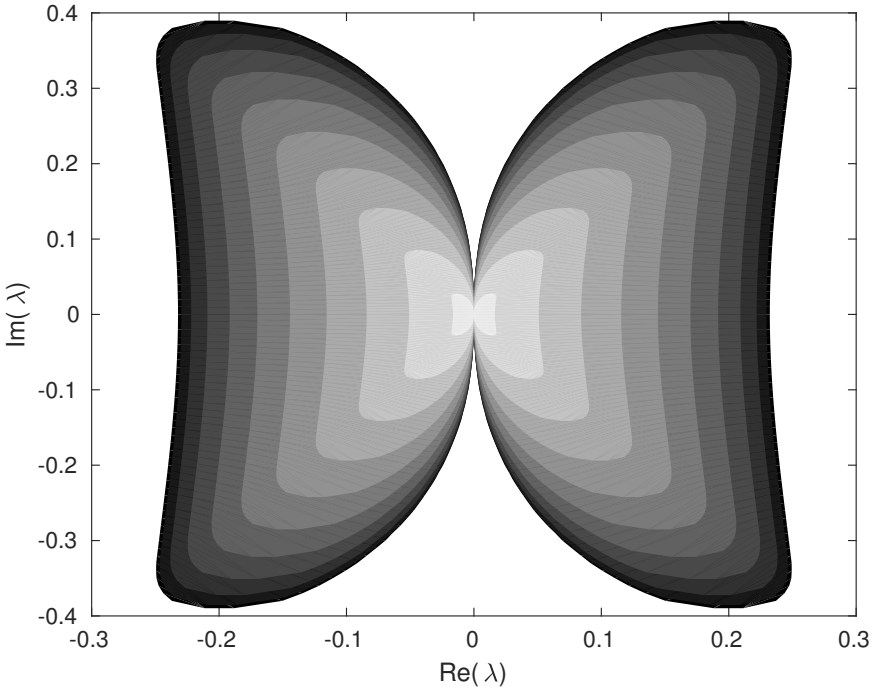

Figure 6.12 – A plot of all possible complex eigenvalues of the three-dimensional linearised problem. These are the eigenvalues of $|\sin\theta|\tilde{a}_y M$, across parameter values $-\frac{1}{2} \leq \tilde{a}_x \leq \frac{1}{2}$, $\tilde{a}_y \in \mathbb{R}$ $\theta \in [0, 2\pi)$. The shading corresponds to $\sin\theta$; larger values of $|\sin\theta|$ are shaded darker. This is the same shape as Figure 6.6, though for smaller values of $\sin\theta$ there are different accessible regions.

In Latushkin, Li and Stanislavova [**LLS04**], it was shown that in the case $\kappa_y/\kappa_x = 1$ the number of nonimaginary eigenvalues of (6.1.1) is less than or equal to twice the number of lattice points inside the unstable ellipse (or in that case, the unstable disc) (2.5.2). The above conjecture states that this can be generalised this to any domain size $\boldsymbol{\kappa} \in \mathbb{R}^2$ and provide an exact count rather than an upper bound. Note the term $2\gcd(p_x, p_y)$, which accounts for values of $\mathbf{a}$ that are inside the unstable ellipse but are parallel to $\mathbf{p}$. These classes contribute no nonzero eigenvalues. If p_x and p_y are coprime, the only such value is $\mathbf{a} = \mathbf{0}$. The final $+1$ term accounts for the fact that $\mathbf{a} = \mathbf{0}$ is counted twice by $2\gcd(p_x, p_y)$ but only occurs once. One should note that all eigenvalues have multiplicity 2; this is due to the symmetry between the class led by $\mathbf{a}$ and the class led by $-\mathbf{a}$. This can be observed in Figure 6.10.

In the three-dimensional case, the system decomposes into classes which have the same spectrum as a corresponding class in the two-dimensional problem, as

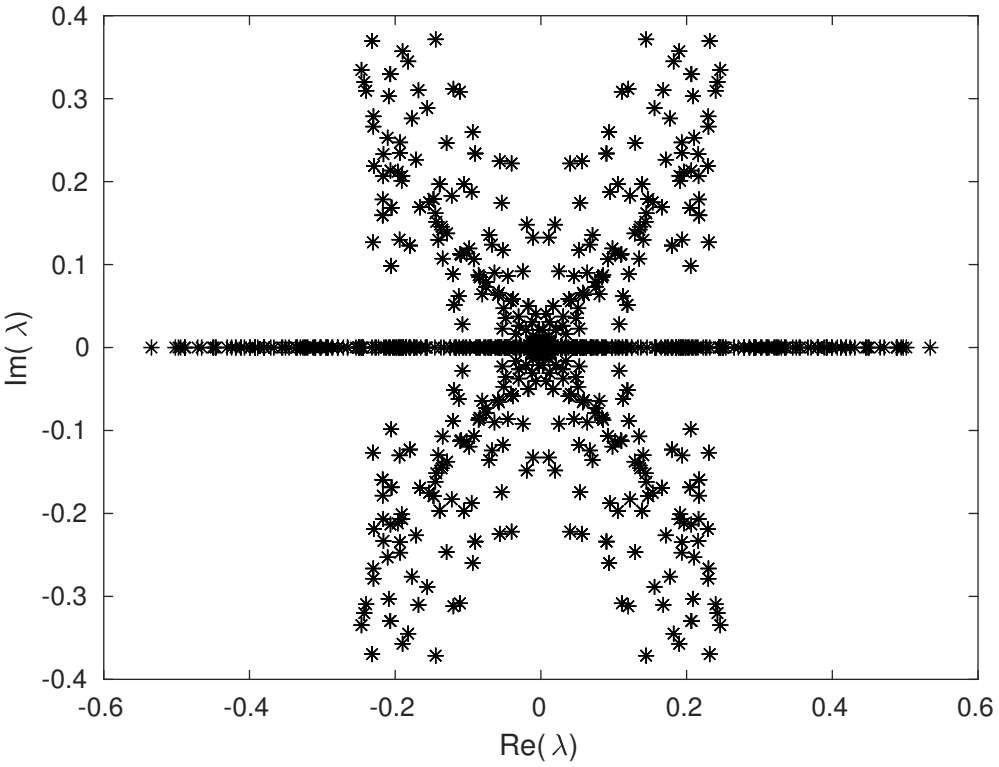

Figure 6.13 – All nonimaginary eigenvalues of the three-dimensional linearised flow for $\mathbf{p} = (5, 3, 1)$, $\mathbf{\Gamma} = (1, -2, 2)$, $\boldsymbol{\kappa} = (1, 1, 1)$. Compare the shape with Figure 6.12. These eigenvalues are calculated by transforming the calculated eigenvalues for the reduced parameters $\tilde{a}_x$, $\tilde{a}_y$ appropriately and scaling by $|\sin\theta|$. Compare this with Figure 6.9; in the three-dimensional case, there are correspondingly more nonimaginary eigenvalues as the unstable ellipsoid contains more lattice points than the unstable ellipse. Eigenvalues occur closer to 0, as the prefactor $|\sin\theta|$ multiplies all eigenvalues, and $|\sin\theta| \leq 1$.

shown in Theorem 4.2.59. We therefore can make a very similar conjecture for the three-dimensional domain, with some minor but important changes.

Conjecture 6.1.10 (Nonimaginary spectrum of linearised equations in three dimensions)**.** *Consider the linearised system in three dimensions with* $\mathbf{p} \in \mathbb{Z}^3$ *and* $\mathbf{\Gamma} \in \mathbb{R}^3$*. For a class led by* $\mathbf{a} \in \mathcal{A} \cap D_{\mathbf{p}}$ *such that* $\mathbf{a}$ *and* $\mathbf{p}$ *are not parallel and* $\mathbf{a}, \mathbf{p}, K^{-1}\mathbf{\Gamma}$ *are not all coplanar,*

- *if* $\mathbf{a} \pm \mathbf{p} \notin D_{\mathbf{p}}$ *(the unstable ellipsoid), the nonimaginary spectrum of the class led by* $\mathbf{a}$ *is a pair of nonzero real eigenvalues* $\pm\lambda$*;*

- *if* $\mathbf{a}+\mathbf{p}\in D_{\mathbf{p}}$ *or* $\mathbf{a}-\mathbf{p}\in D_{\mathbf{p}}$*, the nonimaginary spectrum of the class led by* $\mathbf{a}$ *is either two pairs of nonzero real eigenvalues* $\pm\lambda_1$*,* $\pm\lambda_2$ *or four complex eigenvalues* $\pm u\pm iv$ *for nonzero* $u,v\in\mathbb{R}$*.*

Therefore, if there exists any $\mathbf{a}\in\mathcal{A}\cap D_{\mathbf{p}}$ *such that* $\mathbf{a}$ *is not parallel to* $\mathbf{p}$ *and not coplanar with both* $\mathbf{p}$ *and* $K^{-1}\mathbf{\Gamma}$*, the linearised shear flow is linearly unstable.*

Furthermore, if $\nu\in\mathbb{N}$ *is the number of lattice points in* $D_{\mathbf{p}}$ *the above implies that the number of nonimaginary eigenvalues counting multiplicity in the linearised system is bounded above by*

$$|\sigma_{\text{discrete}}|\leq 2(\nu-2\gcd(p_x,p_y,p_z)+1) \tag{6.1.11}$$

where $\gcd(p_x,p_y,p_z)=\gcd(p_x,\gcd(p_y,p_z))$*.*

Unlike in the two-dimensional case, the conjecture on the number of nonimaginary eigenvalues is an upper bound rather than an inequality here. This is due to the existence of values of $\mathbf{a}\in D_{\mathbf{p}}\cap\mathbb{Z}^3$ such that $\mathbf{a}$, $\mathbf{p}$ and $K^{-1}\mathbf{\Gamma}$ are all coplanar. By Section 4.2.9, such classes are nilpotent and do not contribute any nonzero eigenvalues.

We observe these conjectures in our numerics. For instance, in Figure 6.10 there are 12 lattice points inside the unstable ellipse (not counting $\mathbf{a}=\mathbf{0}$) and 12 nonimaginary eigenvalues, each with multiplicity 2. Similarly in Figure 6.11, there are 36 interior lattice points in the unstable ellipse and 36 nonimaginary eigenvalues, as $\gcd(3,2)=1$. Note that the lattice points in the unstable ellipse are not necessarily in the principal domain $\mathcal{A}$.

6.1.5. An Explicit Bound for Nonimaginary Eigenvalues. In Section 2.9.3, the Gershgorin disc theorem was applied to find an upper bound on the real part of all eigenvalues. For special parameter values, we can find an explicit upper and lower bound on an eigenvalue with positive real part using the same method, without calculating the eigenvalues of a large matrix. As calculating eigenvalues can be computationally expensive, such a bound is very useful. Assume we are in the case $\rho_0=0$, $\rho_1<0$. Consider the eigenvalues of the Jacobi matrix

$$\mathcal{J}=\begin{pmatrix}\ddots & \vdots & \vdots & \vdots & \vdots & \ddots & \\ \dots & a_{-1} & b_0 & 0 & 0 & 0 & \dots\\ \dots & b_0 & a_0 & b_1 & 0 & 0 & \dots\\ \dots & 0 & b_1 & a_1 & b_2 & 0 & \dots\\ \dots & 0 & 0 & b_2 & a_2 & b_3 & \dots\\ \dots & 0 & 0 & 0 & b_3 & a_3 & \dots\\ \ddots & \vdots & \vdots & \vdots & \vdots & \ddots & \end{pmatrix} \tag{6.1.12}$$

with coefficients $a_n=-\rho_{2n}(\rho_{2n+1}+\rho_{2n-1})$, $b_n=\rho_{2n-1}\sqrt{\rho_{(2n-2)}\rho_{2n}}$ from (2.9.4). The eigenvalues of this matrix are the squares of the eigenvalues of (6.1.1). By

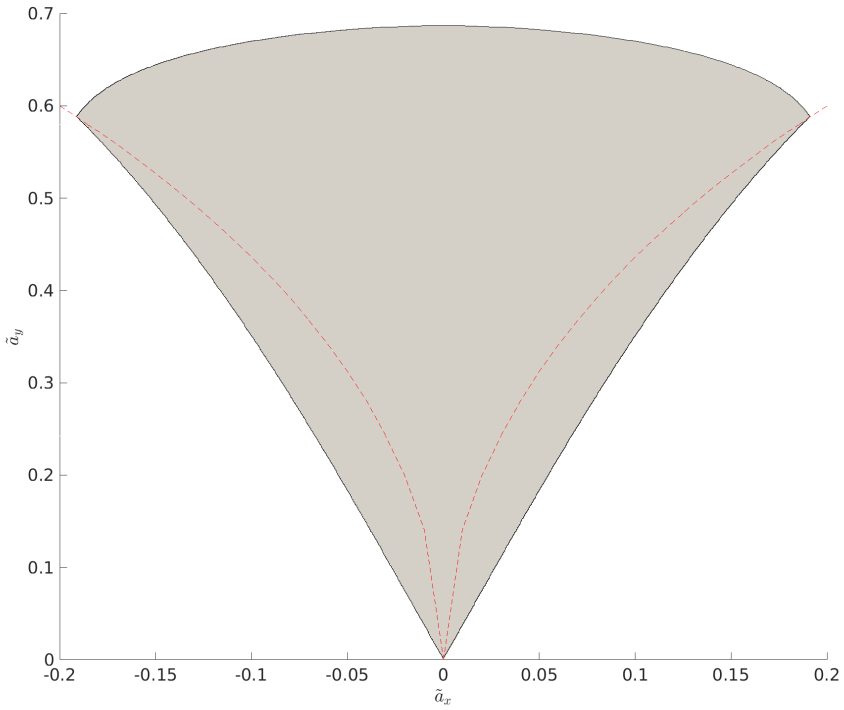

Figure 6.14 – The parameter range of $(\tilde{a}_x, \tilde{a}_y)$ where the Gershgorin disc theorem can be used to calculate an explicit bound on an eigenvalues with positive real part. This bound can be calculated very efficiently and does not require many terms of the matrix (6.1.1). The red dashed lines show the curves $(\tilde{a}_x \pm 1)^2 + \tilde{a}_y^2 = 1$, where $\rho_{\pm 1} = 0$. This region was calculated numerically.

the Gershgorin disc theorem, the eigenvalues must lie in the discs with centres $C_i = a_i = -\rho_{2i}(\rho_{2i+1} + \rho_{2i-1})$ and radii $R_i = |b_i| + |b_{i+1}| = |\rho_{2i-1}\sqrt{\rho_{2i-2}\rho_{2i}}| + |\rho_{2i+1}\sqrt{\rho_{2i}\rho_{2i+2}}|$.

In particular, $C_0 = -\rho_1\rho_2$, and $R_0 = \rho_2\rho_3$. Both of these values are positive and real. If this disc does not intersect any others, it must contain an eigenvalue. Additionally, if $C_0 - R_0 > 0$, then this disc lies entirely within the right half of the plane, so it contains an eigenvalue with positive real part. If these conditions hold we have an explicit bound on an eigenvalue of (6.1.12) with positive real part, and therefore an eigenvalue of (6.1.1) with positive real part. The region where these conditions are met was calculated numerically and is shown in Figure 6.14. An illustrative example is shown in Figure 6.15. Some eigenvalue of (6.1.12) must lie in the isolated disc indicated in that figure.

This method can also be applied in the three-dimensional case; for a problem with reduced parameters $\tilde{a}_x, \tilde{a}_y, \theta$ and $\theta \neq 0, \pi$, the spectrum is equivalent to

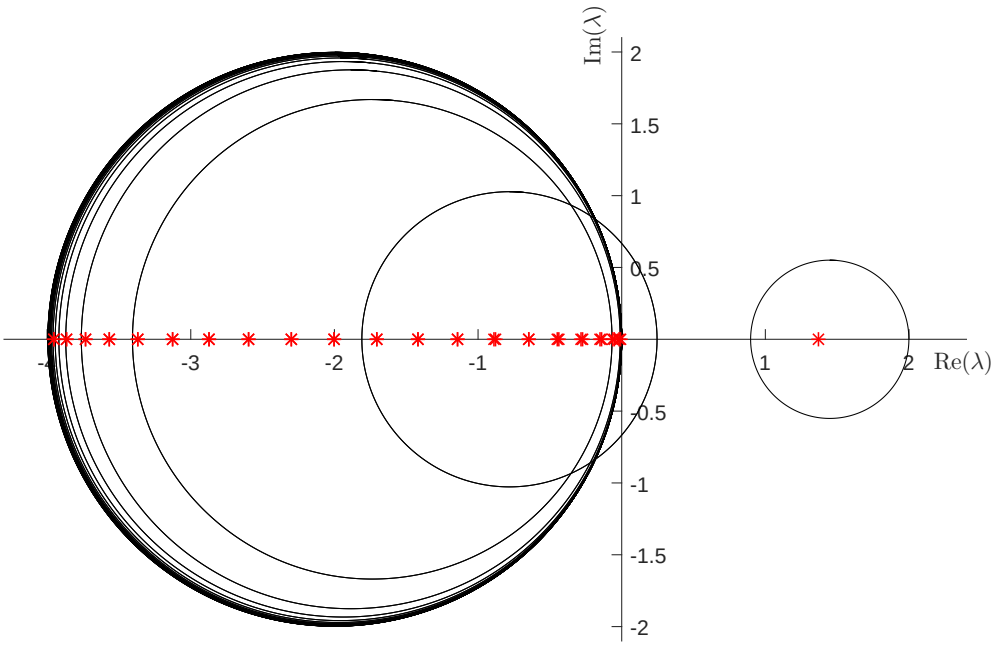

Figure 6.15 – The Gershgorin discs of (6.1.12) truncated from a_{-20} to a_{20} for $(\tilde{a}_x, \tilde{a}_y) = (0, 0.4)$. As these parameters lie in the region indicated in Figure 6.14, there is an eigenvalue with nonzero real part which can be isolated by the Gershgorin disc theorem. There is a disjoint disc in the right half of the plane, which must contain an eigenvalue. Therefore (6.1.12) has an eigenvalue with positive real part, and so (6.1.1) must also have an eigenvalue with positive real part. Also note that the discs accumulate at $(x+2)^2 + y^2 = 2^2$, the limiting disc. This corresponds to the observation that the imaginary eigenvalues lie in the interval $[-2, 2]i$. The calculated eigenvalues of the matrix (6.1.12) are plotted as red asterisks; as expected, they fill the interval $[-4, 0]$ except for an isolated eigenvalue on the positive real axis.

the two-dimensional problem with parameters $\tilde{a}_x, \tilde{a}_y$ by Theorem 4.2.59. We can therefore use the above to calculate an explicit bound by including the factor of $|\sin\theta|\tilde{a}_y$.

6.1.6. The Imaginary Spectrum. We now turn our attention to the imaginary spectrum. Per [**LLS04**], the essential spectrum of the full linearised problem is the full imaginary axis. This is made up of the superposition of the essential spectrum of all classes, which are intervals on the imaginary axis. We now briefly discuss the imaginary spectrum of an individual class, and how it relates to the spectral density.

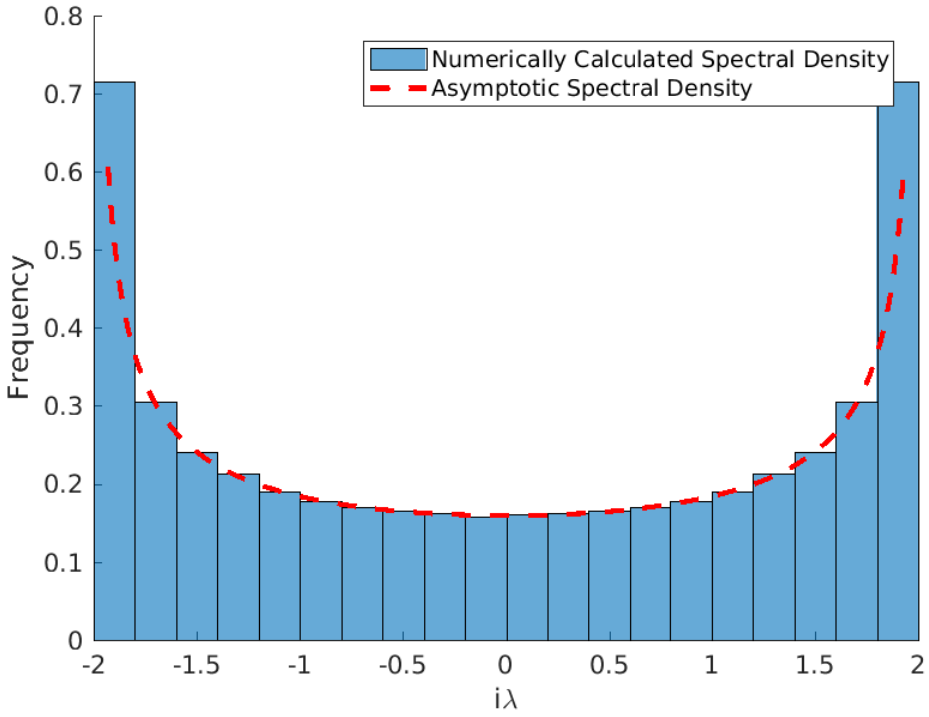

Figure 6.16 – The density of imaginary eigenvalues for $(\tilde{a}_x, \tilde{a}_y) = (0.3, 0.3)$. The blue bars show the density of eigenvalues on the imaginary axis, which occur between $-2i$ and $2i$. The eigenvalues are most dense near these endpoints. These eigenvalues were calculated using a sine-bracket truncation with $N = 500$. The dashed red lines show the spectral density (6.1.14) obtained by the approximation that a_y is sufficiently large and so $\rho_k \approx 1$ for all k.

For any $\varepsilon > 0$, we can choose $\tilde{a}_y \geq 1/\sqrt{\varepsilon}$, so $1 > \rho_k > 1 - \varepsilon$ for all $k \in \mathbb{Z}$ and thus $\rho_k \approx 1$. Notably, in this approximation M is the same as the constant matrix $\tilde{M}_1$ (4.2.44) from Chapter 4. Consider this approximation in the sine-bracket truncated matrix M_T (3.2.14). Under the equivalent approximation in the unreduced parameters $\rho_k \approx \rho_\infty = 1/|\mathbf{p}|^2_{\boldsymbol{\kappa}}$, this matrix is now antisymmetric. A circulant matrix is diagonalised by a discrete Fourier transform as discussed in Section 3.2.2. Thus the eigenvalues are

$$\lambda_j = \frac{2i}{|\mathbf{p}|^2_{\boldsymbol{\kappa}}} \sin\left(\frac{2\pi j}{n}\right) \text{for} j = 0, ..., n-1 \tag{6.1.13}$$

where $n = 2N + 1$, and N is the truncation size used in the sine-bracket system.

Thus the approximate imaginary spectrum of $\Sigma_{\mathbf{a}}$ for sufficiently large $|\mathbf{a}|$ lies inside the interval $\frac{2|\alpha|i}{|\mathbf{p}|^2_{\boldsymbol{\kappa}}}[-1, 1]$ on the imaginary axis. Taking the limit $N \to \infty$ (and so $n \to \infty$), for each $x \in [0, 1]$ there is a correspondence with an eigenvalue

λ_x where $x = \frac{1}{2\pi}\sin^{-1}\left(\frac{\lambda_x|\mathbf{p}|_{\boldsymbol{\kappa}}^2}{2i}\right)$. Differentiating this gives the density function

$$F(x) = \frac{|\mathbf{p}|_{\boldsymbol{\kappa}}^2}{\pi\sqrt{4\alpha^2 - |\mathbf{p}|_{\boldsymbol{\kappa}}^4 x^2}}. \tag{6.1.14}$$

That is, the proportion of the eigenvalues lying between $c_1 i$ and $c_2 i$ on the imaginary axis is $\int_{c_1}^{c_2} F(x)\mathrm{d}x$ for $c_1, c_2 \in \frac{2}{|\mathbf{p}|_{\boldsymbol{\kappa}}^2}[-|\alpha|, |\alpha|]$. The curve $F(x)$ is plotted in Figure 6.16, and it agrees well with the numerically calculated eigenvalues. This is somewhat surprising as the value of $\tilde{a}_y$ is not particularly large for that figure. We conclude that equation (6.1.14) gives a strong approximation of the essential spectrum. The function $G(y) = \int_{c_1}^{y} F(x)\mathrm{d}x$ where $c_1 = \frac{-2\alpha}{|\mathbf{p}|_{\boldsymbol{\kappa}}^2}$ is the spectral density function. In the special cases discussed in Section 2.9.4, this is equivalent up to transformation to the spectral density (2.9.26) that was calculated by considering the problem as a Jacobi operator. Note that (2.9.26) is the spectral density of M^2, and $G(y)$ is the spectral density of M.

In [**LLS04, SL03**], the authors describe the essential spectrum of the linearised operator (6.1.1) in the isotropic case $\kappa_y/\kappa_x = 1$. The essential spectrum for the class led by $\mathbf{a}$ is given in that paper as

$$\sigma_{\text{ess}} = i[-|\beta|, |\beta|], \quad \text{where} \quad \beta = \frac{2\Gamma}{|\mathbf{p}|^2}(\mathbf{a} \times \mathbf{p}). \tag{6.1.15}$$

This is the same as our result in the case $\kappa_y/\kappa_x = 1$.

These results can be applied to the three-dimensional case as well. In terms of the reduced parameters $\tilde{a}_x, \tilde{a}_y, \theta$, by Theorem 4.2.59 the spectrum of a class of the linearised three-dimensional problem is the same as the two-dimensional class with parameters $\tilde{a}_x, \tilde{a}_y$ up to a factor of $|\sin(\theta)|$. The constant secondary part of the matrix (4.2.44) has the same essential spectrum and so contributes no additional eigenvalues. In the exceptional cases $\theta = 0, \pi$, the matrix (4.2.36) is nilpotent per Section 4.2.9, so the eigenvalues are all zero and the result still holds as $\sin 0 = \sin \pi = 0$.

We can now make the following conclusion: the essential spectrum of a class of the linearised three-dimensional equations with reduced parameters $\tilde{a}_x, \tilde{a}_y, \theta$ is

$$|\tilde{a}_y \sin\theta|[-2, 2]i, \tag{6.1.16}$$

an interval on the imaginary axis. As per the two-dimensional case, $\tilde{a}_y$ is unbounded so the essential spectrum of the full linearised operator is the union of these for arbitrarily large $\tilde{a}_y$. Therefore the essential spectrum is the full imaginary axis.

Figure 6.16 shows the density of the imaginary parts of the spectrum for $(\tilde{a}_x, \tilde{a}_y) = (0.3, 0.3)$. These eigenvalues are calculated using the sine-bracket approximation. The spectral density curve $F(x)$ is also shown, and agrees well with the calculated eigenvalues.

6.2. Spectrum of Limiting Domain Sizes

An interesting question is what happens to the nonimaginary eigenvalues and stability of the linearised equations for extreme values of the boundary sizes κ_x, κ_y, κ_z. We have seen in Section 2.6 that the stability of parallel shear flows depends on the size of the unstable ellipse/ellipsoid and thus the size of the domain. Conjectures 6.1.8 and 6.1.10 show that the number of nonimaginary eigenvalues also depends on the size of the unstable ellipse/ellipsoid. Therefore we now study what happens when these sizes are very large or very small. For extreme values of the domain size, the spectrum can either disappear per Section 2.6 or accumulate along a finite number of curves akin the contours in Figure 6.8.

These parameters may be of physical interest, as it may suggest the corresponding behaviour for the Euler equations on a cylindrical domain with periodic boundary conditions in one direction only. These results can be compared to the study of parallel shear flows with a fixed domain but a large number of oscillations [**BFY99**]; this may in some sense be considered the dual problem.

6.2.1. Limiting Domain Sizes in Two Dimensions. We first consider the linearised two-dimensional problem. As the problem only depends on the ratio of the domain sizes κ_y/κ_x, we only need consider when this quantity becomes asymptotically small or large.

For $\kappa_y/\kappa_x \to 0, \infty$, taking the limit of the formulae in (6.1.5) yields the result

$$\lim_{\kappa_y/\kappa_x \to \infty} \tilde{a}_x = \frac{a_y}{p_y}, \quad \lim_{\kappa_y/\kappa_x \to 0} \tilde{a}_x = \frac{a_x}{p_x} \tag{6.2.1}$$

where $\mathbf{a} = (a_x, a_y)$. As $\mathbf{a}, \mathbf{p} \in \mathbb{Z}^2$ and $\mathbf{a}$ only takes a finite set of values, this means that the values of $\tilde{a}_x$ accumulate at multiples of $1/p_y$ in the limit $\kappa_y/\kappa_x \to \infty$ and at multiples of $1/p_x$ in the limit $\kappa_y/\kappa_x \to 0$. This is illustrated in Figure 6.17. In particular, if $p_x = 1$ and $\kappa_y/\kappa_x \to 0$, then $\tilde{a}_x \to 0$ for all $\mathbf{a}$, and all associated eigenvalues will become real.

In these limits typically the number of lattice points inside the unstable ellipse $\nu \to \infty$ and therefore the size of the nonimaginary spectrum $|\sigma_{\text{discrete}}(M)| \to \infty$. In these cases the nonimaginary discrete spectrum appears to converge to some continuous spectrum. This is illustrated in Figures 6.18 and 6.19, which show the nonimaginary spectrum for $\mathbf{p} = (2, 1)$ and $\mathbf{p} = (5, 0)$ respectively across a range of values of κ_y/κ_x. For particularly large or small values, the spectrum accumulates at one or more curves similar to the contours in Figure 6.8, which correspond to the discrete values of $\tilde{a}_x$ that occur in the limit. Note the case with $\mathbf{p} = (2, 1)$ and κ_y/κ_x large, where all eigenvalues are purely real or purely imaginary. This corresponds to the fact that all lattice points have $\tilde{a}_x = 0$ in the limit as $p_y = 1$. We also observe cases with no unstable eigenvalues for $\mathbf{p} = (5, 0)$, corresponding to the stability result for parallel shear flows.

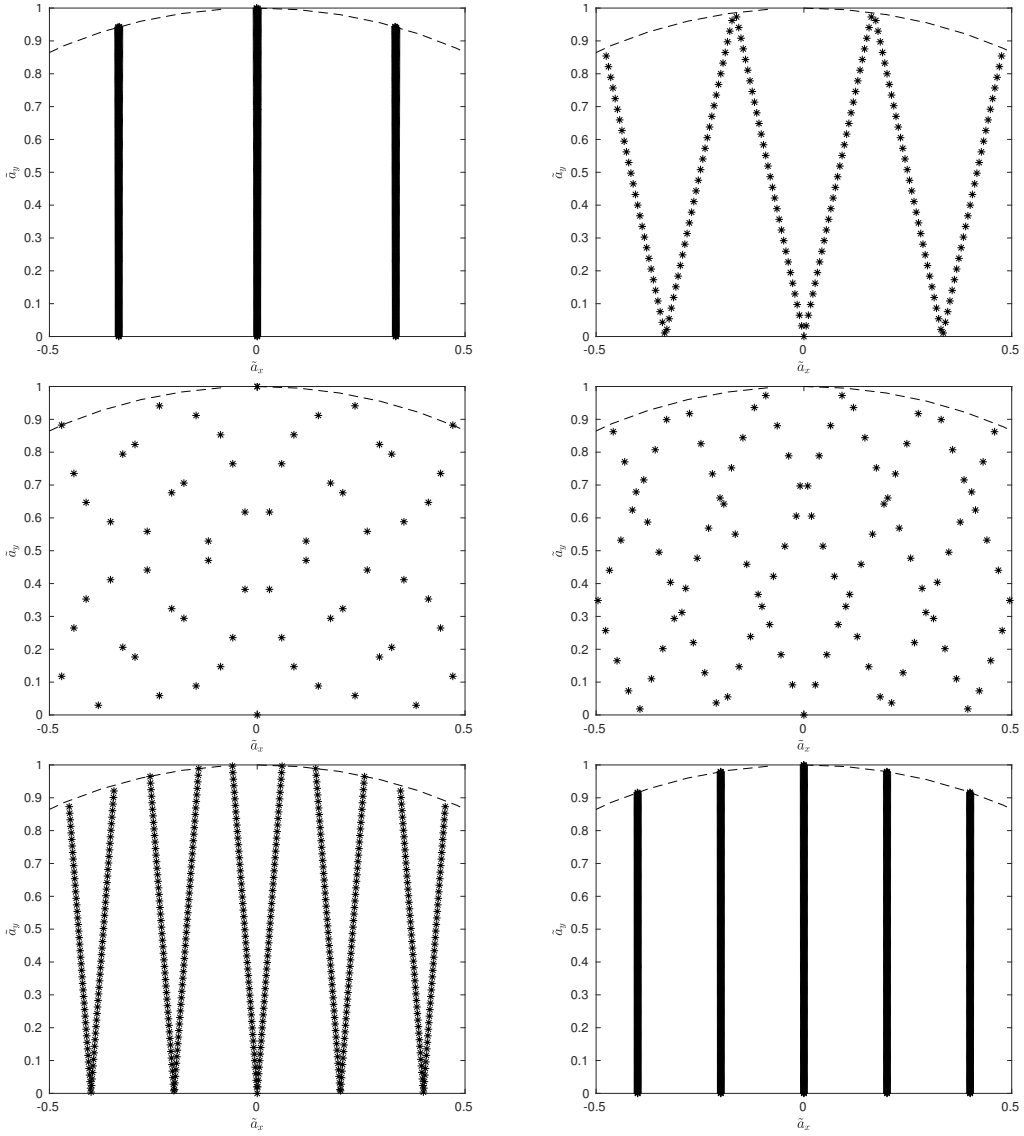

Figure 6.17 – Relevant values of the reduced parameters $\tilde{a}_x$, $\tilde{a}_y$ for $\mathbf{p} = (5, 3)$, $\boldsymbol{\kappa} = (\kappa_x, \kappa_y)$ for various values of κ_y/κ_x. The reduced parameters $\tilde{a}_x, \tilde{a}_y \in \mathbb{R}$ are calculated for all $\mathbf{a} \in \mathbb{Z}^2 \cap D_{\mathbf{p}}$. Only these parameters lead to classes contributing nonimaginary eigenvalues. Top row: $\kappa_y/\kappa_x = 1000$, $\kappa_y/\kappa_x = 10$. Middle row: $\kappa_y/\kappa_x = 1$, $\kappa_y/\kappa_x = 1/2$. Bottom row: $\kappa_y/\kappa_x = 1/10$, $\kappa_y/\kappa_x = 1/1000$. Note that for large or small values of κ_y/κ_z, the values of $\tilde{a}_x$ accumulate at a finite set of discrete values.

We can also study how the condition for Theorem 2.7.53 changes for extreme values of κ_y/κ_x. Figure 6.21 shows the values of $\mathbf{p}$ where Theorem 2.7.53 can be applied, and the values for which the condition (2.7.31) holds for the domain size $\kappa_y/\kappa_x = 100$. For sufficiently large values of κ_y/κ_x, values of $\mathbf{p} = (p_x, p_y)$ with

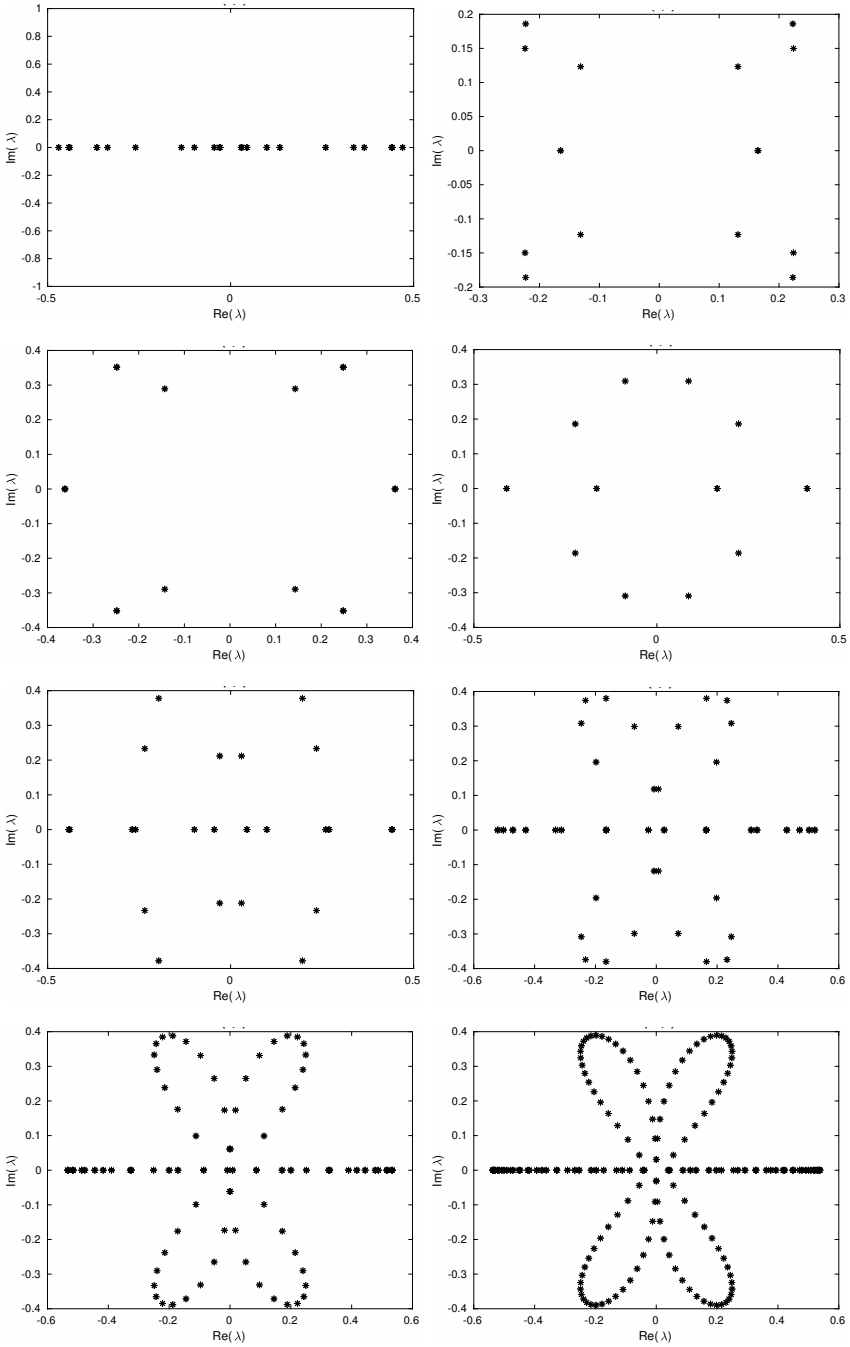

Figure 6.18 – All nonimaginary eigenvalues of αM for $\mathbf{p} = (2, 1)$, varying $\boldsymbol{\kappa}$. First row: $\kappa_y/\kappa_x = 8$, $\kappa_y/\kappa_x = 4$. Second row $\kappa_y/\kappa_x = 2$, $\kappa_y/\kappa_x = 1$. Third row: $\kappa_y/\kappa_x = 1/2$, $\kappa_y/\kappa_x = 1/4$. Fourth row: $\kappa_y/\kappa_x = 1/8$, $\kappa_y/\kappa_x = 1/16$ As $\kappa_y/\kappa_x \to \infty$, $\tilde{a}_x$ accumulates at 0, so all eigenvalues are real. As $\kappa_y/\kappa_x \to 0$, the eigenvalues trace a curve similar to those in Figure 6.8, as $\tilde{a}_x$ accumulates at discrete values as shown in Figure 6.20.

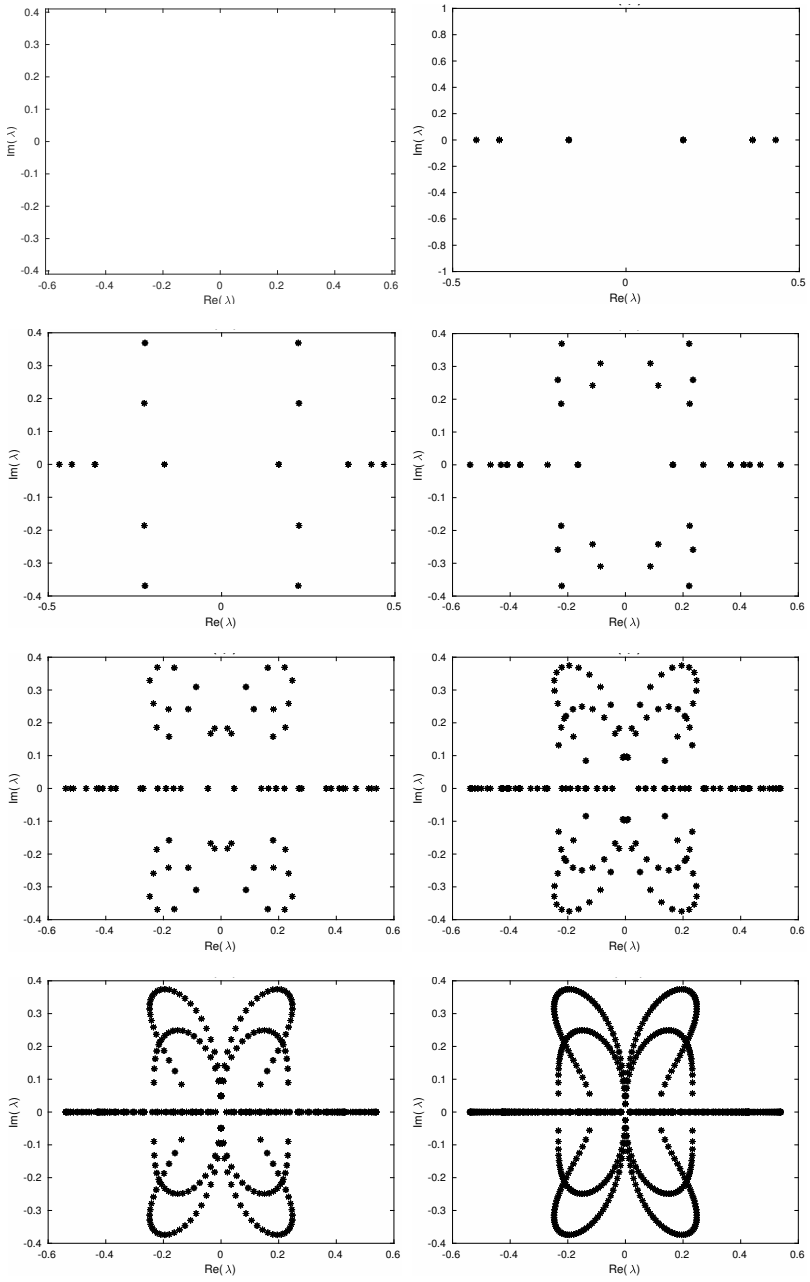

Figure 6.19 – All nonimaginary eigenvalues of αM for $\mathbf{p} = (5, 0)$, varying κ_y/κ_x. First row: $\kappa_y/\kappa_x = 8$, $\kappa_y/\kappa_x = 4$. Second row $\kappa_y/\kappa_x = 2$, $\kappa_y/\kappa_x = 1$. Third row: $\kappa_y/\kappa_x = 1/2$, $\kappa_y/\kappa_x = 1/4$. Fourth row: $\kappa_y/\kappa_x = 1/8$, $\kappa_y/\kappa_x = 1/16$. For $\kappa_y/\kappa_x > 5$, there is no nonimaginary spectrum per Theorem 2.6.1. For small κ_y/κ_x, there are multiple asymptotic values for $\tilde{a}_x$ shown in Figure 6.20 and eigenvalues accumulate along corresponding curves such as those in Figure 6.8.

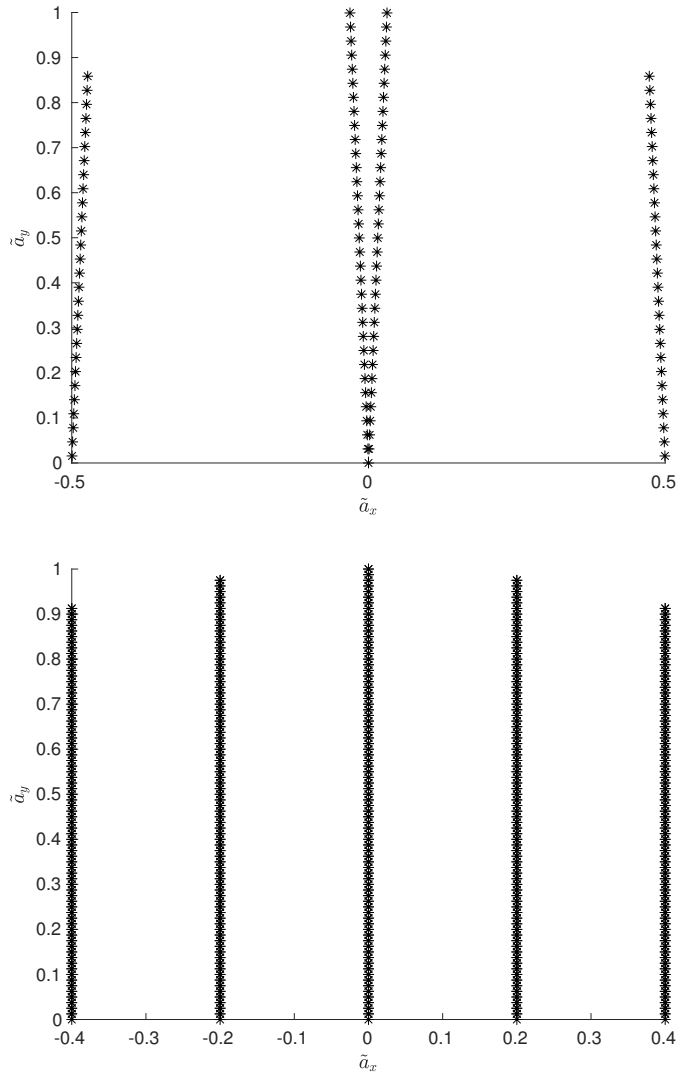

Figure 6.20 – For a fixed $\mathbf{p}$, $\boldsymbol{\kappa}$, across all $\mathbf{a} \in D_{\mathbf{p}} \cap \mathbb{Z}^3$, the associated reduced parameters $\tilde{a}_x, \tilde{a}_y$. In both cases, $\kappa_y/\kappa_x = 1/16$, which is relatively small. Top: $\mathbf{p} = (2, 1)$, corresponding to the bottom right subfigure in Figure 6.18. The values of $\tilde{a}_x$ accumulate at $\tilde{a}_x = 0$, leading to real eigenvalues, and $\tilde{a}_x = \pm 1/2$, leading to complex eigenvalues along a curve equivalent to the contours in Figure 6.8. Bottom: $\mathbf{p} = (5, 0)$, corresponding to the bottom right subfigure in Figure 6.19. The parameters accumulate at $\tilde{a}_x = 0, \pm 1/5, \pm 2/5$. Thus there are real eigenvalues with parameters $\tilde{a}_x = 0$, and two sets of eigenvalues along curves from Figure 6.8 corresponding to $\tilde{a}_x = \pm 1/5, \pm 2/5$. Compare this to Figure 6.17; for all $\mathbf{p} = (p_x, p_y)$, as $\kappa_y/\kappa_x \to 0$ the relevant $\tilde{a}_x$ parameters take only the values $\pm k/p_x$ for $k \in \mathbb{Z}$. Similarly, if $\kappa_y/\kappa_x \to \infty$ the relevant $\tilde{a}_x$ parameters take only the values $\pm k/p_y$.

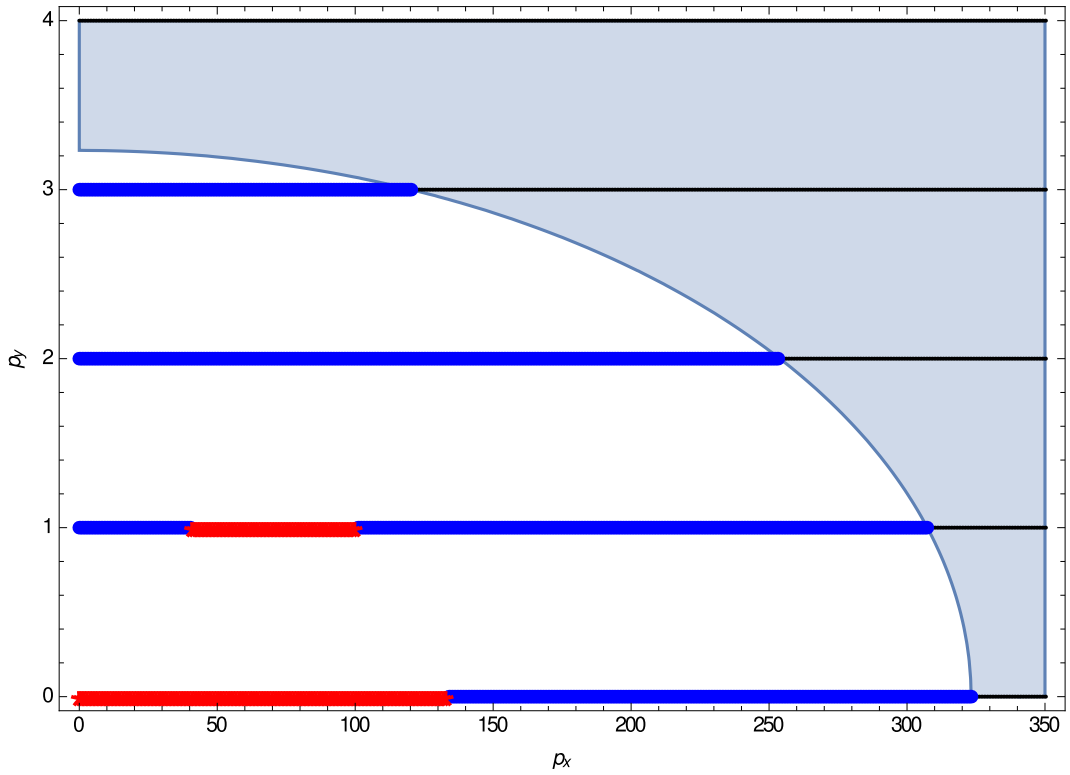

Figure 6.21 – Valid values of $\mathbf{p}$ for Theorem 2.7.53 with $\kappa_y/\kappa_x = 100$. As per Figures 2.13 and 2.14. Here κ_y/κ_x is large so there are a large number of values of $\mathbf{p}$ that do not satisfy the condition per Figure 2.15. The red values that indicate values with no $\mathbf{a}$ leading to a real eigenvalue have $p_y = 0, 1$, which will in general be true for large κ_y/κ_x.

$p_x > \frac{3+2\sqrt{3}}{2}\frac{\kappa_y}{\kappa_x}$ or $p_y > \frac{3+2\sqrt{3}}{2} > 3$ satisfy (2.7.31), and therefore there is linear instability. By observation, in this limit all values $\mathbf{p}$ with $p_y > 1$ have some class $\mathbf{a}$ that satisfies the conditions of Theorem 2.7.53 without satisfying (2.7.31), leading to linear instability. Of course, we expect all steady states not satisfying the conditions of Theorem 2.6.1 to be unstable due to the hypothesis of 2.7.1, but this has not yet been proven.

6.2.2. Limiting Domain Sizes in Three Dimensions. The concepts in Section 6.2.1 can be applied to the three-dimensional problem as well. As there are three domain parameters $\kappa_x, \kappa_y, \kappa_z$, we can consider domains with extreme values of κ_y/κ_x, κ_z/κ_z, or both. Recall that $|\boldsymbol{\kappa}| = 1$ is normalised and $\kappa_x, \kappa_y, \kappa_z \neq 0$ so these ratios uniquely define the size of the domain.

Many of the same observations as for the two-dimensional case apply to the three-dimensional case. Figure 6.22 shows how the nonimaginary eigenvalues for $\mathbf{p} = (1, 1, 1)$ vary as the domain size is varied. Note that as the domain size is

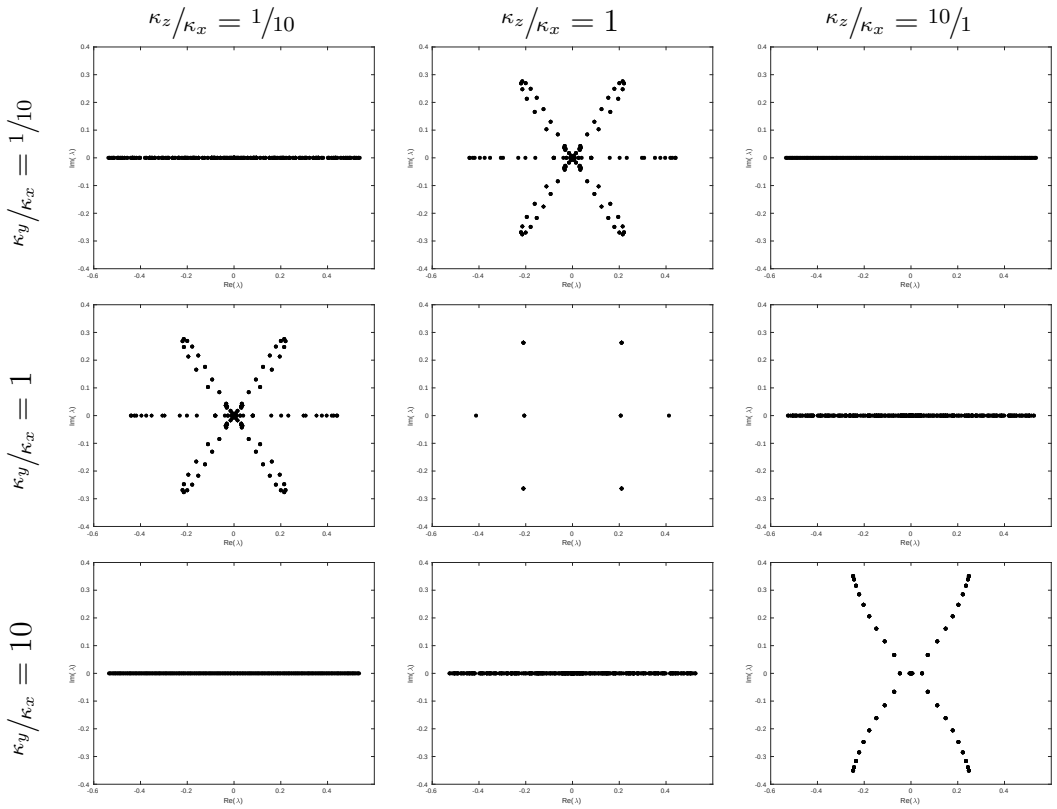

Figure 6.22 – For $\mathbf{p} = (1, 1, 1)$, the change in the nonimaginary spectrum as the domain size is made large or small. Here $\mathbf{\Gamma} = (\Gamma_x, 1, 1)$ with Γ_x chosen to satisfy the divergence-free condition. The three rows from top to bottom have domain $\kappa_y/\kappa_x = 1/10$, $\kappa_y/\kappa_x = 1$, $\kappa_y/\kappa_x = 10$. The three columns from left to right have domain $\kappa_z/\kappa_x = 1/10$, $\kappa_z/\kappa_x = 1$, $\kappa_z/\kappa_x = 10$. Note that as $\mathbf{p}$ is symmetric under cyclic permutations, this figure is symmetric under $\kappa_y \leftrightarrow \kappa_z$. If any two of $\kappa_x, \kappa_y, \kappa_z$ are much smaller than the third, there are only real nonimaginary eigenvalues. This is the same behaviour as in Figure 6.18.

changed, $\mathbf{\Gamma}$ must be altered to preserve the divergence-free condition $\langle \mathbf{p}, K^{-1}\mathbf{\Gamma} \rangle = 0$. This does not qualitatively affect the nonimaginary spectrum. As per the two-dimensional case in Figures 6.18, 6.19 the number of nonimaginary eigenvalues becomes very large when either or both of κ_y/κ_x, κ_z/κ_z become large or small. This is because the unstable ellipsoid $D_{\mathbf{p}}$ become large, corresponding to an increase in ν and therefore an increase in the number of nonimaginary eigenvalues per Conjecture 6.1.10. As $p_x, p_y, p_z \neq 0$, any domain that is sufficiently far from isotropic leads to a large number of nonimaginary eigenvalues. Also note that the figures are symmetric in κ_y/κ_x, κ_z/κ_z as $\mathbf{p}$ is symmetric in each direction and $\mathbf{\Gamma}$ is symmetric in the y and z directions. Note that for $\kappa_y/\kappa_x = 1/10$ and $\kappa_z/\kappa_x = 1$, the spectrum converges towards a curve similar to those in Figure 6.8. This is

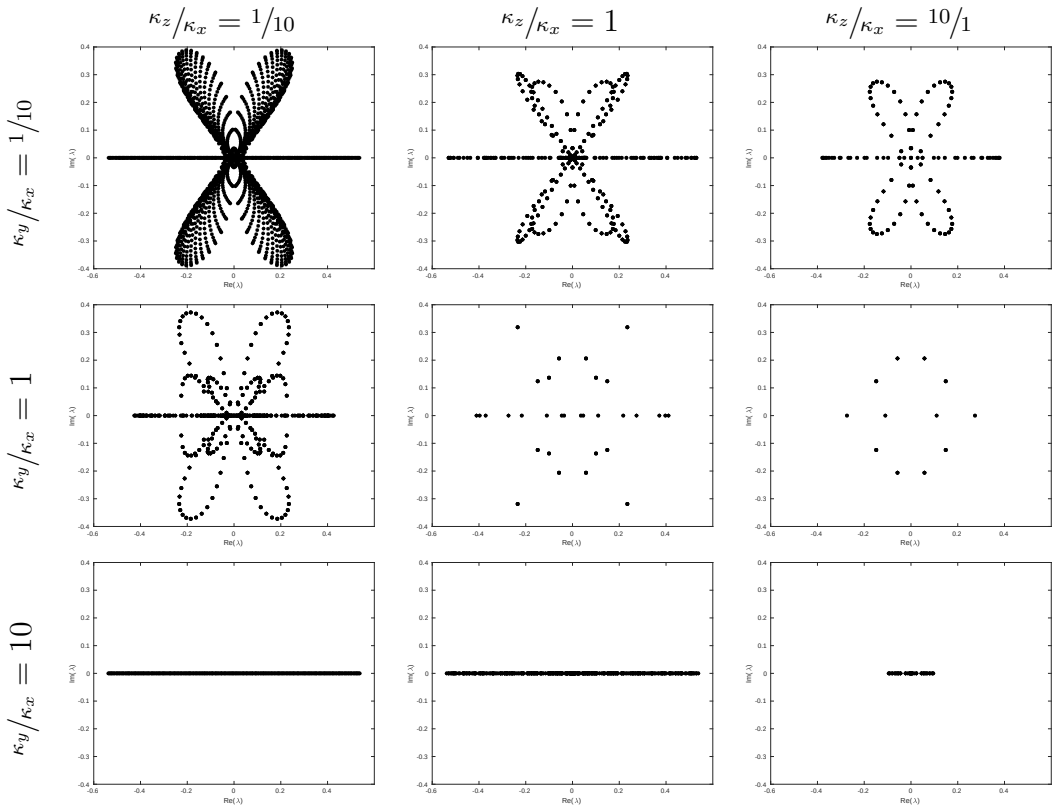

Figure 6.23 – For $\mathbf{p} = (2, 1, 0)$, the change in the nonimaginary spectrum as the domain sizes are made large or small. Here $\mathbf{\Gamma} = (\Gamma_x, 1, 1)$ with Γ_x chosen to satisfy the divergence-free condition. The three rows from top to bottom have domain $\kappa_y/\kappa_x = 1/10$, $\kappa_y/\kappa_x = 1$, $\kappa_y/\kappa_x = 10$. The three columns from left to right have domain $\kappa_z/\kappa_x = 1/10$, $\kappa_z/\kappa_x = 1$, $\kappa_z/\kappa_x = 10$. For sufficiently large values of κ_y/κ_x, the nonimaginary spectrum is real as the unstable ellipsoid becomes sufficiently prolate. For small values of κ_y/κ_x or κ_z/κ_x, the spectrum converges to contours as in the two-dimensional case shown in Figure 6.19. If κ_y/κ_x are both small, new curves arise due to the factor of $\sin\theta$ in the spectrum, as there will be classes with many different values of θ. Finally note that for $\kappa_y/\kappa_x = 1$ and sufficiently large values of κ_z/κ_x, the nonimaginary spectrum is the same as for the two-dimensional class with $\mathbf{p} = (2, 1)$, as shown in Figure 6.10. This is because the unstable ellipsoid is very narrow in the z-direction, so the only nonimaginary spectrum is from the lattice points on the x-y plane, which correspond to the lattice points in the two-dimensional classes.

for the same reason as in Section 6.2.1: the values of the reduced parameters $\tilde{a}_x$ converge to a set of discrete values. Finally for $\kappa_y/\kappa_x = \kappa_z/\kappa_z = 10$, the eigenvalues lie on a different curve to those seen in Figure 6.8. This curve occurs as the

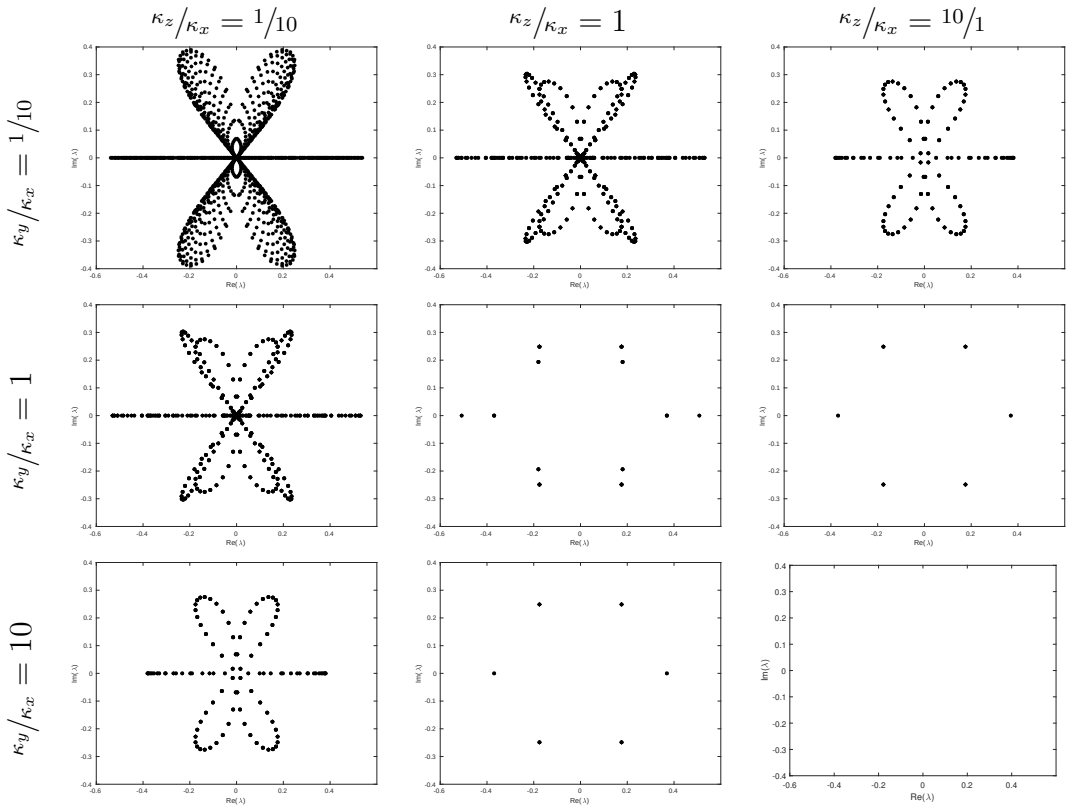

Figure 6.24 – For $\mathbf{p} = (2, 0, 0)$, the change in the nonimaginary spectrum as the domain sizes are made large or small. Here $\mathbf{\Gamma} = (\Gamma_x, 1, 1)$ with Γ_x chosen to satisfy the divergence-free condition. The three rows from top to bottom have domain $\kappa_y/\kappa_x = 1/10$, $\kappa_y/\kappa_x = 1$, $\kappa_y/\kappa_x = 10$. The three columns from left to right have domain $\kappa_z/\kappa_x = 1/10$, $\kappa_z/\kappa_x = 1$, $\kappa_z/\kappa_x = 10$. Note that as $\kappa_y/\kappa_x, \kappa_z/\kappa_x \to 0$ the size of the nonimaginary spectrum increases as the size of the unstable ellipsoid increases. Also if $\kappa_y/\kappa_x, \kappa_z/\kappa_x > 2$ there is no nonimaginary spectrum, as the conditions of Theorem 4.3.6 are satisfied so the shear flow is spectrally stable (though there may still be classes with linear instability, depending on the value of $\mathbf{\Gamma}$).

unstable ellipsoid grows to include classes with more values of θ, which scale the eigenvalues by $|\sin\theta|$.

In Figure 6.23, $\mathbf{p} = (2, 1, 0)$ is fixed and the domain sizes are changed. Again, $\mathbf{\Gamma}$ depends on the domain size to ensure the divergence-free condition is satisfied. In this case, we observe that if $\kappa_y/\kappa_x = 1$ and κ_y/κ_x is large, the spectrum is the same as that of the two-dimensional problem with $\mathbf{p} = (2, 1)$ shown in Figure 6.10. This is because the unstable ellipsoid becomes sufficiently narrow in the z direction so only lattice points of the form $\mathbf{a} = (a_x, a_y, 0)$ in the x-y plane are inside the unstable ellipsoid. The classes led by these values of $\mathbf{a}$ have the same eigenvalues as the two-dimensional class with $\mathbf{p} = (2, 1)$, $\mathbf{a} = (a_x, a_y)$ by Theorem

4.2.59. Also note that for κ_y/κ_x, κ_z/κ_x both sufficiently small, the eigenvalues occur on multiple discrete curves that are scaled copies of one another. This corresponds to the reduced parameter $\tilde{a}_x$ only taking finitely many values, but multiple values of the θ parameter occurring and scaling the resulting curves of eigenvalues. This can also be observed when $\kappa_y/\kappa_x = 1$ and $\kappa_z/\kappa_x = 1/10$, where contours akin to Figure 6.8 occur but are scaled according to $|\sin\theta|$ for different values of θ.

In Figure 6.24, $\mathbf{p} = (2, 0, 0)$. As this is of the form $\mathbf{p} = (p_x, 0, 0)$, we observe that the class is spectrally stable for certain domain sizes, per Theorem 4.3.6. This is visible when $\kappa_y/\kappa_x = \kappa_z/\kappa_x = 10$, where there are no nonimaginary eigenvalues. We also observe the same effects of changing the domain as in Figures 6.22 and 6.23, such as eigenvalues converging to curves corresponding to discrete values of $\tilde{a}_x$.

6.3. Numerically Calculated Flows

We now present some numerically calculated flows of the Euler equations. This allows us to verify the stability results of this thesis, particularly Theorems 2.6.1 and 2.7.53. We also observe the nonlinear dynamics that could not be captured by the linear stability analysis. To calculate these flows we use the Poisson integrator for the sine-bracket truncated nonlinear system developed in Section 3.3. This integrator is computationally efficient thanks to the decomposition and discrete Fourier transform developed in [**McL93**] and described in Section 3.3. It also conserves the Casimirs to machine precision.

The outline of the integration algorithm is as follows:

- Fix a truncation size $N \in \mathbb{N}$.
- For each $\mathbf{k}$ in $\mathcal{D}_N$, define $\sigma_{\mathbf{k}} = \{\widehat{n\mathbf{k}} : n \in \mathbb{N}\}$, a set of commuting coordinates.
- Choose a subset $\mathcal{K} \subseteq \mathcal{D}_N$ such that
$$\bigcup_{\mathbf{k}\in\mathcal{K}} \sigma_{\mathbf{k}} = \mathcal{D}_N. \tag{6.3.1}$$
This is generated algorithmically by adding additional modes $\mathbf{k}$ to $\mathcal{K}$ until the condition is satisfied.
- For all $\mathbf{j} \in \mathcal{D}_N$ define
$$\mu(\mathbf{j}) := \text{number of } \mathbf{k} \in \mathcal{K} \text{ such that } \widehat{n\mathbf{k}} = \mathbf{j} \text{ for some } n \in \mathbb{Z}. \tag{6.3.2}$$
For $2N+1$ prime, there is a choice of $\mathcal{K}$ per [**McL93**] such that $\mu(\mathbf{j}) = 1$ for all $\mathbf{j} \neq \mathbf{0}$. For $2N+1$ non-prime, such a choice of $\mathcal{K}$ is not possible.
- Split the Hamiltonian (3.1.12) as $H = \sum_{\mathbf{k}\in\mathcal{K}} H_{\mathbf{k}}$, where
$$H_{\mathbf{k}} = \frac{1}{2}\sum_{n\neq 0} \frac{1}{\mu(n\mathbf{k})} \frac{\omega_{+n\mathbf{k}}\omega_{-n\mathbf{k}}}{|n\mathbf{k}|_\kappa^2}$$

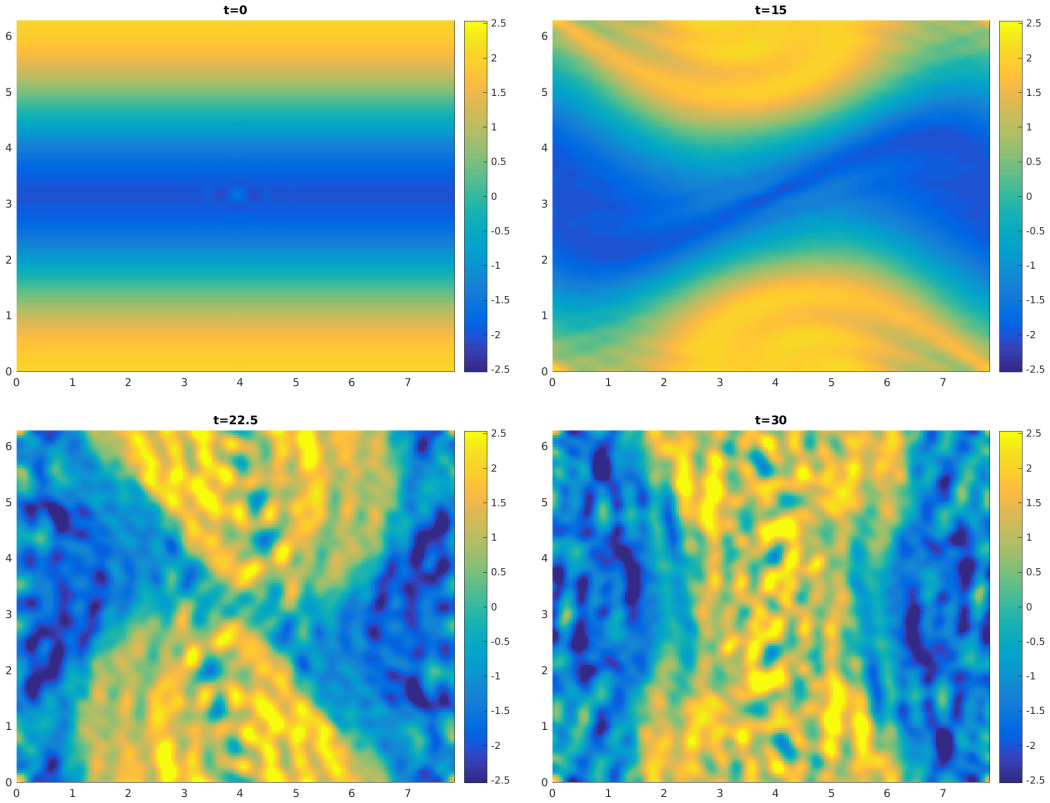

Figure 6.25 – The flow of an initial condition consisting of a small perturbation of $\cos(\kappa_x x)$, the steady state with $\mathbf{p} = (1, 0)$ for domain size $\kappa_y/\kappa_x = 5/4$. The flow is calculated using the Poisson integrator for the sine-bracket truncated system developed in Section 3.3 with truncation size $N = 18$. The domain size satisfies $\kappa_y/\kappa_x = 5/4 > 1$ so this steady state is unstable, as we can observe from the dynamics. From left to right, top to bottom, the system is shown at times $t = 0,\ 15,\ 22.5,\ 30$.

per (3.3.7). Note that this splitting is not necessarily disjoint; the same coordinate $\omega_{\mathbf{j}}$ may appear in multiple $H_{\mathbf{k}}$.

- For each $\mathbf{k} \in \mathcal{K}$, calculate the dynamics generated by $H_{\mathbf{k}}$ and the sine-truncated Poisson bracket. As $H_{\mathbf{k}}$ only depend on the modes in $\sigma_{\mathbf{k}}$ and these modes all commute, the modes in $\widehat{n\mathbf{k}}$ are constant under these dynamics, and all other modes have linear dynamics. We can thus calculate the flow map of $H_{\mathbf{k}}$ as $\phi^t_{\mathbf{k}}(\mathbf{x}_0) = \exp(tJD^2H_{\mathbf{k}})\mathbf{x}_0$. This exponential can be calculated explicitly; by Section 3.3, $JD^2H_{\mathbf{k}}$ is diagonalised by a discrete Fourier transform [**McL93**].

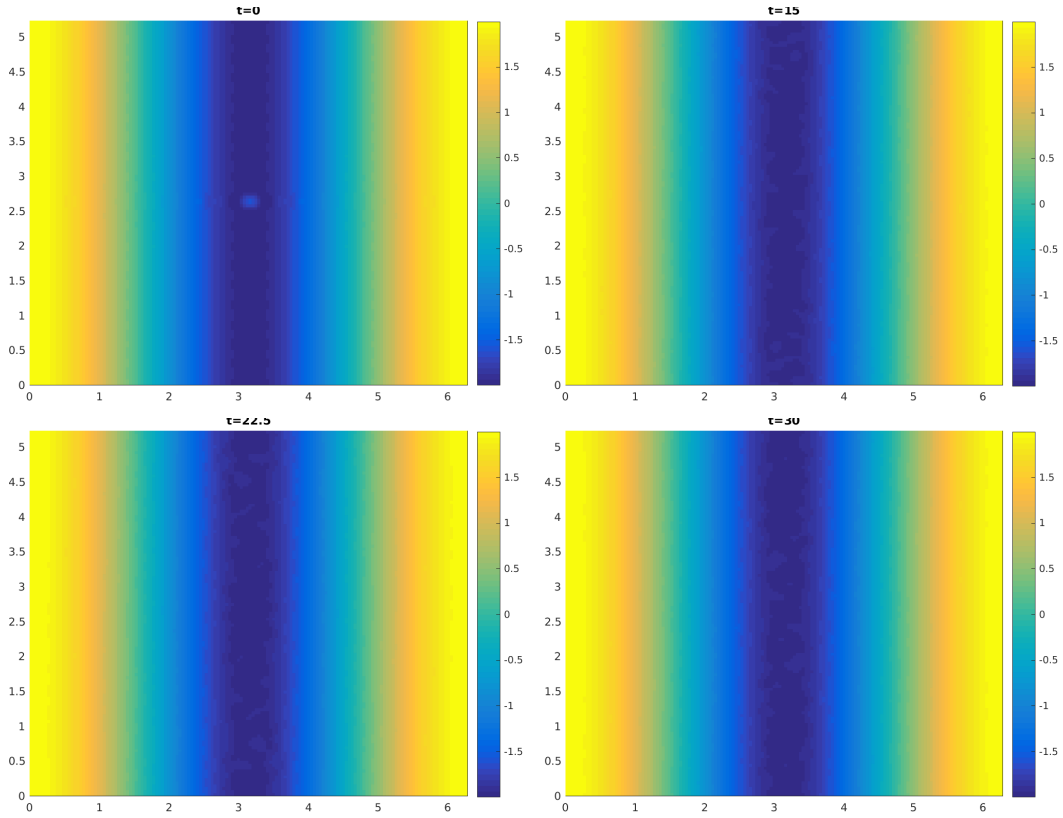

Figure 6.26 – The flow of an initial condition consisting of a small perturbation of $\cos(\kappa_x x)$, the steady state with $\mathbf{p} = (1, 0)$. The flow is calculated using the Poisson integrator for the sine-bracket truncated system developed in Section 3.3 with truncation size $N = 18$. The domain size is $\kappa_y/\kappa_x = 5/6 < 1$. This system is linearly stable by Theorem 2.6.1, and Energy-Casimir stable by [**Arn66b**]. Compare this to Figure 6.25; when the domain size is changed, the stability of the steady state changes accordingly. From left to right, top to bottom, the system is shown at times $t = 0,\ 15,\ 22.5,\ 30$.

- For each timestep, the full flow map is the split-step integrator

$$\phi_t = \prod_{\mathbf{k} \in \mathcal{K}} \phi_{\mathbf{k}}^t.$$

  This integrator preserves the Poisson structure.

We use this integrator to demonstrate the stability theorems of Chapters 2 and 3. Figures 6.25 and 6.26 show how a small perturbation of the flow with vorticity $\Omega = \cos(\kappa_x x)$ evolves depending on the ratio of the domain size κ_y/κ_x. The flow is perturbed by a Fourier-truncated Dirac delta function and the resulting initial condition evolved using the Poisson integrator with truncation size $N = 18$ and

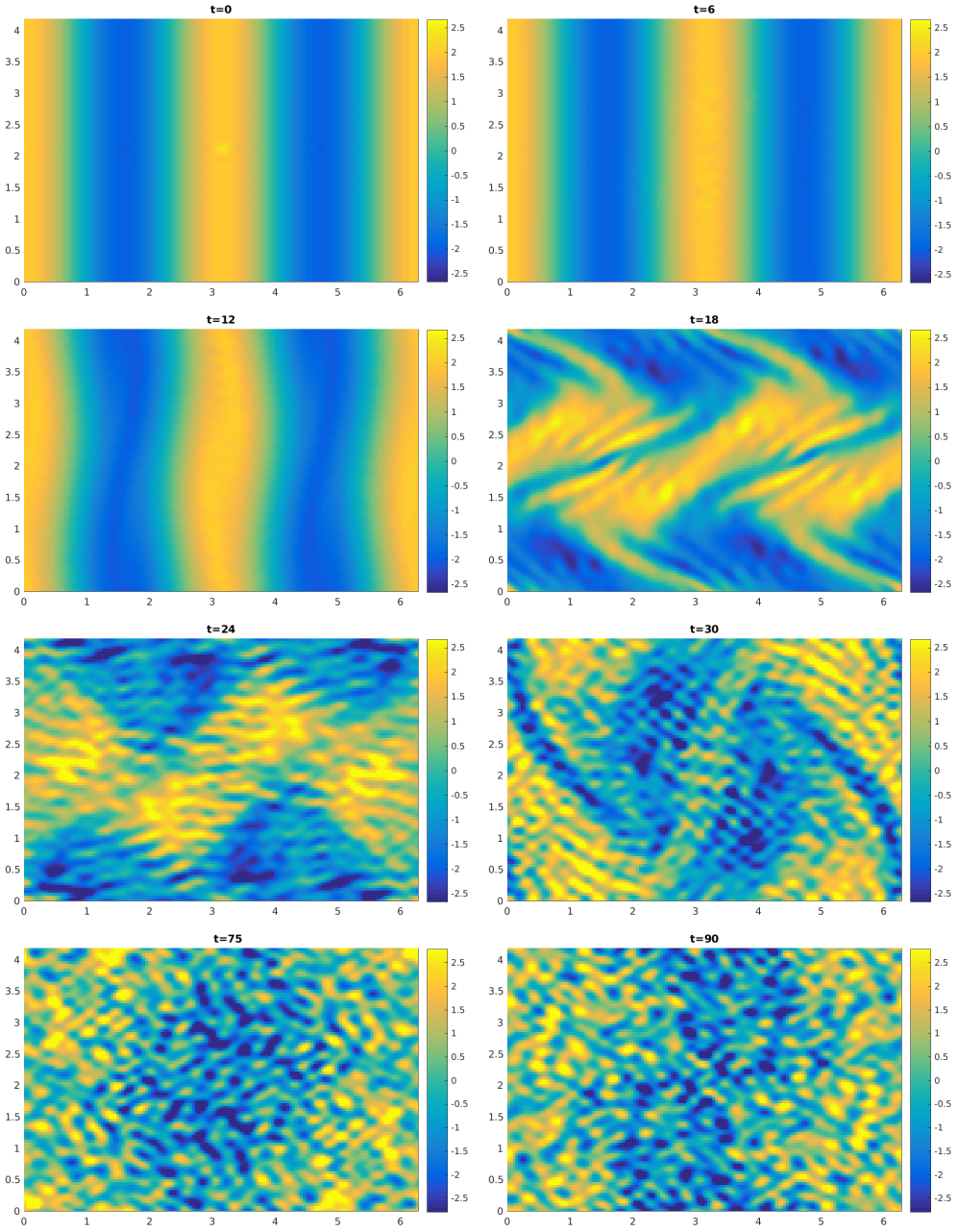

Figure 6.27 – The evolution of an initial condition consisting of a small perturbation of the steady state with parameter $\mathbf{p} = (2, 0)$ on the domain with size $\kappa_y/\kappa_x = 3/2$. As $\kappa_y/\kappa_x < p_x$, the steady state is unstable, which can be observed. The flow is calculated using the Poisson integrator for the sine-bracket truncated system with truncation size $N = 18$. The perturbation used is a Fourier-truncated Dirac delta function at the centre of the domain. The state is shown at times $t = 0,\ 6,\ 12,\ 18,\ 24,\ 30,\ 75,\ 90$.

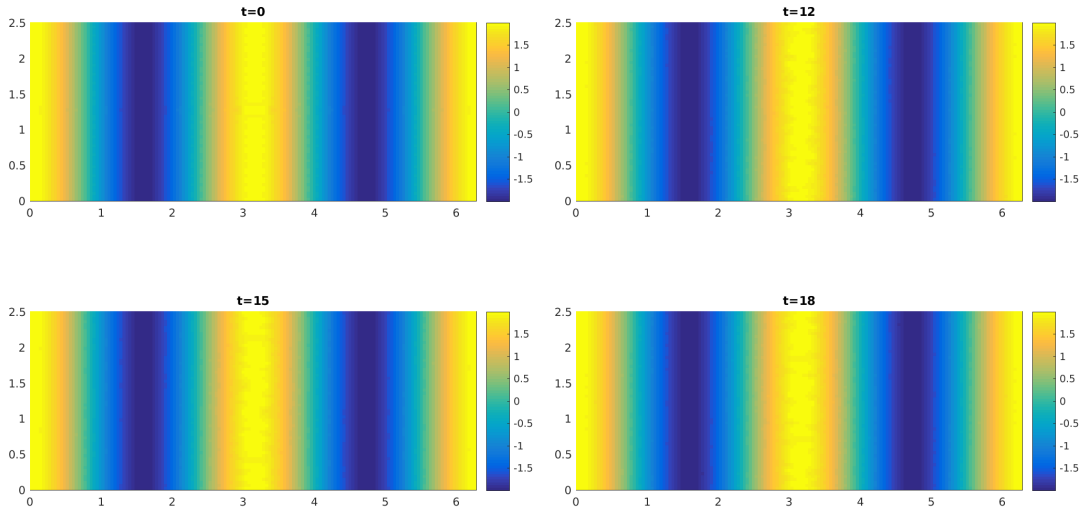

Figure 6.28 – The evolution of an initial condition consisting of a small perturbation of $\cos(2x)$ (i.e., the steady state with parameter $\mathbf{p} = (2, 0)$) on the domain with size $\kappa_y/\kappa_x = 5/2$. As $\kappa_y/\kappa_x > p_x$, the state is linearly stable by Theorem 2.6.1. The flow is calculated using the Poisson integrator for the sine-bracket truncated system with truncation size $N = 18$. In this truncation, the state is also energy-Casimir stable per Proposition 3.2.28 as $2N + 1 = 37$ is prime. The perturbation used is a Fourier-truncated Dirac delta function at the centre of the domain. The state is shown at times $t = 0,\ 12,\ 18,\ 24$.

a timestep $\mathrm{d}t = 0.1$. As per the result in Arnold [**Arn66b**], this flow is energy-Casimir stable if and only if $\kappa_y/\kappa_x > 1$. This is also a special case of Theorem 2.6.1, which shows linear stability for this case. In Figure 6.25, $\kappa_y/\kappa_x = 5/4 > 1$ so the flow is nonlinearly unstable. In Figure 6.26, $\kappa_y/\kappa_x = 5/6 < 1$ so the flow is energy-Casimir stable.

Figure 6.27 shows the evolution of a small perturbation of flow $\cos(2\kappa_x x)$ for a domain with $\kappa_y/\kappa_x = 3/2$. As $p_x = 2$, $\kappa_y/\kappa_x < p_x$ and so we expect nonlinear instability per Theorem 2.7.53. This is clearly observed from the evolution of the vorticity, which diverges towards a seemingly chaotic state.

Figure 6.28 shows the evolution of a small perturbation of the same flow $\cos(2\kappa_x x)$ on a different domain, with aspect ratio $\kappa_y/\kappa_x = 5/2$. Then $\kappa_y/\kappa_x > p_x = 2$ and we expect linear stability per Theorem 2.6.1. Additionally, as the flow is approximated using the sine-bracket truncated system, we expect this steady state to be energy-Casimir stable per Proposition 3.2.28 as $2N + 1 = 37$ is prime so $\gcd(p_x, 2N + 1) = 1$. We observe this stability; the perturbed steady state does not change in any visually recognisable way. This is a striking juxtaposition

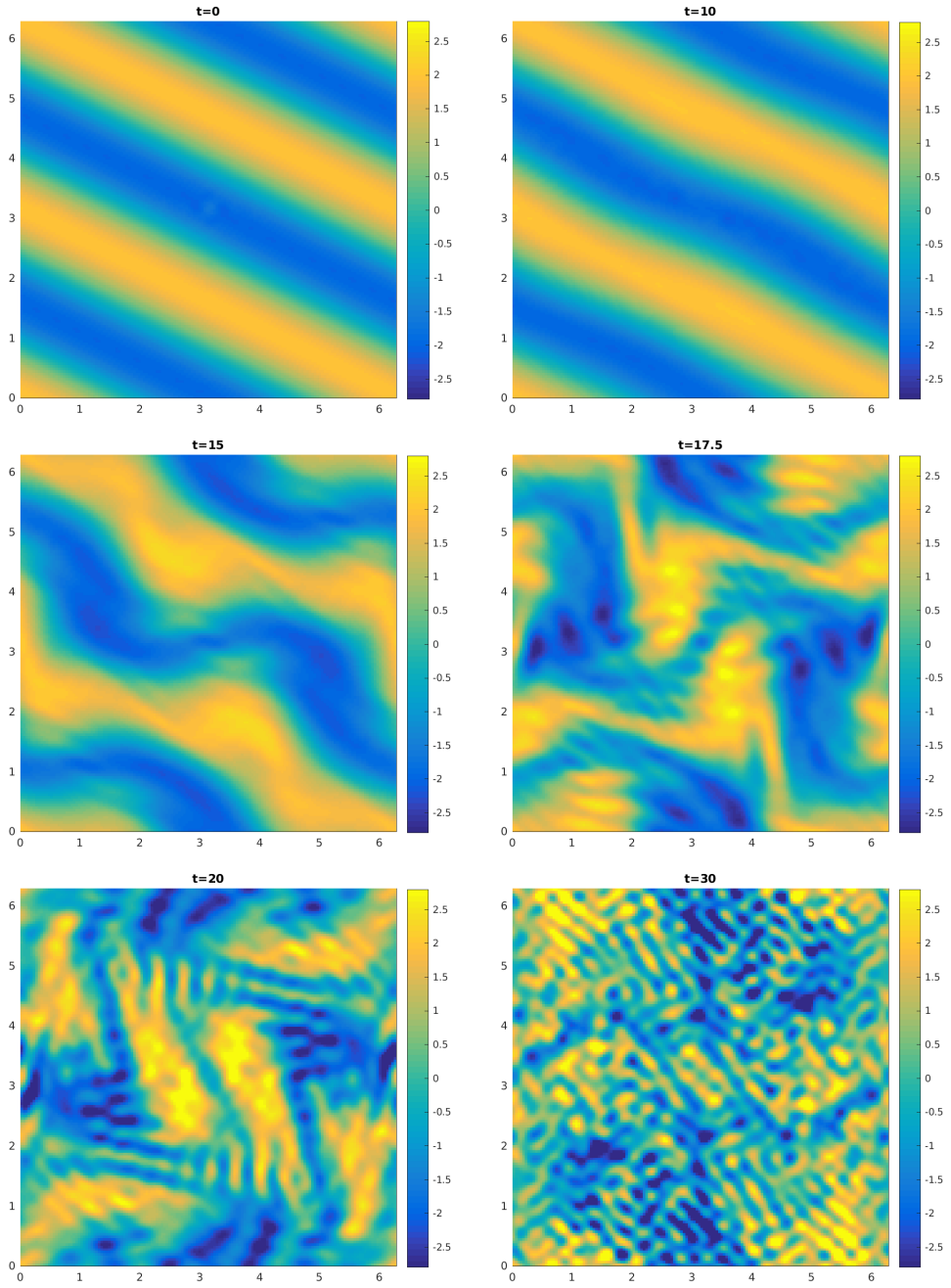

Figure 6.29 – The flow of an initial condition consisting of a small perturbation of the flow with $\mathbf{p} = (2, 1)$ and isotropic domain $\kappa_y/\kappa_x = 1$. For $\mathbf{p} = (2, 1)$, as $p_x, p_y \neq 0$ the flow will be unstable regardless of domain size. The flow is calculated using the Poisson integrator for the sine-bracket truncated system with truncation size $N = 18$. The perturbation used is a Fourier-truncated Dirac delta function at the centre of the domain. The state is shown at times $t = 0,\ 10,\ 15,\ 17.5,\ 20,\ 30$.

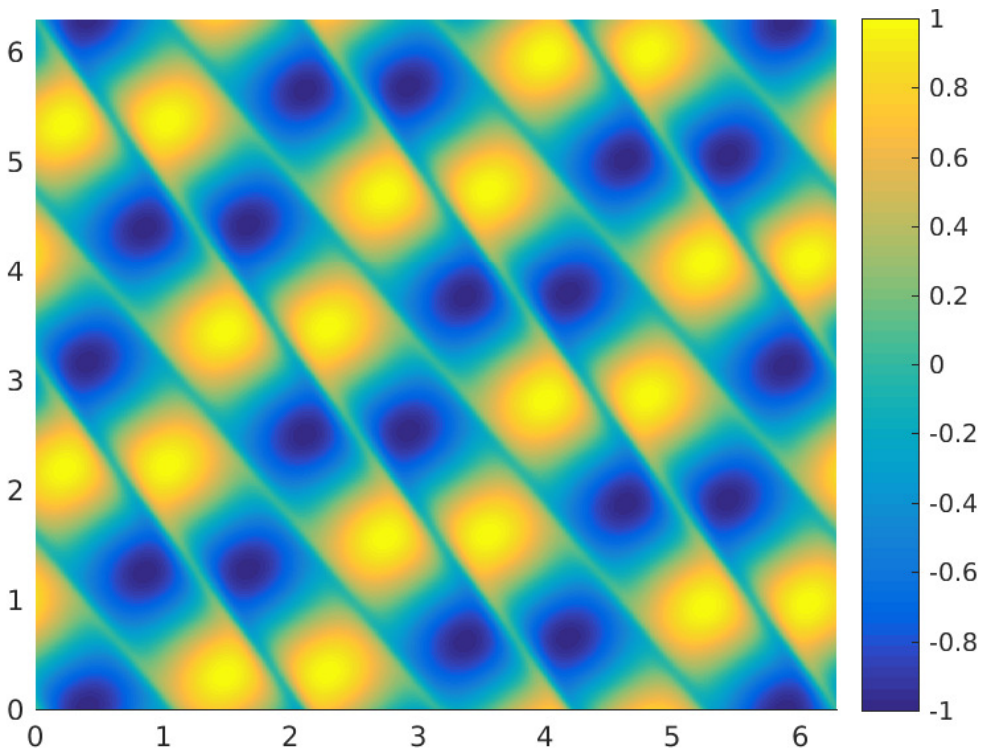

Figure 6.30 – An eigenfunction associated with a positive real eigenvalue of the steady state with $\mathbf{p} = (3, 2)$ and domain size $\kappa_y/\kappa_x = 1$. This eigenfunction is associated with the positive real eigenvalue $\lambda = 0.0420...$, which occurs in the class $\mathbf{a} = (-2, 2)$. A perturbation of the steady state by this function will grow exponentially in the linearised problem.

to Figure 6.27, where the same flow is calculated on a domain with a different aspect ratio.

Figure 6.29 shows the evolution of a small perturbation of the flow with $\Omega = \cos(2x + y)$, which is unstable. The domain size is $\kappa_x = \kappa_y = 1$, the isotropic domain. We observe nonlinear instability for any flow with vorticity of the form $\Omega = \cos(ax + by)$ for $a, b \neq 0$.

A YouTube video showing full videos of the flows shown in Figures 6.25, 6.26, 6.27, 6.28, and 6.29 is available at

`https://www.youtube.com/watch?v=5X3BmwPuCco`.

The full dynamics and the loss of stability can be seen in those videos.

We can also calculate the eigenfunction associated with a positive real eigenvalue; this gives a local approximation of how the flow will lose stability. Figure 6.30 shows an eigenfunction associated with a real eigenvalue in the system linearised around $\mathbf{p} = (3, 2)$ with $\kappa_y/\kappa_x = 1$. If the steady state is perturbed by this eigenfunction, the perturbation will grow exponentially in size.

Chapter 7

Conclusion

In this thesis, we have determined the stability of a large family of sinusoidal shear flows in both two- and three-dimensional periodic domains. We showed analytically that a family of parallel shear flows are linearly stable, and another family of shear flows are nonlinearly unstable in a two-dimensional domain and at least linearly unstable in a three-dimensional domain. Numerically we extended this to classify the stability of all sinusoidal shear flows, per Conjecture 6.1.8. To prove instability, we showed the existence of a positive real eigenvalue in the linearisation of the shear flows; this is a step towards a full analytic description of the spectrum of the linearised system.

Of particular note are the results for the three-dimensional periodic domain. The three-dimensional domain is more complicated and less well-understood than the two-dimensional equivalent. We showed that the linearised system decomposes into classes, and that generically these classes are equivalent to some corresponding class in the two-dimensional problem. We also discussed the exceptional nondiagonalisable classes that occur for a dense set of values of the parameters that set the steady state. This is related to the loss of nonlinear stability through nonnormality, which occurs even in the generic case.

A notable new result of this thesis is the development of a Poisson structure for the Euler equations on the three-dimensional periodic domain. By describing the dynamics of the vorticity Fourier modes as a Poisson system, we have opened the possibility of future study analysing and exploiting this structure. We also calculated the reduced structure on a simplified Poisson manifold, which allows for simpler stability analysis of this system. For the two-dimensional periodic domain, we discussed how the Poisson structure can be truncated to a finite-dimensional Poisson structure. It was shown that the stability results for shear flows also hold in this finite-dimensional system. We also generalised an existing Poisson integrator to an anisotropic domain, allowing for the efficient calculation of ideal fluid flows.

This thesis provides a step towards a complete analytic description of the nonimaginary spectrum. Future work would extend this to describe the full spectrum in terms of the number and type of nonimaginary eigenvalues. It seems hopeful that there is an explicit lower bound akin to the one calculated in Lemma 2.7.20 which can be calculated for all classes with real nonzero eigenvalues. New

techniques would be required to rigorously show the existence of complex eigenvalues as the proof of Lemma 2.7.20 relies on the application of the intermediate value theorem on the positive real axis. A promising avenue for studying such eigenvalues is the associated Jacobi problem discussed in Section 2.9. Studying this problem could prove analytically the existence of the complex eigenvalues calculated numerically in Section 6.1.2. A complete description of the imaginary spectrum per Conjecture 6.1.8 would broaden the instability result of Theorem 2.7.53 to all $\mathbf{p}$ that do not satisfy the conditions of Theorem 2.6.1. Additionally it would provide a more detailed understanding of the mechanisms that cause these steady states to become unstable.

It is hoped that the Poisson structure for the three-dimensional Euler equations described in Chapter 5 may find some use in the broader fluid mechanics research community. The existence of this structure may lead to further stability or instability results, perhaps resulting from a careful studies of the Casimirs and sub-Casimirs of the Poisson bracket. As the bracket has the Lie-Poisson form discussed in [**McL93**], one may formally be able to write down a Poisson integrator analogous to the one discussed in Section 3.3. However, as this is an infinite-dimensional system, there is currently no numerical use for this system. There may still be some way to exploit this structure to develop an accurate numerical integrator.

Another interesting possible avenue of future research is the analysis of the limit $\kappa_y/\kappa_x \to 0/\infty$ in the two-dimensional problem, and any possible physical interpretations of this limit. The numerical results of Section 6.2 show that this limiting problem has a remarkably coherent structure to its eigenvalues. This may be considered the dual to the problem of highly oscillatory flows studied in [**BFY99**]. There are also the equivalent limits on a three-dimensional domain.

It is possible that approaches similar to those used here could shed some light on the study of steady states of the Euler equations on the sphere. This has obvious geophysical applications, especially for the rotating sphere. A structure-preserving truncation analogous to the one discussed in this paper exists for the rotating sphere, in both the Euler and Navier-Stokes problems [**Zei04**]; this may prove useful in further research.

Although it is beyond the scope of this thesis, it is hoped that there are useful connections between these results and the existing body of work on shear flows. For instance, there is significant research on the relationship between the Euler equations and the inviscid limit of the Navier-Stokes equations. The results of this paper may suggest parallel results in the Navier-Stokes problem akin to the results in [**BW13**]. Understanding how the steady states we have studied become unstable may also be useful in the challenge to understand the transition from stable laminar flow to turbulence in the three-dimensional problem. As discussed in Section 4.3.3, the linearised problem can indicate a possible transition

to turbulence. The mechanism by which this transition occurs does not appear in the two-dimensional domain, and merits further study.

List of Figures

References

[AAR01] Ackroyd, J. A., Axcell, B. P., and Ruban, A. I., *Early developments of modern aerodynamics*, Oxford, 2001, Translation of Prandtl, L, 1904.

[Abr02] Abramov, R. V., *Statistically relevant and irrelevant conserved quantities for the equilibrium statistical description of the truncated Burger-Hopf equation and the equations for barotropic flow*, Ph.D. thesis, Rensselaer Polytechnic Institute, 2002.

[AK98] Arnold, V. I. and Khesin, B. A., *Topological Methods in Hydrodynamics*, Springer, 1998.

[Akh65] Akhiezer, N., *The Classical Moment Problem and some related questions in analysis*, Oliver & Boyd, 1965.

[AKN07] Arnold, V. I., Kozlov, V. V., and Neishtadt, A. I., *Mathematical aspects of classical and celestial mechanics*, vol. 3, Springer Science & Business Media, 2007.

[AMdL+11] Avila, K., Moxey, D., Lozar, A., Avila, M., Barkley, D., and Hof, B., *The onset of turbulence in pipe flow*, Science **333** (2011), no. 6039, 192–196.

[Arn66a] Arnold, V. I., *An a priori estimate in the theory of hydrodynamic stability*, Izvestiya Vysshikh Uchebnykh Zavedenii. Matematika (1966), no. 5, 3–5.

[Arn66b] ———, *Sur la géométrie différentielle des groupes de Lie de dimension infinie et ses applications à l'hydrodynamique des fluides parfaits*, Annales de l'institut Fourier, vol. 16, Institut Fourier, 1966, pp. 319–361.

[Arn78] ———, *Mathematical Methods of Classical Mechanics*, Springer, 1978.

[AWH10] Avila, M., Willis, A. P., and Hof, B., *On the transient nature of localized pipe flow turbulence*, Journal of Fluid Mechanics **646** (2010), 127–136.

[Bar72] Bardos, C., *Existence et unicité de la solution de l'équation d'Euler en dimension deux*, Journal of Mathematical Analysis and Applications **40** (1972), no. 3, 769–790.

[BB88] Böberg, L. and Brösa, U., *Onset of turbulence in a pipe*, Zeitschrift für Naturforschung A **43** (1988), no. 8-9, 697–726.

[BDT95] Baggett, J. S., Driscoll, T. A., and Trefethen, L. N., *A mostly linear model of transition to turbulence*, Physics of Fluids **7** (1995), no. 4, 833–838.

[BFY99] Belenkaya, L., Friedlander, S., and Yudovich, V. I., *The unstable spectrum of oscillating shear flows*, SIAM Journal on Applied Mathematics **59** (1999), no. 5, 1701–1715.

[BGS93] Benzel, S., Ge, Z., and Scovel, C., *Elementary construction of higher order Lie-Poisson integrators*, Physics Letters A **174** (1993), no. 3, 229–232.

[BHSS91] Bordemann, M., Hoppe, J., Schaller, P., and Schlichenmaier, M., *$gl(\infty)$ and geometric quantization*, Communications in Mathematical Physics **138** (1991), no. 2, 209–244.

[BM92] Bell, J. B. and Marcus, D. L., *Vorticity intensification and transition to turbulence in three-dimensional Euler equations*, Communications in Mathematical Physics **147** (1992), no. 2, 371–394.

[BN10] Butta, P. and Negrini, P., *On the Stability Problem of Stationary Solutions for the Euler Equation on a 2-Dimensional Torus*, Regular and Chaotic Dynamics **15** (2010), no. 6, 637–645.

[BW13] Beck, M. and Wayne, C. E., *Metastability and rapid convergence to quasi-stationary bar states for the two-dimensional Navier-Stokes equations*, Proceedings of the Royal Society of Edinburgh Section A - Mathematics **143** (2013), no. 5, 905–927.

[CCF+] Castro, A., Córdoba, D., Fefferman, C., Gancedo, F., and Gómez-Serrano, J., Annals of Mathematics. MR 3092476

[CH11] Cohen, D. and Hairer, E., *Linear energy-preserving integrators for Poisson systems*, BIT Numerical Mathematics **51** (2011), no. 1, 91–101.

[Chr07] Christodoulou, D., *The Euler equations of compressible fluid flow*, Bulletin of the American Mathematical Society **44** (2007), no. 4, 581–602.

[Con95] Constantin, P., *A few results and open problems regarding incompressible fluids*, Notices of the AMS **42** (1995), no. 6, 658–663.

[Con07] ———, *On the Euler equations of incompressible fluids*, Bulletin of the American Mathematical Society **44** (2007), no. 4, 603–621.

[CS91] Channell, P. J. and Scovel, J. C., *Integrators for Lie-Poisson dynamical systems*, Physica D: Nonlinear Phenomena **50** (1991), no. 1, 80–88.

[dG06] Gosson, M., *Symplectic geometry and quantum mechanics*, Operator Theory: Advances and Applications, vol. 166, Birkhäuser Verlag, Basel, 2006, Advances in Partial Differential Equations (Basel).

[DH66] Drazin, P. G. and Howard, L. N., *Hydrodynamic stability of parallel flow of inviscid fluid*, Advances in Applied Mechanics **9** (1966), 1–89.

[DP16] Dullin, H. R. and Pelayo, Á., *Generating Hyperbolic Singularities in Semitoric Systems Via Hopf Bifurcations*, Journal of Nonlinear Science **26** (2016), no. 3, 787–811.

[dS01] Silva, A. C., *Lectures on Symplectic Geometry*, Springer, 2001.

[Dul13] Dullin, H. R., *Two New Integrable Systems related to the Euler Equations on a Rotating Sphere*, Presentation at 57th Annual AustMS Meeting, 2013.

[DW92] Dowker, J. S. and Wolski, A., *Finite model of two-dimensional ideal hydrodynamics*, Physical Review A **46** (1992), no. 10, 6417.

[DW14] Dullin, H. R. and Worthington, J., *The vanishing twist in the restricted three-body problem*, Physica D: Nonlinear Phenomena **276** (2014), 12–20.

[DW16] Dullin, H. R. and Worthington, J., *Stability results for idealised shear flows on a rectangular periodic domain*, arXiv preprint arXiv:1608.06109 (2016).

[DWM16] Dullin, H. R., Worthington, J., and Marangell, R., *Instability of Equilibria for the Two-Dimensional Euler Equations on the Torus*, SIAM Journal on Applied Mathematics **76** (2016), 1446–1470.

[Egi95] Egilsson, Á., *On embedding the 1:1:2 resonance space in a Poisson manifold*, Electronic Research Announcements of the American Mathematical Society **1** (1995), no. 2, 48–56.

[EP87] Elsner, L. and Paardekooper, M., *On measures of nonnormality of matrices*, Linear Algebra and its Applications **92** (1987), 107–123.

[ESHW07] Eckhardt, B., Schneider, T. M., Hof, B., and Westerweel, J., *Turbulence transition in pipe flow*, Annual Review of Fluid Mechanics **39** (2007), 447–468.

[Eul55] Euler, L., *Principes generaux de l'etat d'equilibre des fluides; Principes generaux du mouvement des fluides; Continuation des recherches sur la theorie du mouvement des fluides*, Histoire de l'Acacdernie de Berlin (1755).

[Fav36] Favard, J., *Sur les polynomes de Tchebicheff*, Comptes Rendus de l'Académie des Sciences **200** (1936), 2052–2053.

[Fef06] Fefferman, C. L., *Existence and smoothness of the Navier-Stokes equation*, The millennium prize problems (2006), 57–67.

[FFZ89] Fairlie, D. B., Fletcher, P., and Zachos, C. K., *Trigonometric structure constants for new infinite-dimensional algebras*, Physics Letters B **218** (1989), no. 2, 203–206.

[FMRT01] Foias, C., Manley, O., Rosa, R., and Temam, R., *Navier-Stokes equations and turbulence*, vol. 83, Cambridge University Press, 2001.

[FS02] Friedlander, S. and Serre, D. (eds.), *Handbook of mathematical fluid dynamics. Vol. I*, North-Holland, Amsterdam, 2002. MR 1942463

[FS03] Friedlander, S. and Serre, D. (eds.), *Handbook of mathematical fluid dynamics. Vol. II*, North-Holland, Amsterdam, 2003. MR 1983587

[FS04] Friedlander, S. and Serre, D. (eds.), *Handbook of mathematical fluid dynamics. Vol. III*, North-Holland, Amsterdam, 2004. MR 2099032

[FSV97] Friedlander, S., Strauss, W., and Vishik, M., *Nonlinear instability in an ideal fluid*, Annales de l'Institut Henri Poincare (C) Non Linear Analysis, vol. 14, Elsevier, 1997, pp. 187–209.

[FZ89] Fairlie, D. B. and Zachos, C. K., *Infinite-dimensional algebras, sine brackets, and $SU(\infty)$*, Physics Letters B **224** (1989), no. 1, 101–107.

[GG94] Gebhardt, T. and Grossmann, S., *Chaos transition despite linear stability*, Physical Review E **50** (1994), no. 5, 3705.

[GGK00] Gibbon, J. D., Galanti, B., and Kerr, R. M., *Stretching and compression of vorticity in the 3D Euler equations*, Turbulence structure and vortex dynamics (Cambridge, 1999), Cambridge Univ. Press, Cambridge, 2000, pp. 23–34.

[Gib08] Gibbon, J. D., *The three-dimensional Euler equations: Where do we stand?*, Physica D: Nonlinear Phenomena **237** (2008), no. 14, 1894–1904.

[Gra06] Gray, R. M., *Toeplitz and circulant matrices: A review*, now publishers inc, 2006.

[Gro00] Grossmann, S., *The onset of shear flow turbulence*, Reviews of Modern Physics **72** (2000), no. 2, 603.

[Hel68] Helmholtz, H. v., *XLIII. On discontinuous movements of fluids*, The London, Edinburgh, and Dublin Philosophical Magazine and Journal of Science **36** (1868), no. 244, 337–346.

[Hen81] Henry, D., *Geometric theory of semilinear parabolic equations*, LNM 840, Springer, 1981.

[HJ12] Horn, R. A. and Johnson, C. R., *Matrix analysis*, Cambridge university press, 2012.

[HLW06] Hairer, E., Lubich, C., and Wanner, G., *Geometric numerical integration: structure-preserving algorithms for ordinary differential equations*, vol. 31, Springer Science & Business Media, 2006.

[HMH14] Hirota, M., Morrison, P. J., and Hattori, Y., *Variational necessary and sufficient stability conditions for inviscid shear flow*, Proceedings of the Royal Society of London A: Mathematical, Physical and Engineering Sciences, vol. 470, The Royal Society, 2014, p. 20140322.

[HMRW85] Holm, D. D., Marsden, J. E., Ratiu, T., and Weinstein, A., *Nonlinear stability of fluid and plasma equilibria*, Physics Reports **123** (1985), no. 1, 1–116.

[HN01] Hunter, J. K. and Nachtergaele, B., *Applied Analysis*, World Scientific Publishing Co Inc, 2001.

[Hop89] Hoppe, J., *Diffeomorphism groups, quantization, and $SU(\infty)$*, International Journal of Modern Physics A **4** (1989), no. 19, 5235–5248.

[IP06] Iftimie, D. and Planas, G., *Inviscid limits for the Navier–Stokes equations with Navier friction boundary conditions*, Nonlinearity **19** (2006), no. 4, 899.

[KB08] Krstulovic, G. and Brachet, M.-É., *Two-fluid model of the truncated Euler equations*, Physica D: Nonlinear Phenomena **237** (2008), no. 14, 2015–2019.

[Kol07] Kolev, B., *Poisson brackets in Hydrodynamics*, Discrete and Continuous Dynamical Systems **19** (2007), 555–574.

[Lax68] Lax, P. D., *Integrals of nonlinear equations of evolution and solitary waves*, Communications on Pure and Applied Mathematics **21** (1968), no. 5, 467–490.

[Li00] Li, Y. C., *On 2D Euler equations. I. On the energy-Casimir stabilities and the spectra for linearized 2D Euler equations*, Journal of Mathematical Physics **41** (2000), no. 2, 728–758.

[Lin03] Lin, Z., *Instability of some ideal plane flows*, SIAM Journal on Mathematical Analysis **35** (2003), no. 2, 318–356.

[Lin04] ———, *Some stability and instability criteria for ideal plane flows*, Communications in Mathematical Physics **246** (2004), no. 1, 87–112.

[LLS04] Latushkin, Y., Li, Y. C., and Stanislavova, M., *The Spectrum of a Linearized 2D Euler Operator*, Studies in Applied Mathematics **112** (2004), 259–270.

[McH94] McHugh, J. P., *Surface waves on an inviscid shear flow in a channel*, Wave motion **19** (1994), no. 2, 135–144.

[McL93] McLachlan, R. I., *Explicit Lie-Poisson integration and the Euler equations*, Physical Review Letters **71** (1993), no. 19, 3043.

[Mei07] Meiss, J. D., *Differential Dynamical Systems*, SIAM Mathematical Modelling and Computing, 2007.

[Mey82] Meyer, R. E., *Introduction to mathematical fluid dynamics*, Dover Publications, Inc., New York, 1982, Corrected reprint of the 1971 original. MR 691853

[MG80] Morrison, P. J. and Greene, J. M., *Noncanonical Hamiltonian density formulation of hydrodynamics and ideal magnetohydrodynamics*, Physical Review Letters **45** (1980), no. 10, 790.

[MMSE09] Mellibovsky, F., Meseguer, A., Schneider, T. M., and Eckhardt, B., *Transition in Localized Pipe Flow Turbulence*, Phys. Rev. Lett. **103** (2009), 054502.

[Mor98] Morrison, P. J., *Hamiltonian description of the ideal fluid*, Reviews of Modern Physics **70** (1998), no. 2, 467.

[Mor06] ———, *Hamiltonian fluid dynamics*, Encyclopedia of Mathematical Physics **2** (2006).

[MQR98] McLachlan, R. I., Quispel, G., and Robidoux, N., *Unified approach to Hamiltonian systems, Poisson systems, gradient systems, and systems with Lyapunov functions or first integrals*, Physical Review Letters **81** (1998), no. 12, 2399.

[MS61] Meshalkin, L. and Sinai, I. G., *Investigation of the stability of a stationary solution of a system of equations for the plane movement of an incompressible viscous liquid*, Journal of Applied Mathematics and Mechanics **25** (1961), no. 6, 1700–1705.

[Olv00] Olver, P. J., *Applications of Lie groups to differential equations*, vol. 107, Springer Science & Business Media, 2000.

[OPBR05] Ortega, J.-P., Planas-Bielsa, V., and Ratiu, T. S., *Asymptotic and Lyapunov stability of constrained and Poisson equilibria*, Journal of Differential Equations **214** (2005), no. 1, 92–127.

[Orr07] Orr, W. M. F., *The stability or instability of the steady motions of a perfect liquid and of a viscous liquid. Part II: A viscous liquid*, Proceedings of the Royal Irish Academy. Section A: Mathematical and Physical Sciences, vol. 27, JSTOR, 1907, pp. 69–138.

[Ors77] Orszag, S. A., *Fluid Dynamics: Les Houches - Statistical Theory of Turbulence*, 1977.

[PMO01] Peradzynski, Z., Makaruk, H. E., and Owczarek, R. M., *On Group-Theoretic Finite-Mode Approximation of 2D Ideal Hydrodynamics*, arXiv preprint math-ph/0112011 (2001).

[PR90] Pope, C. N. and Romans, L. J., *Local area-preserving algebras for two-dimensional surfaces*, Classical and Quantum Gravity **7** (1990), 97–109.

[PRW04] Patrick, G. W., Roberts, M., and Wulff, C., *Stability of Poisson equilibria and Hamiltonian relative equilibria by energy methods*, Archive for Rational Mechanics and Analysis **174** (2004), no. 3, 301–344.

[Pum96] Pumir, A., *Turbulence in homogeneous shear flows*, Physics of Fluids (1994-present) **8** (1996), no. 11, 3112–3127.

[PW82] Pierrehumbert, R. T. and Widnall, S. E., *The two-and three-dimensional instabilities of a spatially periodic shear layer*, Journal of Fluid Mechanics **114** (1982), 59–82.

[Ray79] Rayleigh, L., *On the stability, or instability, of certain fluid motions*, Proceedings of the London Mathematical Society **1** (1879), no. 1, 57–72.

[Rey83] Reynolds, O., *An experimental investigation of the circumstances which determine whether the motion of water shall be direct or sinuous, and of the law of resistance in parallel channels.*, Proceedings of the Royal Society of London **35** (1883), no. 224-226, 84–99.

[RS78] Reed, M. and Simon, B., *Methods of modern mathematical physics IV: Analysis of Operators*, vol. 4, Elsevier, 1978.

[Rut83] Ruth, R. D., *A canonical integration technique*, IEEE Transactions on Nuclear Science **30** (1983), no. 4, 2669–2671.

[SL03] Shvidkoy, R. and Latushkin, Y., *The essential spectrum of the linearized 2D Euler operator is a vertical band*, Contemporary Mathematics **327** (2003), 299–304.

[Som08] Sommerfeld, A., *Ein beitrag zur hydrodynamischen erklaerung der turbulenten fluessigkeitsbewegungen*, Atti Del **4** (1908), 116–124.

[Ste99] Sternberg, S., *Lectures on differential geometry*, American Mathematical Soc., 1999.

[Sto51] Stokes, G. G., *On the effect of the internal friction of fluids on the motion of pendulums*, vol. 9, Pitt Press, 1851.

[Str83] Strutt, J. W., *Investigation of the character of the equilibrium of an incompressible heavy fluid of variable density*, Proc. London Math. Soc **14** (1883), no. 1, 8.

[Sze39] Szegő, G., *Orthogonal Polynomials*, American Mathematical Society, 1939.

[Tao16] Tao, M., *Explicit symplectic approximation of nonseparable Hamiltonians: Algorithm and long time performance*, Physical Review E **94** (2016), no. 4, 043303.

[Tay50] Taylor, G. I., *The instability of liquid surfaces when accelerated in a direction perpendicular to their planes. I*, Proceedings of the Royal Society of London A: Mathematical, Physical and Engineering Sciences, vol. 201, The Royal Society, 1950, pp. 192–196.

[Tay71] ———, *The Scientific Papers of Sir Geoffrey Ingram Taylor: Volume 4, Mechanics of Fluids: Miscellaneous Papers*, vol. 4, Cambridge University Press, 1971.

[TE05] Trefethen, L. N. and Embree, M., *Spectra and pseudospectra: the behavior of nonnormal matrices and operators*, Princeton University Press, 2005.

[Tes00] Teschl, G., *Jacobi operators and completely integrable nonlinear lattices*, no. 72, American Mathematical Soc., 2000.

[Tho71] Thomson, W., *XLVI. Hydrokinetic solutions and observations*, The London, Edinburgh, and Dublin Philosophical Magazine and Journal of Science **42** (1871), no. 281, 362–377.

[TTRD93] Trefethen, L. N., Trefethen, A. E., Reddy, S. C., and Driscoll, T. A., *Hydrodynamic Stability Without Eigenvalues*, Science **261** (1993), no. 5121, 578–584.

[WG96] Wolansky, G. and Ghil, M., *An extension of Arnol'd's second stability theorem for the Euler equations*, Physica D: Nonlinear Phenomena **94** (1996), no. 4, 161–167.

[WG98] ———, *Nonlinear stability for saddle solutions of ideal flows and symmetry breaking*, Communications in Mathematical Physics **193**

(1998), no. 3, 713–736.

[Whi99] White, F. M., *Fluid Mechanics*, ed: McGraw-Hill, Boston (1999).

[Wu97] Wu, S., *Well-posedness in Sobolev spaces of the full water wave problem in 2-D*, Inventiones Mathematicae **130** (1997), no. 1, 39–72.

[Wu99] ———, *Well-posedness in Sobolev spaces of the full water wave problem in 3-D*, Journal of the American Mathematical Society **12** (1999), no. 2, 445–495.

[YM16] Yoshida, Z. and Morrison, P. J., *Epi-two-dimensional flow and generalized enstrophy*, arXiv preprint arXiv:1604.02339 (2016).

[YMC03] Yin, Z., Montgomery, D. C., and Clercx, H. J. H., *Alternative statistical-mechanical descriptions of decaying two-dimensional turbulence in terms of "patches" and "points"*, Physics of Fluids (1994-present) **15** (2003), no. 7, 1937–1953.

[Yud65] Yudovich, V. I., *Example of secondary stationary flow or periodic flow appearing while a laminar flow of a viscous incompressible fluid loses its stability*, Appl. Math. Mech **29** (1965), no. 3, 453–467.

[Yud03] ———, *Eleven great problems of mathematical hydrodynamics*, Moscow Mathematical Journal **3** (2003), no. 2, 711–737.

[Zei91] Zeitlin, V., *Finite-mode analogs of 2D ideal hydrodynamics: Coadjoint orbits and local canonical structure*, Physica D: Nonlinear Phenomena **49** (1991), no. 3, 353–362.

[Zei04] ———, *Self-consistent finite-mode approximations for the hydrodynamics of an incompressible fluid on nonrotating and rotating spheres*, Physical Review Letters **93** (2004), no. 26, 264501.

[Zei05] ———, *On self-consistent finite-mode approximations in (quasi-)two-dimensional hydrodynamics and magnetohydrodynamics*, Physics Letters A **339** (2005), 316–324.

[Zha08] Zhang, X., *Dynamics and numerics of generalised Euler equations*, Ph.D. thesis, Massey University, Palmerston North, New Zealand, 2008.